Synthesis and Characterisation of $CuInS_2$ Quantum Dots

Matthew Booth

Submitted in accordance with the requirements for the degree of
Doctor of Philosophy

The University of Leeds
School of Physics & Astronomy

September, 2014

The candidate confirms that the work submitted is his/her own and that appropriate credit has been given where reference has been made to the work of others.

The candidate confirms that the work submitted is his/her own, except where work which has formed part of jointly authored publications has been included. The contribution of the candidate and the other authors to this work has been explicitly indicated below. The candidate confirms that appropriate credit has been given within the thesis where reference has been made to the work of others.

This thesis is based on work published in the following three articles:

1) Booth, M.; Brown, A. P.; Evans, S. D and Critchley, C., Determining the Concentration of $CuInS_2$ Quantum Dots from the Size-Dependent Molar Extinction Coefficient, *Chemistry of Materials*, **2012**, 24, 11, 2064-2070

These experimental results are credited to Matthew Booth and form the basis of Chapters 3 and 5 of this thesis. The contribution of all co-authors was related to data analysis and manuscript editing. Atomic absorption spectroscopy was performed by Ian Blakely.

2) Booth, M.; Peel, R.; Partanen, R.; Hondow, N.; Vasilca, V.; Jeuken, L. J. C. and Critchley, K., Amphipol-encapsulated $CuInS_2$/ZnS quantum dots with excellent colloidal stability, *RSC Advances*, **2013**, 3, 20559-20566

The results published in this article are used in Chapter 6 of this thesis. Contributions from R. Peel include fluorescence spectroscopy of nanoparticles in presence of metal ions; contributions from R. Partanen, L. J. C. Jeuken and V. Vasilca include cell viability assays; contributions from N. Hondow include STEM images; and contributions from K. Critchley include data anlysis and manuscript editing.

3) Kraatz, I.; Booth, M.; Whitaker, B. J.; Nix, M. and Critchley, K., Sub-Bandgap Emission and Intraband Defect-Related Excited State Dynamics in Colloidal $CuInS_2$/ZnS Quantum Dots Revealed by Femtosecond Pump-Dump-Probe Spectroscopy, *Journal Physical Chemistry C*, **2014**, X, X, X

The results published in this article are used in Chapter 4 of this thesis. Ingvar Kraatz is credited as the first author of this publication and was responsible for the transient absorption spectroscopy and ‘pump-dump-probe’ spectroscopy data acquisition. B. J. Whitaker, M. Nix and K. Critchley are attributed with data analysis and manuscript editing.

Acknowledgments

First and foremost I would like to thank my primary supervisor Dr. Kevin Critchley for his continuing support and guidance. I feel fortunate to have been Kevin's first PhD student and have learnt much about all aspects of doing research over the last four years. I would also like to thank Prof. Stephen Evans and Dr. Andy Brown for their less frequent but equally invaluable advice.

I would like to thank Dr. Mike Ward and Dr. Nicole Hondow for their constant willingness to help with electron microscopy, Dr. Tim Comyn for sharing his talents in X-ray diffraction and Dr. Jo Galloway for her general advice and input.

I am greatly indebted to Dr. Mike Nix, Prof. Ben Whitaker and Ingvar Kraatz for introducing me to transient absorption spectroscopy and PDP spectroscopy, and for forming a very satisfying collaboration with Kevin and myself.

I would like to mention Lars Jeuken, Riita Partanen and Vlad Vasilca for their much-appreciated efforts in the toxicological evaluation of CIS QDs.

I gratefully acknowledge the funding institutions which enabled this research, in particular ESPRC and BHRC in Leeds.

I would like to thank all in the Molecular and Nanoscale Physics group for being a source of good advice - both academic and non-academic.

Finally, I would like to thank my family and friends, who have put up with the inevitable moments of panic and stress and have ultimately kept me on track.

Abstract

The interesting optical properties of quantum dots (QDs) may be important for many applications including bioimaging, LEDs and solar cells. Until recently, cadmium-based QDs have been by far the most developed, since the synthesis is straight-forward and their band gaps lie in the visible region of the spectrum, allowing for simple characterisation. However, cadmium is toxic and its commercial use in such applications has therefore been limited by legislation worldwide, motivating research into alternative, less ‘toxic’ QD materials such as $CuInS_2$.

The ternary nature of $CuInS_2$ (CIS) results in an abundance of intrinsic point defects which introduce additional complexities into the excited state dynamics. Although the optoelectronic properties of cadmium-based QDs are very well understood, the apparent defect-related photoluminescence emission in CIS QDs is not understood completely. In addition, the synthesis of CIS QDs is not as well developed and can only currently be performed in high temperature solvothermal reactions, producing hydrophobic QDs.

This thesis is concerned with the synthesis and characterisation of CIS and CIS/ZnS core/shell QDs and attempts to elucidate the excited state dynamics of these technologically important QDs as well as developing alternative synthesis and post-synthesis methods to produce water-soluble CIS QDs.

Transient absorption spectroscopy and 'pump-dump-probe' spectroscopy were used to resolve excited state dynamics, showing that the emission does not originate from the conduction band, as hypothesised in the literature, but from a high-lying intra-gap donor state.

An established synthesis procedure for CIS QDs was modified to provide alternative stabilising surface ligands such as hydroxyl and carboxylic acid terminated thiol ligands, which enabled QDs to be dispersed in methanol and water. A post-synthesis modification step, involving the encapsulation of hydrophobic $CuInS_2$/ZnS QDs with amphiphilic polymers (amphipols) to produce hydrophilic QD/polymer hybrid nanoparticles that is stable in the aqueous phase, was also shown to be an effective method.

Contents

List of Figures

Figure 2.11: Schematic diagram showing the components and lay-out of the TA spectroscopy set-up.

Figure 2.12: Schematic diagram showing the components of a typical photoelectron spectroscopy set-up enabling XPS, UPS and LEED/Auger analysis to be performed.

Figure 2.13: CIS/ZnS QD solutions deposited in 1:1 methanol: chloroform solution. Columns from left to right: 0 minutes, 3 minutes, 10 minutes and 15 minutes beam exposure time. Rows from top: 10μM, 5μM and 2.5μM QD concentration.

Figure 3.1: a) Low magnification HR-TEM image of CIS QDs showing uniform size distribution (scale bar 10 nm). The triangular morphology of the QDs projected in TEM suggests tetrahedral morphology; b) High magnification HR-TEM image (Scale bar 5 nm). Measured lattice fringe separations of 0.195 nm and 0.320 nm correspond to the (220) and (112) crystal planes, respectively. The definition of QD size, *d*, used throughout this thesis is illustrated.

Figure 3.2: Gray value profile of a line drawn through a series of lattice fringes in the high magnification HR-TEM shown in Figure 3.1 b). The black solid line represents a fit using a sine waveform.

Figure 3.3: a) HAADF image of CIS QDs at high magnification (900 kx) showing tetrahedral morphology; and b) at lower magnification (320 kx) showing uniform size distribution.

Figure 3.4: Histograms showing the size distributions of four CIS QDs of increasing size from a) to d). Bin widths in a) to c) are 0.1 nm and in d) is 0.2 nm. Black lines represent a Gaussian fit to the histogram. Measured size and size dispersion (FWHM) were as follows: a) 2.9 ± 0.8 nm; b) 3.1 ± 0.8 nm; c) 3.5 ± 1.1 nm; and d) 3.8 ± 1.4 nm. Each sample was sized by counting at least 100 individual particles

Figure 3.5: XRD pattern for powdered CIS QDs. A good correlation with reference data for CIS chalcopyrite (shown as vertical lines on the x-axis (JPCDS File Card No. 75-0106)) is observed with peaks indexed to the Miller indices of this phase.

Figure 3.6: Survey XPS spectrum of CIS QDs on Au substrate. The individual peaks used for quantitative compositional analysis are labelled.

Figure 3.7: XPS spectra (solid grey line), fitted with Voigt distributions (dashed lines) in Casa XPS. a) C 1s; b) Cu 2p; c) In 3d; and d) S 2p.

Figure 3.8: UPS spectrum of CIS QDs showing the valence band structure (grey line). A Tougaard baseline is used to fit a total of 7 Voigt functions (thin black lines) to the data, giving a good envelope fit (dashed black line). These fits are a guide to the eye only.

Figure 3.9: The low energy side of Figure 3.8 magnified. The red line represents an extrapolation of a linear fit to the x-axis, intercepting at 0.89 eV.

Figure 3.10: a) Typical PL emission spectrum (red line) and UV/Vis spectrum (black line) for $CuInS_2$ QDs. The second derivative of the absorption spectrum is shown (dashed line); b) Digital photograph of CIS QDs illuminated with a UV lamp.

Figure 3.11: Absorption (black circles) and excitation (white circles) spectra of 3 nm CIS QDs.

Figure 3.12: a) Two ‘tauc’ plots showing $(Ah\nu)^2$ and $(Ah\nu)^{1/2}$ against photon energy $h\nu$ where α is the absorption from Figure 3.12. The red lines represent linear fits to the data in the region $h\nu > E_g$ and are extrapolated to the *x*-axis to determine the band gap of the CIS QDs. b) Illustration showing the approximate position of the Fermi level within the band gap of the CIS QDs.

Figure 3.13: Plot of the integrated PL area against absorption as measured by UV/visible spectroscopy for both CIS QDs (filled circles) suspended in hexane and Lucifer Yellow dye suspended in water (hollow circles). The black solid and dashed lines represent linear fits to the Lucifer Yellow and CIS QD data, respectively.

Figure 3.14: Normalised PL spectra for five CIS QD samples of increasing size from left to right. The first four samples correspond to the QDs for which size-histograms are shown in Figure 3.4: a) 2.9 ± 0.8 nm; b) 3.1 ± 0.8 nm; c) 3.5 ± 1.1 nm; and d) 3.8 ± 1.4 nm (dot-dashed line). The fifth spectrum e) corresponds to large QDs grown for 30 minutes under the conditions described in section 2.1.1 (size unknown).

Figure 3.15: Second derivatives of PL spectral peaks a), b) c), d) and e) from Figure 3.15.

Figure 3.16: Second derivatives of 5 CIS QD samples of increasing size (from bottom to top): a) 3.0 nm; b) 3.2 nm; c) 3.4 nm; d) 3.6 nm; and e) 3.8 nm as determined by HR-TEM imaging (not shown).

Abbreviations

AAS – atomic absorption spectroscopy
CB – conduction band
CCD- charge coupled device
CFS – copper iron disulfide ($CuFeS_2$)
CIS – copper indium disulfide ($CuInS_2$)
DAP – donor-acceptor pair
DCD – diafiltration centrifugation device
DDT – dodecanethiol
DLS – dynamic light scattering
EDX – energy-dispersive X-ray spectroscopy
ESA – excited state absorption
FLIM – Fluorescence lifetime imaging microscopy
GSB – ground state bleach
HAADF – high-angle annular dark field
HB – hole-burning
IPA – isopropyl alcohol
IR – infra-red
LED – light emitting diode
MeOH – methanol
MNP – magnetic nanoparticle
MRI – magnetic resonance imaging
MUA – mercaptoundecanoic acid
MUD – mercaptoundecanol
NaOH – sodium hydroxide
NC – nanocrystal
NIR – near infra-red
NOPA – non-linear optical parametric amplification
OD – optical density
ODE – octadecene
OLA – oleylamine
PEG – polyethylene glycol
PL – photoluminescence
PLQY- photoluminescence quantum yield
PMAL-d – poly(maleic anhydride-alt-1-octadecene), 3-(dimethylamino)-1-propylamine derivative
PTFE – polytetrafluoroethylene
QD – quantum dot
SE- stimulated emission
STED – stimulated emission depletion microscopy
STEM – scanning transmission electron microscopy
TA- transient absorption
TEM – transmission electron microscopy

TFF – tangential flow filtration
TOP - tricotylphosphate
TOPO – trioctylphosphine oxide
UV – ultra-violet
VB – valence band
XPS – X-ray photoelectron spectroscopy
XRD – X-ray diffraction
ZDEC – zinc diethyl-dithiocarbamate

Chapter 1

Introduction

1.1 Quantum Dots

Nanotechnology is a sensational development not simply because of the ability to produce quantitatively smaller structures, components and devices; but rather it is the qualitatively different phenomena that arise at the nanoscale which open up entirely new avenues for the application of materials in technology [1].

Colloidal semiconductor nanocrystals provide an excellent illustration of this concept. As the crystal size is reduced below a critical value, typically 5-20 nm, charge carriers experience spatial confinement in all three dimensions and the electronic structure becomes intermediate between the discrete quantised energy levels associated with a single atom and the continuous energy bands observed in bulk semiconductors [2]. Semiconductor nanocrystals in this confinement regime are therefore commonly known as quantum dots (QDs) or artificial atoms.

Furthermore, the surface area per unit volume increases significantly as the crystal dimensions are reduced to the nanoscale. For the smallest nanocrystals the majority of atoms are at the QD surface. The foreseen applications of the large surface area and discrete electronic structure were initially limited to photocatalysis [3]; the irradiation of nanocrystals suspended in water was deemed to be more efficient approach towards water splitting than electrolysis. In the 1990s, however, optical investigations into quantum confined semiconductor nanocrystals revealed the more far-reaching implications for science and technology [4]. Colloidal QDs have now developed into one of the most rapidly developing areas of nanotechnology with a market size of approximately $ 316 million in 2013 that is expected to increase by more than ten times by 2020 [5].

The large surface area, tunable band gap and atom-like electronic structure of QDs has led to their being advocated as integral components for numerous applications, including: as emissive constituents in light emitting diodes (LEDs), producing brighter, more efficient light over a wider range of wavelengths than most current display technologies [6]; as a lasing medium [7] and as a sensitising component in the next generation of solar cells, since strong absorption throughout the entire solar spectrum can be achieved and multiple exciton generation enables quantum efficiency greater than 100% [8].

This thesis focuses on the study of colloidal QDs as fluorescent probes for potential use in imaging of biological systems and processes [9]. Since the first fluorescence microscopes were used to observe the auto-fluorescence of biological specimens over a century ago, developments in both instrumentation and in the ability to stain or label biological samples with fluorescent molecules have occurred concomitantly and have significantly extended the utility of fluorescence in the life sciences [10, 11].

Due to improved excitation sources and photon detection mechanisms, modern fluorescence microscopes display a significantly improved ability to resolve detail in the imaged object and a higher sensitivity to low concentrations of fluorophores. Furthermore, variations on the microscopic technique have been developed which offer various advantages. The invention of two-photon imaging eradicates the need for excitation in the UV, enabling *in vivo* imaging up to a depth of 1 mm [12] with reduced photo-toxicity [13], and fluorescence lifetime imaging microscopy (FLIM) provides a better means of contrast for systems which strongly scatter light, and depends on the environment rather than fluorophore concentration [14]. Stimulated emission depletion (STED) further improves the resolution of fluorescence microscopy; a second laser tuned to the fluorescence spectral peak position of the fluorophore suppresses the fluorescence far away from the centre of the excitation beam, and the ‘point spread function’ of the excitation beam is improved [15].

The ability to selectively bind fluorescent probes to a particular biomolecule enables the specific fluorescence imaging of molecules in living cells and organisms. In this context, QDs display a major advantage over fluorescent molecules [16] and promise to open up new capabilities for the application of fluorescence techniques in biology [17]; the large surface area of QDs coupled with a versatile surface chemistry provides a platform for bioconjugation that enables a multi-functional surface to be tailored to incorporate for example both diagnostic and therapeutic qualities [18]. Additionally, superior optical and chemical stability enables the dynamics of biological systems to be monitored over extended periods which promises to be extremely useful for studying the metastasis of cancerous cells [19].

Despite the fact that QDs in general emit fewer photons per photon absorbed than many fluorescent organic molecules (i.e. they have a lower quantum efficiency or photoluminescence quantum yield (PLQY)) the typical extinction coefficient [20, 21] and multi-photon [22] absorption cross-sections are orders of magnitude larger, resulting in stronger absorption and brighter emission on a molar basis. Furthermore, the typically broad excitation band of QDs in combination with a narrow emission band permits multiplexed imaging of biological systems using a single excitation source [23, 9]. In addition, many QDs can be size-tuned to emit in the NIR to ‘operate’ entirely within the biological window, enabling an increased penetration depth through biological tissue [24].

The application of QDs as imaging agents *in vivo* has, however, been held back over concerns regarding the role that size, shape and surface chemistry play in the toxicity of nanomaterials in cells and living organisms, although the emerging field of nanotoxicity is beginning to address these issues [25, 26]. Furthermore, the development of colloidal QDs over the past few decades has mostly focused on binary cadmium-based compounds primarily due to their band gaps being ideal for visible PL. Although this approach has inspired great progress in the field, the inherent toxicity of these materials has hindered their translation into clinical reality [27]. Indeed, the utilisation of heavy-metals in commercial products is being increasingly restricted by regulatory bodies worldwide, meaning that even devices employing QDs for non-biological applications must consider the use of alternative materials.

Naturally, this has led to a diversification in reports of QD synthesis in the literature; colloidal InP [28], Ge [29], Si [30, 31] and more recently nanodiamonds, carbon and graphene [32] QDs have been investigated as alternatives to cadmium-based QDs for biological imaging applications. Ternary I-IIII-

VI_2 chalcopyrite semiconductors such as $CuInS_2$ (CIS) have emerged as particularly exciting materials for the synthesis of nanomaterials, not only since the inherent toxicity of the readily available constituent elements, copper and indium, appears to be significantly lower than that of cadmium and lead [33, 34], but also due to the unique structural and electronic properties that arise from the composition and structure of ternary semiconductor compounds in general [35, 36].

The development of CIS QDs for biological applications is currently facing three important concerns which this thesis attempts to resolve.

i) The specific origins of the photoluminescence observed in CIS QDs, i.e. the nature of the states involved, remains ambiguous in the literature.

ii) State-of-the-art CIS QDs are synthesised by high temperature solvothermal reaction and are hydrophobic. This is a hindrance to their biological application and is environmentally harmful.

iii) The acute and chronic toxicity of CIS QDs *in vivo* remains unknown.

The introductory chapter of this thesis is intended as a review of the literature, detailing the theoretical underpinning of the optoelectronic properties which emerge as a result of quantum confinement in semiconductor nanocrystals and discussing the general development of colloidal nanocrystals over the last three decades in the context of biological imaging applications.

The second chapter describes the solvothermal synthesis and subsequent ‘cleaning’ of CIS-based QDs as well as the spectroscopic, microscopic and crystallographic experimental techniques used for their morphological and optical characterisation. Three individual methods are outlined for the synthesis of CIS QDs, each ultimately differing by the resulting QD surface chemistry, and the method for post-synthesis encapsulation of hydrophobic CIS QDs with amphiphilic polymer (amphipol) as a method of transferring the QDs into the aqueous phase is described.

Chapter 3 details the basic characterisation of hydrophobic CIS-based QDs synthesised following an established literature method. The morphology of the QDs is determined to be tetragonal chalcopyrite by electron microscopy and X-ray diffraction, and the composition is determined to be stoichiometric by energy-dispersive X-ray spectroscopy and X-ray photoelectron spectroscopy. The optical properties are characterised by UV/visible spectroscopy and fluorescence spectroscopy, showing absorption across the entire UV/visible spectrum and strong photoluminescence in the red region of the spectrum, with quantum efficiency greater than 5%. The size dependent spectral properties of CIS QDs are discussed within the effective mass approximation and empirical formulae are derived relating the QD size and the spectral positions of the principal features in the photoluminescence and absorption spectra, respectively. Deviations between the observed empirical trends and theoretical expectation are discussed.

Chapter 4 examines the impact of ZnS shell formation on the optical and morphological properties of CIS QDs. Slightly blue-shifted photoluminescence and an order of magnitude increase in quantum efficiency are observed in agreement with the literature. The excited state dynamics of CIS QDs are determined by transient absorption spectroscopy. The origin of the observed highly radiative emission in CIS/ZnS QDs is investigated by a modified transient absorption spectroscopy experiment with an additional ‘hole-burning’ source tuned to the observed stimulated emission to depopulate the highly radiative state. The negligible response of the excited state absorption to the hole-burning indicates that the emission originates from intra-gap donor states rather than the conduction band. It is argued that these states arise from anti-site point defects.

In Chapter 5 the size-dependent molar extinction coefficient is determined for CIS QDs. This is a vital parameter for bioconjugation techniques which depend on an accurate estimation of the concentration of QDs in suspension. The atomic concentration of copper in a digested QD suspension was determined by atomic absorption spectroscopy. The molar concentration of the initial QD suspension was calculated from the estimated copper content of a single QD, based on the known QD size and the density of bulk CIS. The molar extinction coefficient of the QD suspension was calculated using the Beer lambert law from the absorption as measured by UV/Visible spectroscopy at 400 nm and at the size-dependent spectral position of the lowest excitation. An exponential increase in extinction was observed with increasing QD size, and the data fit well to theoretical models, although the determined exponent from an empirical fit indicates an exponent that is significantly larger than expected.

The utility of this data is illustrated in chapter 6 where the CIS QDs discussed in chapters 3, 4 and 5 are optimally encapsulated with a zwitterionic amphiphilic polymer (PMAL-d) in order to render the surface hydrophilic. Excellent colloidal stability across a wide pH-range in deionised water was illustrated by dynamic light scattering and zeta potential measurements, and the polymer layer was shown to protect the QDs from quenching by copper ions in solution. Finally, the *in vitro* cytotoxicity of CIS/ZnS/PMAL-d nanoparticles to HaCat cells is evaluated separately by MTT and WST-1 assays against controls of PMAL-d only and of thioglycolic-acid (TGA) stabilised CdTe/ZnS QDs. Whilst *in-vivo* studies are required to gain a clear idea of the toxicity of NPs at the organism level, *in-vitro* viability assays can provide useful information about toxicity on individual cells. It is concluded that the polymer itself is responsible for the cytotoxicity identified and discrepancies between the two assays are discussed. Novel methods for the direct synthesis of CIS QDs with polar surface ligands are also evaluated.

1.2 Optoelectronic Properties of Quantum Confined Semiconductor Nanocrystals

This section is intended to highlight the key concepts in condensed matter physics and quantum mechanics that are relevant to the performance of QDs as biological imaging agents. These include mathematical formulations for the size-dependent band gap and the absorption coefficient of a single QD. The interaction between QDs and incident radiation is discussed as a process of excitation and de-excitation of charge carriers and the absorption and emission of photons. The synthesis of colloidal QDs is discussed theoretically from a thermodynamics perspective and the established synthesis techniques for QDs are outlined. Finally, the suitability of QDs for application as fluorescent probes for biological imaging is discussed, and the desirable optical and chemical properties of QDs in this context are outlined.

1.2.1 Optical Properties of Semiconductors

The short-range repulsive forces which arise between two atoms in close proximity are compensated for by long-range attractive forces which arise from the valence electrons [37]. The atomic orbitals in a periodic lattice of N atoms each separate into N orbitals, or energy levels, and as N becomes large effectively continuous bands of accessible energy levels become dispersed over momentum space [37]. This produces the characteristic 'band' structure of the material according to band theory, providing a definitive distinction between insulators and conductors, as illustrated in Figure 1.1.

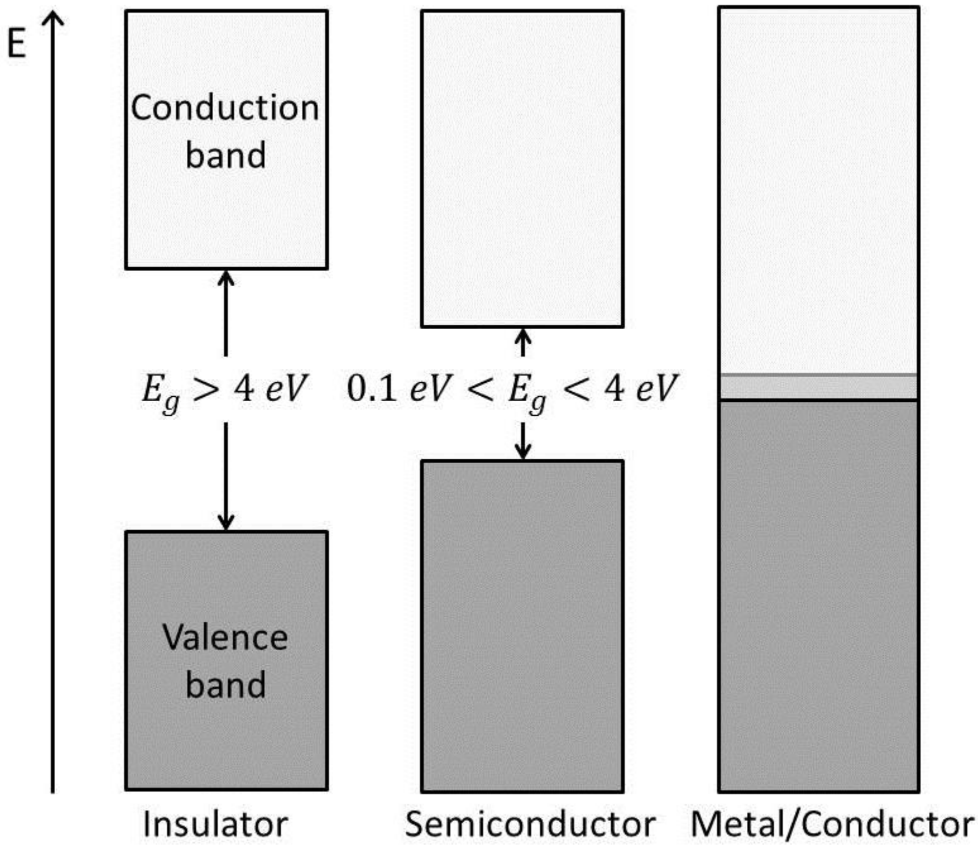

Figure 1.1: An illustration depicting the categorisation of materials into insulators, semiconductors and conductors based on the magnitude of the band gap.

A 'forbidden' energy band gap (Eg) may exist between a lower energy band of occupied orbitals (called the valence band) and a conduction band in which the orbitals are either partially occupied or completely unoccupied. The nature of this band gap is generally what dictates the electronic properties of a material; in the case of a conducting material, electrons in the conduction band are delocalised and have a high mobility, and are therefore free to move within the periodic atomic lattice, enabling electrical current to flow. In materials with a large band gap (> 4 eV) the conduction band has a negligible number of free electrons and insulating properties arise, whilst materials with a band gap smaller than the thermal energy at room temperature (< 0.1 eV) are good electrical conductors.

A third, intermediate class of materials known as a semiconductors are characterised by a mostly filled valence band with only a small band gap (0.1 eV< Eg <4 eV). According to the Fermi-Dirac equation (equation 1.1) the conduction band in semiconducting materials is mostly unoccupied by electrons at room temperature; only a small fraction of intrinsic electrons have enough thermal energy to populate the conduction band [37]. Near the band edges, the relationship between energy and momentum is generally quadratic and the dispersion of energy over momentum space ($\boldsymbol{k}$-space) is well approximated by that of a free particle [37,38].

When an electron is excited into the conduction band, an electron 'hole' is created in the valence band that has charge opposite to that of the electron. The effective mass of the hole, however, is not necessarily equal to the effective mass of the electron. The relative population of electrons and holes in a semiconductor influence conductivity. Semiconductors with an equal number of electrons and holes are 'intrinsic' whilst a semiconductor with an unequal electron and hole population are 'extrinsic' and can be further separated into two categories: semiconductors with a higher population of electrons than holes are said to display 'n-type' conductivity whilst those with more holes than electrons display 'p-type' conductivity.

The Fermi level E_F quantifies the amount of energy needed to add an electron to a system [38]. The Fermi-Dirac equation describes the probability $P(E_i)$ that an electron is in the state with energy E_i and is given by:

$$P(E_i) = \frac{1}{1 + e^{E_i - E_F/K_B T}}, \tag{1.1}$$

where K_B is the Boltzmann constant and T is the absolute temperature. The Fermi level E_F can also be understood as the energy for which the probability P for an electron to be in the state E_i is 0.5. An intrinsic semiconductor has a Fermi level midway between the valence band and conduction band, i.e. in the centre of the band gap. However, chemical and structural defects can donate extrinsic electrons which manifest as donor states within the band gap influencing the position of the Fermi level; in a n-type semiconductor the Fermi level lies closer to the conduction band and in a p-type semiconductor it lies closer to the valence band. Impurities can also create a local electron 'hole' acting as extrinsic electron acceptors, again producing an acceptor state within the band gap.

Besides thermal excitation, an electron can be promoted from the valence band to the conduction band into an unoccupied excited state as a consequence of an incident photon (a more rigorous discussion of such an excitation event is given in section 1.2.3). The transition of an electron into the conduction band leaves behind a hole in the reservoir of valence electrons, which has an effective mass as well as electronic charge opposite to that of the electron [38]. As such, if an excitation does not have enough energy to create a completely ‘free’ electron, the excited electron is electrostatically bound to the hole.

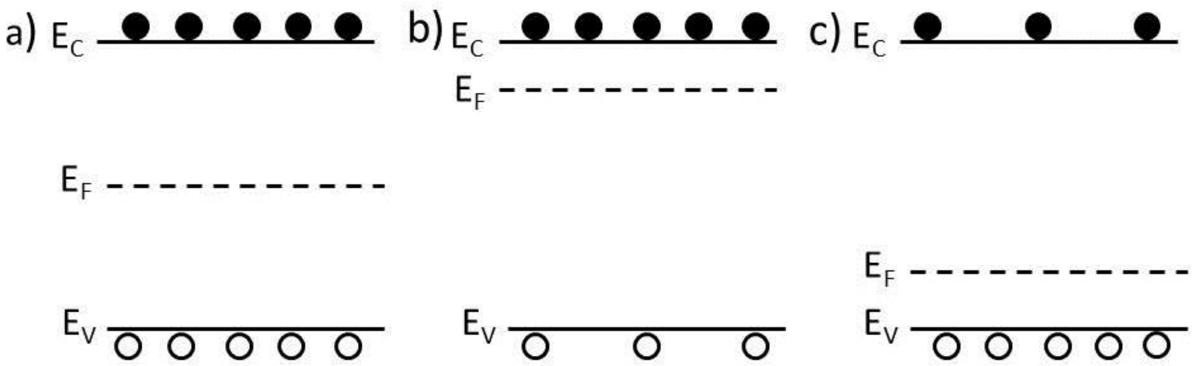

Figure 1.2: a) Intrinsic semiconductor with equal population of electrons (filled circles) and holes (hollow circles), with Fermi level (E_F) in the middle of the band gap; b) n-type semiconductor with a majority of electrons, with Fermi level greater than for intrinsic semiconductors (lying closer to the conduction band E_C); and c) p-type semiconductor with an excess of holes and Fermi level lower than for an intrinsic semiconductor (lying closer to the valence band E_V).

The electron-hole pair can be treated as a single quasi-particle, called an exciton, which is free to move within the atomic lattice. Typically, excitons in semiconductors have large hydrogenic wave functions and small binding energies and are named Wannier-Mott excitons [39]. This is opposed to Frenkel excitons which have compact wave functions and high binding energies [40]. The exciton has a reduced mass $1/\mu_{eff}$ equal to that of the combined reduced effective masses of the electron (m_e^*) and hole (m_h^*)

$$\frac{1}{\mu_{eff}} = \frac{1}{m_e^*} + \frac{1}{m_h^*} \tag{1.2}$$

The hydrogenic wavefunction of an exciton permits the concept of the Bohr radius of an atom to be applied to QDs. An exciton in a specific semiconductor has a characteristic radius governed by the equilibrium position between the Coulomb attraction of the electron and hole and the kinetic energy

$$\mu_{eff}v^2 = \frac{1}{4\pi\varepsilon_0}\frac{e^2}{r} \tag{1.3}$$

where r is the separation between the electron and hole pair, μ_{eff} is the reduced exciton mass, v is the velocity and ε_0 is the permittivity of vacuum. Given that in the semi-classical Bohr model the momentum

$$L = \mu_{eff}vr \tag{1.4}$$

is quantised, with a minimum value of $\hbar$, equation (1.3) can be re-arranged to give an expression for the Bohr radius a_B

$$a_B = \frac{4\pi\varepsilon_0\hbar^2}{\mu_{eff}e^2}. \tag{1.5}$$

1.2.2 Quantum Confinement and Size-dependent Properties

When the dimensions of a semiconductor crystal are reduced to below the characteristic Bohr radius charge carriers become spatially confined and the electronic structure becomes intermediate between that of a single atom and a bulk semiconductor; the continuous bands associated with bulk split into discrete states and the magnitude of the band gap is increased [2, 41,42]. The size of QDs presents a problem in that a typical system contains 10^3 to 10^6 atoms and is too complex for basic molecular orbital models, yet the simplifications associated with bulk theory are not applicable. However, a variety of models exist that attempt to describe optoelectronic properties. Density functional theory (DFT) applied to electron densities is commonly applied to resolve the band structure of QDs, although the shortcomings of this approach are that the band gap is often underestimated and the empirical adjustments used to correct for this are often too simplistic for many applications [43].

The quantised kinetic energy of a confined exciton can be most simply modelled as a ‘particle in a box’, within the effective mass approximation. In spherical radial coordinates the Schrödinger equation for an exciton with wavefunction $\psi(r,\varphi,\theta)$ trapped in a spherically symmetric potential $V(r,\varphi,\theta)$ representing a QD of radius d

$$V(r,\varphi,\theta)=\begin{cases}0, & r<d\\ \infty, & r\geq d\end{cases} \tag{1.6}$$

defined by an infinite potential outside of the QD, is

$$\left[\frac{-\hbar^2}{2\mu}\nabla^2+V(r,\varphi,\theta)\right]\psi(r,\varphi,\theta)=\left[\frac{-\hbar^2}{2\mu_{eff}}\left(\nabla_r^2+\frac{1}{r^2}\nabla_{\varphi,\theta}^2\right)+V(r,\varphi,\theta)\right]\psi(r,\varphi,\theta)$$

$$=i\hbar\frac{\partial\psi(r,\varphi,\theta)}{\partial t} \tag{1.7}$$

The angular component $Y(\varphi,\theta)$ of the wavefunction can be separated from the radial function $X(r)$ [44] and is related to the eigenvalue L of the angular momentum operator angular momentum $\hat{L}$

$$L^2=-\hbar^2\nabla_{\varphi,\theta}^2=l(l+1)\hbar^2 \tag{1.8}$$

such that the equation 1.6 becomes

$$\left[\nabla_r^2-\frac{l(l+1)}{r^2}+\frac{2\mu_{eff}}{\hbar^2}(E-V(r))\right]X(r)=\left[\nabla_r^2-\frac{l(l+1)}{r^2}+\varkappa^2+\frac{2\mu_{eff}}{\hbar^2}V(r)\right]X(r)=0 \tag{1.9}$$

where

$$\varkappa^2=\frac{2\mu_{eff}E}{\hbar^2} \tag{1.10}$$

The Schrödinger equation is simplified by taking the simplest case of purely radial motion, i.e. when the angular momentum is zero ($l=0$):

$$\left[\nabla_r^2+\varkappa^2+\frac{2\mu_{eff}}{\hbar^2}V(r)\right]X(r)=0 \tag{1.11}$$

Inside the QD, i.e. at $r<d$, the potential terms vanishes and

$$[\nabla_r^2+\varkappa^2]X(r)=0\,. \tag{1.12}$$

This has the generic solution

$$X_0(r)=A_0 si\,n(\varkappa r)+B_0 cos(\varkappa r). \tag{1.13}$$

The specific solution requires matching the interior spherical Bessel functions with the zero amplitude wavefunction outside of the QD region. This is achieved by setting the boundary conditions such that at the origin and outside of the QD the wavefunction is zero, i.e. $X(d=0)=X(d>r)=0$. The coefficient B_0 vanishes

$$X_0(0) = A_0 si\,n(0) + B_0 cos(0) = 0$$

$$\Rightarrow\ B_0 = 0 \tag{1.14}$$

and the substitution parameter $\varkappa$ must be an integer of π, scaled by the QD size d:

$$X_0(d > r) = A_0 si\,n(\varkappa d) = 0 \tag{1.15}$$

$$\Rightarrow \varkappa = \frac{n\pi}{d}. \tag{1.16}$$

The additional energy E_{conf} that the exciton experiences due to quantum confinement can be calculated by re-arranging equation 1.10 for E:

$$E_{conf} = \frac{\varkappa^2 \hbar^2}{2\mu_{eff}} = \frac{\pi^2 \hbar^2 n^2}{2\mu_{eff} d^2}. \tag{1.17}$$

This is the increase in energy that an exciton gains due to confinement within a semiconductor nanocrystal with radius d. For the lowest allowed inter-band transition ($1S_e$ – $1S_h$),

$$E_{g,QD} = E_{g,bulk} + \frac{\pi^2 \hbar^2}{2\mu_{eff} d^2} - 1.8\frac{q^2}{2\pi\varepsilon\varepsilon_0 d}, \tag{1.18}$$

where the addition of the last term takes into account the attraction between the oppositely charged electron and hole. The confinement term scales with the inverse square of the QD size and it is clear that the critical nature of the characteristic Bohr radius is imparted through the effective mass $\mu_{eff}$of the exciton. The coulomb term has a linear inverse dependence on d and decreases the band gap for larger particles although this is only significant for materials with a large dielectric constant such as ZnO.

1.2.3 Interactions Between Light and Semiconductor Nanocrystals

1.2.3.1 Excitation

The non-resonant excitation of QDs, i.e. the promotion of an electron from the valence band into the conduction band, can be induced by the absorption of a photon with greater energy than the band gap, i.e. $E = \hbar\omega_{exc} > E_g$. In the case of an incident classical electric field of the form

$$\boldsymbol{E}(\boldsymbol{r}, t) = \hat{e}_f E_0 \cos\omega_{exc} t = \hat{e}_f \frac{E_0}{2}\left[e^{i(\omega_{exc}t - \boldsymbol{k}_0\cdot\boldsymbol{r})} + e^{-i(\omega_{exc}\,t - \boldsymbol{k}_0\cdot\boldsymbol{r})}\right] \tag{1.19}$$

The interaction is described semi-classically by considering the perturbing effect of the corresponding interaction Hamiltonian

$$\hat{H}' = -\hat{\mu}\frac{E_0}{2}\left[e^{i(\omega_{exc}t-\boldsymbol{k}_0\cdot\boldsymbol{r})} + e^{-i(\omega_{exc}t-\boldsymbol{k}_0\cdot\boldsymbol{r})}\right] \tag{1.20}$$

where E_0 is the electric field amplitude, $\boldsymbol{k}_0$ is the wave-vector and $\hat{\mu}$ is the electric dipole transition matrix element

$$\hat{\mu} \equiv q(\hat{e}_f \cdot \boldsymbol{r}) \tag{1.21}$$

where $\hat{e}_f$ is the polarisation vector and q is the electron charge. Since $\widehat{H'}$ is oscillating with angular frequency ω_{exc} then an electron can be excited from the ground state $|i\rangle$ into an excited state $|j\rangle$ with energy E_j that differs from the ground state energy E_i by $E = \hbar\omega_{exc}$. The probability P of such a transition occurring is given by Fermi's Golden rule [45]:

$$P_{|i\rangle\to|j\rangle} = \frac{2\pi}{\hbar}\left|\hat{H}'\right|^2\delta\left(E_j - E_i - E\right) = \frac{2\pi}{\hbar}\frac{\tilde{\mu}^2 E_0^2}{4}\delta\left(E_j - E_i - E\right), \tag{1.22}$$

where

$$\tilde{\mu} = q\int u_j^*(\boldsymbol{r})u_i(\boldsymbol{r})\left(\hat{e}_f \cdot \boldsymbol{r}\right)e^{-i(\boldsymbol{k}_j-\boldsymbol{k}_i\pm\boldsymbol{k}_0)\cdot\boldsymbol{r}}dr. \tag{1.23}$$

Here, u_i and u_f are the Bloch functions in the initial and final state, respectively, such that the wavefunction in state $|i\rangle$ is given by

$$\psi_i(\boldsymbol{r}) = u_i(\boldsymbol{r})e^{i\boldsymbol{k}_i\cdot\boldsymbol{r}}. \tag{1.24}$$

As such, the transition matrix element is negligible unless the condition $\boldsymbol{k}_j - \boldsymbol{k}_i \pm \boldsymbol{k}_0 = 0$ is met. At optical wavelengths $\boldsymbol{k}_0$ is three orders of magnitude smaller than $\boldsymbol{k}_i$ and $\boldsymbol{k}_j$ which implies that $\boldsymbol{k}_j \cong \boldsymbol{k}_i \equiv \boldsymbol{k}$ and therefore that optical transitions occur vertically in $\boldsymbol{k}$-space. Consequently, direct band gap semiconductors are generally superior optical materials to indirect band gap semiconductors [45].

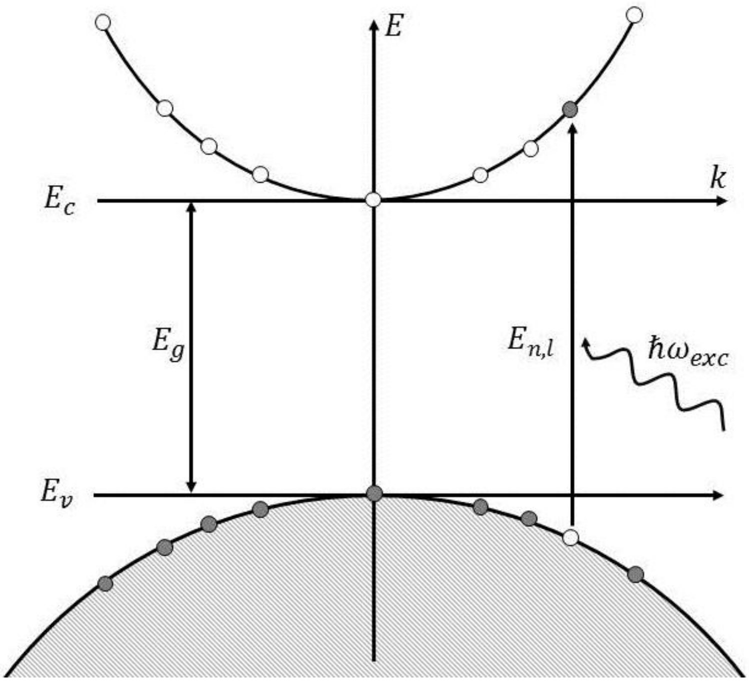

Figure 1.3: An illustration depicting the momentum conserving promotion of an electron from the valence band into the conduction band by the absorption of a photon with energy $\hbar\omega_{exc} > E_g$.

The transition energy $E_{n,l}$ between the initial and final states is larger than the band gap E_g by the combined kinetic energies of the electron and hole,

$$E_{n,l} = E_j - E_i = \frac{\hbar^2 k^2}{2\mu_{eff}} + E_g, \tag{1.25}$$

and equation (1.22) can be re-written as

$$P_{|i\rangle \to |j\rangle} = \frac{\tilde{\mu}^2 E_0^2}{4} \delta\big(E_{n,l} - E\big). \tag{1.26}$$

In bulk materials the number of transitions per unit time N, per unit volume V, is equal to the product between the transition rate given by equation 1.26 and the density of states $g(E)$. In reality, QDs are not ideal zero-dimensional materials, although from a theoretical point of view this is a good approximation for QDs stabilised in an organic layer and which display large work functions. Since there is no $\boldsymbol{k}$-space to be filled and the available states exist at discrete energy, the density of states for a QD consists of a delta function inversely proportional to the volume of the QD (V_{QD})

$$g(E) = \frac{1}{V_{QD}} \sum_{n,l} (2l + 1)\, \delta\big(E - E_{n,l}\big). \tag{1.27}$$

For a single QD therefore,

$$\frac{N}{V}=\frac{2\pi}{\hbar}\frac{\tilde{\mu}^2E_0^2}{4}\frac{1}{V_{QD}}\delta\left(E_{n,l}-E\right)\sum_{n,l}(2l+1)\,\delta\left(E-E_{n,l}\right). \tag{1.28}$$

The absorption coefficient α is defined as the ratio between the energy removed from the incident beam and the incident flux and is by given by multiplying this equation by the photon energy $\hbar\omega_{exc}$ and dividing by the Poynting vector, $S,$ which describes the directional energy flux of the electric field

$$\alpha=\frac{\hbar\omega_{exc}N/V}{S}=\frac{\hbar\omega_{exc}N/V}{c\varepsilon_0E_0^2} \tag{1.29}$$

where c is the velocity of light and ε_0 is the vacuum permittivity. Since delta functions are even functions, i.e. $\delta(x)=\delta(-x)$, the two delta functions in equation 1.26 are equivalent and furthermore they can be replaced by a Gaussian distribution in order to account for the size dispersion of QDs, characterised by the width of the first excitonic transition $\Delta E_{n,l}$ [20]:

$$\alpha(E)=A\sum_{n,l}\frac{(2l+1)}{E\sqrt{2\pi}\Delta E_{n,l}}exp\left[-\frac{\left(E-E_{n,l}\right)^2}{2\Delta E_{n,l}{}^2}\right], \tag{1.30}$$

where

$$A=\frac{1}{V_{QD}}\frac{\pi e^2E_pa_p}{2m_0cn_r\varepsilon_0\omega_{exc}}\,. \tag{1.31}$$

At high energy, the density of states is mostly continuous; it is only the states close to the band edge which are discrete. The absorption is thus similar to that of bulk semiconductors and can be modelled according to a classical approach which considers scattering by small spherical particles. The absorption cross-section at wavelength λ has been shown by Ricard to be represented by the expression [46]

$$\alpha(\lambda)=\frac{2\pi}{n_s\lambda}|f_{LF}|^2 2nk\,, \tag{1.32}$$

where n and k are the refractive index and wave number, respectively, and a local field factor f_{LF}

$$|f_{LF}|^2=\frac{9n_s^4}{(n^2+k^2-2n_s^2)^2+4(nk)^2} \tag{1.33}$$

accounts for the fact that the nanocrystals are embedded within a surrounding dielectric medium of refractive index n_s.

Experimentally the attenuation of light by gases, molecules or small particles in solution is quantified by the molar extinction coefficient $\varepsilon(\lambda)$ of the material, on the basis of linear absorption. The relationship between $\varepsilon(\lambda)$ and the absorption coefficient $\alpha(\lambda)$ of a QD is given by

$$\varepsilon(\lambda) = \frac{N_A V_{QD} \alpha(\lambda)}{1000 \ln(10)} \tag{1.34}$$

where N_A is Avogadro's number, V_{QD} is the average volume of the QD. The denominator accounts for the different conventions in logarithm base for the two coefficients.

1.2.3.2 De-excitation

The excited state initially decays rapidly due to scattering processes such as phonon scattering and the lowest electronic states in the conduction band become populated [47]. The corresponding positively charged holes left in the valence band relax to the VB maximum in a similar manner and each combined electron-hole pair are electrostatically bound and can be treated as a quasi-particle, namely the exciton. A more thorough discussion of excitons is given in section 1.2.1. The exciton lifetime is relatively long compared to organic dyes, typically on the order of 1-100 ns, over which non-radiative exciton recombination processes or the cooling of the system by the emission of photons, known as photoluminescence (PL), returns the carrier population to the ground state.

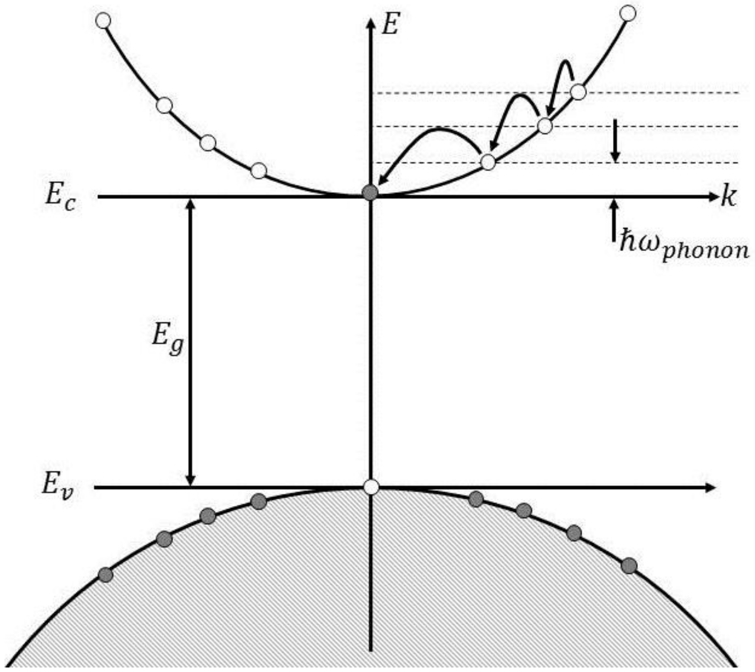

Figure 1.4: An illustration depicting the phonon-assisted relaxation of charge carriers, specifically of an electron, by the emission of a series of phonons with energy $\hbar\omega_{phonon}$.

In bulk materials, the initial non-radiative decay is due to the emission of a series of phonons, as illustrated in Figure 1.4, where $\hbar\omega_{phonon}$ is the phonon energy. For QDs however, where the energy level spacing is discrete and often larger than typical acoustic phonon energies, the emission of optical phonons requires precise resonance between the phonon energy and transition energy. As such, a "phonon bottleneck" effect whereby carrier relaxation times should significantly increase with reduced QD size due to the increased energy spacing is expected [48, 49]. However, electron-phonon interactions in QDs may induce the formation of polarons that assist relaxation by enabling the conservation of energy to be violated and thus for the system to undergo 'virtual' transitions [50, 51].

A large 'Stokes shift' between the excitation and photoluminescence spectral peak positions can indicate a strong exciton-phonon coupling in QDs, although the same phenomena can also originate from large size dispersions or the trapping of charge carriers in defect-related intra-gap states prior to emission. The experimental determination of phonon interactions in QD suspensions is difficult and although these processes are extremely important for QDs in applications such as solar harvesting, in biological imaging applications the ultra-fast nature of these processes renders them negligible.

Therefore, the precise mechanism behind phonon-assisted de-excitation in $CuInS_2$ (CIS) QDs is not investigated in any depth in this thesis and as such the limited discussion above is sufficient.

Multi-exciton interactions can promote non-radiative recombination by transferring energy to an electron in the conduction band as opposed to the emission of a photon. Auger decay constants are typically of the order 10 – 100 ps and have been demonstrated to have a linear dependence on QD volume [52].

Compared to bulk semiconductors the behavior of QDs is significantly influenced by surface effects, due to their relatively large surface area-to-volume ratio. Experimentally, defects formed during fabrication invariably include unsaturated ‘dangling’ bonds at the edge of the crystal structure [53, 54, 55], as well as internal point defects found in bulk. Defect states associated with a disordered surface are termed ‘shallow’ since electrons trapped in these states are spatially delocalised, and depopulation is rapid. Therefore these states are often associated with non-radiative recombination and poor quality QDs [53-55]. Internal point defects related to chemical or structural deviations from the ideal crystal structure generate ‘deep’ intra-gap states; charge carriers trapped in deep states tend to be localised and experience much longer lifetimes and as a result these states can act as efficient centres for radiative relaxation of charge carriers in chalcopyrite compounds [56]. In the case of CIS an abundance of internal point-defects generates intra-gap states which can act as emissive centres, providing an alternative recombination pathway [57]. The influence of these states is usually treated phenomenologically due to a limited understanding of the perturbative effect that the defects have on the ideal crystal structure as is the case in Chapter five.

Fermi’s Golden rule, as described in the previous section, is time-independent and can be applied to the process of optical relaxation as well as excitation. Photoluminescence refers to the emission of a photon as a result of a momentum-conserving recombination of the electron-hole pair. Similarly as for excitation, optical transitions only occur vertically in ***k***-space and direct band gap semiconductors are more efficient photon emitters than indirect band gap semiconductors. The emitted photon has energy corresponding to the difference between the initial electron and hole energies and is typically, in the absence of intra-gap states, from the CB minimum to the VB maximum.

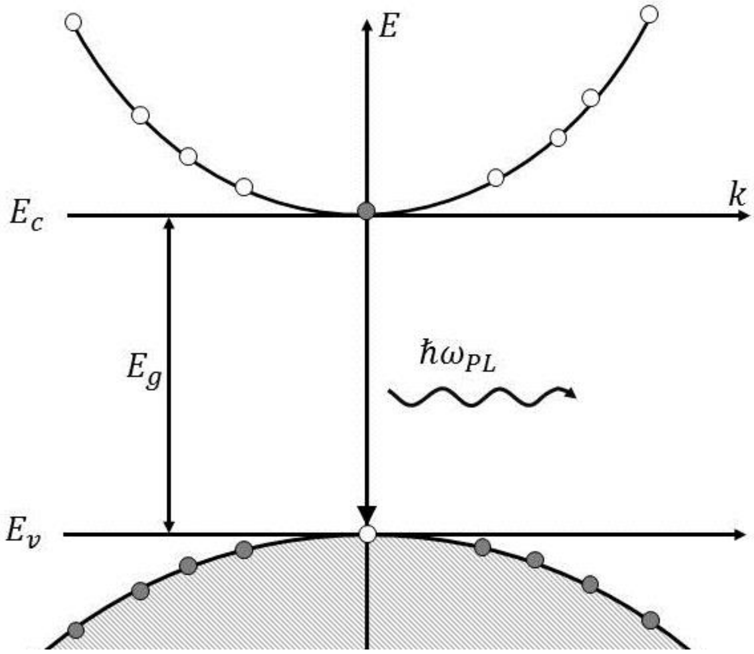

Figure 1.5: An illustration depicting photoluminescence; the recombination of the electron-hole pair and the associated emission of a photon with energy $\hbar\omega_{PL}$.

The photoluminescence follows first order kinetics and the lifetime can be quantified by a exponential decay equation with a characteristic radiative decay constant Γ_r

$$I_t = I_0 e^{-\Gamma_r t} \tag{1.35}$$

The PL quantum yield (PLQY, ϕ) describes the conversion efficiency of electrical energy into photons by the system and is defined as the ratio of absorbed photons to emitted photons

$$\phi = \frac{\#\, photons\ emitted}{\#\, photons\ absorbed} = \frac{\Gamma_r}{\Gamma_r + \Gamma_{nr}} \tag{1.36}$$

where Γ_{nr} is the non-radiative decay constant. Many QDs have low PLQY compared to most molecular dyes due to disorder in the crystal structure, especially at the QD surface. Cd-based QDs typically show the highest PLQY above 60%. Photoluminescence is the integral process for the application of QDs as probes for the imaging of biological systems and as such the measured PLQY of a QD suspension provides a good indicator as to the quality of the sample in this context.

1.3 Quantum Dots in Biological Imaging Applications

Optical imaging of biological systems is non-invasive, clinically safe and relatively inexpensive and is therefore a patient-friendly technique [9, 58, 59]. However, despite great advances in laser technology, the invention of charge-coupled devices and the introduction of numerical models for light propagation through biological tissue, the resolution available with optical imaging is limited by the contrast agent [10]. In this sense the emergence of QDs as alternative optical imaging contrast agents to fluorescent dyes has been of great benefit to optical imaging of biological systems due to their much ‘brighter’ emission [60]. In addition QDs display broad excitation spectra and narrow emission spectra allowing for multiplexed imaging [61, 62] and the surface functionality can be tailored for bioconjugation with specific targeting molecules [9]. Furthermore, QDs are more resistant to photo-bleaching in comparison with molecular dyes [60], enabling real-time imaging of biological systems for much longer periods [63]. This is an exciting prospect for the study of metastasis *in vivo* and the study of cellular molecular dynamics *in vitro*.

The prospects for QDs as fluorescence probes for *in vitro* biological imaging applications were demonstrated independently in 1998 by two seminal papers. Chan and Nie conjugated CdSe/ZnS QDs with the iron transport protein transferrin and demonstrated the possibility of receptor mediated endocytosis in HeLa cells; a dramatic increase in cell uptake was observed for the transferrin conjugated QDs compared to the control QDs (no protein present) [64]. Bruchez *et al* used two different sized CdSe/CdS QD suspensions to image a dual-labelled 3T3 mouse fibroblast cell. Green emitting QDs stabilised with acetate groups were found to bind with high affinity to the cell nucleus while red emitting QDs were used to specifically label the F-actin filaments of the cell [65]. This work highlighted the difference between non-specific cell uptake of QDs and the specific targeted delivery of QDs into cells. In this sense, bio-imaging with QDs can be split up into four main categories defined by combinations of two distinctions: either non-specific or targeted (specific) labelling; or either intracellular or extracellular delivery [9].

Generally, non-specific extracellular labelling is deemed to be an adverse quality in QDs as it limits the precision of specific extracellular labelling. The size, shape and surface chemistry of nanoparticles strongly influences the response of biological systems [66]. A neutral surface charge in general minimises cellular interaction [67]; negatively charged QDs would be expected to display low levels of nonspecific interactions with the negatively charged cell membrane, yet several groups have reported contradictory observations [68, 69]. Non-specific interactions have been shown to be inhibited for QDs stabilised with polyethylene glycol (PEG) chains [70, 71]; PEG is known to be resistant to protein interactions and is therefore an especially ideal surface functionality for QDs suspended in biological medium [72]. Zwitterionic, i.e. featuring both positive and negative charged chemical species, surface functionality has also been shown to provide QDs with good colloidal stability and reduced cytotoxicity and therefore represents an excellent low-molecular weight alternative to PEGylation [73, 74].

Bioconjugation chemistry has advanced significantly over the last decade and it is now feasible to specifically functionalise QDs with antibodies for specific labelling of cell membranes. A classic route towards bio-inorganic conjugation is through use of the biotin-streptavidin bond [75]; streptavidin conjugated QDs bind with high affinity to biotinylated antibodies that bind directly to a specific target protein. Such functionalised antibodies are now widely commercially available and this approach has been applied to the imaging of cancer cells by targeting over-expressed receptor proteins. Wu *et al* targeted the cancer cell surface receptor Her2 in addition to the cytoskeleton components and nuclear antigens in cultured live cells, fixed cells and tissue sections [60], demonstrating the expansive scope for the application of QDs as bio-imaging agents. Many reports of specific targeting of cancer cells have been published since including *in vivo* targeted imaging of prostate cancer [76], breast cancer [77] and neck cancer [78].

The intracellular delivery of quantum dots can also be categorised by the specific and non-specific cases. Non-specific cellular uptake of QDs can occur naturally through endocytosis or be instigated by applied methods such as nano-injection [79] or electroporation [80]. The nonspecific uptake of QDs by cells is detrimental to the efficiency of specific cell uptake; cells engulf a wide variety of foreign bodies as an immune response, including nanoscale objects such as QDs by endocytosis [81]. QDs can bind to cell membrane receptors and become trapped in clathrin-coated pits that are subsequently ‘pinched’ from the membrane, aided by the enzyme dynamin, resulting in QD-loaded endosomes inside the cell. Endocytosis can therefore also be utilised as a specific mechanism for the delivery of QDs into cells since the QD surface chemistry can be functionalised to target the surface cell receptors in a similar manner to specific extracellular labelling.

1.3.1 Cytotoxicity of QDs

The drive towards alternative QD materials to cadmium and lead based compounds is motivated by the inherent toxicity expected upon prolonged internal exposure to heavy metals. The inorganic composition dominates the chronic toxicity; the leaching of free radicals from the QDs into the cellular environment has been shown to accumulate in certain organs [82, 83].

State-of-the-art wet-chemical techniques now enable exceptionally high quality QDs to be synthesised, yet as the prospect of their use as *in vivo* and *in vitro* imaging agents approaches the clinical stage questions have arisen as to whether the cytotoxicity of QDs may be too significant to be considered for safe clinical use, especially those based on heavy metals such as Cd and Pb. The *in vitro* cytotoxicity of CdSe QDs to cultured cells under prolonged UV irradiation was investigated by Derfus *et al* [84]. Severe cytotoxicity was observed and was found to be due to oxidation of the surface and subsequent release of free Cd ions and dependent upon the synthesis route and surface chemistry.

In general in vitro studies find the cytotoxicity to be strongly dependent on the capping molecule and that an inert ZnS or silica shell increases the concentration limit of CdSe QDs before cytotoxic effects are observed [84, 85, 86, 87]. However, all these studies were performed *in vitro*, and concerns are still present as to the *in vivo* toxicity of Cd based QDs.

The *in vivo* toxicity of CdSe/ZnS was probed by Hauck *et al*, examining the surface chemistry on the short and long term toxicity to Sprague-Dawley rats, surprisingly finding no toxicity over a period of 4 weeks for doses up to 60 nM [88]. A first study observing primates intravenously injected with micelle-encapsulated CdSe/CdS/ZnS QDs did not show any acute toxic effects; however, their spleen, kidneys, and lungs contained raised levels of toxic elements (Cd and Se)[82]. More recently the dietary administration of CdS nanoparticles was shown to stimulate upregulation of stress response genes and cause significant mitochondrial dysfunction in zebrafish [83]. In addition accumulation of Cd was observed in the brain and muscles after 60 days.

In conclusion, although the acute toxicity of QDs appears to be more dependent upon the size, shape and surface chemistry rather than composition, the chronic toxicity of Cd-based QDs is due to the inherent inorganic nature. The cytotoxicity can be significantly reduced by the subsequent growth of a more biocompatible layer, for example of ZnS or silica. However, such strategies do not completely remove the possibility of cytotoxicity *in vivo* and the accumulation of toxic heavy metals in organs presents a major hurdle for the safe clinical use of QDs *in vivo*.

1.3.2 QD Surface Chemistry

Many synthesis techniques produce hydrophobic QDs that must be modified post-synthesis in order to enable aqueous suspensions to be formed; this is a particularly desired property for applications within the aqueous cellular environment. Even QDs synthesised in the aqueous phase with polar surface chemistry may require post-synthesis modification, for example to improve colloidal stability or introduce additional functionality.

Ligand exchange is a commonplace approach to transforming the surface chemistry, although it is notoriously sensitive to the solution temperature, the solution pH, the solubility of the respective ligands and their binding affinity to the QD surface [89, 90, 59]. For example, QDs are often synthesised with the surfactant TOPO which is then replaced for a thiol ligand post-synthesis, yet this process is irreversible; the thiol ligands are much more difficult to replace. Furthermore, failure to carefully optimise the specific ligand exchange can result in significantly diminished PLQY due to incomplete or disordered surface thiol layer.

An alternative approach is to conceal the QD surface chemistry by their incorporation into a protective, biocompatible structure such as a phospholipid micelle or a silica ‘bead’ [91, 92, 93], effectively shielding the QD surface from the environment.

Polymer encapsulation has been demonstrated to be an efficient method for incorporating a range of functionality onto the QD surface, whilst also improving the stability of QDs in the biological environment [94] and can be based on covalent, electrostatic [95] or hydrophobic binding [96]. A successful approach for the transfer of hydrophobic QDs into the aqueous phase is by their encapsulation with amphiphilic polymer (Amphipol) [97]. A common example is encapsulation with poly-maleic anhydride (PMAL) polymer derivatives functionalised with long carbon chains that bind to the hydrophobic surface as well as polar groups that are exposed at the surface, promoting stability in water [98]. A wide range of derivatives have been synthesised in the literature [99, 100, 74] and several are commercially available, making this an ideal method for this task.

1.3.3 Multi-Modal Imaging

The inorganic nature and large surface area of QDs enables their performance to be enhanced with multi-modal imaging capabilities [101, 102] extending both diagnostic and therapeutic applications [103, 104]. For example, magnetic properties can be incorporated into the QD design in order to provide contrast for magnetic resonance imaging (MRI) as well as fluorescence imaging. The approaches are diverse: QDs can be doped with paramagnetic ions [105, 106, 107], encapsulated alongside magnetic nanoparticles (MNPs) in a silica 'bead' [108, 109, 110], or stabilised with paramagnetic ligands [111] or chelates [112]. Gao *et al.* also demonstrated the synthesis of FePt/CdX (where X = O, S and Se) nanoparticles which displayed fluorescence quantum yields of up to 10% and were superparamagnetic at room temperature [113]; if the crystal size is smaller than the magnetic domain size, thermal fluctuations are large enough to flip the magnetic moment and superparamagnetism arises, enabling contrast to be formed in MRI [114]. Superparamagnetic nanocrystals also have additional applications within bionanotechnology, for example magnetic hyperthermia [104] and magnetofection-aided delivery of drugs [108] and genes [115].

1.4 Synthesis of Colloidal Quantum Dots

Since the band gap and consequently the photoluminescence emission wavelength of quantum dots is size-dependent, synthesis techniques must allow for a high level of control over size in order to attain a narrow size distribution about the desired radius. 'Top-down' fabrication techniques for ultra-small particles, such as chemical etching, do not afford the control associated with more elegant 'bottom-up' self-assembly techniques [116]. Arrested precipitation in water has been shown to be relatively successful although it was not until pioneering high temperature solvothermal reactions based on organometallic chemistry were performed that the synthesis of monodisperse Cd-based nanocrystals with high crystallinity and bright, narrow emission was achieved. The seminal work by Murray *et al* demonstrated successful synthesis of colloidal CdTe, CdSe and CdS QDs by the pyrolysis of organometallic precursors, resulting in size-tunable band-edge emission [117]. Cadmium based QDs have direct band gaps that are ideal for photoluminescence in the visible to near infra-red, and also happen to be relatively simple to synthesise and are more robust against oxidation than other semiconductors such as Ge and Si. It is for these reasons that cadmium was the system of choice for many early researchers in the field of QD synthesis.

Much experimental work has since focussed on understanding and optimising reaction kinetics through control over various parameters; the duration and temperature of the reaction [118], the concentration of precursors, and the solvent composition [119] have all been observed to significantly influence the morphology of nanocrystals [119, 120]. In the case of CdSe QDs, the diversity of suitable solvents and cadmium precursors was first demonstrated by Peng *et al* who determined that the most successful solvent/ligand to be fatty acids and the most favourable cadmium precursor to be cadmium acetate [121].

In general, nanocrystal synthesis in organic solvents remains more practical and successful than aqueous-based synthesis methods, although it is common for nanoparticles composed of various materials, including noble metals, iron oxide and zinc sulfide, to be synthesised in water. This is unfortunate since aqueous synthesis methods are considered ‘greener’, i.e. they involve lower temperatures and produce bi-products that are less damaging to the environment, and as such there is great incentive to develop aqueous synthesis techniques which can challenge the success of solvothermal reactions performed at high temperature [122]. For example, nanocrystals can be synthesised inside inverse micelles, can be synthesised with the assistance of irradiation with UV or microwaves and can be biotemplated.

An integral aspect of research regarding the synthesis of QDs for many applications is their surface modification; core QDs can be capped with Silica or semiconductor shells, and can be further modified with a variety of molecules in order to provide the desired surface chemistry. The epitaxial growth of semiconductor shells onto QDs has multiple benefits; it improves their chemical stability by reducing the risk of oxidation of the surface and can also provide a more biocompatible platform for bioconjugation than the core surface. Additionally, shell growth can also dramatically improve the PLQY due to passivation of surface defects.

The band offset between the core and shell regions strongly influences the electronic properties, and generally falls into one of two categories; type I or type II, as depicted in Figure 1.6. Type I band offsets are characterised by a shell in which both band edges lie outside those of the core, whilst type II band offsets are defined as having a ‘staggered’ band offset in which either the CB or VB of the shell region lies inside the corresponding band edge of the core. First-principles calculations reveal the charge density distribution varies between type I and type II structure [123]. Type I structures demonstrate enhanced confinement in the core region whilst charge carriers in type II structures may be delocalised, with the wavefunction extending into the shell region. In these structures, exciton recombination can occur at the core/shell interface, such that the band offset between the two semiconductor layers can be engineered to produce red-shifted emission compared to the core-only QD.

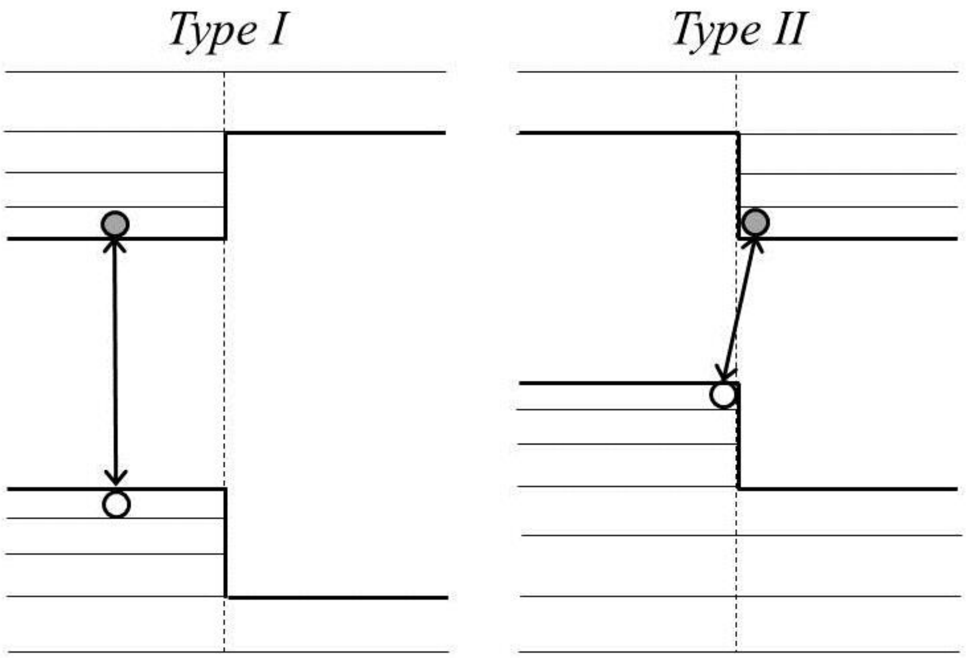

Figure 1.6: The band structure of core/shell QD heterostructures is generally either ‘Type I’ (left) in which the band edges of the shell material out lie those of the core QD, or ‘Type II’ (right) in which either the CB minimum or VB maximum lies inside the corresponding core band edge.

ZnS is the most common QD shell material since it has a wide band gap and is relatively inert and is therefore beneficial to both the optical and chemical stability. In addition ZnS has a small lattice mismatch (<5%) with common QD materials such as CdS, CdSe and CIS, enabling a shell to be formed without introducing stress and strain at the core/shell interface. The first report of CdSe/ZnS type I QDs by Kortan *et al* in 1990 demonstrated that a monolayer of foreign material on the surface of a semiconductor crystal can grow an epitaxial shell rather than undergo separate nucleation [124]. The PLQY of ZnS capped QDs generally display a significant enhancement relative to the bare core QDs whilst the absorption spectrum remains comparatively unchanged, suggesting the epitaxial growth of ZnS as opposed to alloying or surface etching. The ZnS layer has been shown to have an optimal thickness that depends on the specific system; the subsequent reduction in PLQY after this critical thickness is attributed to dislocations in the ZnS layer arising from strain, and depends strongly on the lattice mismatch between ZnS and the QD core material [125].

1.4.1 The Thermodynamics of Nanocrystal Nucleation and Growth

In this section a simple thermodynamic description of the formation of spherical colloidal nanocrystals from a super-saturated solution of reactive monomers is presented, in order to elucidate the influence of various parameters on the resulting crystal structure and size distribution of the nanocrystals. The bottom-up approach to the synthesis of nanoparticles fundamentally consists of two processes: the nucleation of nanoparticles from a solution of monomers; and their subsequent growth, which ideally should occur subsequently.

1.4.1.1 Nanocrystal Nucleation

A nucleation event occurs when a small number of monomers overcome an energetic barrier and assemble into an ultra-small cluster that is thermodynamically stable, and is effectively a transition from the solution phase to the crystal phase. The barrier to nucleation originates in the surface tension that arises when n atoms spontaneously form a solid volume from the solution phase. The difference in free energy ΔG between the two phases is given by

$$\Delta G = n\left(\mu_{crystal} - \mu_{solution}\right) + 4\pi r^2 \sigma \tag{1.37}$$

where $\mu_{crystal}$ and $\mu_{solution}$ are the chemical potentials of the crystal and solution phases, respectively. The second term represents the total surface energy and is determined by the product of the surface tension σ and the surface area $4\pi r^2$ where r is the cluster radius. An alternative formulation is given by taking into account the volume of the nanocrystal and the number of atoms per unit volume N

$$\Delta G = \frac{4\pi}{3} N r^3 \left(\mu_{crystal} - \mu_{solution}\right) + 4\pi r^2 \sigma. \tag{1.38}$$

In the case where $\mu_{crystal} < \mu_{solution}$when the cluster is small, the change in free energy is greater than zero and the cluster is unstable; the energy gained by creating the volume is not enough to create a stable interface between the cluster and the surrounding medium. However, once the cluster becomes large enough, the change in free energy is negative, and it becomes stable.

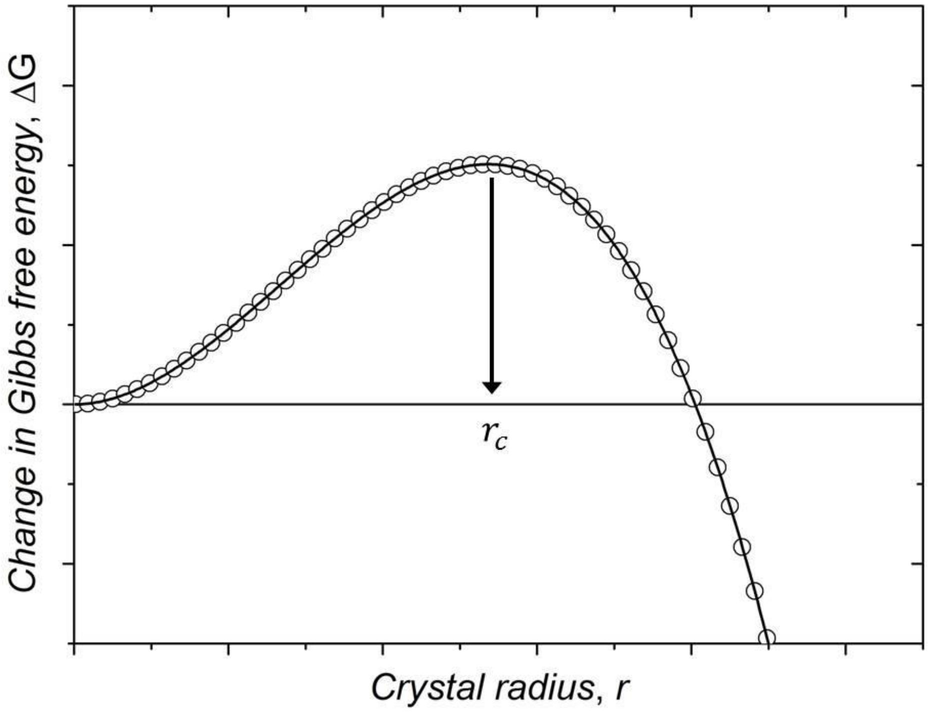

Figure 1.7: A sketch of the shape of equation 1.37 illustrating the barrier to nucleation at the critical radius, r_c.

The critical radius r_c at which the phase transition may occur can be determined by equating the derivative of ΔG with respect to r to zero

$$\frac{d\Delta G}{dr} = 4\pi N r^2 \left(\mu_{crystal} - \mu_{solution}\right) + 8\pi r \sigma = 0. \tag{1.39}$$

such that the critical radius represents the nanocrystal radius for which equilibrium is reached with the concentration of monomers in solution

$$r_c = \frac{-2\sigma}{N\left(\mu_{crystal} - \mu_{solution}\right)} . \tag{1.40}$$

For clusters with $r > r_c$ the addition of new molecules releases free energy; it is more favourable for monomers to adsorb onto the crystal surface than to stay in solution. Figure 1.7 shows a sketch of the potential for nucleation, $\Delta G,$ as a function of radius.

1.4.1.2 Nanocrystal Growth and Size Focussing

The growth of subsequent atomic monolayers onto the surface of nuclei depends on the diffusion of monomers towards the nanocrystal, characterised by a flux J which far away from the crystal surface $(x \gg r)$ is related to the diffusion coefficient β and the concentration gradient of monomers dC/dx in solution by Fick's law:

$$J(x \gg r) = 4\pi x^2 \beta \frac{dC}{dx}. \tag{1.41}$$

At equilibrium the flux is independent of x and a second order differential equation for the concentration profile is formulated:

$$\frac{dJ}{dx} = 4\pi\beta\left(2x\frac{dC}{dx} + x^2\frac{d^2C}{dx^2}\right) = 0$$

$$\Rightarrow \quad \frac{d^2C}{dx^2} = -\frac{2}{x}\frac{dC}{dx}\,. \tag{1.42}$$

If boundary conditions are set such that the concentration of monomers at the nanocrystal surface is C_r and the concentration of monomers far away from the crystal surface is C_x, then the solution to equation 1.42 is:

$$C(x) = C_x - \frac{r(C_x - C_r)}{x}\,. \tag{1.43}$$

The derivative of the concentration can be inserted into equation 1.41

$$J(x > r) = 4\pi\beta r(C_x - C_r) \tag{1.44}$$

giving a nanocrystal growth rate of

$$\frac{dr}{dt} = \frac{J}{4\pi r^2 N} = \frac{\beta(C_x - C_r)}{rN}\,. \tag{1.45}$$

The above equation for growth rate assumes constant pressure and temperature; in order to elucidate the effect that synthesis temperature has on growth rate a different formulation based on the general gas equation with the monomer concentrations treated as vapour pressures is useful:

$$C_r = C_\infty exp\left\{\frac{2\sigma}{rNk_BT}\right\} \approx C_\infty\left(1 + \frac{2\sigma}{rNk_BT}\right) \tag{1.46a}$$

$$C_x = C_\infty exp\left\{\frac{2\sigma}{r_c N k_B T}\right\} \approx C_\infty\left(1 + \frac{2\sigma}{r_c N k_B T}\right) \qquad (1.46b)$$

where C_∞ is the vapour pressure of a flat surface. These equations relate the concentration of monomers at a distance from the surface to the critical radius discussed in the previous section for which the nanocrystals are in equilibrium with that concentration. Substituting these expressions into equation (1.45) gives a temperature dependent growth rate:

$$\frac{dr}{dt} = \frac{2\sigma\beta C_\infty}{N^2 k_B T}\left(\frac{1}{r_c} - \frac{1}{r}\right). \qquad (1.47)$$

The overall sign of the term within the brackets dictates whether a crystal has a positive or negative growth rate, based on the crystal radius r relative to r_c. If $r > r_c$ the crystal grows, if $r < r_c$ the crystal will shrink and if $r = r_c$ the crystal phase and solution phase are in equilibrium and the crystal growth rate is zero. The implications of this are such that smaller crystals shrink and larger crystals grow, broadening the size distribution in a process known as Ostwald ripening and reducing the concentration of nanoparticles produced [126]. The form of equation (1.47) is sketched in Figure 1.8. Importantly, a maximum growth rate can be identified at $r = 2r_c$. If the entire size distribution lies above this value then smaller crystals grow faster than larger crystals and the average size is focused, i.e. the size distribution becomes narrower. In practice, the most common method of achieving this is to keep the monomer concentration high enough by repeated injection of precursors [121].

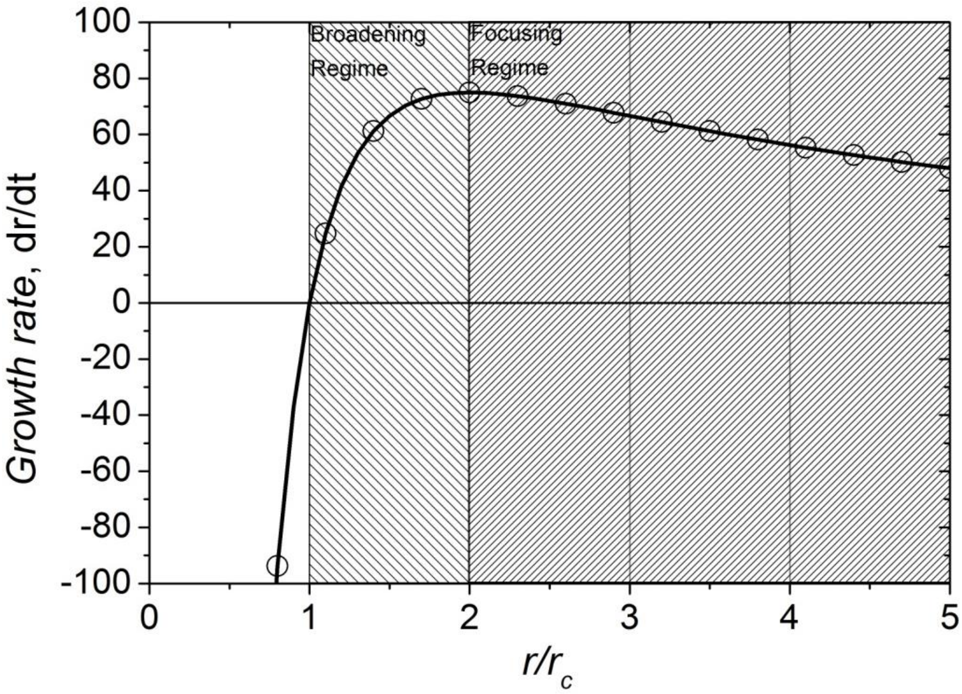

Figure 1.8: A sketch of the shape of equation 1.47 illustrating the size-broadening and size-focussing regimes defined by an average crystal radius $r_c < r < 2r_c$ and $r > 2r_c$, respectively.

The extent to which a sample can be size focussed is dependent upon the growth temperature, the surface tension and the initial size distribution of nuclei. Therefore, the nature of the nucleation event is critical to the quality of the final nanocrystals. Ideally, the nucleation should be partially quenched and the growth stage immediately initiated by injection of additional precursors. Nucleation occurring alongside growth removes monomers from the growth solution and increases the critical radius and therefore the potential for ripening. A reduction in the temperature between the nucleation and growth phases has been demonstrated to eliminate this risk. The translation of cation exchange to the nanoscale has had significant implications for material synthesis and post-synthesis transformations of surfaces due to the quick dynamics compared to bulk [127]. This is a convenient tool for QD shell formation since it does not require elevated temperatures and enables the stoichiometry and morphology to be extended beyond the capabilities of conventional high temperature techniques that are limited by temperature and composition phase diagrams.

Finally, the simplifying spherical approximation in the above formulations neglects the difference in surface energy of the various crystal facets. In reality certain facets will grow preferentially and therefore control over the morphology is enabled by diffusion limited reaction kinetics or the presence of stabilizing ligands which preferentially bind to specific facets.

1.5 $CuInS_2$ Quantum Dots

An emerging class of QDs synthesised from ternary compounds demonstrate exciting properties for a variety of applications. For example, ternary I-III-VI_2 chalcopyrite semiconductor compounds such as $CuInS_2$ (CIS) exhibit inherent strain due to the bond length mismatch ($R_{I\text{-}VI} \neq R_{III\text{-}VI}$). A tetragonal anion displacement is manifest in the tetragonal distortion of the crystal lattice and an abundance of intrinsic defects are formed which strongly influence the electronic and optical properties. [128, 129]

The band gaps of I-III-VI_2 materials are anomalously reduced relative to the band gaps of their binary II-VI 'analogues' [35]. Mixing, or hybridisation, between *p* and *d* orbitals in the upper valence band shifts the valence band maximum to higher energy [130, 131]. This phenomenon is enhanced in cuprous compounds such as CIS with a strong *d*-character in the upper valence band. Furthermore, a dynamic interplay between the band edge positions and defect formation energies renders the band gap stable against off-stoichiometry, and either n-type or p-type behaviour can be selected by tuning the off-stoichiometry without introducing external impurities [132].

Table 1.1 List of values for the effective mass μ, Bohr radius a_B and bulk band gap $E_{g,bulk}$ of various QD materials including CIS.

Material	$\mu\ /m_e$	a_B/nm	$E_{g,bulk}$/eV
$CuInS_2$	0.14 [133]	4.1[135]	1.53 [35]
CdTe	0.09 [134]	7.3 [136]	1.44 [139]
CdS	0.16 [134]	2.4 [137]	2.42 [140]
CdSe	0.10 [134]	5.4 [37]	1.74 [139]
PbS	0.13 [134]	18 [138]	0.37 [141]

The synthesis of high quality CIS QDs has been reproduced by various groups [142-149] and the highly luminescent and long lived emission has been characterised primarily by steady-state and time-resolved PL spectroscopy [142-149]. Based on the observed broad emission band and large Stokes shift it is clear that defect states dominate the emission of CIS QDs. This is consistent with low temperature PL spectroscopy studies which show that the abundance of intra-gap defect states contribute significantly to the available de-excitation pathways in bulk CIS and that it is likely that the PL is related to defects [149]. In contrast to the small Stokes shift and narrow emission band observed for example in CdTe QDs [53, 54], which indicate ‘band-edge' emission, instead these characteristics suggest that the PL dynamics of CIS QDs are in fact related to deep intra-gap defect states.

This is supported by the observation that the PLQY of copper-poor CIS QDs which are expected to have a high density of defects associated with the copper-poor phase is greater than that of an equivalent stoichiometric sample. It has been postulated that this defect-related emission originates from donor-acceptor pair (DAP) recombination between donor and acceptor states associated with a local absence of a copper atom [143]. The possible defects include copper vacancies (V_{Cu}) and indium-copper anti-sites (In_{Cu}), although there are theoretical indications that neutral defect complexes such [$2V_{Cu}^{-} + In_{Cu}^{2+}$] and [$In_{Cu}^{2+} + Cu_{In}^{2-}$] are preferentially formed in copper-poor $CuInSe_2$, explaining the experimentally observed increase in copper-indium anti-sites [151]. All of the point defects that may exist in CIS are illustrated in Figure 1.9. The defects that arise in real samples are dependent on the composition and synthesis conditions, amongst a multitude of factors. For example, exposure of the QDs to oxygen during or post-synthesis may result in oxygen-sulfur anti-sites.

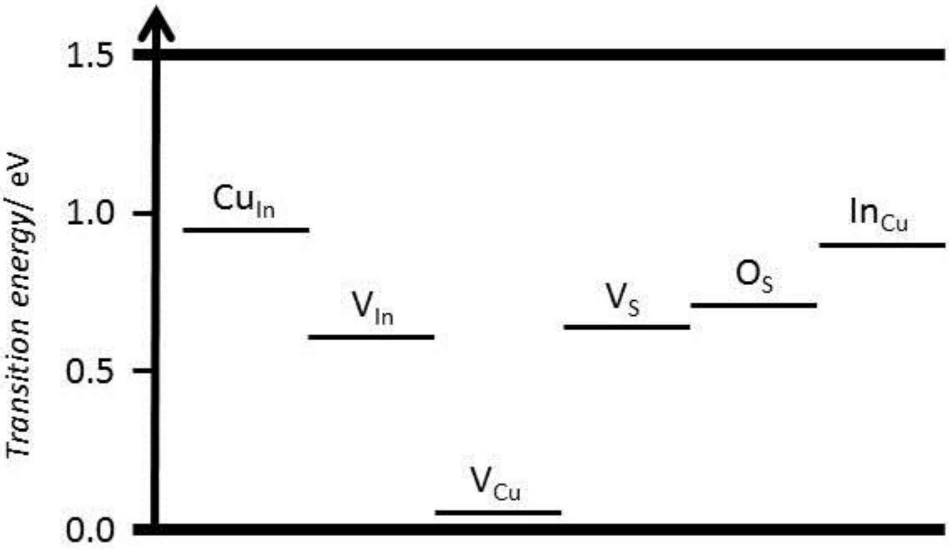

Figure 1.9: The calculated transition energy of intra-gap states associated with various point defects in bulk CIS. The zero transition energy is taken as the position of the valence band maximum.

An order of magnitude increase in PLQY is associated with CIS/ZnS QDs and a blue-shift in the PL spectral peak position is consistently observed. It is generally accepted that the binary sulfide layer saturates the 'dangling' bonds at the QD surface. The reduced surface disorder is associated with the suppression of intra-gap trap states that promote non-radiative recombination. Despite this understanding, the mechanism behind the highly radiative component observed in CIS/ZnS QDs remains uncertain [142,143]

Time-resolved (nanosecond) photoluminescence (PL) spectroscopy of CIS and CIS/ZnS QDs typically indicates two decay components. A highly radiative component with a long lifetime (on the order of 100 ns) is enhanced upon ZnS shell formation, whilst a much smaller (~ 10 ns) decay constant associated with surface trap states is suppressed [142-149]. These studies mainly conclude that the emission originates from the CB since it appears to be 'instantaneous' upon excitation, which contradicts the DAP recombination postulated by Nam *et al* [143].

A coupling between the conduction band (CB) and a donor state could be possible on an ultra-fast time-scale; a first attempt to gain information about possible ultra-fast non-radiative de-excitation channels in CIS/CdS QDs following photo-excitation was undertaken by Li *et al* in the form of (femtosecond) transient absorption (TA) spectroscopy [142]. A loss feature was observed at the band edge position and was attributed to the bleaching of the ground state (GSB), yet no contribution from stimulated emission (SE) or excited state absorption (ESA) was identified. Furthermore, no time-resolved TA spectra were presented. Several recent studies have performed more thorough TA studies on CIS QDs [150, 153-154], although there is still no general conclusion in the literature as to the origin of the long-lived PL in CIS QDs. A detailed study of the size-dependent PL properties in CIS QDs was performed by Omata *et. al* [155] and the conclusion that the PL originates from intra-gap donor states such as In_{Cu} antisite defects was made.

The advantage of TA spectroscopy is that the kinetics of the non-radiative as well as the radiative decay processes can be resolved, allowing for a more complete model of the excited state dynamics to be formed [47]. The TA experiment performed in this work is described in section 2.2.3 and the results are discussed in chapter 4.

Chapter 2

Experimental Procedures

This chapter describes the various synthesis methods for CIS-based QDs employed in this work. In addition, the experimental techniques used for the characterisation of the morphological, structural and optical properties are presented, and the underlying principles are discussed where it is relevant to later discussions.

2.1 Nanoparticle Synthesis

2.1.1 Dodecanethiol stabilised CIS and CIS/ZnS Quantum Dots

2.1.1.1 Synthesis

The synthesis of hydrophobic QDs was achieved by adapting a literature method in which the surfactant dodecanethiol (DDT) acts not only as both stabilising ligand and source of sulphur for the nanoparticles, but also as the reaction solvent [142, 146, 149]. The underlying principle behind this method is that a large (1000x) molar excess of thiol promotes complete surface ligand coverage and therefore good colloidal stability.

A wide range of indium and copper precursors have been shown to be compatible with this general method, including single source thiolate complexes [156, 157]. For the synthesis of CIS-based QDs in this work, indium (III) acetate and copper (I) iodide were used, because of their demonstrated reactivity and solubility [119]. For the synthesis of stoichiometric CIS QDs, equal molar quantities of copper and indium compounds were mixed with a molar excess (1000x) of DDT at room temperature in a glass round-bottom three-necked flask (100 mL) that was then fitted with a condenser reflux column and bubbler, as illustrated in Figure 2.1. The reaction was performed inside a fume hood to mitigate the risks associated with the potential for toxic gases being released during the reaction and the elevated temperature of the equipment. The typical volume of a single synthesis was between 10 and 100 mL; the upper limit was not explored whilst the lower limit arises due to the minimum depth in the flask required for an accurate reading from a thermometer placed through one of the necks.

The reaction solution was purged with argon for 30 minutes and continuously stirred. This crucial step prevents oxygen (O_2) from reacting with sulfur vacancies $V_S^{2+}$and forming oxygen-sulfur anti-site defects O_S^x which have been shown to be incorporated into CIS thin films formed by atomic layer deposition, influencing the p-type conductivity [158]:

$$\frac{1}{2}O_2 + V_S^{2+} \leftrightarrows O_S^x + 2h^+. \tag{2.1}$$

After purging with argon, the solution was heated to 100°C at which point metal-thiolate complexes are formed [119], as indicated by a transition from a cloudy mixture to a clear solution. These metal-thiolate complexes act as the monomers for nucleation. Incidentally, the specific nature of the metal precursors does not appear to directly influence nanocrystal nucleation since a homogenous solution of metal-thiolate complexes is formed regardless of the particular oxidation state of the precursors. The addition of a small amount of high-boiling point oil such as octadecene (ODE) or oleylamine (OLA) increases solubility and speeds the production of monomers. It has also been demonstrated that these solvents also play a coordinating role during nanocrystal growth and that their presence has important implications for the final crystal structure of the synthesised QDs [119, 120]. Specifically, the tetragonal zinc-blend phase of CIS is formed in the presence of ODE, whilst spherical wurtzite CIS nanocrystals are formed in the presence of OLA or trioctylphosphine oxide (TOPO). Interestingly there appears to be little to no variation in band gap between the two phases.

Once metal-thiolate complexes are present at high concentrations (i.e. if the solution is super-saturated) and the solution is at a high enough temperature (> 200°C), nucleation occurs, indicated by a relatively sudden colour change from yellow through orange to red, as shown in Figure 2.2. Gradually increasing the temperature to 150°C over a period of 10 minutes maximises the fraction of reagents that are transformed into the metal-thiolate monomers before nucleation occurs. As discussed in section 1.4.1 this minimises the size distribution of the product nanoparticles. Furthermore, the exact temperature at which nucleation occurs depends on the extent of super-saturation of the monomer.

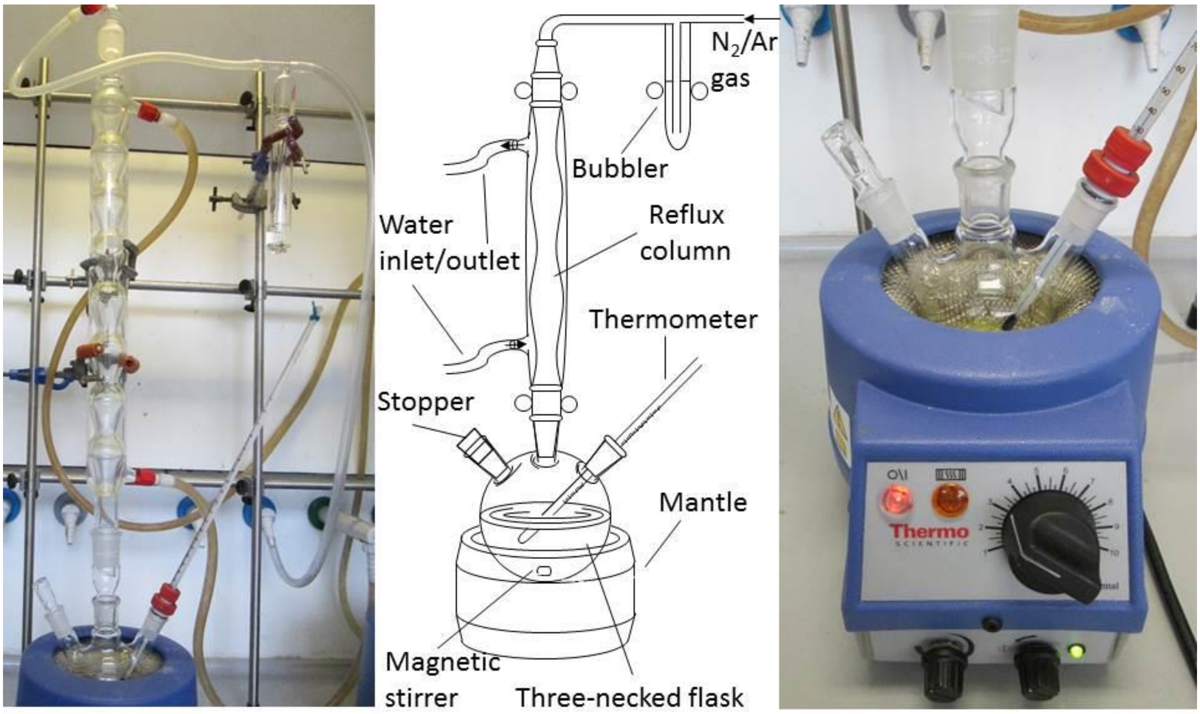

Figure 2.1: Apparatus required for the solvothermal synthesis of CIS-based QDs.

The subsequent growth phase was performed at a slightly lower temperature than the nucleation phase. Typically, the temperature was reduced to 200°C immediately after nucleation and the colour of the solution over ten minutes became very dark red (Figure 2.2). This colour change is a result of reduced confinement, as discussed in Chapter 1. The absorption band of the nanocrystal is red-shifted towards that of the bulk material, indicating nanocrystal growth. After 30 minutes the solution was almost black, indicating that the nanoparticles absorb strongly throughout the entire visible spectrum. Given the absorption spectra of bulk CIS this suggests that the nanoparticles are larger than the exciton Bohr radius of CIS (~ 4 nm) [158].

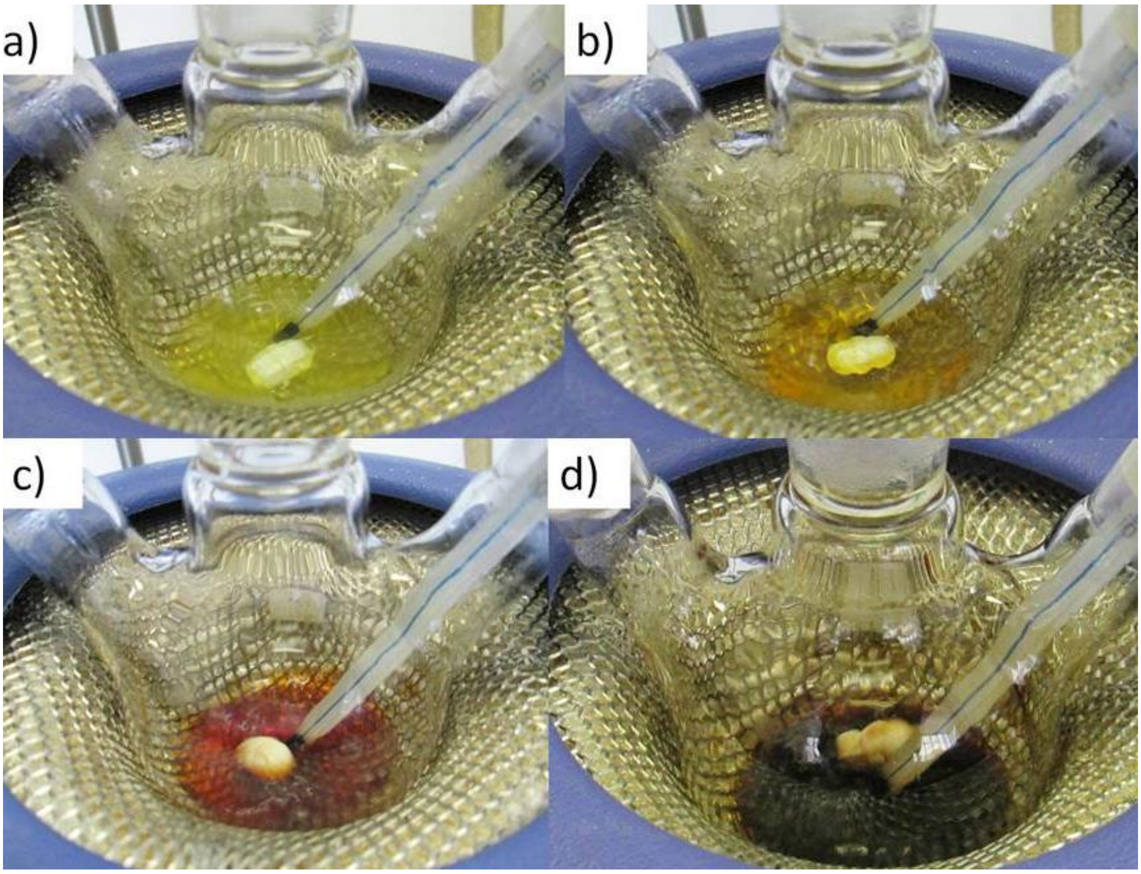

Figure 2.2: Digital photographs illustrating the colour of the solution at the four main stages of CIS QD synthesis: a) room temperature precursor mixture, opaque yellow; b) heated to 100-150°C, transparent yellow-orange metal-thiolate complexes; c) heated to 220°C, red indicating nucleation; and d) solution refluxed at 200°C for 30 minutes, very dark red indicates large nanoparticles.

The reaction was quenched once the desired size (colour) was achieved by removing the heat source and immersing the glass flask in a water-bath. A slow cooling process has been shown to be detrimental to the size-dispersion of the final QD product; therefore every effort was taken to speed up this process, such as replacing the water in the bath after 30 seconds.

A passivating ‘shell’ of ZnS was formed by the injection of a zinc precursor solution into the CIS QDs after the core growth had been partially quenched by immersion of the flask in a cold water bath until the temperature of the solution was below 100℃. Typically, 0.5 mmol zinc stearate was dissolved in ODE by heating to 80°C under continuous stirring before injection. The solution was refluxed for one hour at 180°C before being quenched in the same manner as for CIS QDs.

At room temperature the QD solution was removed from the flask by pipette and a small amount of organic solvent such as hexane or chloroform was added to encourage a stable colloidal suspension of the CIS QDs to be formed.

2.1.1.2 Quantum Dot Cleaning

A purification method based on centrifugation and solvent extraction was used to separate unreacted precursors and reaction by-products from the as-synthesised hydrophobic QDs suspended in an organic solvent. The principle is to develop a mixture of solvents that when combined will:

i) be miscible with the solvent in which the QDs are suspended;
ii) promote precipitation of the quantum dots; and
iii) dissolve any unreacted precursors and reaction bi-products.

Therefore, the extraction solvent used to clean the CIS and CIS/ZnS QDs suspended in hexane consisted of a mixture of chloroform, methanol (MeOH) and isopropyl alcohol (IPA) in a 1:1:10 volume ratio. A ten-fold volume of this mixture was added to the as-prepared CIS QDs and mixed by sonication and vortexing. At this point the poor solubility of the QDs in the polar solvents was indicated by a slow precipitation of the QDs from the solvent. The solution was then transferred in equal parts into two centrifugation tubes. The solutions were then centrifuged at 4000 rpm for ten minutes, after which the QDs were compressed at the bottom of the tubes in a ‘pellet’. The extraction solvent was then decanted and the pellet was dispersed in hexane. The precipitation and centrifugation process was repeated at least three times. The cleaned QDs were stored in glass vials at low temperature (< 5°C).

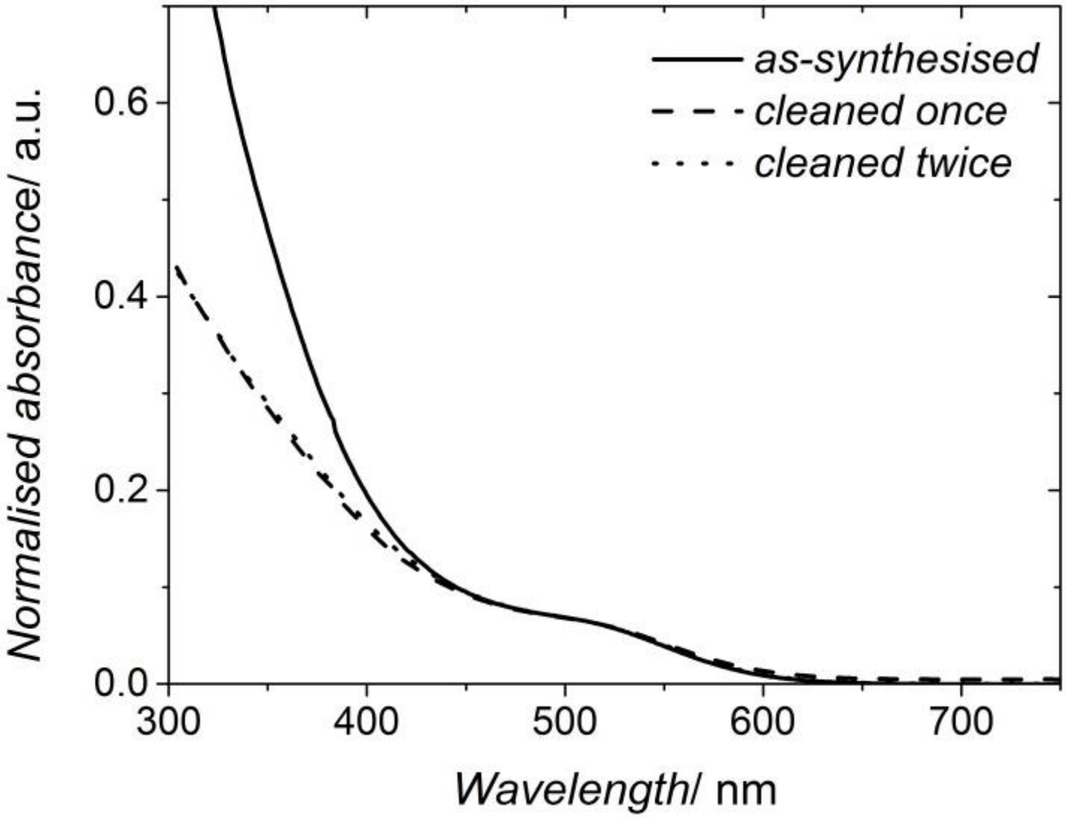

Figure 2.3: UV/vis data showing the spectral absorption of as-synthesised CIS QDs (solid line) and the absorption spectrum after one (dashed line) and two (dotted line) cleaning iterations.

The absorption spectrum, measured by UV/Visible spectroscopy (see 2.2.2), of the as-synthesised CIS QDs and the corresponding spectra after both one and two purification steps are shown in Figure 2.3. The spectra are normalised to their values at 500 nm. It is apparent that absorption is increasingly weakened below 400 nm, indicating that unreacted material has been removed from the QD solution. The absorption above 400 nm remains relatively unchanged throughout the cleaning process, and can be attributed to the QDs.

It appears that since very little difference can be identified between the absorption spectrum after one precipitation/centrifugation steps and the absorption spectrum after two steps. This suggests that the majority of unreacted precursors that can be removed by this technique are so after the first iteration. Despite this indication, the CIS QDs used in this thesis underwent at least two iterations to ensure sample quality.

2.1.2 MUA stabilised CIS and CIS/ZnS Quantum Dots

Mercaptoundecanoic acid (MUA) stabilised CIS QDs were synthesised by similar solvothermal reaction to the DDT stabilised CIS QDs, although the solvent MUA is a powder at room temperature. For the synthesis of stoichiometric CIS QDs, equal molar quantities (0.25 mmol) of indium acetate and copper iodide were mixed with a two-fold molar excess of thiourea (0.5 mmol) and a four-fold molar excess of MUA (1 mmol). This mixture is a powder at room temperature and was therefore heated slowly to 110 ℃ under gentle magnetic stirring in a three necked flask until a yellow opaque liquid was observed. The solution was then purged with argon for 30 minutes. Further heating to 180 ℃ resulted in the solution becoming transparent, and a gradual colour change from yellow to dark red was observed, indicating nanoparticles nucleation. The reaction was quenched by immersing the flask in a cold water bath.

MUA stabilised CIS/ZnS QDs were synthesised following the injection of 0.5 mmol thiourea and 0.5 mmol zinc nitrate hexahydrate, dissolved in deionised water, into the as-synthesised CIS QD solution and refluxing at 100℃ for 4 hours. The shell precursor solution was adjusted to pH 10 by the drop-wise addition of NaOH to avoid aggregation of the carboxylic acid functionalised CIS QDs during ZnS shell growth. The reaction was quenched by immersing the flask in a cool water bath.

Purification of the MUA stabilised CIS and CIS/ZnS QDs was achieved by repeated precipitation by addition of isopropanol followed by centrifugation.

2.1.3 Mercaptoundecanol CIS and CIS/ZnS Quantum Dots

Mercaptoundecanol (MUD) stabilised CIS QDs were synthesised by one-pot solvothermal method. First, 47.5 mg (0.25 mmol) copper (I) iodide, 146.0 mg (0.5 mmol) indium (III) acetate, 76.4 mg (1.0 mmol) thiourea and 204.4 mg (1.0 mmol) MUD were dissolved in 6 mL ethylene glycol. The solution was sonicated for 30 minutes and then transferred into a three-necked round-bottomed glass flask by glass pipette. The flask was placed inside a heating mantle and the solution was purged with argon whilst being magnetically stirred continuously for 30 minutes. Then, the solution was heated to 100°C at which point an opaque yellow solution was formed. Further heating from 100°C to 160°C caused a gradual colour change from yellow, through orange, to red. Refluxing at 160°C for a further 15 minutes was sufficient to form QDs emissive at red-to-NIR wavelengths.

To form the ZnS layer, the CIS core QDs were cooled to 100°C and 181 mg (0.5 mmol) of the single-source precursor zinc diethyl-dithiocarbamate (ZDEC) was added to the solution. This solution was then refluxed for 1 hour at 110°C, at which point a second batch of ZDEC was added into the solution and refluxed for another hour. The reaction was quenched by rapidly cooling the flask to room temperature in a water bath.

For cleaning, the QDs were removed from the flask by glass pipette directly into centrifugation tubes and diluted once with the addition of methanol. The same extraction solution as for the DDT stabilised CIS QDs described in section 2.1.1 was used.

2.1.4 Encapsulation of CIS/ZnS Quantum Dots with Amphiphilic Polymer (Amphipol)

Hybrid QD/amphipol NPs were formed by self assembly between CIS/ZnS QDs and the amphipol poly(maleic anhydride-*alt*-1-octadecene), 3-(Dimethylamino)-1-propylamine derivative (PMAL-d, purchased from Sigma Aldrich, Figure 2.4). PMAL-d has two charged groups, namely a carboxylic acid and a tertiary amide. At high pH the carboxylic suspended is deprotonated and thus has a negative charge and at low pH the amide is protonated and has a positive charge. This zwitterionic nature, where a net charge is present across the entire pH range (except at neutral pH), is useful for dispersing QDs in solution by electrostatic repulsion. PMAL-d (a white powder at room temperature) was dissolved in chloroform (10 mg/mL) and added to the purified CIS/ZnS/DDT QDs dispersed in hexane to give a QD:PMAL-d molar ratio of 1:30.

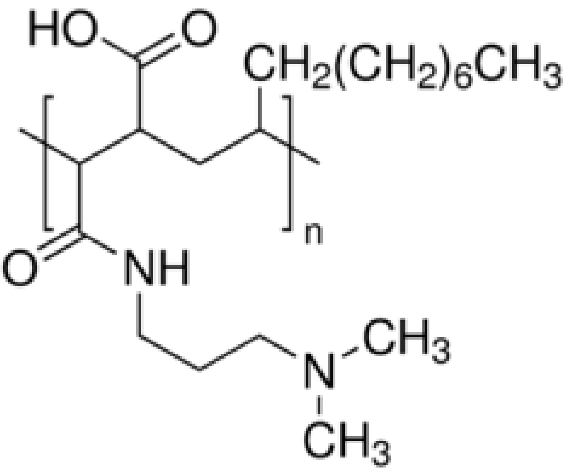

Figure 2.4: Molecular structure of PMAL-d. The molecular weight of PMAL-d is 12 kDa. Reproduced from [159].

The solution was then stirred continuously under argon flow for 2 hours and the solvent was evaporated overnight in the dark, at room temperature, forming a dried film of QDs embedded in PMAL-d at the bottom of the vessel. Deionised water was added and adjusted to pH 10 by the drop-wise addition of NaOH. The complete suspension of the QD/PMAL-d NPs in the aqueous phase was ensured via the ultra-sonification of the suspension for 15 minutes. The standard QD:PMAL-d ratio used was 1:25, based on simple calculations. The volume V of a regular tetrahedral QD is related to the area A_{face} of each face and the height h by

$$V = \frac{1}{3} A_{face} h \tag{2.2}$$

The face area can also be related to h, by

$$A_{face} = \frac{\sqrt{3}}{4} a^2 = \frac{3\sqrt{3}}{8} h^2 \tag{2.3}$$

where a is the edge length of the tetrahedral QD. The volume of the tetrahedral CIS QDs can therefore be related to the length d of the triangular projection in TEM, which is equivalent to the height:

$$V_{QD} = \frac{\sqrt{3}}{8} d^3 \tag{2.4}$$

The corresponding QD total surface area is simply $4A_{face}$ and is therefore given by

$$A_{total} = \frac{3\sqrt{3}}{2}d^2 \tag{2.5}$$

For example a QD of size $d = 3\,nm$ has a total surface area of approximately $24\,nm^2$. A surface coverage of 15 PMAL-d monomer units per nm^2, or 0.5 polymer chains per nm^2, is assumed based on the molecular mass of PMAL-d, indicating that a minimum of 12 polymer chains per QD is required for complete surface coverage. Typically the molar excess of PMAL-d was doubled so that the QD:polymer ratio was 1:25, in order to ensure optimal encapsulation.

Two methods were evaluated for the separation of excess unbound PMAL-d from the suspension. Firstly, an iterative centrifugation method (Figure 2.5) requires the NP solution containing unbound PMAL-d to be repeatedly filtered through the membrane of a diafiltration centrifugation device (DCD), retaining the QD-polymer NPs and removing free PMAL-d. The flow through the membrane is driven by centrifugation, so that the larger mass of the QD/PMAL-d NPs compared to a single PMAL-d polymeric chain results in increased transport through the membrane.

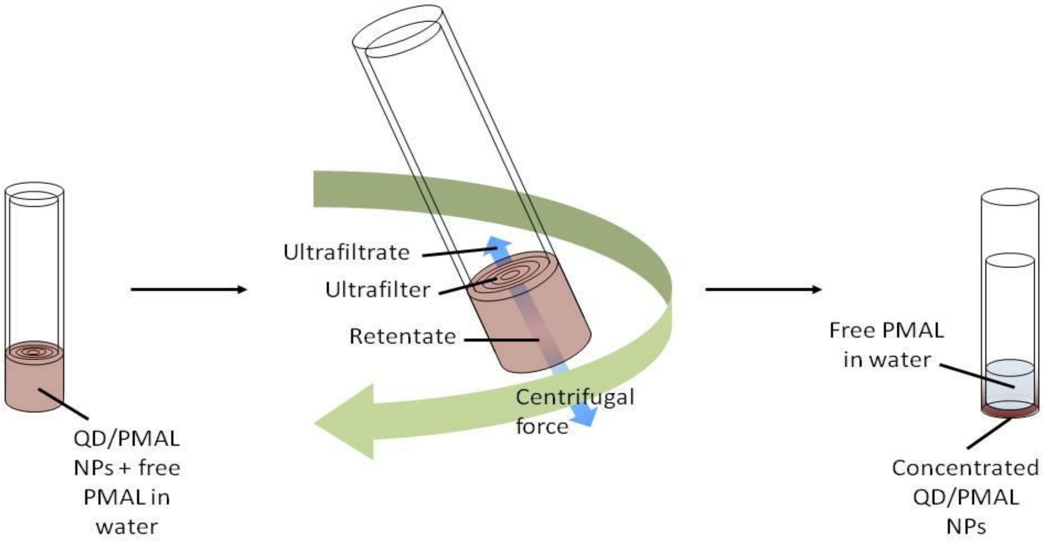

Figure 2.5: Illustration depicting dead-end membrane filtration by centrifugation.

Secondly, a tangential flow filtration (TFF) system was evaluated (Figure 2.6). An electric pump draws from a feed of CIS/ZnS/PMAL-d NPs suspended in water through a vertical filtration membrane at a higher pressure than the permeate side of the membrane. The tangential flow of the suspension relative to the membrane has a rinsing effect and decreases fouling, and the continuous nature of the flow is a significant practical advantage over dead-end filtration.

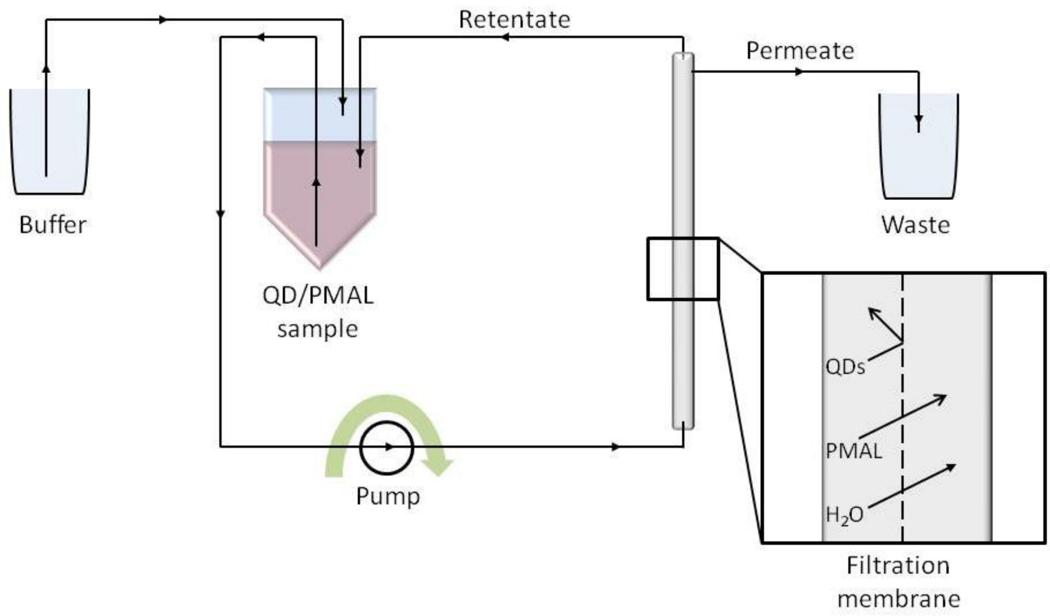

Figure 2.6: Illustration depicting the tangential flow filtration system used for removal of unbound PMAL-d from the QD/Amphipol NP suspension.

The retentate is returned to the stock solution through PTFE tubing and the permeate was discarded as waste. Fresh solvent was added to the feed to conserve the NP concentration although this can be neglected in order to perform sample concentration simultaneously.

2.1.5 Dodecanethiol stabilised $CuFeS_2$ and $CuFeS_2$/ZnS Quantum Dots

Dodecanethiol stabilised $CuFeS_2$ (CFS) and CFS/ZnS QDs were synthesised in an identical manner to the CIS and CIS/ZnS QDs described in section 2.1.1, except that the indium acetate was replaced with an equivalent molar quantity of iron (III) acetylacetonate. The band gap of CFS is much smaller than that of CIS and as such the absorption of CFS nanocrystals is significantly red-shifted in comparison. The result of this is that the colour changes described for the synthesis of CIS QDs does not apply to CFS NCs; the solution is very dark from the start and no change in colour is observable by eye.

2.1.6 CdTe-based Quantum Dots

CdTe core QDs were synthesised following a literature method [160, 161]. First, 0.9113g cadmium perchlorate hexahydrate and 0.397mL thioglycolic acid (TGA) were dissolved in 200mL of deionised water, forming a solution with pH ~5. Sodium hydroxide (1 M) was added by drop-wise addition until the solution pH was 11.2 and the solution was then transferred to the reaction flask by glass pipette and purged with argon for 30 minutes. In a separate reaction flask, 0.2g aluminium telluride was purged with nitrogen for 15 minutes. With nitrogen still flowing through the two flasks, 15mL sulfuric acid (0.5M) was injected into the flask containing the aluminium telluride, forming tellurium gas which was carried with the nitrogen into the main reaction flask. After 15 minutes the nitrogen flow was turned off and the tubing between the flasks was removed. The main reaction flask was heated to 100°C and refluxed for 40 minutes after which the reaction was quenched by immersing the flask in a cold water bath.

The synthesis of CdTe/ZnS core/shell QDs was performed in a similar manner. First, 34mg of zinc nitrate is dissolved in 60mL CdTe QD solution synthesised as above. The solution was refluxed at 100°C for one hour with an additional 5mg of thiourea added after 30 minutes. The reaction was quenched by immersing the flask in a cold water bath.

The removal of unreacted reagents and reaction bi-products was achieved by the precipitation of the QDs from solution by the addition of an equal volume of isopropyl alcohol, followed by centrifugation at 14 rpm for 5 minutes at 17°C, forming a pellet of QDs at the bottom of the centrifugation tube. The supernatant was decanted and the pellet was re-suspended in isopropyl alcohol and centrifuged again. The pelleted QDs were then suspended in 1mL of deionised water modified to pH 11 with sodium hydroxide.

2.2 Optical Spectroscopy

Optical spectroscopy refers to the study of the interaction between light and matter as a function of wavelength in the ultra-violet (UV), visible and near infra-red (IR) regions of the electromagnetic spectrum. A variety of materials, from organic molecules to inorganic structures such as quantum dots, undergo electronic transitions at these energies and it is therefore a widely useful technique to characterise the spectral properties of absorption, excitation, and emission. Furthermore, the use of pulsed lasers enables the temporal dynamics of these processes to be studied on a sub-femtosecond time scale. Optical spectroscopy in general is therefore a highly useful technique for studying both the ultra-fast and long lived excited state dynamics of both dark and emissive states in CIS/ZnS QDs. Specific spectroscopic techniques relevant to this thesis are described in more detail in the following sections.

2.2.1 Fluorescence Spectroscopy

Fluorescence spectroscopy (spectro-fluorometry) enables quantification of the spectral properties of excitation and emission and thus provides a basis on which the origin of photoluminescence in CIS-based QDs can be investigated.

Briefly, high intensity light from an excitation source is directed at a QD suspension held in a quartz cuvette. The interaction between a single photon and a QD results in an electron being excited from the valence band into the conduction band. Subsequently, the electron and hole recombine, with a probability of emitting a photon at some point in the process dependent upon the photo-luminescence quantum yield (PLQY) of the quantum dot. The intensity of emitted photons as a function of energy is measured by a photo-detector, which is orientated at 90° to the excitation beam in order to minimise the probability of detecting a transmitted or reflected photon. The detector is usually based on a photomultiplier, photo-diode, or a charge-coupled device and the recorded intensity profile is usually resolved by wavelength, resulting in an emission (or excitation) spectrum.

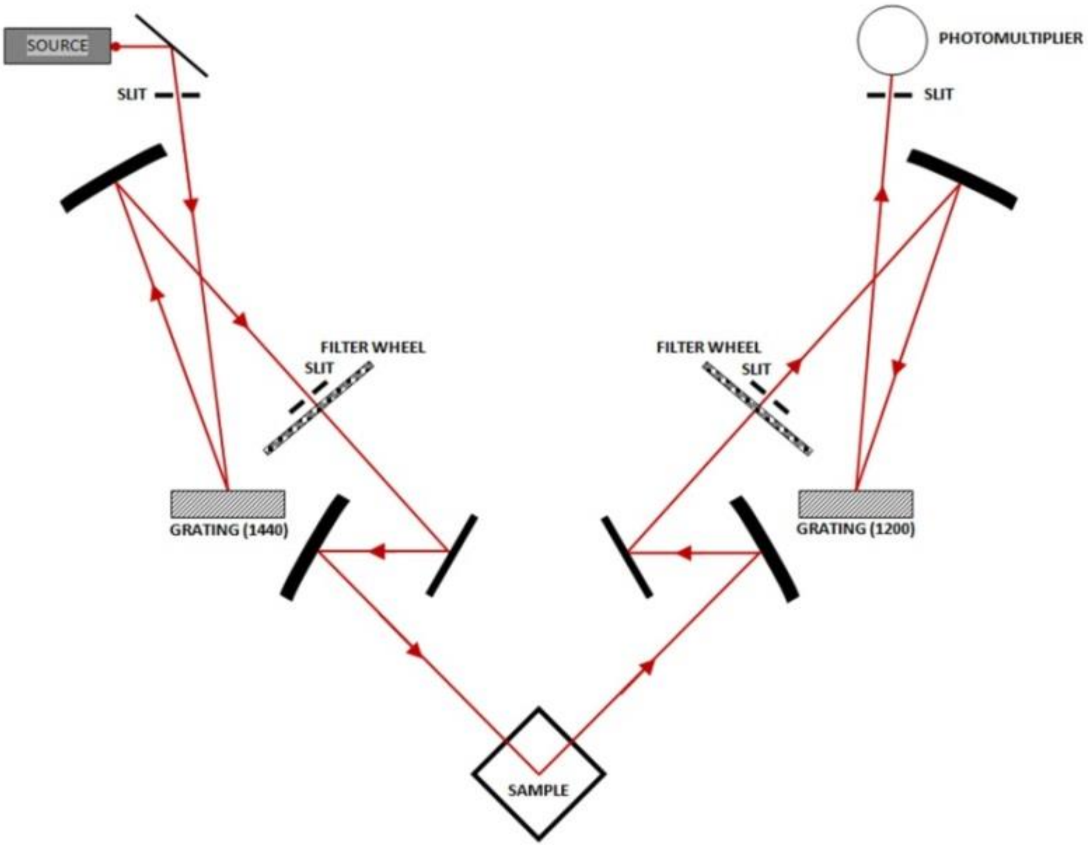

Figure 2.7: Schematic diagram showing the components and mechanism of the Perkin Elmer LS55 fluorescence spectrometer.

The excitation beam can be produced from various types of light source, including lasers, light-emitting diodes (LEDs) and lamps. Tuneable laser systems provide many benefits: a high power density is achievable in comparison to other sources, improving the sensitivity of detection; and the associated temporal coherence allows excitation with extremely narrow spectral distribution (nm), simplifying the detection process and increasing the information content of measurements. Although the situation is changing, the impracticality and initial set-up cost of tuneable bench-top laser systems typically prevent them from being feasible; lamps provide a much more practical alternative to lasers, in terms of ease-of-use. Usually, xenon arcs or mercury vapour lamps are used, enabling the entire visible spectrum to be probed. Mercury vapour lamps are less often used, since their spectral power output consists of several narrow peaks between 350 nm and 600 nm and the available excitation wavelengths are therefore restricted, whereas the power output of xenon arcs is almost constant throughout the visible spectrum.

The Perkin Elmer LS55, the instrument used to record all photoluminescence spectra presented in this thesis, contains a pulsed xenon arc lamp in order to minimise photo-bleaching in the sample and extend the lifetime of the lamp. Spectral resolution of the excitation and emission processes is afforded by a monochromator at either side of the sample, consisting of a collimator, which converts the diverging light of the light source to collimated light; and a diffraction grating, which reflects the incident light at a wavelength-dependent angle. The wavelength to be transmitted is selected by adjusting the monochromator to block reflected light at all angles except that corresponding to the desired wavelength.

In order to record an emission spectrum, the excitation monochromator is kept fixed at the desired excitation wavelength, and the emission monochromator swept over the desired spectral range. On the contrary, when recording excitation spectra, the emission monochromator is kept fixed and the excitation monochromator is swept.

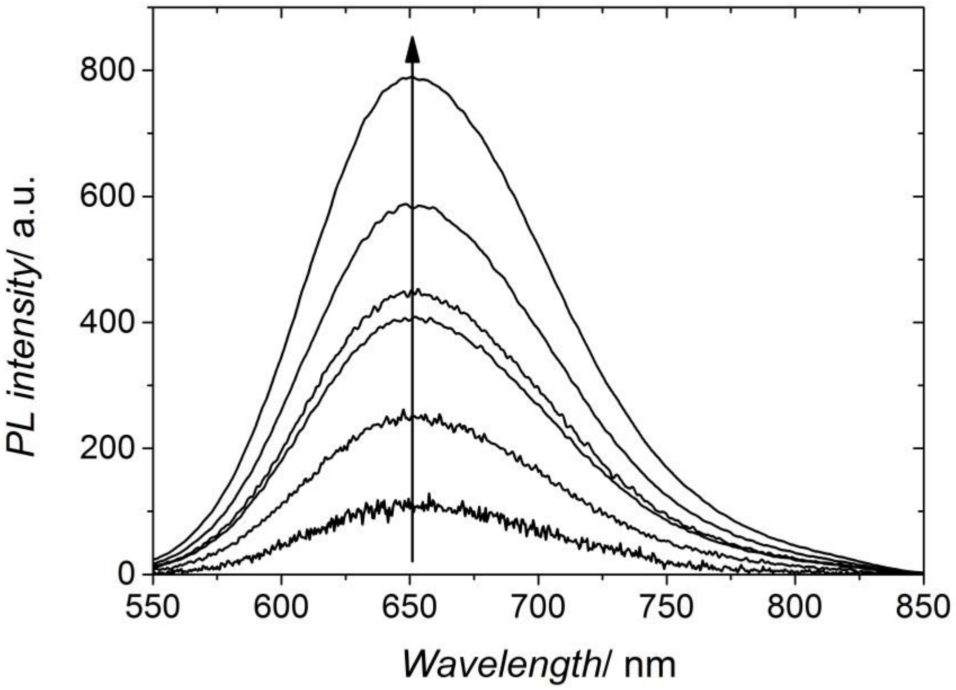

Figure 2.8: A typical PL spectral peak of CIS QDs measured at varying slit widths, demonstrating the increased noise as the slit is closed. The arrow indicates the direction of increasing slit width.

Each monochromator includes a variable slit with a width limited to between 2.5 and 13 nm controlling the spectral distribution of the transmitted light. The slit width also influences the intensity of light incident on the sample and on the detector and thus the signal-to-noise ratio for a given sample. The transmitted light intensity is proportional to the square of the slit width and the signal-to-noise ratio decreases as the slit width is reduced. Alternatively, the system can be modified by the addition of neutral density filters to the same end, giving more quantifiable data.

2.2.2 Ultraviolet/visible Spectroscopy

Ultraviolet/visible spectroscopy (absorption spectroscopy) measures the absorption of the light source by the sample in the ultraviolet (UV), visible and near-infra-red (IR) regions of the spectrum. In this case it is the transmitted light, which does not interact with the sample, which is detected, indicating how much light was absorbed by the sample. The transmission through a reference consisting of the solvent alone is also recorded, the difference between the sample and reference spectra giving the contribution from the sample alone. The transmission spectrum is then converted to an absorption spectrum, quantifying the amount of light 'lost' due to interactions with the sample.

Typically, the light source is a tungsten, deuterium or halogen lamp. Multiple lamps are often incorporated into commercial UV/Visible spectrometers in order to extend the accessible region of the spectrum. The excitation light is passed through a monochromator enabling the excitation wavelength to be scanned across the entire spectrum and typically an adjustable slit affords control over the intensity of light incident on the sample. As for fluorescence spectroscopy, a smaller slit width improves resolution but decreases the power incident upon the sample.

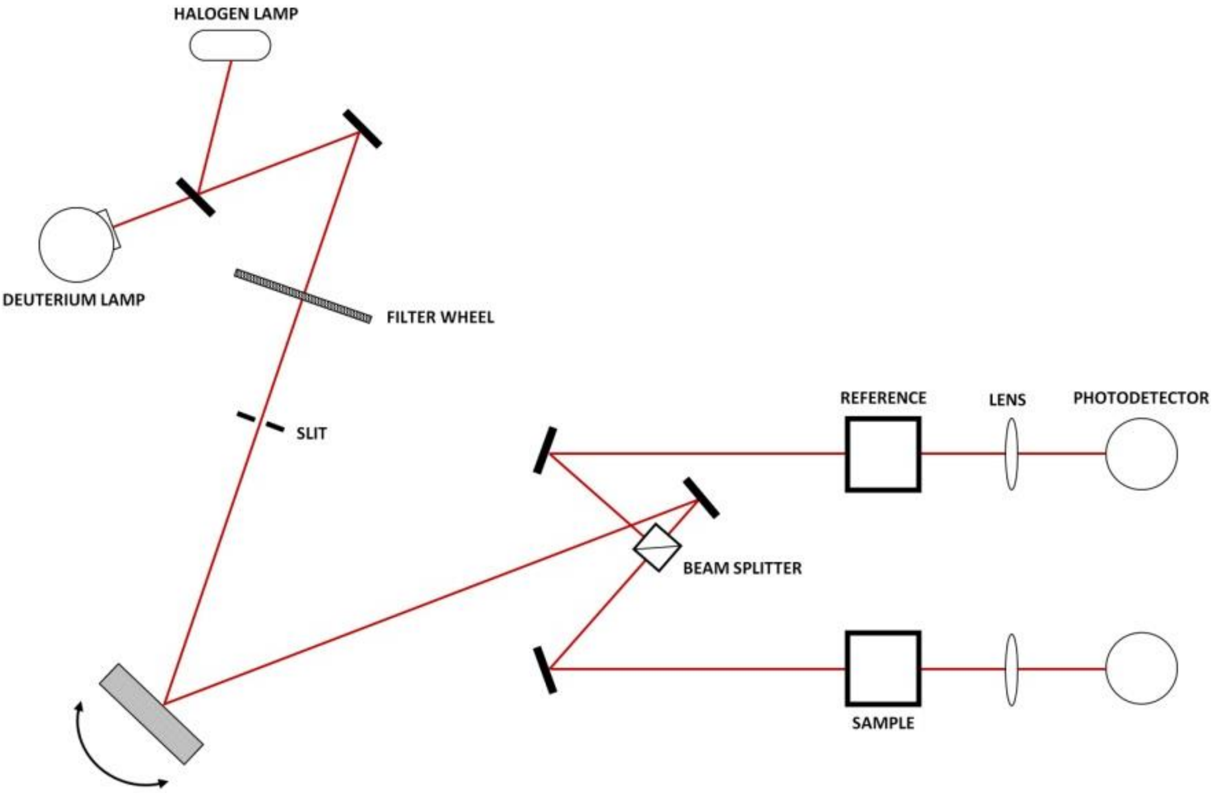

Figure 2.9: Schematic diagram showing the components and mechanism of the Perkin Elmer Lambda 35 UV/vis spectrometer.

The excitation light is then directed through a beam splitter; half of the initial intensity is incident upon the sample and the other half on the reference. The sample and reference beams are then focused onto separate photodetectors. The measured change in excitation intensity I_x over a distance dx through a QD suspension, relative to the reference, is related to the attenuation cross section σ and the concentration of particles N by the following equation:

$$-\frac{dI_x}{dx} = \sigma N I_x \tag{2.6}$$

Over a path length l this can be reduced to

$$\ln(I_l) - \ln(I_0) = -\sigma l N, \tag{2.7}$$

and the transmittance through the sample is expressed as

$$\mathrm{T} = \frac{I_l}{I_0} = e^{-\sigma l N}. \tag{2.8}$$

Since the absorbance, A, is equal to the logarithm of the transmittance through the sample,

$$A = -\ln(T) = \sigma l N \tag{2.9}$$

and the macroscopic absorbance by a QD solution is related to the molar extinction coefficient ε and the molar concentration of QDs, C, via the Beer-Lambert law [162]:

$$A = \varepsilon C l \tag{2.10}$$

The practical significance of this equation is that the concentration of a given sample can be easily determined by routine absorption spectroscopy if $\varepsilon(\lambda)$ is known.

2.2.3 Transient Absorption Spectroscopy

Transient absorption spectroscopy measures the absorbance at a certain wavelength of a material or molecule as a function of time after excitation, providing information about the temporal dynamics of non-emissive states as well as emissive states and is therefore a powerful technique for investigating the non-radiative excited state dynamics of CIS/ZnS QDs.

Briefly, two separate beams are generated from a pulsed laser source and are directed so as to spatially overlap in the sample. A temporally short, high intensity 'pump' beam excites the sample into an excited state, and variably delayed 'probe' pulses are used to measure its linear absorbance as a function of time after excitation. The measured quantity is the difference between the optical density of the excited sample and the sample in its ground state:

$$\Delta OD(\lambda) = -log\frac{I_{pumped}}{I_{unpumped}} \tag{2.11}$$

The three primary processes which may contribute towards a non-zero ΔOD signal in CIS/ZnS QDs are illustrated in Figure 2.10 and are described below:

i) Ground state bleach (GSB): Immediately after excitation by the pump pulse, a fraction of QDs will exist in the excited state; the number of QDs in the ground state is reduced. Consequently, ground state absorption with the pump is lower than with the pump off, and a negative ΔOD signal is observed in the λ region corresponding to ground state absorption.

ii) Stimulated emission (SE): Stimulated emission is the process by which the probe beam induces QDs in the excited state to relax to the ground state, emitting photons in the process that have the same frequency, polarisation, phase and direction as the incident photons. The resulting increase in light intensity on the photo-detector translates to a negative ΔOD which generally resembles the photoluminescence spectrum of the sample, since this phenomenon occurs only for optically allowed transitions.

iii) Excited state absorption (ESA): Upon excitation by the pump pulse, transitions from the excited state into higher states can occur due to absorption of the probe beam, resulting in a positive ΔOD signal.

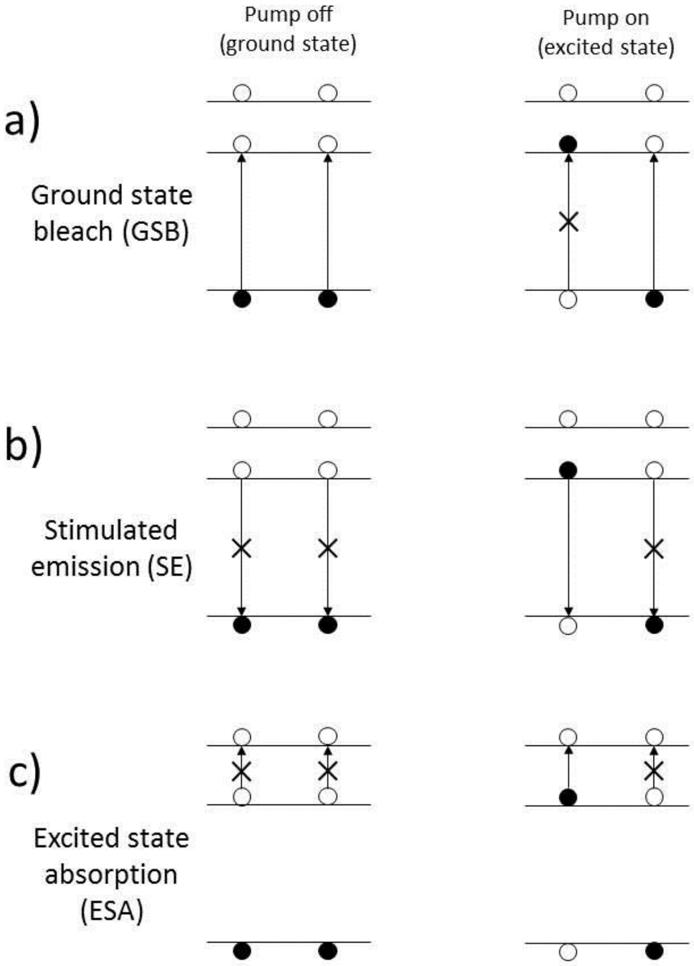

Figure 2.10: Diagrams of a simplified three level model of a QD in the excited state (left hand side) and ground state (right hand side) showing the processes which contribute to a non-zero signal in TA spectroscopy: a) ground state bleach (GSB); b) stimulated emission (SE); and c) excited state absorption. Filled circles represent electrons and hollow circles represent holes. Arrows describe the possible probe induced transitions and crossed arrows indicate transitions which are not available.

In this work, a femtosecond laser system (Clark-MXR CPA-2110) was used to generate pulses of 150 fs centred at 772 nm with energy 1 mJ and a repetition rate of 1 kHz. Both the pump and probe pulses were generated from a fraction of the 772 nm fundamental laser output. About a third (350 µJ) was used to generate a 40 fs pump pulse with a variable wavelength (480 nm to 700 nm) and with energy of up to 25 µJ, by a non-linear optical parametric amplification (NOPA) process.

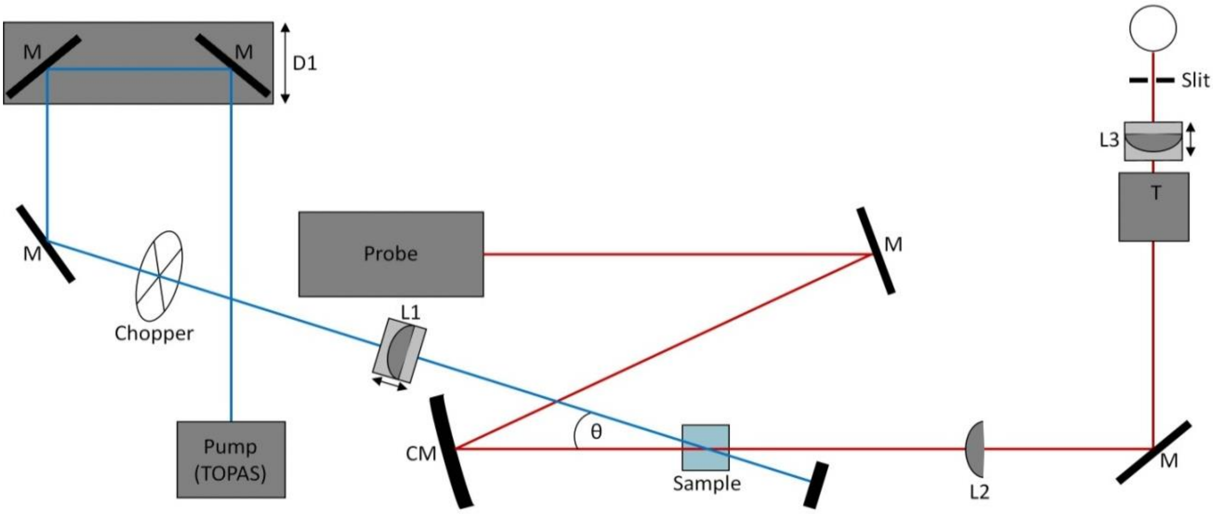

Figure 2.11: Schematic diagram showing the components and lay-out of the TA spectroscopy set-up.

The white light continuum 'probe' was generated by focusing (f = 30 mm) a small fraction (5 μJ) into a 1 cm fused silica cuvette filled with deionised water, generating a stable continuum from 480 nm to approximately 1100 nm, and was collimated with an off-axis parabolic mirror.

The sample medium is pumped at a sufficient high flow rate through a fused silica flow cell to avoid re-excitation of the same sample portion. The foci position of the pump beam is set slightly before the sample position and optimised on the excited state absorption signal of a Rhodamine 6G dye solution, and the pump beam is aligned to cover the whole interaction region of the probe beam in the sample medium.

The probe light was spectrally dispersed by a fused silica prism in a modified Yvon-Horiba spectrometer and mapped into space onto a line scan camera. Each experiment acquired between 500 to 2500 laser shots per time delay on a shot-to-shot base (pump on/off). The signal processing was carried out in LabView 2012. The temporal chirp of the probe continuum was mathematically corrected for after the spectra were collected, based on the experimentally observed coherence spike.

2.2.3.1 Hole-burning

A third variable wavelength laser beam can be introduced into the scheme which may be locked onto a transition in order to produce stimulated emission. This allows selective depopulation of emissive or absorbing states at a chosen time after excitation. Therefore an intense laser pulse is needed that can be provided by the fundamental 772 nm pulse, its second harmonic 387 nm or any light that is not required for the pump or probe pulse from the NOPA. The wavelength tunability of the NOPA allows an electronic transition to be tuned onto and state to be selectively depopulated.

2.2 X-ray Photoelectron Spectroscopy

X-ray photoelectron spectroscopy (XPS) is a technique based on the liberation of an electron from an atom in a sample by a high energy incident X-ray photon. The kinetic energy E_k of an emitted electron is related to the binding energy E_b of the initial state

$$E_b = hv - (E_k + \phi) \tag{2.12}$$

where hv is the energy of the incident photon and the work function ϕ is the energy required to remove an electron from the surface of a material and is described by the equation:

$$\phi = E_{vac} - E_F \tag{2.13}$$

where E_{vac} is the vacuum energy and E_F is the Fermi-energy of the material.

The composition and chemical state of a sample can therefore be determined by measuring the number of emitted electrons resolved over a range of binding energies (0 – 1kV) and comparing to reference values of elemental binding energies. Furthermore, small (eV) shifts in binding energy peak positions can convey information pertaining to chemical bonds in the sample.

The attenuation of the X-rays by the sample enables a typical penetration depth of approximately 10 nm; therefore XPS is an inherently surface-sensitive technique. Although applications are therefore limited to either ultra-thin samples or the surfaces of larger structures, etching techniques can be introduced to ‘depth-profile’ the sample. The surface-sensitivity of XPS is of great benefit in the context of colloidal QDs, however, since both the composition of the entire semiconductor core (if < 10 nm) and the organic surface chemistry can be quantified.

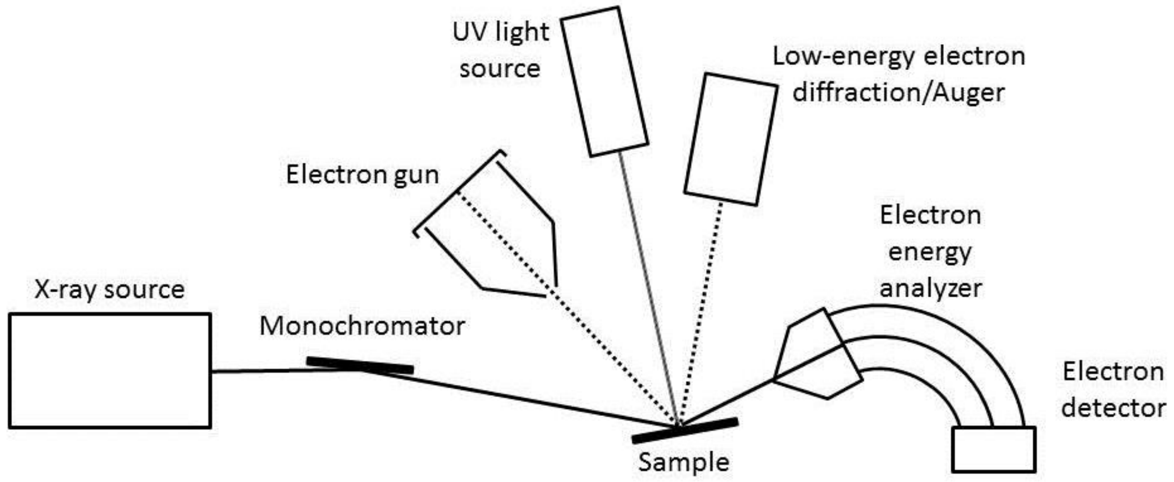

Figure 2.12: Schematic diagram showing the components of a typical photoelectron spectroscopy set-up enabling XPS, UPS and LEED/Auger analysis to be performed.

Generally, K_α X-rays are directed onto a grating diffraction monochromator before being directed onto the sample stage. The resulting X-ray photoelectrons from the sample are decelerated by a retarding electric field and their kinetic energy is analysed by the variation of the orbit in a magnetic field.

The removal of an electron from an atom within the sample creates a local positive charge, which in turn affects the binding energy of the remaining electrons, potentially skewing the data. An electron gun can be used to ‘flood’ the sample with electrons at a rate which negates this effect, and any remaining charge induced shifts can be corrected for by the addition or subtraction of a charge correction value calculated from the measured shift in the C1s peak position from the characteristic reference position. The accuracy of this value is vital to the sensitivity of XPS in identifying small chemical shifts.

2.3 Ultraviolet Photoelectron Spectroscopy (UPS)

UPS is a complimentary technique to XPS, except that it probes the weakly bound valence electrons, which all materials have within a few eV of the Fermi level, rather than the core electronic states. These valence electrons are involved in bonding and electrical conduction and are thus important to understand. In bulk, these states are broad and the valence spectrum appears continuous. In QDs however, the valence states are more discrete and can theoretically be identified, although this requires averaging over all angles, which typically broadens the spectrum significantly.

2.4 X-ray Diffraction Crystallography (XRD)

Bragg's law describes the constructive interference of radiation reflected of various crystal planes at angles of incidence θ that correspond to the spacing d between the planes:

$$n\lambda = 2d\sin\theta \tag{2.14}$$

The diffraction peaks are due to the scattering of the radiation by the atomic nuclei and are characteristic of the crystal structure. The width of the diffraction peaks also carries information about the crystalline grain size and the strain in the crystal structure, although instrumental broadening must be accounted for prior to this analysis.

The Scherrer equation (equation 2.15) relates the line-broadening β of a diffraction peak at angle θ with the grain size D and is valid for nano-sized crystals only (i.e. smaller than $0.1\mu m$) [163]:

$$D = \frac{\kappa\lambda}{\beta_D\cos\theta} \tag{2.15}$$

where κ is a shape factor, close to one, that accounts for the shape of the crystallite. Typically, the value of κ is around 0.9. The Scherrer equation can be combined with the Stokes and Wilson formulation for strain-induced broadening $\beta_s$which depends on the inhomogenous strain γ and a constant C

$$\beta_s = C\gamma\tan\theta \tag{2.16}$$

The Williamson-Hall approach [164] combines the size and strain broadening by

$$\beta_{Total} = \beta_D + \beta_s = \frac{\kappa\lambda}{D\cos\theta} + C\gamma\tan\theta \tag{2.17}$$

Which can be simplified by multiplying through by $\cos\theta$:

$$\beta_{Total}\cos\theta = \frac{\kappa\lambda}{D} + C\gamma\sin\theta \tag{2.18}$$

Therefore, by plotting $\beta_{Total}\cos\theta$against $\sin\theta$ can quantify the size-induced broadening by the magnitude of the intercept and the strain induced broadening from the slope $C\gamma$.

In this work diffraction data was collected in the range 2θ = 20 – 65° with a step size of 0.05° for ca. 1 hour, using a P'Analytical X'Pert MPD (Almelo, The Netherlands), in Bragg-Brentano geometry, using Cu kα_1/kα_2 radiation ($\lambda = 0.15418$ nm). The powders were placed on a low background silicon sample holder which was rotated at 15 rpm, to minimise the effect of texture/preferred orientation. A silicon standard was run under identical conditions, in order to determine the instrumental broadening. Rietveld refinements were prepared using the program ‘X’Pert HighScore Plus’, encompassing the ICDD (International Centre for Diffraction Data) PDF4 database.

2.5 Electron Microscopy

The Rayleigh criteria [165] for the resolution of two point-like objects viewed through an optical microscope with a circular aperture state that the first minimum in the diffraction pattern of one must be located far enough away from the central maximum of the other, and that the minimum angular separation at which two object can be separately resolved depends on the wavelength λ of the illumination source

$$d = \frac{1.22\lambda}{2\sin\theta}, \tag{2.19}$$

where 2θ is the angle of collection of the microscope and the numerical factor 1.22 takes into account the Airy disc of the diffraction pattern. A more rigorous formulation was provided by Abbe [166], taking into account the numerical aperture ($NA = n\sin\theta$) of the microscope:

$$d = \frac{\lambda}{2(n\sin\theta)}. \tag{2.20}$$

Whereas the resolution of optical microscopes, with operational wavelengths on the order of 100 nm, is therefore diffraction-limited to approximately 200 nm, electron microscopes benefit from the much shorter de Broglie wavelength of electrons and are theoretically able to achieve resolution on the pm scale, making it an extremely powerful tool for imaging the structure of biological and inorganic materials at the nanoscale. The resolution achievable with light microscopy is limited by the wavelength of the light source used. The development of UV microscopes increased the resolution by a factor of two, but sub-micron resolution was thought to be impossible. However, the de Broglie wavelength of a typical electron used in TEM is a few thousandths of a nanometre, allowing for much higher resolution approaching the atomic scale. Because of the nature of electrons, the lenses used in electron microscopy are actually electrostatic or magnetic lenses and are designed to behave like optical lenses and be radially symmetric to prevent astigmatism.

2.5.1 High Resolution Transmission Electron Microscopy (HR-TEM)

Standard transmission electron microscopy is a form of microscopy where electrons are passed through a thin sample interacting with the sample as it is transmitted. At low magnification this is conceptually similar to absorption spectroscopy in that it is the transmission or absorption of the electrons that provides contrast. At high magnification however, complex wave interactions mean that more advanced image analysis is required to resolve structures.

The TEM must be evacuated to low pressures (10^{-4} Pa) in order to reduce electron-gas collisions and minimise the noise in the image. A beam of electrons from an electron gun is passed through two condenser lenses which produce a thin coherent beam of monochromatic electrons. A condenser aperture removes electrons which are far from the optical centre, before the beam is transmitted through the sample. At low magnifications, the thickness and composition of the sample determines the extent to which the electrons are absorbed. The image is formed by an objective lens which focuses the transmitted portion of electrons. An objective aperture provides higher contrast in the image. Two intermediate lenses and a projection lens then enlarge the image before it is detected by a CCD camera.

Various modes of TEM are differentiated by the way in which image contrast is provided. The specific modes used in this thesis are high resolution transmission electron microscopy, which produces fringes in the image which arise from the periodic crystal lattice, and high angle annular dark field imaging, which provides excellent z-contrast enabling analysis of the size and shape of QDs.

The substrates used for imaging with HR-TEM were approximately 5 mm x 5 mm holey carbon grids (Agar Scientific) comprising of a 50 micron copper mesh supporting an amorphous carbon thin film, onto which the sample is deposited. Samples were prepared for TEM by diluting the as-prepared QD solution with alcohol (typically isopropyl alcohol) and placing the solution in an ultra-sonicator for 30 seconds. A glass pipette was then used to place a single drop on the centre of the grid and allowed to dry. Once dried, the grid was then mounted onto a standard Omicron holder. Sample preparation was optimised to provide even grid coverage by systematically varying the concentration of solution being drop-cast. This is an important step to take since solvent drying effects often cause large aggregates of QDs to form on the grid, rather than an even single layer. This can make size-dispersion analysis and resolving lattice fringes difficult. In addition, contamination is typically worse for thick samples, meaning the time available for imaging before the area of interest is severely deteriorated by the electron beam is significantly reduced.

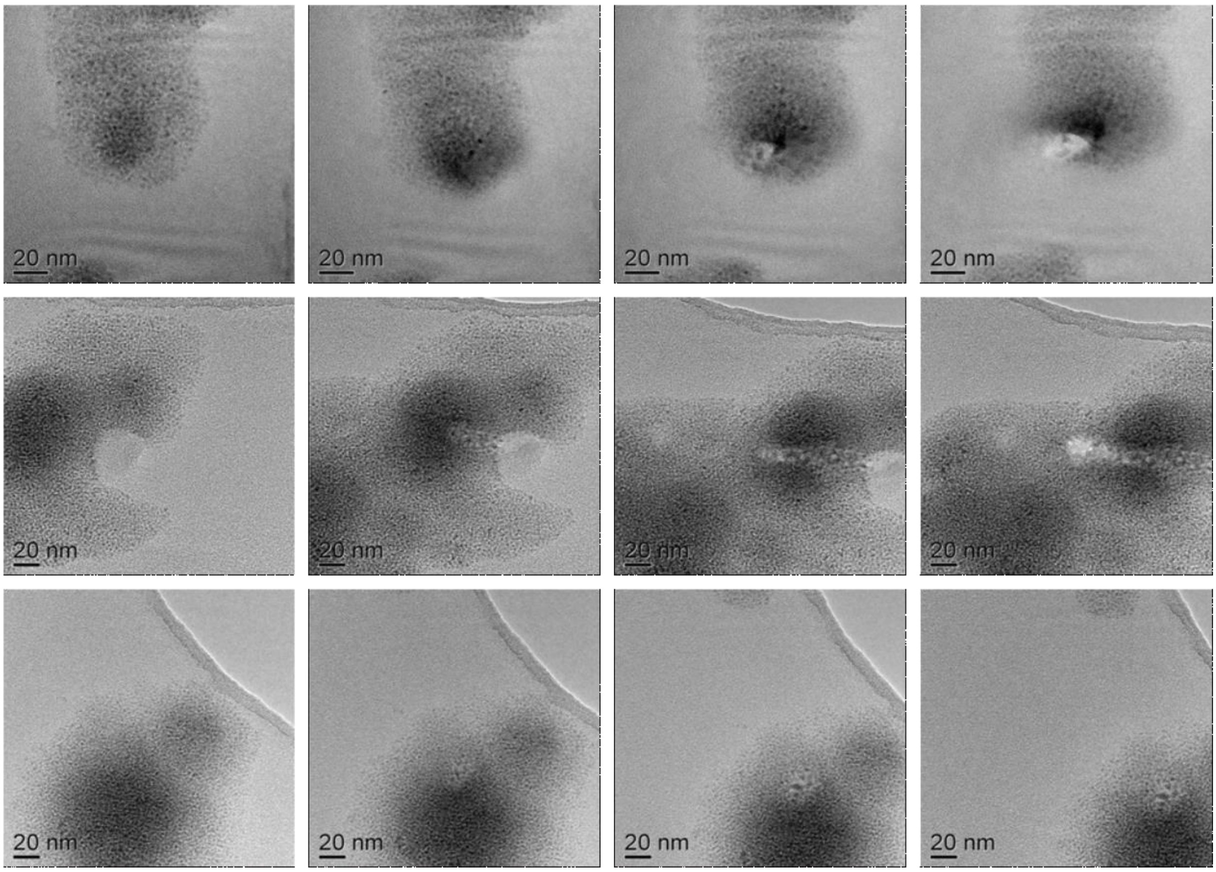

Figure 2.13: CIS/ZnS QD solutions deposited in 1:1 methanol: chloroform solution. Columns from left to right: 0 minutes, 3 minutes, 10 minutes and 15 minutes beam exposure time. Rows from top: 10μM, 5μM and 2.5μM QD concentration.

The series of TEM images in Figure 2.13 show the extent of charging over 15 minutes beam exposure of identical samples dropcast at concentrations of 10 μM, 5 μM and 2.5 μM, from top to bottom. As expected, contamination does not occur as quickly at lower concentrations, although the down-side to this approach is that it is harder to find well populated areas to image.

2.5.1 High Angular Annular Dark Field Imaging (HAADF) in Scanning Transmission Electron Microscopy (STEM)

Scanning TEM differs from standard TEM in that the electron beam is highly focused on a single spot and scanned over an area of interest. The raster process enables spatially-resolved mapping by EDX or EELS and in combination with a high-angle (HA) detector STEM enables annular dark field (ADF) imaging, hence the acronym HAADF. The advantage of HAADF is that the contrast is provided by the atomic mass, or Z-number of the sample.

2.5.2 Energy-dispersive X-ray Spectroscopy (EDX)

EDX is an analytical characterisation technique used to determine the elemental composition of a sample. The characteristic X-rays emitted by a sample illuminated by a beam of charged particles such as electrons are detected and the atomic percentages of individual elements within a sample can be determined. Due to the need for a beam of charged particles, EDX is often performed in conjunction with TEM. The incident beam of electrons excites a bound electron in an inner shell of the atom out of the shell, leaving behind a hole. An electron from an outer shell relaxes to fill the hole, emitting an X-ray with energy equal to the energy difference between the inner and outer shell. For example, K_α X-rays are emitted when an electron drops from a 2p orbital to the innermost ‘K’ shell (principal quantum number 1). Because each element has a unique atomic structure, and therefore for example X-rays with characteristic energies, the X-rays emitted by a sample can provide information about its composition.

Sample preparation for EDX is identical for TEM, except that for the compositional analysis of CIS QDs, samples must be deposited on grids made from an alternative material to copper, as the copper in the grid contributes significantly to the EDX spectrum, even when focusing on the centre of a single carbon section.

2.6 Atomic Absorption Spectroscopy (AAS)

Atomic absorption spectroscopy (AAS) is an analytical spectroscopic method for the compositional characterisation of a sample. The technique is based on the characteristic visible absorption of up to 60 elements. A nebuliser creates a fine aerosol from a liquid sample that is then mixed with a fuel such as acetylene and an oxidant (air) before being vaporised by a high temperature flame. Light from a hollow-cathode lamp is then passed through the atomised sample and a detector measures the transmission/absorption. Importantly, the hollow-cathode lamp emits light at the same wavelength as the analyte and a different lamp must be used for each element to be analysed.

In this work, the CIS QD dispersions to be characterised were dried under vacuum and the residual digested with aqua-regia before being diluted with deionised water to form an aqueous solution for AAS measurements of Cu concentration. The AAS measurements in this thesis were performed using a Perkin−Elmer Model Analyst 100 system.

2.7 Dynamic Light Scattering (DLS) and Zeta Potential

Dynamic light scattering (DLS) is a spectroscopic method for measuring the size dispersion of a colloidal suspension of particles. A coherent light source is directed through the suspension and an autocorrelation of the time-resolved intensity of light scattered by the particles reveals characteristic time-scales related to the Brownian motion of small particles in solution. This correlation decays exponentially due to diffusion of the particles. For monodisperse samples the decay follows a single exponential with a decay rate that is proportional to the translational diffusion coefficient. The random re-orientation of the particles is size-dependent and the spectral profile of the hydrodynamic radius of particles in suspension can be determined from the Stokes-Einstein equation. The analysis is greatly simplified by the initial assumptions of a monodisperse suspension of spherical particles, and the measured hydrodynamic radius for samples for which either of these assumptions does not hold must be treated as an approximation.

The accuracy which DLS affords can be enhanced by working at low nanoparticle concentrations and at neutral pH; inter-particle collisions and electrostatic interactions are not accounted for and can be avoided in diluted samples with a high salt concentration.

2.8 Cell Viability Assays: WST-1and MTT

HaCat (human keratinocyte) cells were provided by Dr. Routledge (University of Leeds) and cultured in RPMI media (Gibco, Paisley, Scotland) containing 10% fetal calf serum (FCS, Sigma) at 37°C in humidified 5% CO_2. After seeding at a density of 20.000 cells/well in a 96 well plate, HaCat cells were incubated overnight in RPMI and 10% FCS. The spent medium was removed and replaced with fresh RPMI (without FCS) in addition to QDs (or polymer) with concentrations ranging from 0.01 to 100 µg/mL and incubated for a further 24 hours. Positive and negative controls were done by omitting the QDs and incubating with 100 μM hydrogen peroxide, respectively. After incubation with the QDs in medium, either a WST-1 or MTT viability assay was performed. The WST-1 (Roche) was performed according the manufacturer's instructions.

For the MTT assay, the cells were washed with phosphate-buffered saline PBS (Sigma) and 100 µL MTT1 solution (5 mg/mL mg MTT in PBS, filter sterilised) was added to each well (containing 100 µL medium with QDs or PMAL-d). The cells were then incubated for 4 hours, avoiding exposure to light. Each well was topped up with 100 µL of MTT2 (10% SDS (w/v), 10 mM HCl) and incubated overnight at 37 °C. The optical absorbance at 540 nm was measured with plate reader and the results expressed as percentage viability compared with untreated cells. For the MTT assay the QDs remain in the well during the spectroscopic aspect of the assay. Control experiments where therefore performed without HaCat cells to determine the light dispersion and adsorption due to the QDs. These 'background' values became significant at 10 and 100 µg/mL QDs and the background was subtracted from the viability assay data (as a result, cell viability data for the MTT assay can have values slightly below 0%).

Chapter 3

Synthesis and Characterisation of $CuInS_2$-based Quantum Dots

This chapter presents the morphological, structural and optical characterisation of CIS QDs. First, the morphological and compositional characterisation of standard 3 nm $CuInS_2$ nanoparticles is probed by TEM, EDX, XPS and XRD, indicating the presence of chalcopyrite crystal structure and stoichiometric composition. Next, the size-dependent optical properties of $CuInS_2$ nanoparticles are quantified by fluorescence and UV/Vis spectroscopy and are discussed in terms of quantum confinement.

3.1 Structural Characterisation of $CuInS_2$ Quantum Dots

3.1.1 Electron Microscopy

The morphology of the CIS QDs synthesised by the method described in section 2.1 was imaged using HR-TEM (see section 2.5.1 for preparation details). At low magnification, the QDs show triangular morphology, as is shown in Figure 3.1a).

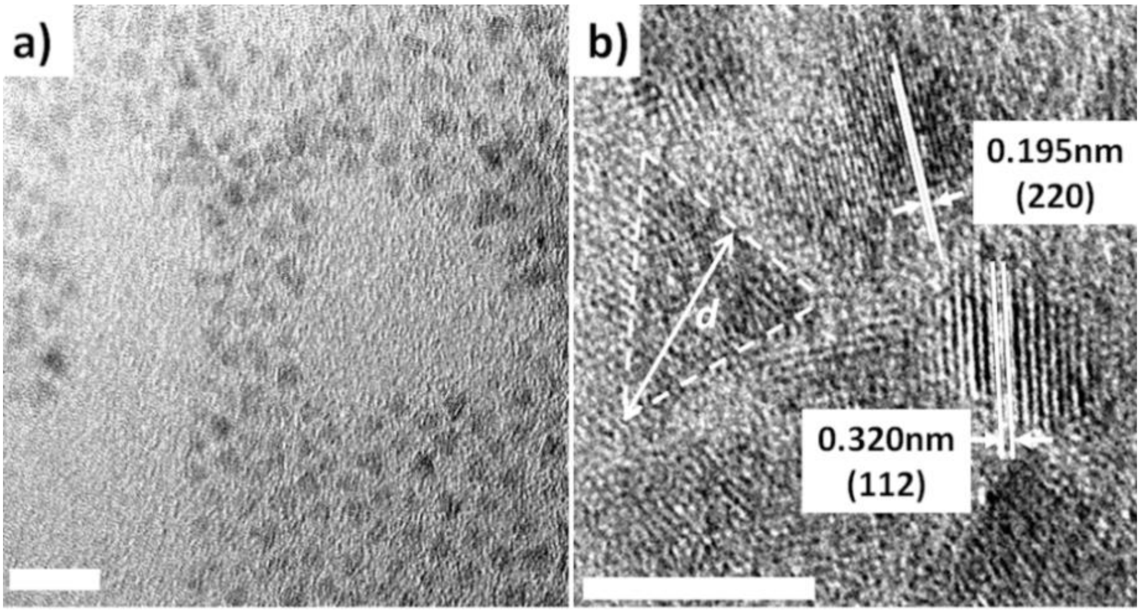

Figure 3.1: a) Low magnification HR-TEM image of CIS QDs showing uniform size distribution (scale bar 10 nm). The triangular morphology of the QDs projected in TEM suggests tetrahedral morphology; b) High magnification HR-TEM image (Scale bar 5 nm). Measured lattice fringe separations of 0.195 nm and 0.320 nm correspond to the (220) and (112) crystal planes, respectively. The definition of QD size, *d*, used throughout this thesis is illustrated.

At higher magnifications HR-TEM enables columns of atoms to be imaged due to the lattice fringes produced from complex wave interactions, as can be seen in Figure 3.1b). An image analysis programme, Image J, was used to plot the ‘gray scale’ as a function of distance for pixels lying along on a line drawn perpendicularly through a series of fringes. The line profile was then fitted with a sine waveform with the determined periodicity corresponding to the fringe seperation. An example for the 0.32 nm fringe separation visible in Figure 3.1b) is shown in Figure 3.2, with this particular fit giving a fringe separation of 0.3 ± 0.1 nm. The accuraccy of this process relies on finding an area where there is an even intensity in the image, since the sine fitting function becomes less accurate as the amplitudes of each period deviate outside a constant range. The precision in the measurement is dependent on the process of calibrating the scale of the image in Image J to the scale bar from the TEM image, and on ensuring that the line runs perpendicularly through the lattice fringes. The scaling error is small, since the image was magnified and the end points of each scale bar were determined to within ± 2 pixels. Since the 20 nm scaled TEM images contained approximately 50 pixels per nm, the error in the final measurement that arises from the calibration was calculated to be less than ± 0.1 nm for the smallest QDs in this study (2.9 nm), for which this systematic error is most significant. Errors arising from non-perpendicular line profiles were minimised by first determining the angle of orientation of the lattice fringes and ensuring the line was drawn at 90° to this. At least twenty line profiles such as the one shown in Figure 3.2 were analysed and a clear bi-modal population emerged, indicating two distinct fringe separations. Both are labelled in Figure 3.1b) and were determined to be 0.3 ± 0.1 nm and 0.2 ± 0.1 nm, corresponding to the (112) and (220) crystal planes of chalcopyrite CIS, respectively [149].

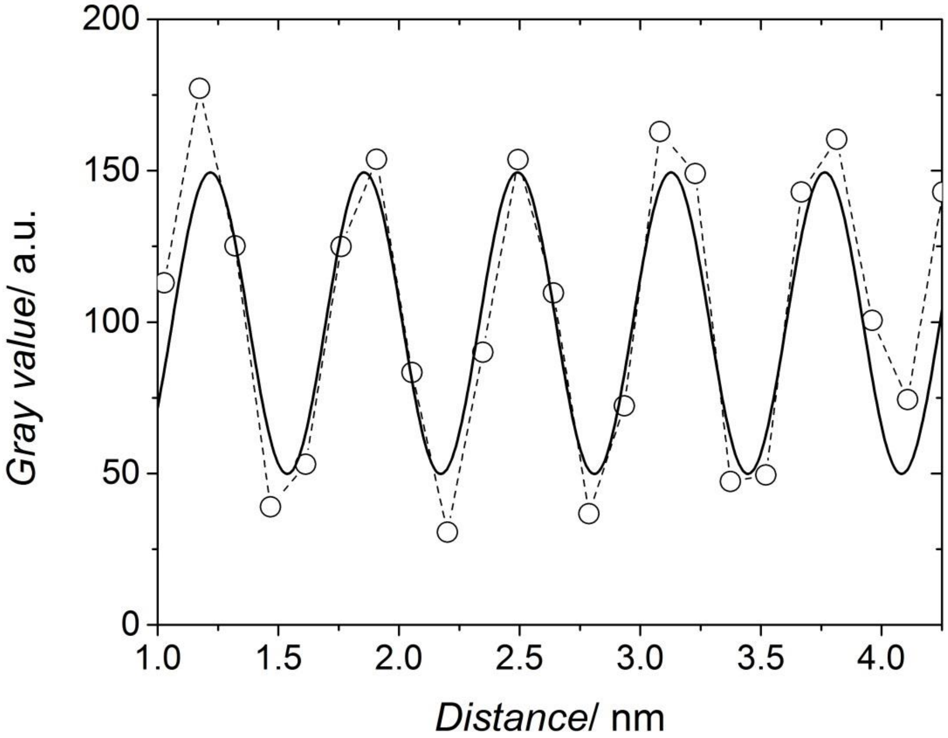

Figure 3.2: Gray value profile of a line drawn through a series of lattice fringes in the high magnification HR-TEM shown in Figure 3.1 b). The black solid line represents a fit using a sine waveform.

The improved ability of high angle STEM (HAADF) to reveal the tetraganol morphology of the CIS QDs is shown when comparing Figure 3.3 against Figure 3.1. Relative to HAADF, even at higher magnifications in HR-TEM the edges of individual QD are not well defined. HAADF provides improved contrast between the CIS QDs and the carbon film due to the large difference in atomic number: the tetragonal morphology can be clearly resolved even at smaller magnification. As discussed in section 2.1.1, the tetraganol morphology is expected to be produced when DDT is used as surfactant [119].

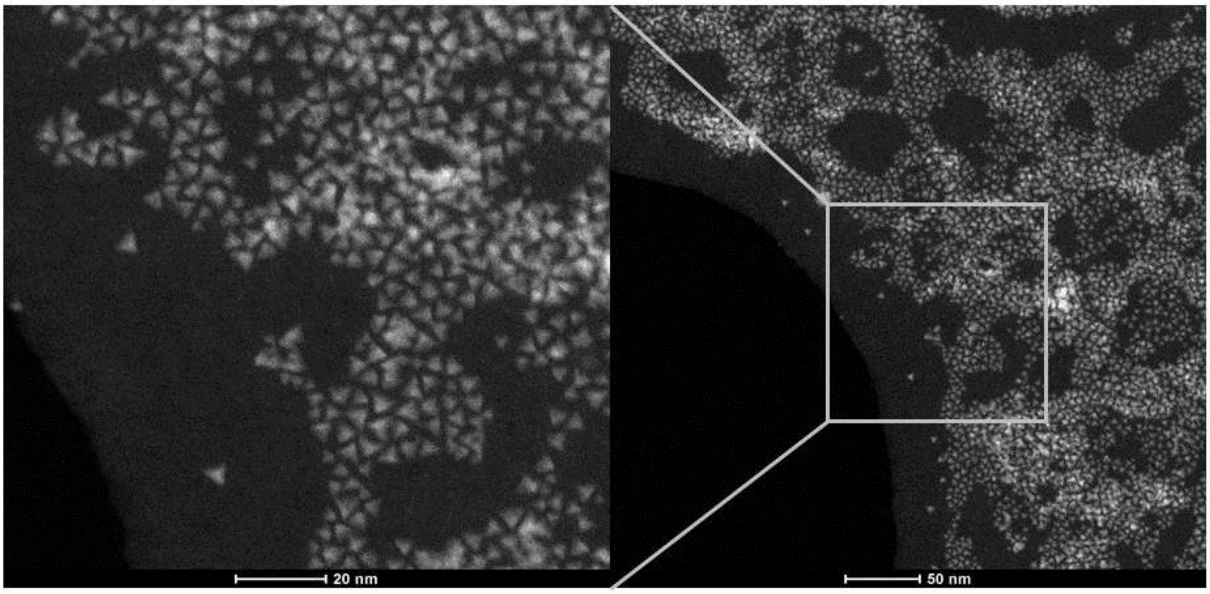

Figure 3.3: a) HAADF image of CIS QDs at high magnification (900 kx) showing tetrahedral morphology; and b) at lower magnification (320 kx) showing uniform size distribution.

The QD size-dispersion was measured from the HAADF and HR-TEM images manually in Image J. The ‘size’, *d*, of a tetragonal QD is defined within this thesis as the longest corner-to-side distance of the triangular projection in TEM. The size distribution of four samples with varying synthesis reaction times are shown in Figure 3.4 in the form of histograms. All of the measured distributions fit well to a Gaussian normal function, with size-dispersions of approximately 20-30%, increasing as with synthesis time. This fits the picture of size broadening described in section 1.4.1.2.

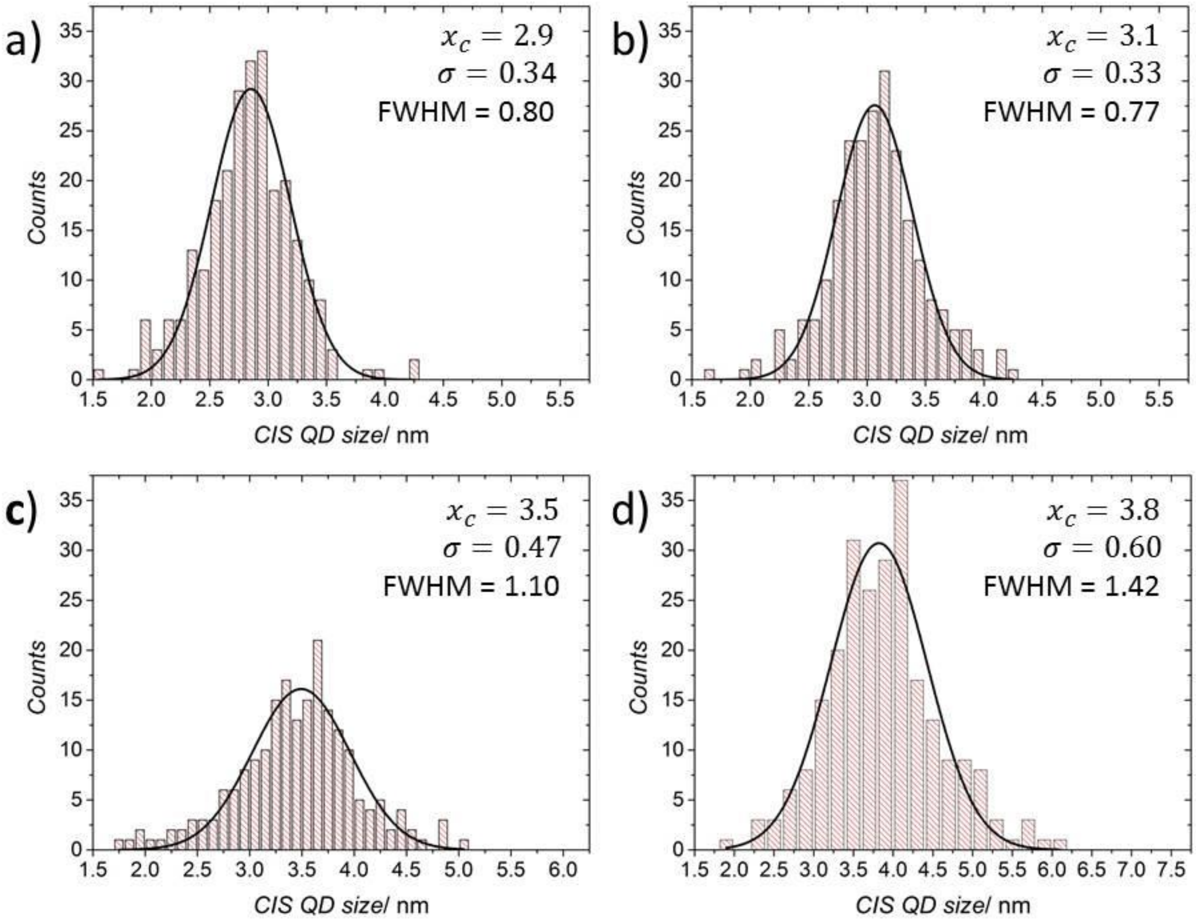

Figure 3.4: Histograms showing the size distributions of four CIS QDs of increasing size from a) to d). Bin widths in a) to c) are 0.1 nm and in d) is 0.2 nm. Black lines represent a Gaussian fit to the histogram. Measured size and size dispersion (FWHM) were as follows: a) 2.9 ± 0.8 nm; b) 3.1 ± 0.8 nm; c) 3.5 ± 1.1 nm; and d) 3.8 ± 1.4 nm. Each sample was sized by counting at least 100 individual particles.

3.1.2 X-ray Diffraction

The presence of chalcopyrite crystal structure in the as-synthesised CIS QDs was further demonstrated by means of X-ray diffraction (XRD). The XRD pattern, shown in Figure 3.5, is in good agreement with the JPCDS reference pattern (file card number 75-0106). The diffraction peaks are assigned with the lattice planes from which they arise. The two strongest peaks at $2\theta \cong 27.8°$ and 46.3° correspond to the (112) and (220) planes, respectively. It is interesting to note that it is these two planes that are identifiable through the lattice fringes observed in HR-TEM.

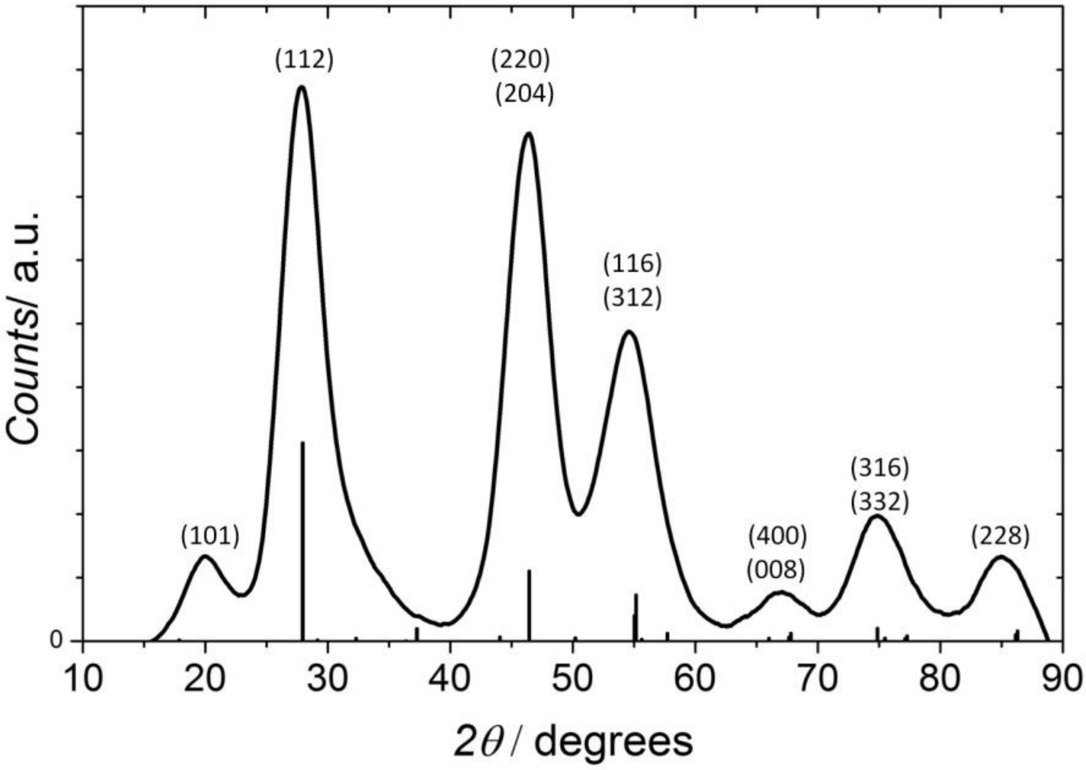

Figure 3.5: XRD pattern for powdered CIS QDs. A good correlation with reference data for CIS chalcopyrite (shown as vertical lines on the x-axis (JPCDS File Card No. 75-0106)) is observed with peaks indexed to the Miller indices of this phase.

In the absence of strain, the line-broadening β of a diffraction peak at angle θ is related to the crystalline grain size D.

$$D = \frac{\kappa\lambda}{\beta\cos\theta} \tag{3.1}$$

where κ is a shape factor, close to one, that accounts for the shape of the crystallite. For a tetrahedron the value of κ is around 0.9. The wavelength, λ, of the incident X-rays was 0.15418 nm. For the XRD data shown in Figure 3.5 the grain size was determined to be 3.6 ± 0.6 nm.

3.1.3 Compositional Analysis of CIS Quantum Dots

EDX analysis was performed on CIS QDs of size 3 nm. The QDs were dropcast onto SiN grids in the same manner as for TEM, rather than on to copper grids, allowing the background signal from the grid to be distinguished from the CIS QDs (containing copper). Spectra were taken over an area of approximately 200 nm x 200 nm, and over a period of 60 seconds. Spectra were recorded at at least ten sites that displayed good QD coverage, and the data was averaged. Within an accuracy of ± 0.1, the Cu : In : S ratio was determined to be 1.0 : 1.0 : 2.0, indicating stoichiometric CIS.

Complimentary XPS analysis was performed on the same sample as EDX. A sample survey is shown in Figure 3.6. The peaks used for compositional analysis are labelled: Cu 2p, In 3d, C 1s and S 2p. The signal from the Au substrate (Au 4f) can be seen at around 85 eV.

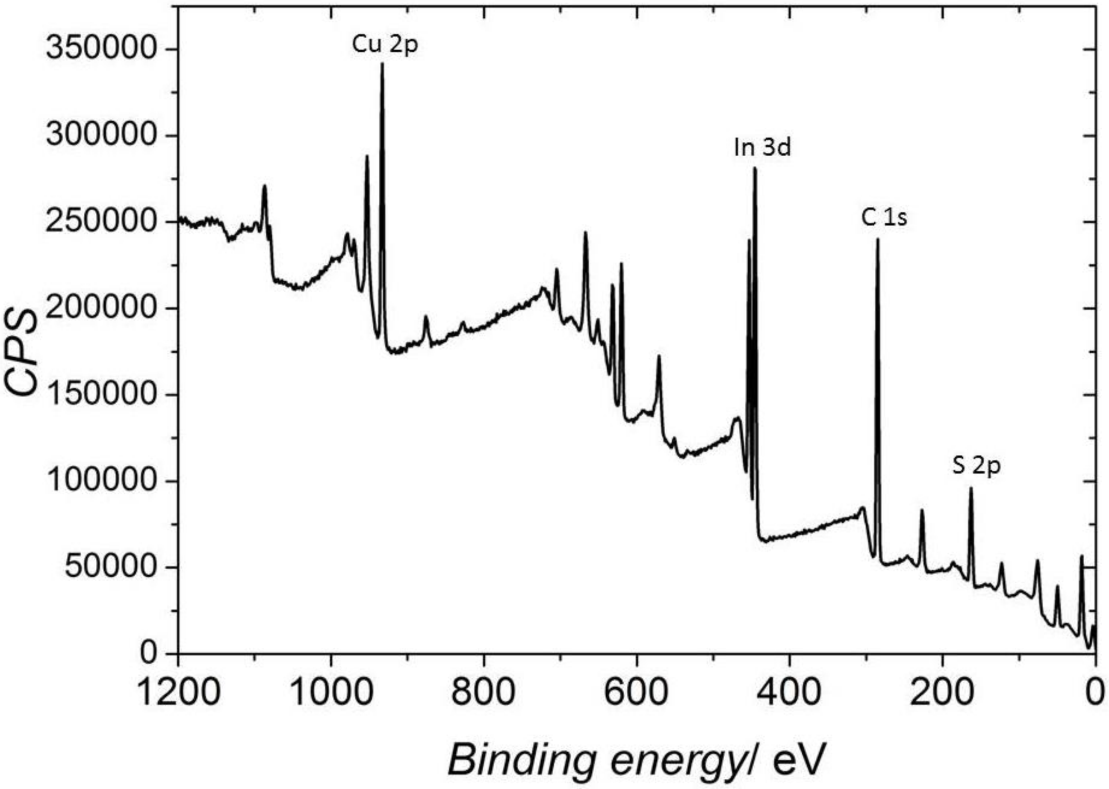

Figure 3.6: Survey XPS spectrum of CIS QDs on Au substrate. The individual peaks used for quantitative compositional analysis are labelled.

The C 1s profile shown in Figure 3.7a) is spectrally consistent with a QD surface stabilised with DDT, i.e. a long carbon chain with a terminal methyl group. However, since carbon-carbon bonds are expected to dominate the signal and the C 1s peak was centred at 285.4 eV a calibration was performed on the entire sample data-set, shifting each spectrum down in energy by 0.7 eV to the reference value 284.7 eV.

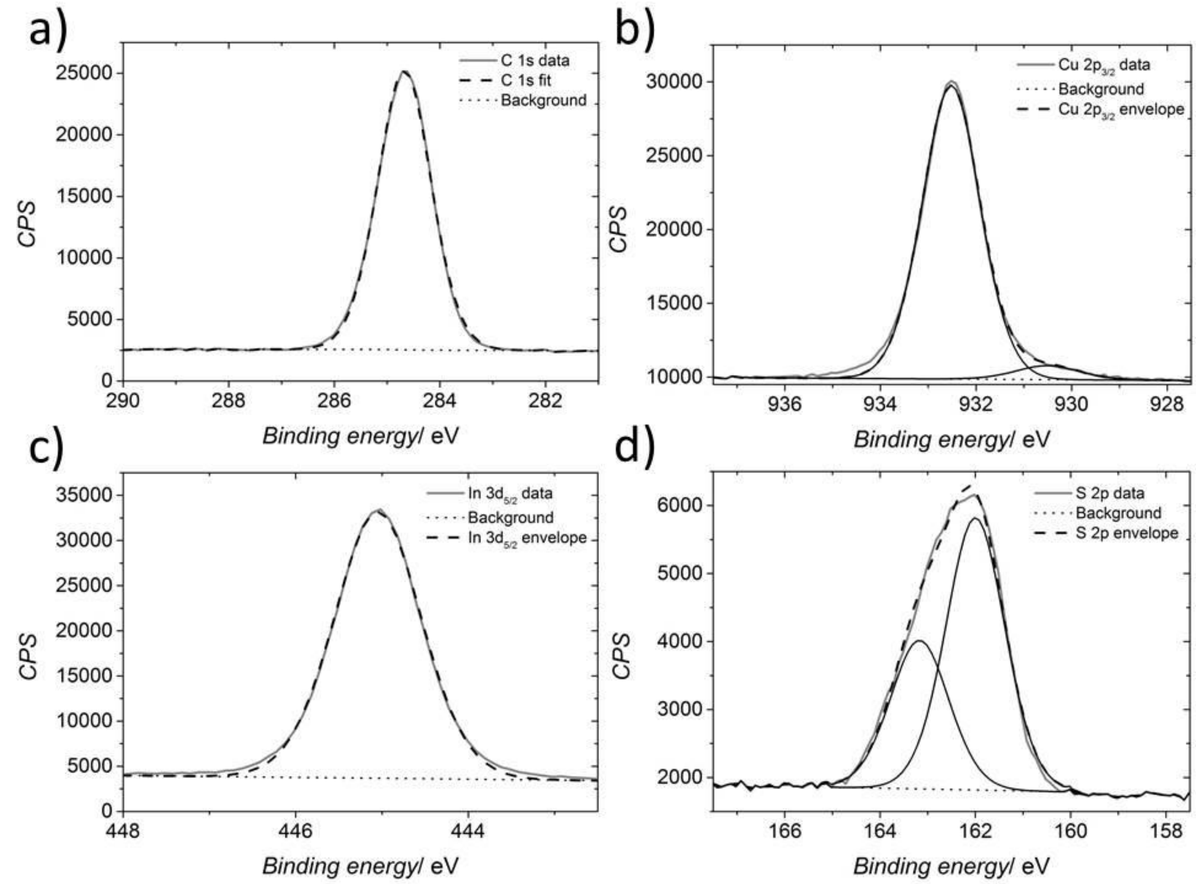

Figure 3.7: XPS spectra (solid grey line), fitted with Voigt distributions (dashed lines) in Casa XPS. a) C 1s; b) Cu 2p; c) In 3d; and d) S 2p.

The individual Cu 2p, In 3d and S 2p profiles of the CIS QDs are shown in Figure 3.7 b), c) and d), respectively. The inherent surface sensitivity of XPS makes an accurate compositional evaluation difficult for CIS QDs; XPS is suited to the characterisation of surface chemistry. However, in conjunction with EDX, a qualitative picture of the cross-sectional distribution of elements through the QD can be developed. Table 3.2 shows the atomic percentage of each element (Cu, In and S) in the sample and the corresponsing Cu:In:S atomic ratio as measured by XPS and EDX. XPS over-estimates the sulfur content relative to EDX, suggesting that the CIS QDs have a sulfur-rich surface, consistent with a thiol passivation layer.

Table 3.2: Atomic percentage of Cu, In and S, and the Cu:In:S ratio in CIS QDs as measured by EDX and XPS.

	Cu atomic %	In atomic %	S atomic %	Cu:In:S (± 0.1)
XPS	25.0 ± 0.5	22.3 ± 0.5	52.3 ± 0.5	1.1 : 1.0 : 2.3
EDX	25.5 ± 0.7	24.3 ± 0.8	50.2 ± 0.6	1.0 : 1.0 : 2.0

The valence states of the CIS QDs, as measured with UPS, are shown in Figure 3.8. The valence band edge of bulk CIS is known to consist of hybridised Cu 3d and S 4p orbitals, resulting in a significantly reduced band gap [128-131]. The baseline used to fit the spectrum was a Tougarrd [168].

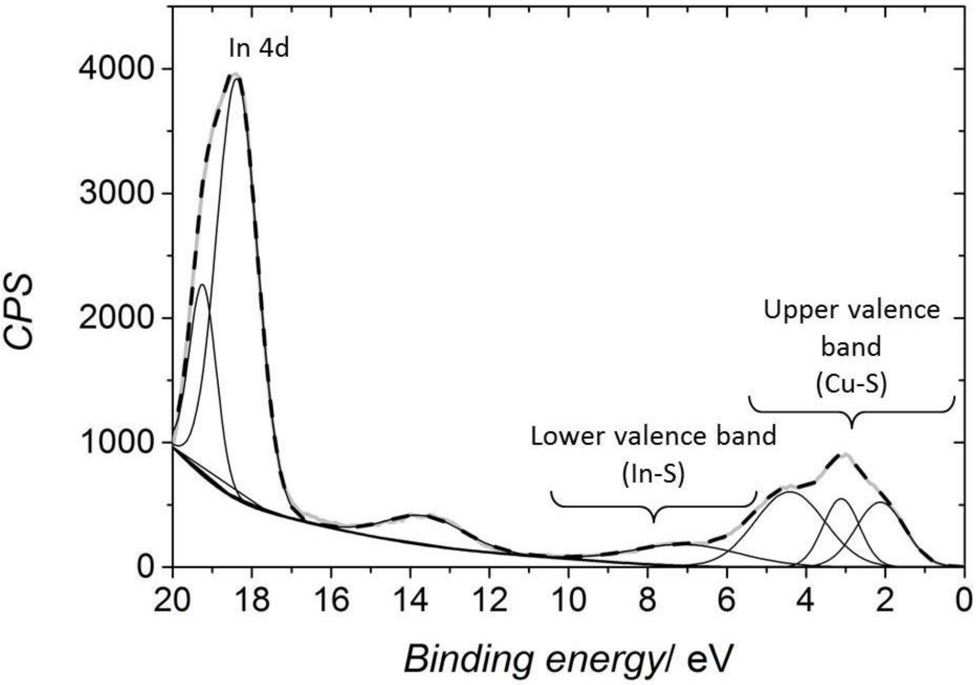

Figure 3.8: UPS spectrum of CIS QDs showing the valence band structure (grey line). A Tougaard baseline is used to fit a total of 7 Voigt functions (thin black lines) to the data, giving a good envelope fit (dashed black line). These fits are a guide to the eye only.

The analysis of this spectrum must take into account the valence states of the ligands on the QD surface. These features are expected at 6-9 eV below the valence band edge of the CIS QDs [169]. This is convenient for determining the position of the valence band, but complicates the elemental identification of states from CIS. Figure 3.9 shows the first 3 eV of the valence spectrum. Extrapolating a linear fit from between 1.75 eV and 1.20 eV to the *x*-axis indicates that the valence band edge lies at 0.89 ± 0.01 eV. If we assume that the Fermi level is in the centre of the band gap, this would suggest a band gap of 1.788 eV, which is qualitatively consistent with quantum confinement in CIS QDs. The broad tail below the Fermi edge is attributed to the non-isotropic arrangement of QDs on the gold surface and size inhomogeneity in the QD suspensions [169].

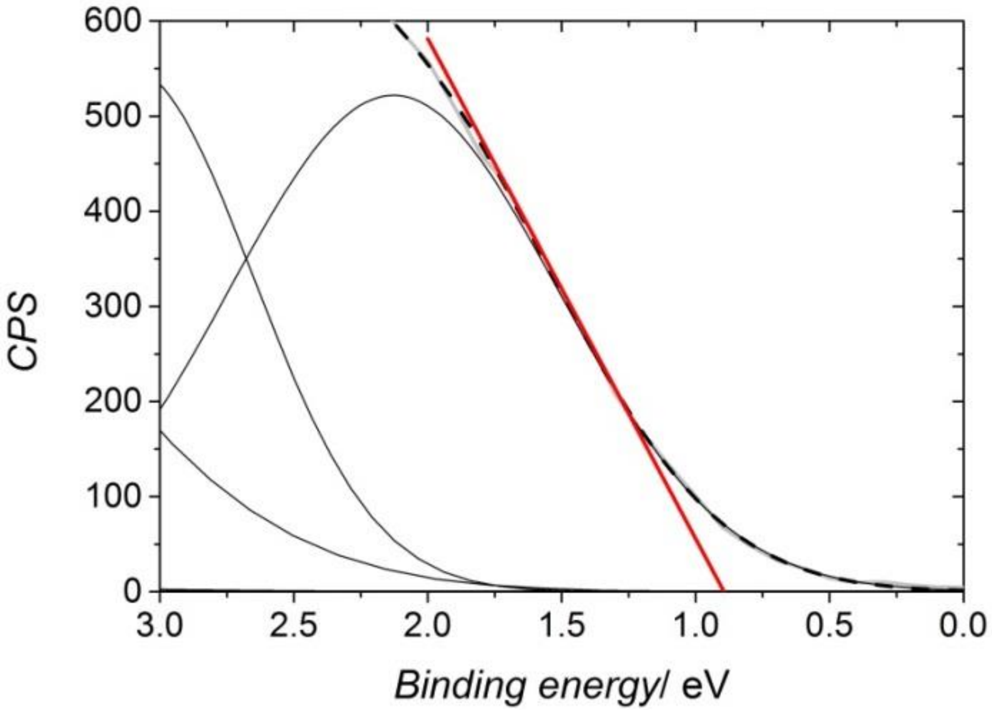

Figure 3.9: The low energy side of Figure 3.8 magnified. The red line represents an extrapolation of a linear fit to the x-axis, intercepting at 0.89 eV.

3.2 Optical Characterisation of CuInS$_2$ Quantum Dots

3.2.1 General Characteristics

The emissive properties of CIS QDs synthesised following the method outlined in section 2.1.1 were probed with fluorescence spectroscopy; a typical PL spectrum for 3 nm QDs is shown in Figure 3.10. The broad nature of the PL spectral peak compared to the CdTe QDs presented in section 2.1.6 is immediately obvious; the full width of the spectral peak measured at half of the maximum amplitude (FWHM) is 125 nm, compared to approximately 85 nm for CdTe QDs. The reasons for the broad PL are most likely a broad size distribution and that the emission originatesfrom intra gap defect states; the energetic position of these defect levels within the band gap depend to a high degree on local properties of the crystal structure and as such an ensemble of QDs would be expected to have a range of positions.

A typical absorption spectrum of CIS QDs is also shown in Figure 3.10, showing absorption out to approximately 700 nm. The shape of the absorption spectrum appears at first glance to be a steep negative gradient that tails off above 400 nm. This ‘tail’ however is actually a single, broad excitonic feature, comparable to the narrower excitonic features observed in the absorption spectrum of CdTe QDs. The broad nature of this exciton band, as for that of the broad PL band, cannot be accounted for by size-dispersion alone.

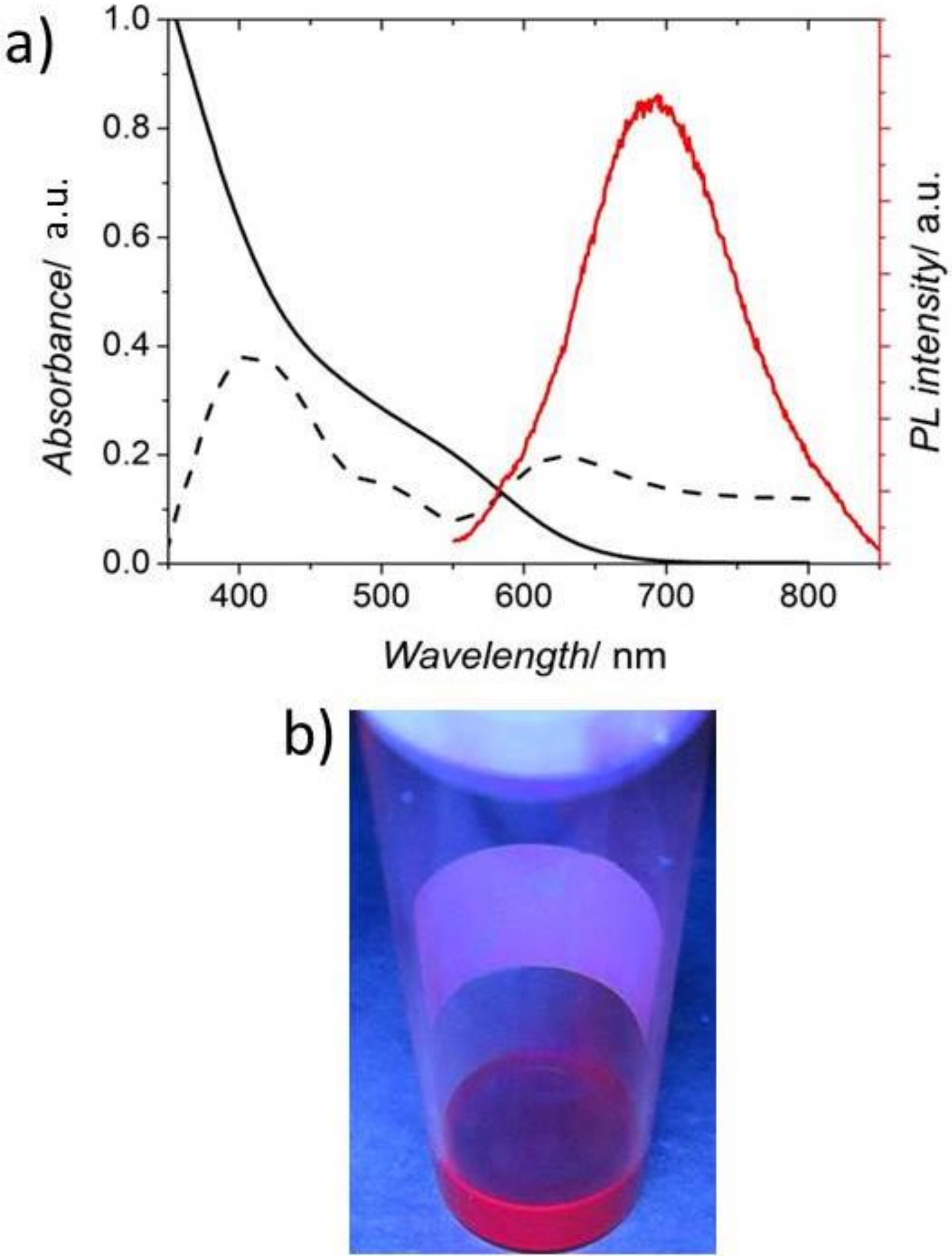

Figure 3.10: a) Typical PL emission spectrum (red line) and UV/Vis spectrum (black line) for $CuInS_2$ QDs. The second derivative of the absorption spectrum is shown (dashed line); b) Digital photograph of CIS QDs illuminated with a UV lamp.

Although synthesis methods for CdTe QDs are more developed than those for CIS QDs and thus smaller size distributions can be achieved, the absorption spectrum of CdTe QDs with size distributions similar to the CIS QDs shown here still demonstrate much narrower excitonic features than CIS QDs. A possible explanation for the observed broad absorption could be that the subsequent higher excitations are energetically closer in CIS than in CdTe and thus the multiple Gaussians overlap to a higher degree and the first excitonic feature is broadened as a result.

CIS QDs demonstrate a large energetic difference between the first excitonic feature in the absorption spectrum and the PL spectral peak position, called the Stokes shift. This large Stokes shift, although possibly contributed to by large phonon coupling (large Hunag-Rhys factor), also indicates the involvement of intra-gap states in the PL process. This view is supported by two further observations: firstly, that for large CIS nanoparticles the 'red' side of the PL spectral peak extends to longer wavelengths (> 850 nm) than a band edge transition would permit, given the bulk band gap of CIS; and secondly, that the PLQY of copper poor CIS QDs, which would be expected to have a high density of defects associated with a copper deficiency, is greater than that of an equivalent stoichiometric sample. [57, 170] This latter observation suggests that a point defect associated with a deficiency of copper is involved in the PL process. This is feasible since an inherent abundance of point defects arises in CIS due to a tetraganol distortion of the crystal field and the corresponding mismatch between the In-S and Cu-S bond lengths

Figure 3.11 shows the absorption spectrum from Figure 3.10 alongside the corresponding excitation spectrum. The informational difference between the two is that the excitation spectrum reflects only absorption events which result in a PL response, whereas the absorption spectrum includes contributions from scattering and from absorption by non-emissive states. Thus, if the two spectra are normalised between zero and one, this analysis can at least qualitatively demonstrate which excitation wavelengths produce the most efficient PL response. The excitation spectrum shown in Figure 3.11 indicates a rising feature above 700 nm at longer wavelengths than the absorption onset.

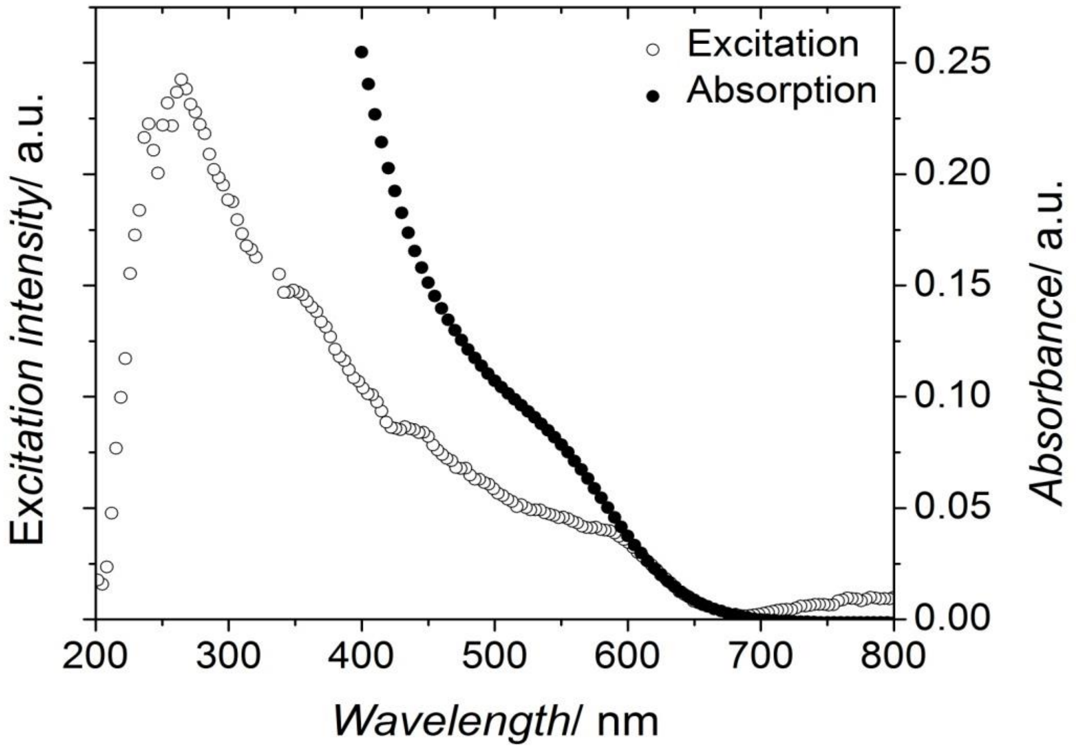

Figure 3.11: Absorption (black circles) and excitation (white circles) spectra of 3 nm CIS QDs.

The Tauc plot in Figure 3.12 shows $(\boldsymbol{Ah\nu})^{\boldsymbol{2}}$ and $(\boldsymbol{Ah\nu})^{\boldsymbol{1/2}}$ against the excitation photon energy $h\nu$. The exponents of 2 and ½ correspond to direct and indirect transitions, respectively. For incident photon energy greater than the band gap ($h\nu > E_g$), a linear fit extrapolated to the x-axis can provide an estimate for the band gap of the QDs. The problem here is that this is a method for estimating the band gap, yet the band gap must be known in order to determine the appropriate fitting region. The two tauc plots extrapolated linear fit intercepts the *x*-axis at an average point of 2.9 eV. This is extremely large for CIS QDs. Since the valence band maximum binding energy was determined to be 0.9 eV below the Fermi level, this places the Fermi level ~ 2 eV below the conduction band. This is extremely large, considering that minimal p-type behaviour is expected due to the only slightly Cu-rich phase as determined by EDX (see section 3.2).

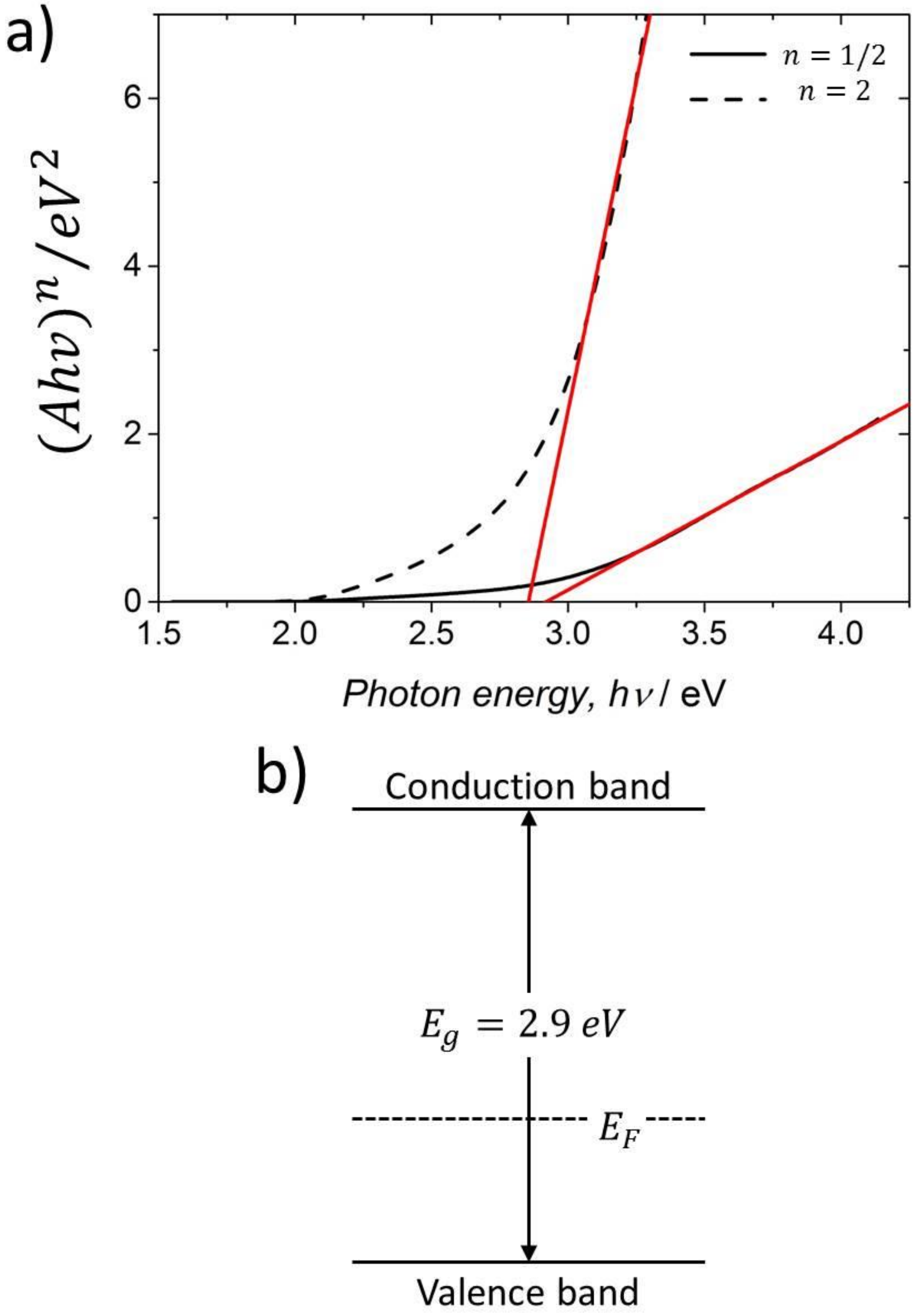

Figure 3.12: a) Two ‘tauc’ plots, showing $(\boldsymbol{Ahv})^{\boldsymbol{2}}$ and $(\boldsymbol{Ahv})^{\boldsymbol{1/2}}$ against photon energy hv where α is the absorption from Figure 3.11. The red lines represent linear fits to the data in the region $hv > E_g$ and are extrapolated to the x-axis to determine the band gap of the CIS QDs. b) Illustration to scale showing the approximate position of the Fermi level within the band gap of the CIS QDs.

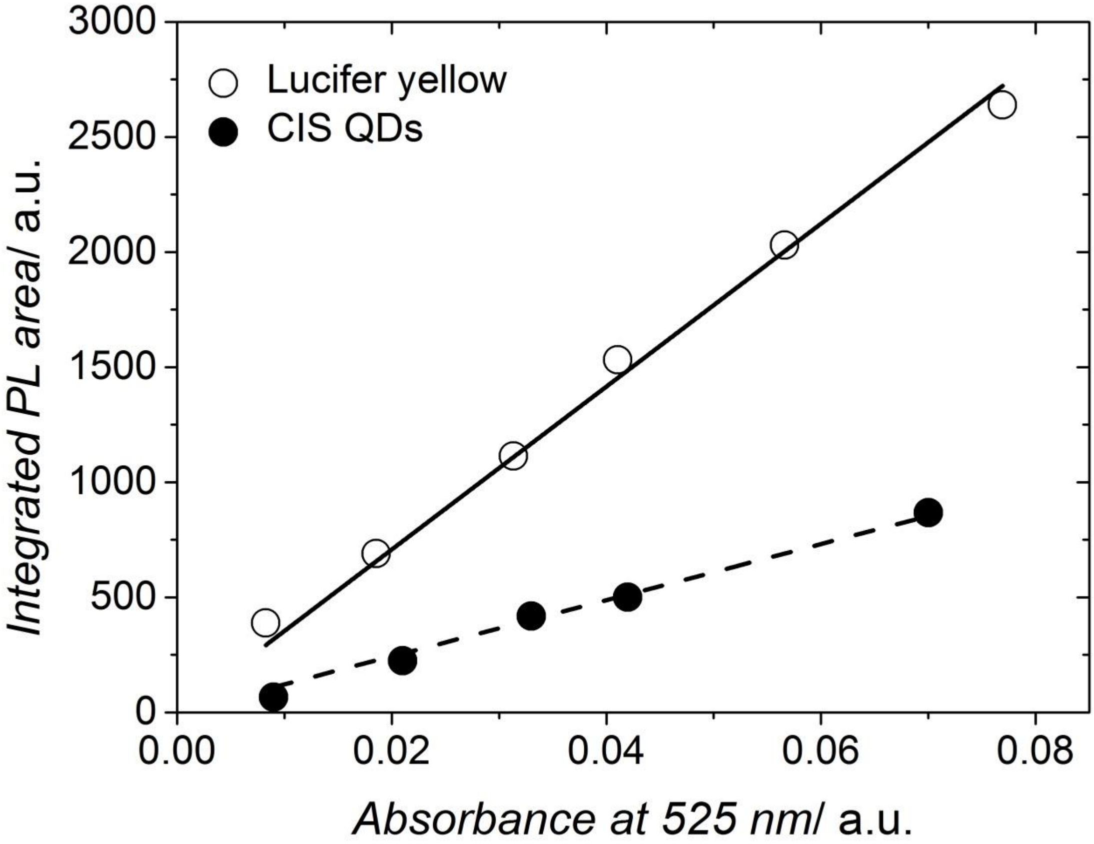

Figure 3.13: Plot of the integrated PL area against absorption as measured by UV/visible spectroscopy for both CIS QDs (filled circles) suspended in hexane and Lucifer Yellow dye suspended in water (hollow circles). The black solid and dashed lines represent linear fits to the Lucifer Yellow and CIS QD data, respectively.

The PL quantum yield (PLQY) of the CIS QDs was determined by comparing the absorption and emission to a standard dye (Lucifer Yellow, LY) of known PLQY. Figure 3.13 shows the integrated area of the PL emission spectrum of CIS QDs dispersed in hexane and LY dispersed in water over a range of absorption. The PLQY of the CIS QDs is thus determined by the equation:

$$PLQY_{CIS\,QD} = PLQY_{LY}\left(\frac{G_{CIS\,QD}}{G_{LY}}\right)\left(\frac{n_{hexane}}{n_{water}}\right)^2 \tag{3.2}$$

Where G is the gradient of the linear fit to the data in Figure 3.13 and n is the refractive index of the relevant solvent. For the CIS QDs shown in Figure 3.13 the gradient was determined to be 12188 and the gradient determined for Lucifer Yellow was 35384. Given that the PLQY of Lucifer Yellow is 0.21 and that the refractive index of hexane and water is 1.375 and 1, respectively, the PLQY of the CIS QDs was calculated to be approximately 0.13.

3.2.2 Size-dependent Trends

The dependency of the PL spectral peak position on CIS QD size is illustrated in Figure 3.14. As the QD size is increased from 2.9 nm to 3.8 nm the PL spectral maximum is increased from 660 nm to 720 nm. This is consistent with the expected reduction of the band gap as the QD size is increased towards bulk. The most interesting obesrvation is the evolution of the PL spectral peak shape as the QD size is increased. Curve a) fits well to a Voigt fitting function except for a slight tail at the red end of the spectrum.

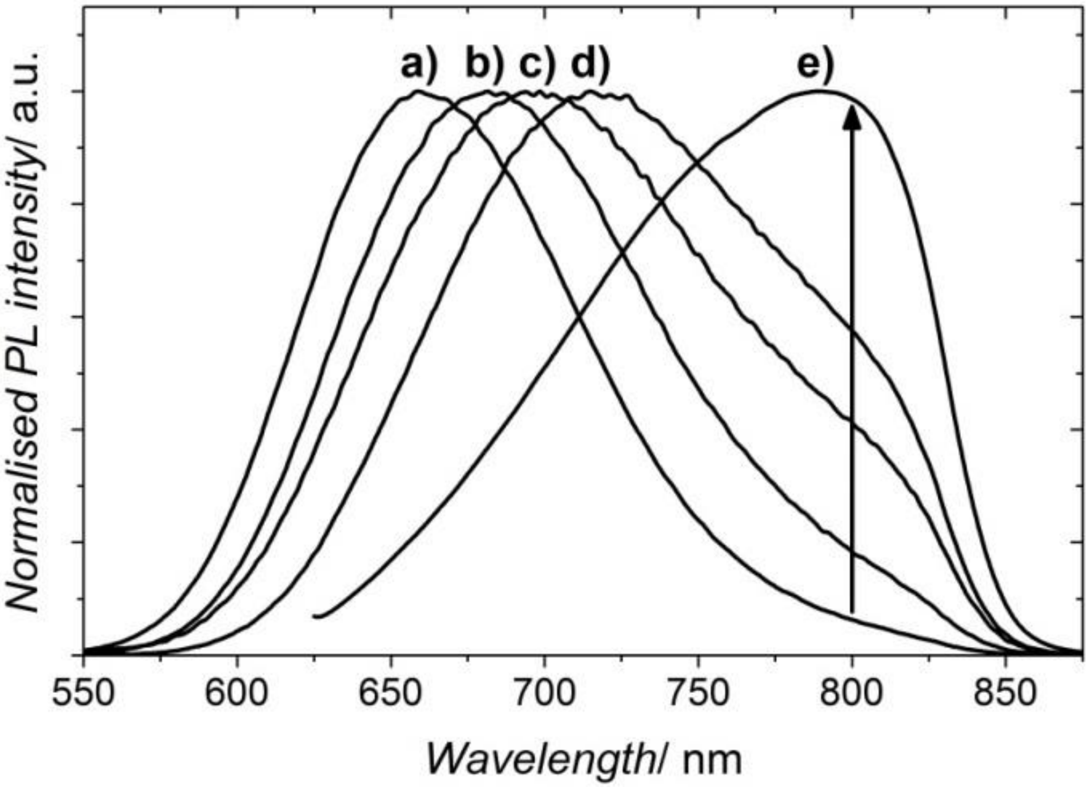

Figure 3.14: Normalised PL spectra for five CIS QD samples of increasing size from left to right. The first four samples correspond to the QDs for which size-histograms are shown in Figure 3.4: a) 2.9 ± 0.8 nm; b) 3.1 ± 0.8 nm; c) 3.5 ± 1.1 nm; and d) 3.8 ± 1.4 nm (dot-dashed line). The fifth spectrum e) corresponds to large QDs grown for 30 minutes under the conditions described in section 2.1.1 (size unknown).

The sample shown in Figure 3.14 e), which was grown at 200°C for 30 minutes, displays a PL spectral peak at 800 nm. Bulk CIS has a band gap of 1.53 eV [35, 171], corresponding to a wavelength of 810 nm. As the QD size is increased, the spectral peak red-shifts and the blue side of the spectra remains well characterised by peak fitting functions which get broader as the size is increased. The slight tail however appears to develop into a intense shoulder as the QD size is increased, and appears to be relatively static in energy. The second derivatives of the PL curves were analysed to illustrate this phenomenon further, as shown in Figure 3.15. The size-dependent component is clearly visible between samples a) to d), shifting from 650 nm to 706 nm. This component cannot be easily located in the second derivative of spectrum e), although by eye it appears to be located at approximately 740 nm.

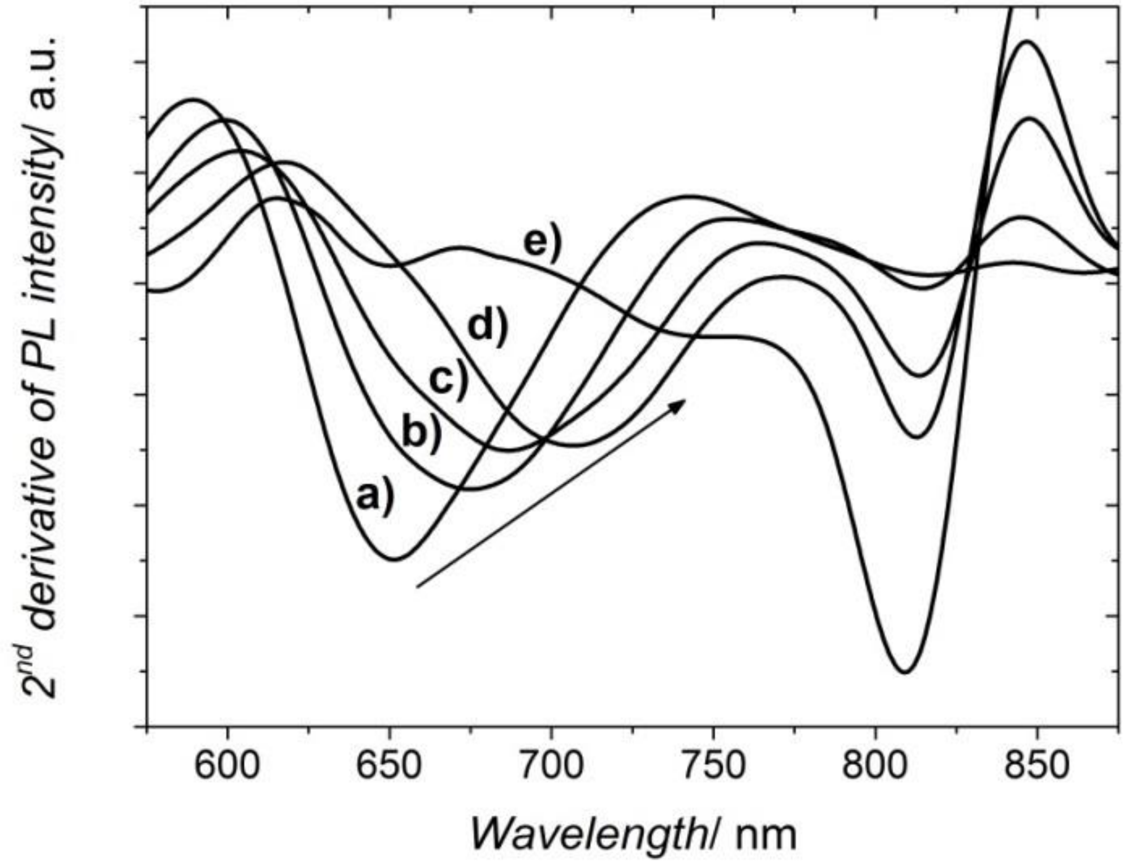

Figure 3.15: Second derivatives of PL spectral peaks a), b) c), d) and e) from Figure 3.14.

The relatively size independent component at approximately 810 nm corresponds almost exactly to the bulk band gap of CIS (1.53 eV). The intensity of this component is largest in spectrum e), i.e. the largest QDs. The surprising observation is the presence of this peak even at smaller QD sizes. This latter point suggests that the PL in this region may arise from a fraction of QDs in the sample that have ‘bulk’ electronic structure. On the other hand it could be an artefact which arises from a drop in the sensitivity of the ‘R928’ photo-multiplier tube (PMT) in the NIR [172].

The origins of the room-temperature PL observed in CIS QDs are known to involve intra-gap states, although the specific relaxation mechanisms have not been identified. The size independence of the PL feature at 810 nm suggests the possibility of a donor-acceptor-pair recombination process, involving ‘deep’ levels that do not shift with the band edges as the QD size varies. A more thorough analysis of the defect-related PL properties of CIS QDs based on time-resolved spectroscopic data is given in Chapter 4.

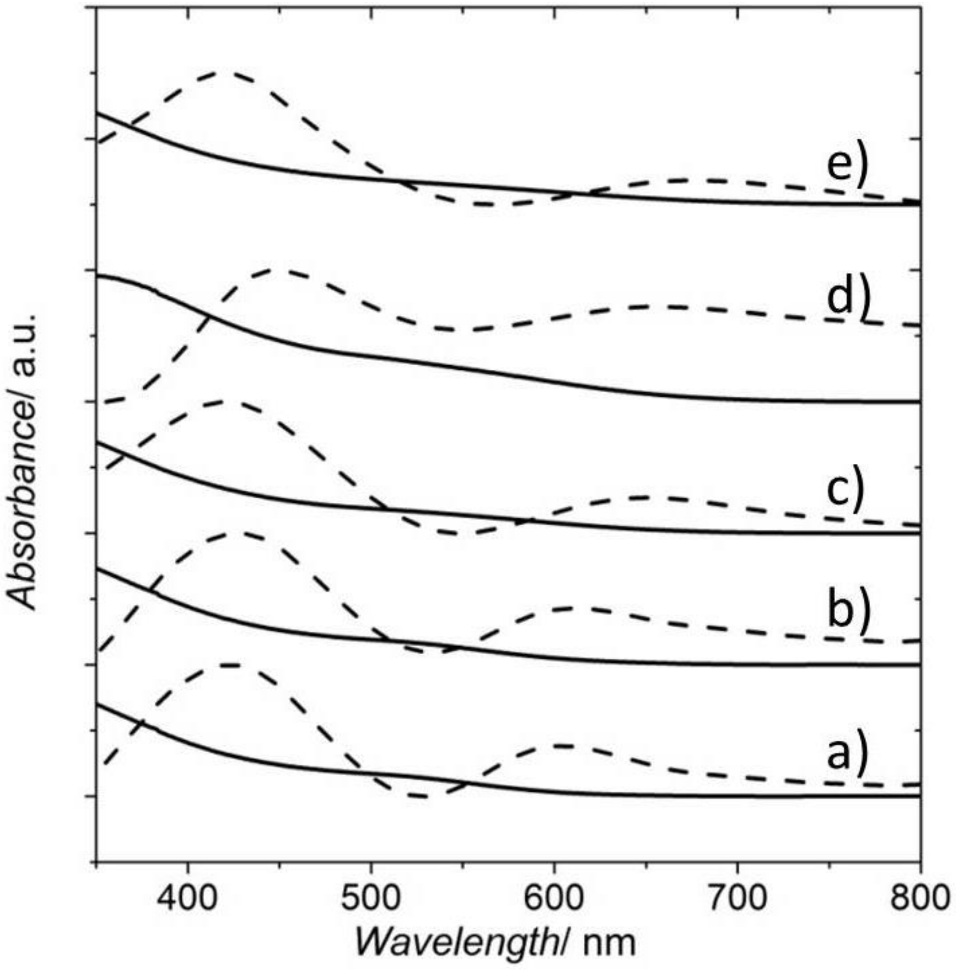

Figure 3.16: Second derivatives of 5 CIS QD samples of increasing size (from bottom to top): a) 3.0 nm; b) 3.2 nm; c) 3.4 nm; d) 3.6 nm; and e) 3.8 nm as determined by HR-TEM imaging (not shown).

The location of the first excitonic transition E_1 can be difficult to observe in absorption spectra as measured by UV/visible spectroscopy, due to the broad nature of the spectral features (see Figure 3.10). A Gaussian curve was fitted to the low energy end of the spectrum to give an estimate of the position of E_1. This method only provides an accurate value for smaller QDs where the sample size distribution is small, and the electronic states are discrete. A more universal and more accurate method is to calculate the second derivative of the absorption spectra; the local minima in the region 500 nm to 600 nm correspond to E_1 and can be located even for larger QD samples. The broadening associated with increased QD size can be seen in Figure 3.16 more clearly than in the zero order spectra.

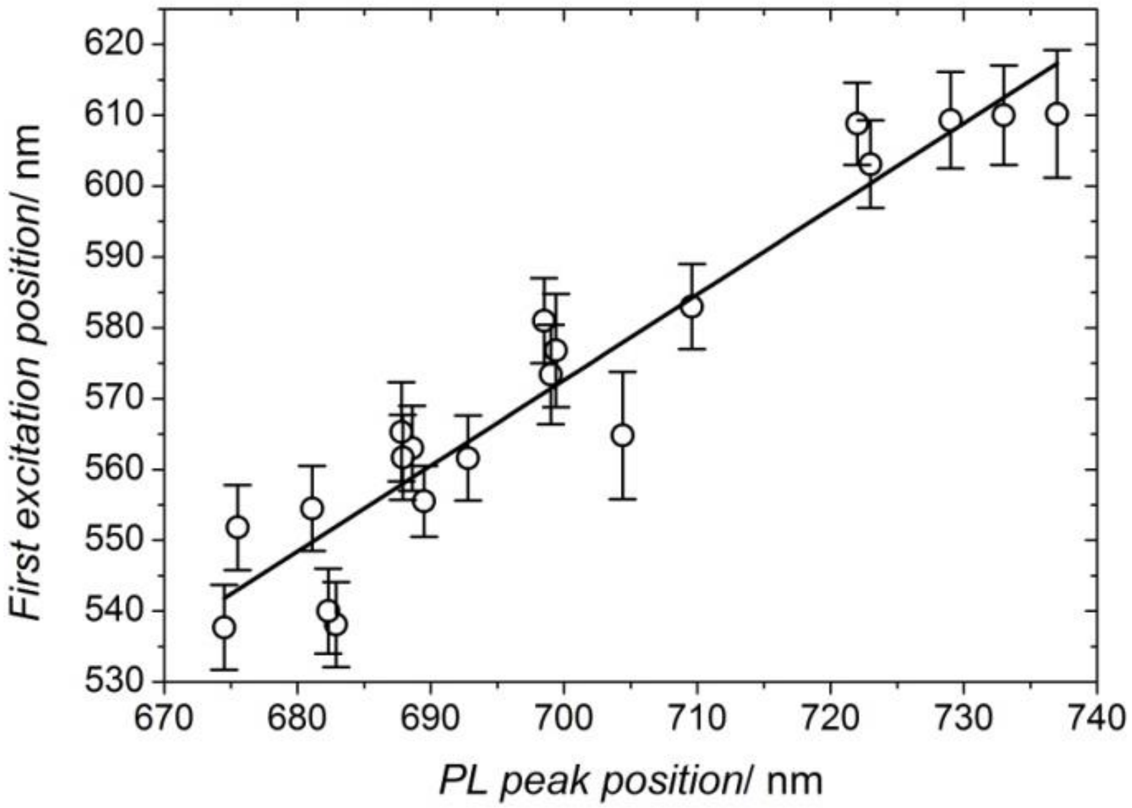

Figure 3.17: First excitonic transition spectral position plotted against PL spectral peak position for 20 CIS QD samples of various sizes, ranging from 2.9 nm to 5.1 nm. The black line represents a linear fit with no constraints.

The dependence of the Stokes shift CIS QD size is illustrated in Figure 3.17 where the wavelength of E_1 is plotted against the corresponding PL spectral peak position. A linear fit to the data reveals a gradient of 1.21 ± 0.11, showing that the Stokes shift decreases as the PL spectral peak position is red shifted, i.e. as the QD size increases. This is understood in terms of quantum confinement: the conduction band in small QDs is expected to comprise of discrete states, which become more energetically seperated with reduced size; and the lower conduction band states of large QDs resembles more closely the bulk behaviour. For the largest QDs in Figure 3.17, the Stokes shift is approximately 120 nm (0.33 eV), in agreement with PL studies on bulk CIS in the literature [142]. The Stokes shift for the smallest CIS QDs (2.9 nm) in this data is 135 nm (0.48 eV).

In order to directly quantify the size dependency of each of the spectral features, the size distributions of 10 QD samples, in addition to the four shown in Figure 3.4, were with emission covering the entire range of wavelengths achievable with this synthesis method, were determined by

TEM. The relationship between QD size, d, and the wavelength of the PL spectral peak, λ_{PL}, and first excitonic transition, λ_{E_1}, are shown in Figure 3.18 and were empirically modelled by fitting each set of data with growth equations parameterised with the corresponding values in bulk CIS (870 nm and 670 nm, respectively):

$$\lambda_{PL} = 810 - (600 \pm 60)d^{(-1.3\pm0.1)} \qquad (3.3a)$$

and

$$\lambda_{E_1} = 670 - (588 \pm 96)d^{(-1.4\pm0.1)} \qquad (3.3b)$$

These empirical equations relating QD size and the spectral peak positions enable an estimate for the average size of a given QD sample to be made from routine optical spectroscopy, avoiding the need to perform time-consuming and expensive TEM analysis.

The effective mass of electrons and holes in CIS is 1.3 m_0 and 0.16 m_0 [173], respectively, and the Bohr radius given by equation 1.4 is 3.8 nm. The calculated Bohr radius for CIS QDs is drawn as a vertical arrow on Figure 3.18.

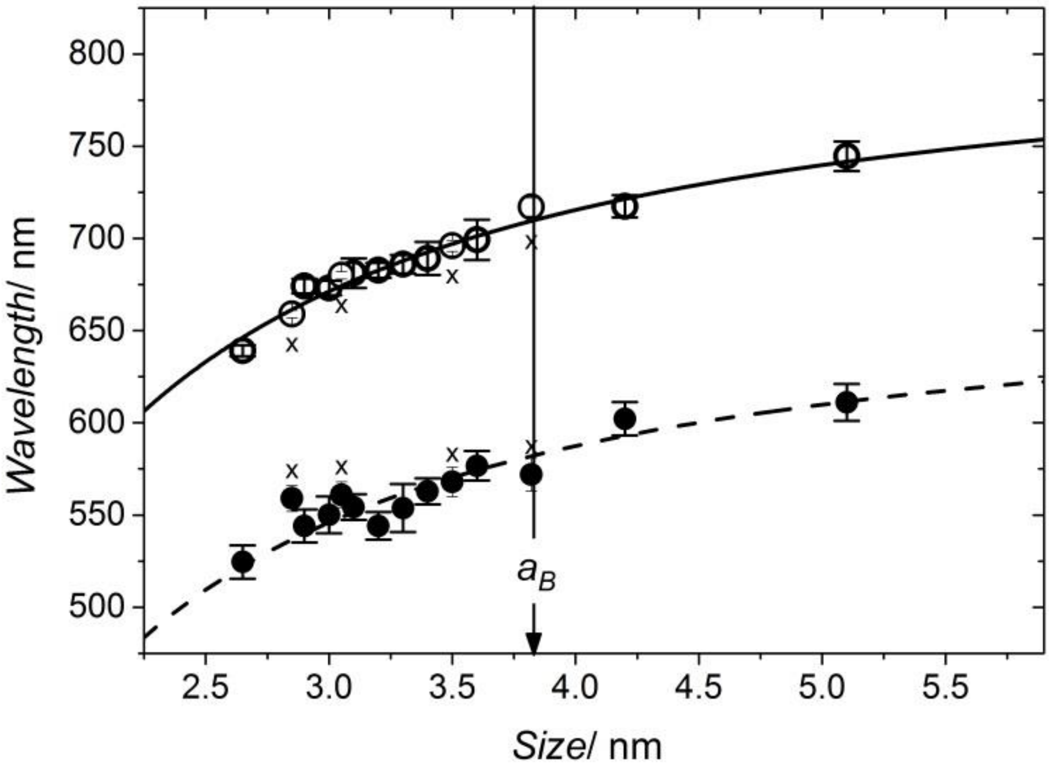

Figure 3.18: The spectral positions of the first excitation (filled circles) and the PL emission (hollow circles) of CIS QDs suspended in hexane, plotted against QD size as measured by HR-TEM (see Figure 3.4). Points marked with an ‘x’ represent the QDs sized by HAADF imaging (see Figure 3.4). The excitation wavelength was set at 400 nm for all measurements.

Within the effective mass approximation the additional energy experienced by an exciton in the first-excited state in a quantum-confined semiconductor crystal, relative to bulk, is given by

$$E_{conf} = \frac{\pi^2\hbar^2}{2\mu_{eff}d^2} = \frac{\pi^2\hbar^2}{2d^2}\left(\frac{1}{m_e^*} + \frac{1}{m_h^*}\right) \tag{3.4}$$

The form of the expected size dependency of the conduction band and valence band edges based on equation 3.4 is shown in Figure 3.19. Because of the much larger effective mass of holes in CIS compared to electrons, and the inverse dependence of the band edge position on the effective mass of the relevant charge carrier, the conduction band edge shifts much more with reduced QD size. In absolute terms this formulation is inaccurate since the CIS QDs are not spherical particles. Qualitatively however the relative response of each individual band edge position to changes in size is elucidated.

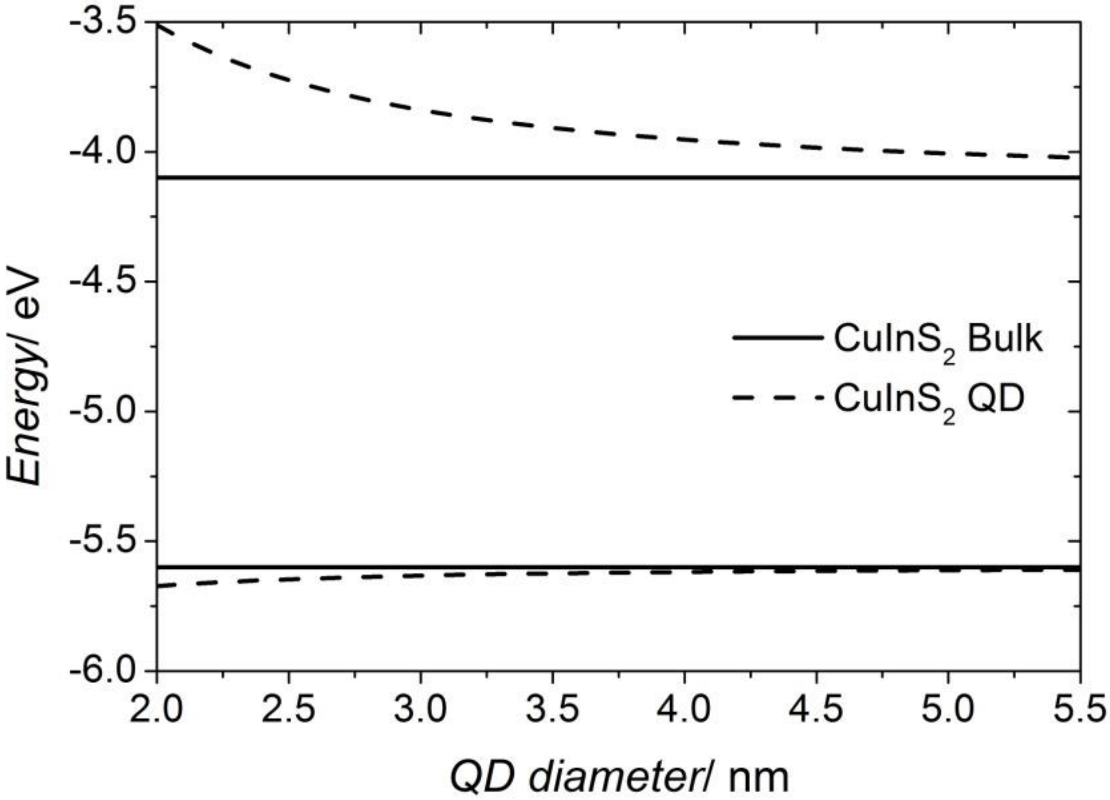

Figure 3.19: The individual band position shifts with QD size (dotted lines) relative to the bulk band edge positions (solid line), as calculated within the effective mass approximation.

For CIS the shift in VBM may be under-estimated by a straight-forward calculation within the EMA since it neglects that the bulk VBM is significantly increased in energy due to *p*-*d* hybridisation between Cu 3d and S 2p orbitals [128-131]. The extent to which this hybridisation is affected by QD size is unknown. Given that quantum confinement increases the spacing between energy levels it is expected that the resulting decrease in exchange integral between the *p* and *d* levels may supress the hybridisation and lead to an enhanced VB size-dependency.

3.3 Concluding Remarks

The morphology of the CIS QDs synthesised as described in section 2.1 was determined by HR-TEM, HADDF and XRD showed tetragonal morphology, chalcopyrite crystal structure and narrow size distribution. The composition was determined to be close to stoichiometric by EDX and XPS although the relative surface-sensitivity of XPS revealed a slightly sulfur-rich surface. Fluorescence spectroscopy showed a broad emission band in the red region of the spectrum that could be size-tuned into the NIR by extending the synthesis reaction time to produce larger QDs. The broadband emission and the large Stokes shift indicate that the PL is related to intra-gap states. The PL spectral profile appears to resemble a single distribution for small QDs and can be tuned between 600 and 800 nm, although for larger QDs a bimodal PL spectral profile emerged. This is unlikely due to the formation of a bimodal QD size distribution for longer synthesis times and is more likely to be associated with a competing radiative de-excitation channel that is suppressed in small QDs. The non-radiative and radiative excited state dynamics are discussed in the next chapter.

Chapter 4

Excited State Dynamics in CIS/ZnS Quantum Dots

In this chapter the morphological and optical characterization of CIS/ZnS core/shell QDs are shown. A dramatic increase in PLQY and a slightly blue-shifted PL spectral peak were observed in agreement with the literature. The ultra-fast excited state dynamics of CIS/ZnS QDs are determined by transient absorption (TA) spectroscopy and the nature of the highly-radiative but broad PL component in CIS/ZnS QDs is shown to be related to high-lying donor state rather than the conduction band.

4.1 $CuInS_2$/ZnS Quantum Dots

The effects of ZnS shell formation on the morphology of CIS QDs was investigated with TEM (Figure 4.1). Because of the extremely thin nature of the ZnS shell (1-2 monolayers from calculations based on starting quantities of zinc) and the small lattice mismatch (<2%) between the crystal structures of CIS and ZnS [145], it would be unreasonable to expect to resolve the interface between the two phases by HR-TEM, especially in ultra-small nanoparticles such as QDs. However the relative size before and after ZnS shell growth can provide an estimate for shell thickness.

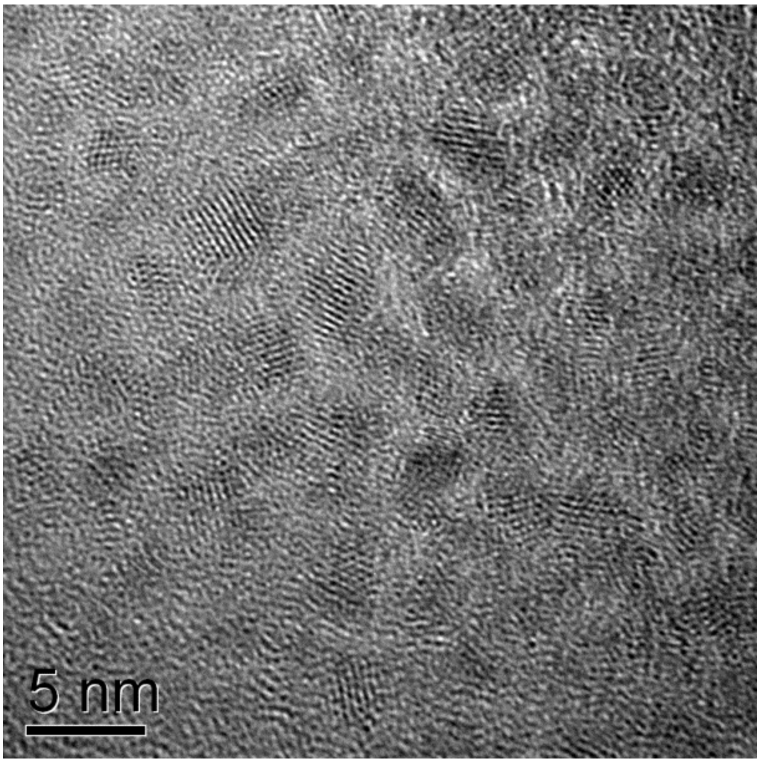

Figure 4.1: HR-TEM of CIS/ZnS QDs.

The structural nature of the CIS/ZnS QDs was investigated by XRD, shown in Figure 4.2. The characteristic XRD peaks for the zinc-blend ZnS lie very close to those of CIS and would only expected to be observed as shoulders on the CIS peaks for a very thin ZnS shell. This is consistent with the pattern shown in Figure 4.2. The CIS/ZnS QD XRD data indicates a crystalline grain size of 3.0 ± 0.7 nm, as determined from the Scherrer equation (see section 2.4).

The Cu:Zn ratio was determined to be 1:4 by XPS (profiles shown in Figure 4.3), although the surface sensitivity may exaggerate the atomic percentage of zinc. A typical EDX spectrum of CIS/ZnS QDs is shown in Figure 4.4. However, this data was taken using a copper grid and quantitative analysis is therefore difficult.

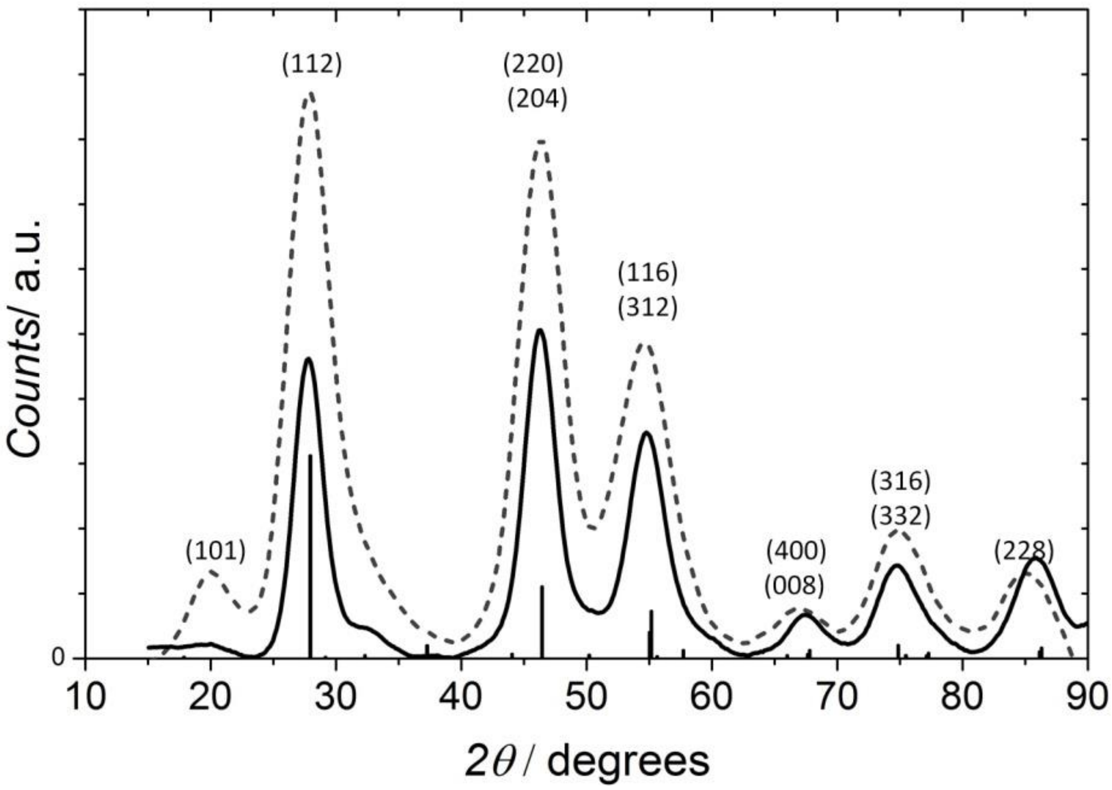

Figure 4.2: XRD pattern for CIS/ZnS QDs (black line). The pattern for the CIS QDs presented in section 3.1 is shown for comparison (dashed line).

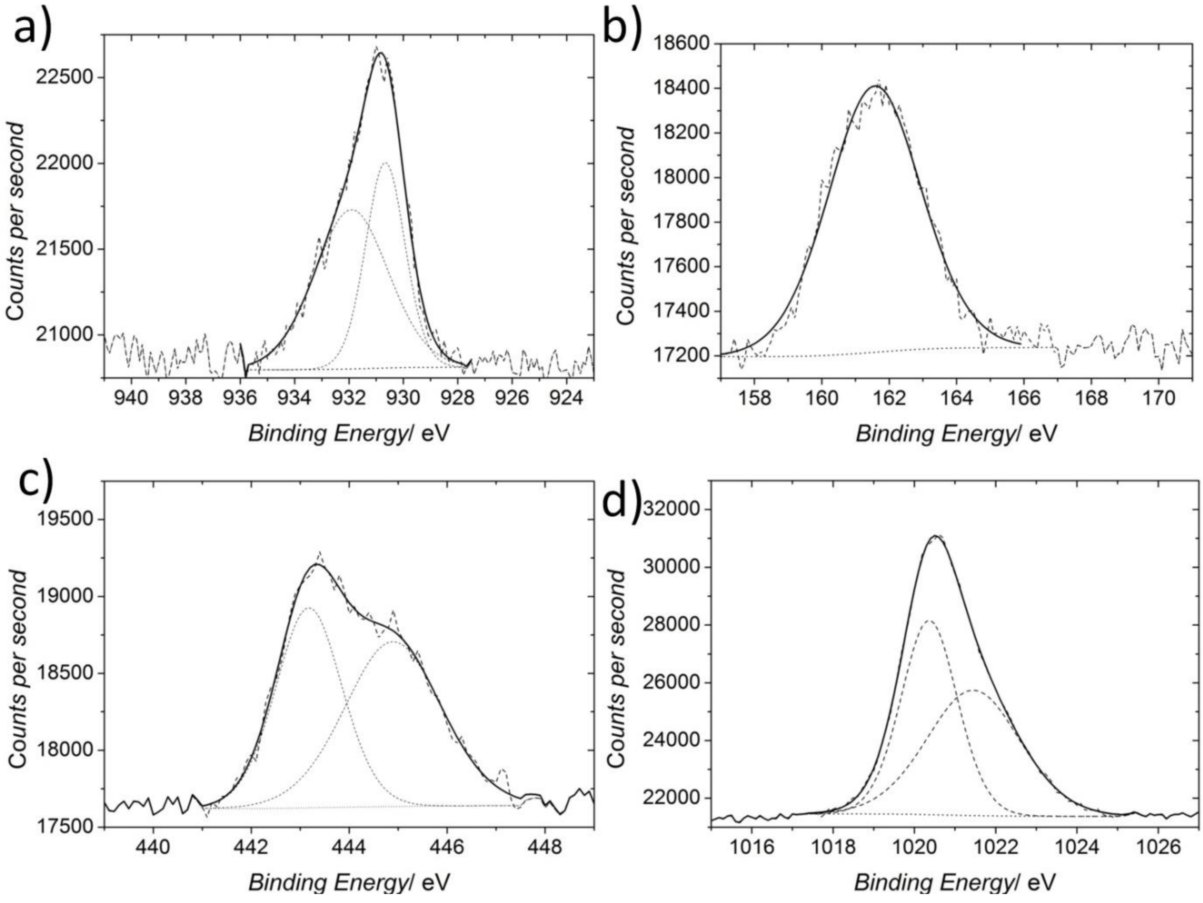

Figure 4.3: XPS profiles of a) Cu 2p region; b) In 3d5 region; c) S 2p region and d) Zn 2p region.

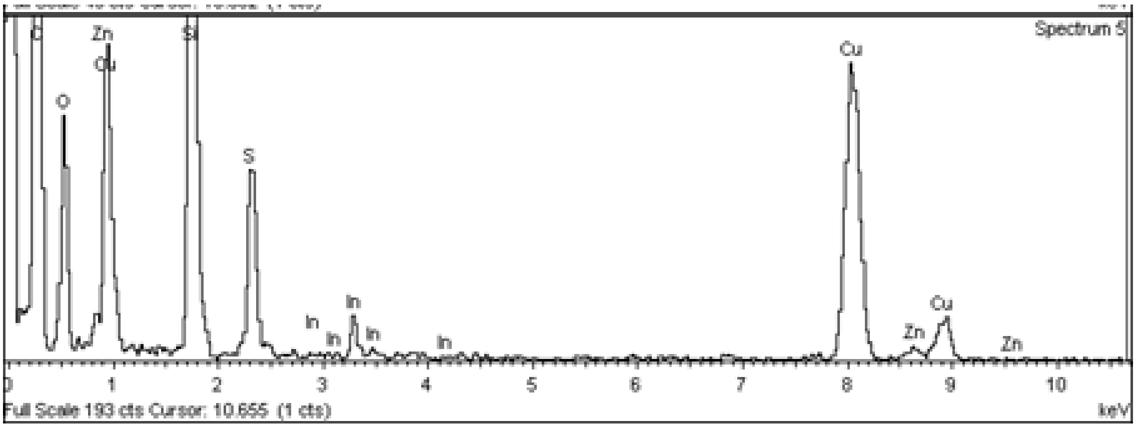

Figure 4.4: EDX spectrum of CIS/ZnS QDs.

Upon ZnS shell formation a blue-shift of up to 100 nm in the PL spectral peak position was consistently observed. The temporal dependence of this blue-shift in CIS/ZnS QDs synthesised from zinc stearate is shown in Figure 4.5. It is postulated in the literature that the highly reproducible blue-shift arises due to cation exchange during shell formation [144]. The Gibbs free energy of formation for ZnS is only marginally higher than that for CIS (-206.0 and -221 $kJ\,mol^{-1}$, respectively [144]) and the high temperature and excess of reactive zinc in solution enables zinc to replace either copper or indium in the outermost layers of the CIS QD, as opposed to forming a monolayer of ZnS directly onto the QD surface and growing outwards. A study by Klimov *et. al* [142] observed that upon forming a CdS shell by the drop-wise addition of a cadmium oleate solution in trioctylphosphate (TOP) to the CIS QDs at 210 ℃, the emission intensity was dramatically improved as for the case of ZnS shell growth, but the PL spectral peak position was blue-shifted only slightly and after 10 minutes a red-shift was observed. The formation energy for CdS (-156.5 $kJ\,mol^{-1}$[174]) is much higher than both CIS and ZnS and Cd ions are thus less likely to diffuse into the interior and reduce the CIS core QD size. The red-shifted PL observed for CIS QDs stabilised with thicker CdS shells is likely to result from a transition from type I to type II heterostructure, i.e. electrons are delocalised throughout the entire QD and radiative recombination at the core/shell interface produces red-shifted emission (see section 1.4).

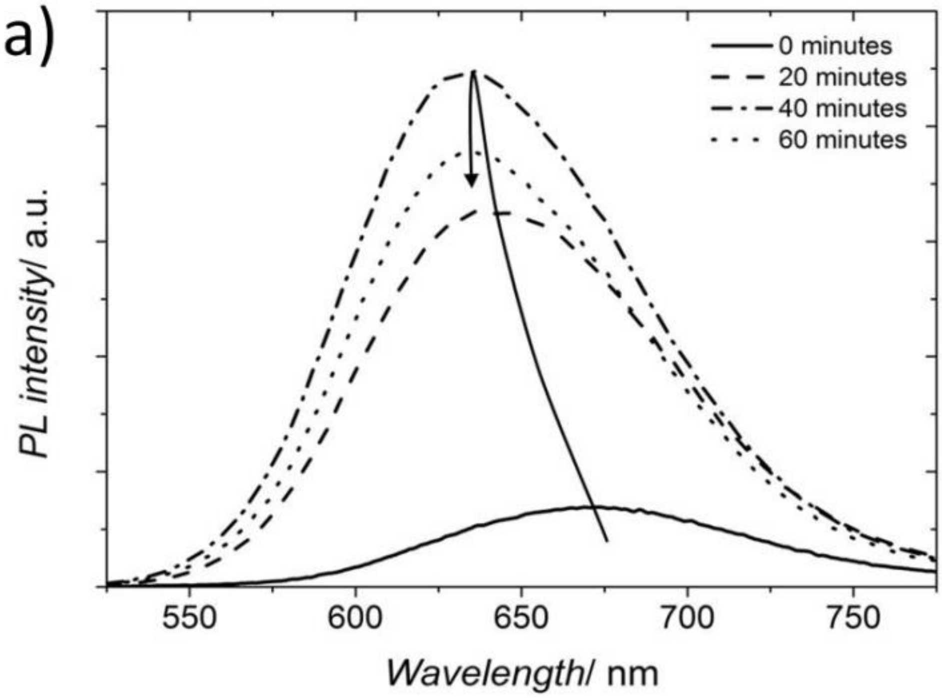

Figure 4.5: Evolution of the PL spectral profile over the duration of 60 minutes shell growth, with the arrow serving as a guide to the eye.

In addition to the observed blue-shift, the PL intensity is significantly enhanced, as shown in Figure 4.5. Given that the PLQY of the CIS QDs was determined to be approximately 13% (see equation 3.2), the PLQY of the CIS/ZnS QDs is estimated to be in the range 60-80%. The improved emission is attributed to the passivation of surface defects, suppressing the non-radiative recombination channel associated with core-only CIS QDs. The optimum reflux time is shown to be between 40 and 60 minutes, at which point the integrated area of the PL spectral peak is an order of magnitude larger than that of the core-only CIS QDs. The reduction in PLQY after 60 minutes of growth can be explained by increased strain as the ZnS layer becomes thicker and interfacial defects form which act as non-radiative trap states just like the case of surface defects for CIS QDs.

4.2 Transient Absorption Spectroscopy

Figure 4.6 shows the spectral transient absorption expressed as the change in optical density (OD) with respect to the optical density at time-zero in units of mOD (ΔOD/mOD). The strong negative band between 550 nm and 700 nm corresponds to a reduction in absorption compared to the ‘un-pumped’ QDs and since it aligns with the first excitonic feature of the absorption, indicates a ground state bleach (GSB) that slowly recovers over the first 50 ps. The broad positive signal observed within the first 5 ps at both longer and shorter wavelengths is attributed to excited state absorption (ESA).

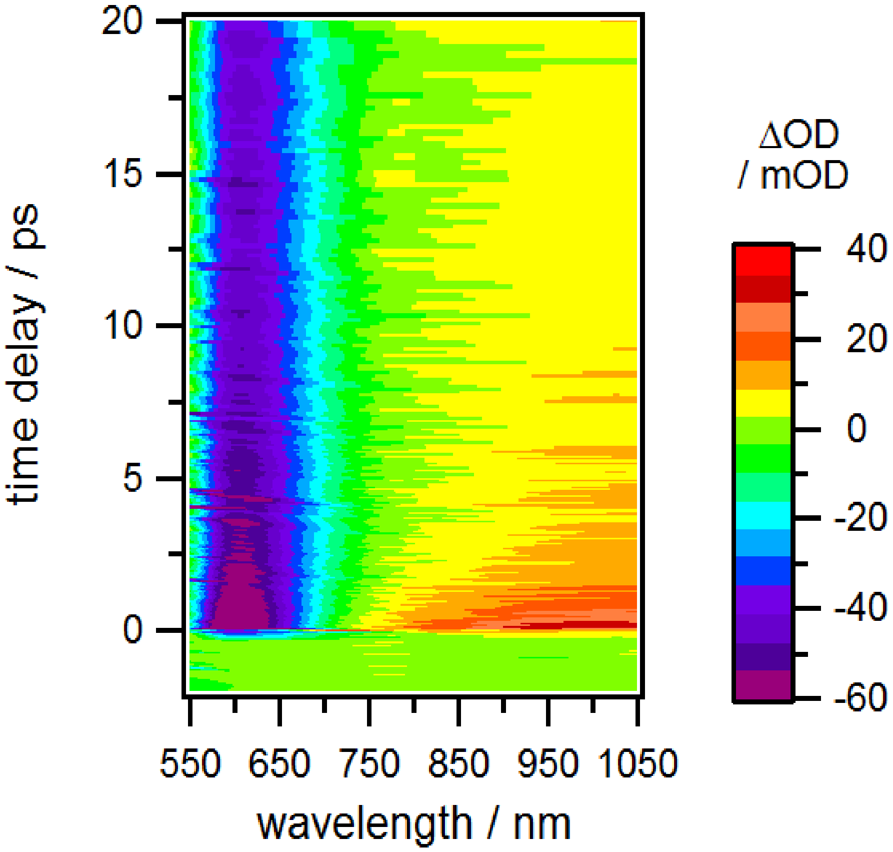

Figure 4.6: Transient absorption spectrum of CIS/ZnS QDs over the first 20 ps after excitation at 540 nm.

Besides GSB, a negative signal can also imply a radiative process; an emitted photon incident upon the detector is expressed as decreased absorption. Despite the large stokes-shift observed in CIS QDs, the features in the absorption and the PL spectra are both broad enough to overlap significantly between 550 nm and 700 nm (see Figure 3.10), such that the negative TA signal in this region may be expected to be contributed to by stimulated emission (SE) in addition to GSB. These three processes (GSB, SE and ESA) are discussed in detail in section 2.2.3 (see Figure 2.10).

The transients in Figure 4.7 show the excited state evolution over the first 20 ps after excitation, with increasing pump wavelength (a-d). Spectral profiles through the transients at 1 ps show that the negative signal is red-shifted and becomes broader with increased pump wavelength.

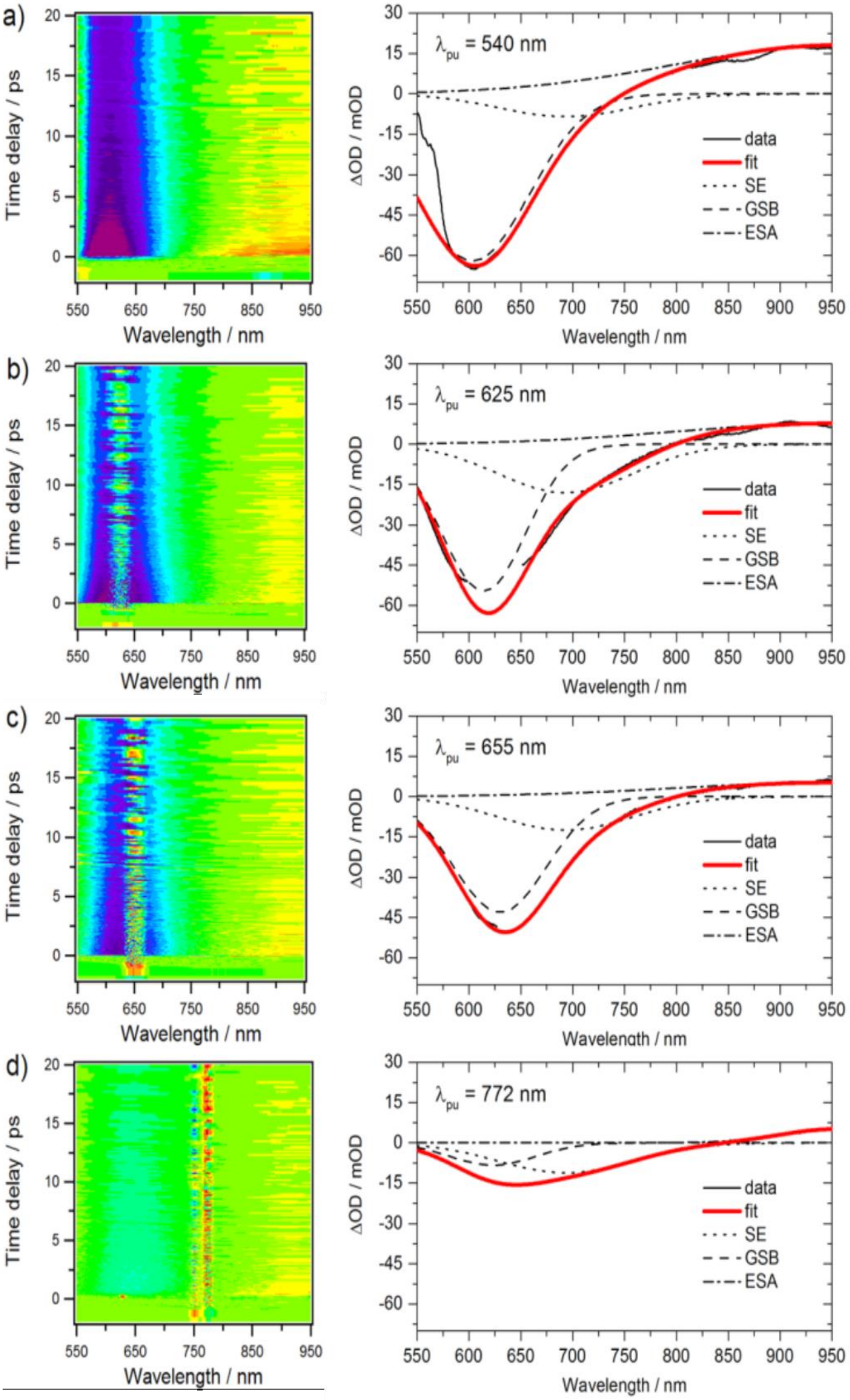

Figure 4.7: TA data with spectral cut (at ~1 ps) of CIS/ZnS QDs acquired with varying excitation wavelength and pump intensity. a: λ = 540 nm, 1.1 μJ; b: λ = 625 nm, 0.6 μJ; c: λ = 655 nm, 0.7 μJ; d: λ = 772nm, 4.5 μJ. TA data colour scale as in Figure 4.6.

Since the GSB component is not expected to shift with pump wavelength, the observed red-shift could be related to a SE component stretching out to longer wavelengths. The lines of best fit in figure 3 were comprised of three Gaussian components: one positive, centred at 950 nm, representing ESA; and two negative, representing GSB and SE. No constraints were imposed on the GSB component, whilst the centre position (693 nm) and the FWHM (100 nm) were fixed for the SE component on the basis of the steady state PL spectrum (see Figure 3.10) The strong positive signal at the excitation wavelength is an artefact of the excitation laser and was removed manually from each profile prior to fitting.

Fitting reveals that the 'red' part of the negative signal stretches out to about 850 nm and can therefore be assigned to SE, in agreement with our PL studies and those in the literature [142-149]. The red-shift of the negative band as a function of excitation wavelength can thus be understood as a change in the relative proportion between the fixed GSB and the SE components. The relative area of the SE component increases with pump wavelength, pointing to a saturation effect of the state which is involved in the relaxation process and providing further grounds for the assertion that the observed negative signal is partly due to SE.

Time-zero and scattered-light corrected kinetic traces close to the GSB and ESA centre positions (620 nm and 950 nm, respectively) are shown in Figure 4.8 a). The inset figure shows a magnification of the first 5 ps of the 950 nm and 620 nm data points that have been used in the initial fitting (the 620 nm data set and its corresponding fitting function has been inverted prior to the normalization step for easier comparison). The 620 nm data were fitted with a bi-exponential growth function (blue line) with extracted time constants (27 ± 1) ps and (1.8 ± 0.1) ps.

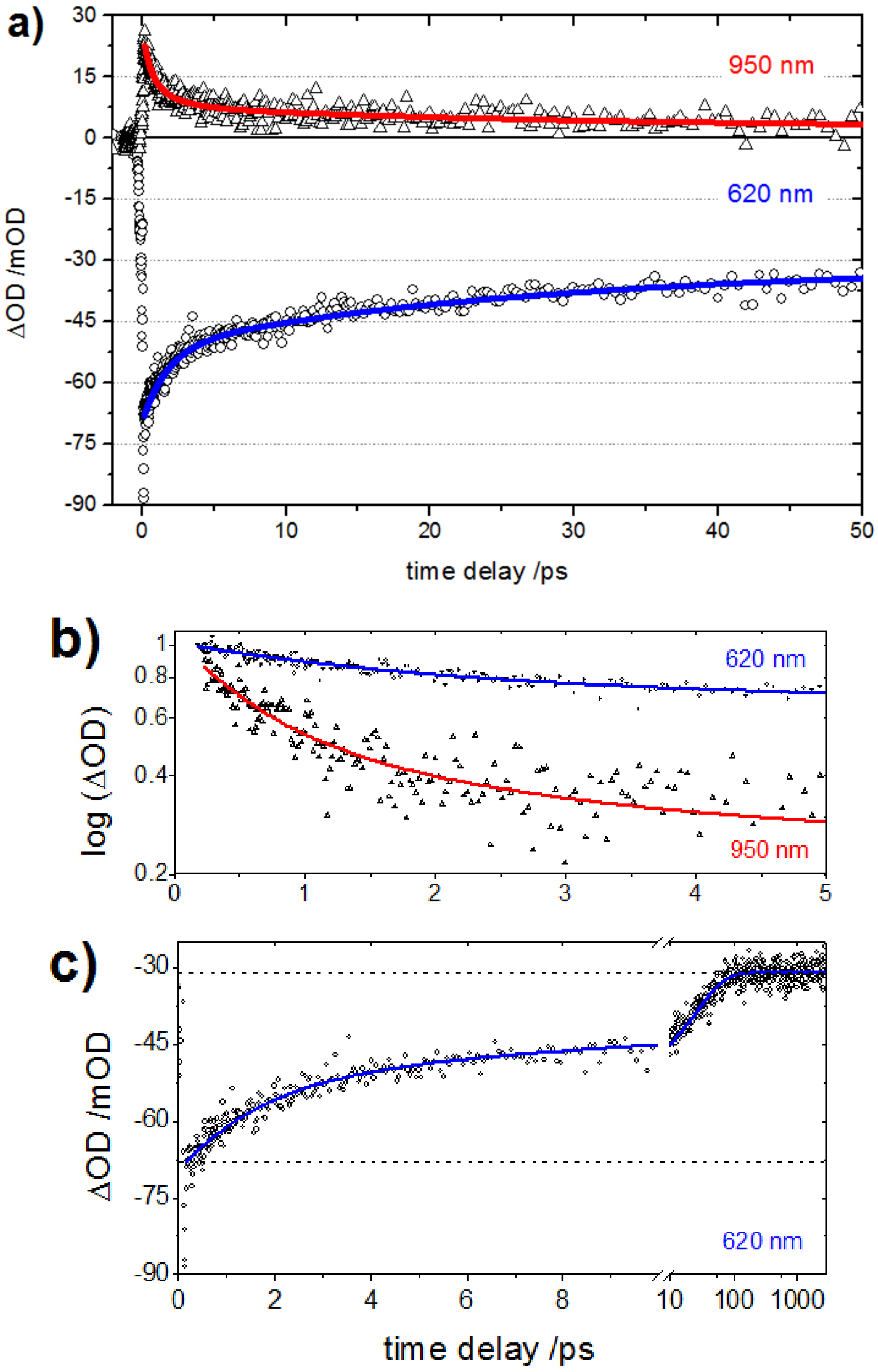

Figure 4.8: a) Kinetic cuts at 620 nm (circles) with the blue line representing a bi-exponential fit and at 950 nm (triangles) with the red line representing a tri-exponential fit. b) First 5 ps with normalized data points for the fitted range on a logarithmic scale. c) Kinetics showing initial signal amplitude and final amplitude at 2.8 ns for the 620 nm data.

We associate the slower growth component of ~27 ps with Auger decay. A correlation between the amplitudes of the 27 ps component in the 620 nm and the 950 nm signals was observed, each making up ~30 % of the total amplitude, once the data was normalised to exclude the carriers trapped in the long-lived state (see Table 4.1).

Table 4.1: Normalised amplitudes expressed as percentages of the 27ps and 1.8 ps growth/decay components in the 620 nm and 950 nm kinetic traces, respectively, and the offset in each signal at 2.8 ns.

	620 nm	950 nm
$\tau(27\,ps)$	30 %	32 %
$\tau(1.8\,ps)$	24 %	51.3%
Offset (at 2.8 ns)	46%	16.7 %

This indicates a direct coupling between the CB and VB that can be described by Auger recombination. Multi-excitation processes such as Auger effects require high pump fluences, which our experimental conditions provide. The average occupation number $\langle N\rangle$ can be calculated by multiplying the absorption cross-section of the QDs, σ_{QD}, calculated to be $2.12 \times 10^{-15}\text{cm}^2$ from the empirically determined molar extinction coefficient (see Chapter 5), with the pump fluence j_{pump} which was estimated to be $2.72 \times 10^{16}\text{cm}^{-2}$ based on a spot size of 50-60µm and a pump power of 1.1 µJ:

$$\langle N\rangle = \sigma_{QD} j_{pump} = 58 \tag{4.1}$$

The average occupation number of the 1s electron state, $\langle n_{1s}\rangle$, can then be calculated via equation 4.2:

$$\langle n_{1s}\rangle = 1 - e^{\langle N\rangle}\left(1 + \frac{\langle N\rangle}{2}\right) = 1 \tag{4.2}$$

We calculate $\langle n_{1s}\rangle$ to be close to unity with at least 50 absorbed photons per particle on average (equation 4.1). However, this model is only valid in the case that either the pump fluence is low or the excitation energy is much greater than the band gap. The experiments in this work do not fulfil these conditions and thus the values for $\langle N\rangle$ and $\langle n_{1s}\rangle$ may be exaggerated. Nevertheless, comparing the high pump fluence here with Figure 2(b) and 4(b) in the work by Sun *et. al* [154] and Li *et. al* [142], respectively, indicates that the experiments were conducted in the saturated regime.

After 2.8 ns (not shown) the transient at 620 nm levels off to an intensity of -31 mOD, which corresponds to ~45 % of the initial value at time zero. That the GSB recovery is incomplete is consistent with a fraction of excitons being trapped in the emitting state on a timescale of 10-100 ns, as previous time-resolved PL studies suggest. In addition, given the high fluence used in this experiment, the offset in the 620 nm data could also include a contribution from Auger recombination.

We assign the faster growth component (1.8 ps) with carrier trapping, most likely at remaining surface defects due to incomplete surface passivation with ZnS. These surface traps arise from unsaturated bonds and limit the symmetry of the system, giving rise to ultra-fast, broadband absorption signals.

The kinetics at 950 nm were fitted with the two time constants derived from the 620 nm data (i.e. 1.8 ps and 27 ps) but required an additional fast component to describe an early decay component, determined to be (0.5 ± 0.2) ps, assumed to be into a deep donor state arising from an internal point defect.

4.3 Hole-Burning or 'Pump-Dump-Probe' Spectroscopy

To determine if this state is related to the observed photoluminescence in CIS/ZnS QDs, hole-burning (HB) was used to drive the stimulated emission process and monitor the effect on the dynamics at the GSB and ESA positions. The TA shown in Figure 4.9a) was excited at 540 nm and hole-burned at 772 nm after 6 ps. Kinetic profiles at 600 nm, 685 nm and 900 nm are shown in Figure 4.9b). At the HB position the negative signal at 600 nm and 695 nm is reduced by ~45 % and ~72 %, respectively, whereas the excited state absorption at 900 nm is unaffected. The latter qualitative observation is the most interesting since it provides direct evidence that the absorbing excited state is not depopulated by the dump laser and is therefore not the emissive state. The instant appearance of the ESA signal with the excitation laser implies it originates in the CB, whilst the delayed rise of the SE component (~0.4 ps), which fits well with the 0.5 ps time constant assigned to a decay into an intra-gap state, implies that the SE originates from a sub-bandgap state. Therefore, the traditional picture of both ESA and SE originating from the CB [153] is not consistent with the pump-dump-probe data. This observation lends support to the idea that the observed room temperature PL in CIS/ZnS QDs can be attributed to the fraction of electrons which undergo an ultra-fast, non-radiative relaxation from the CB into a long-lived, high-lying donor state. Whether the PL originates from a coupling with a low-lying acceptor state or with the valence band cannot be determined from this data. However, the conclusion can be drawn that the emission does not originate from the CB edge, but from intra-gap donor states.

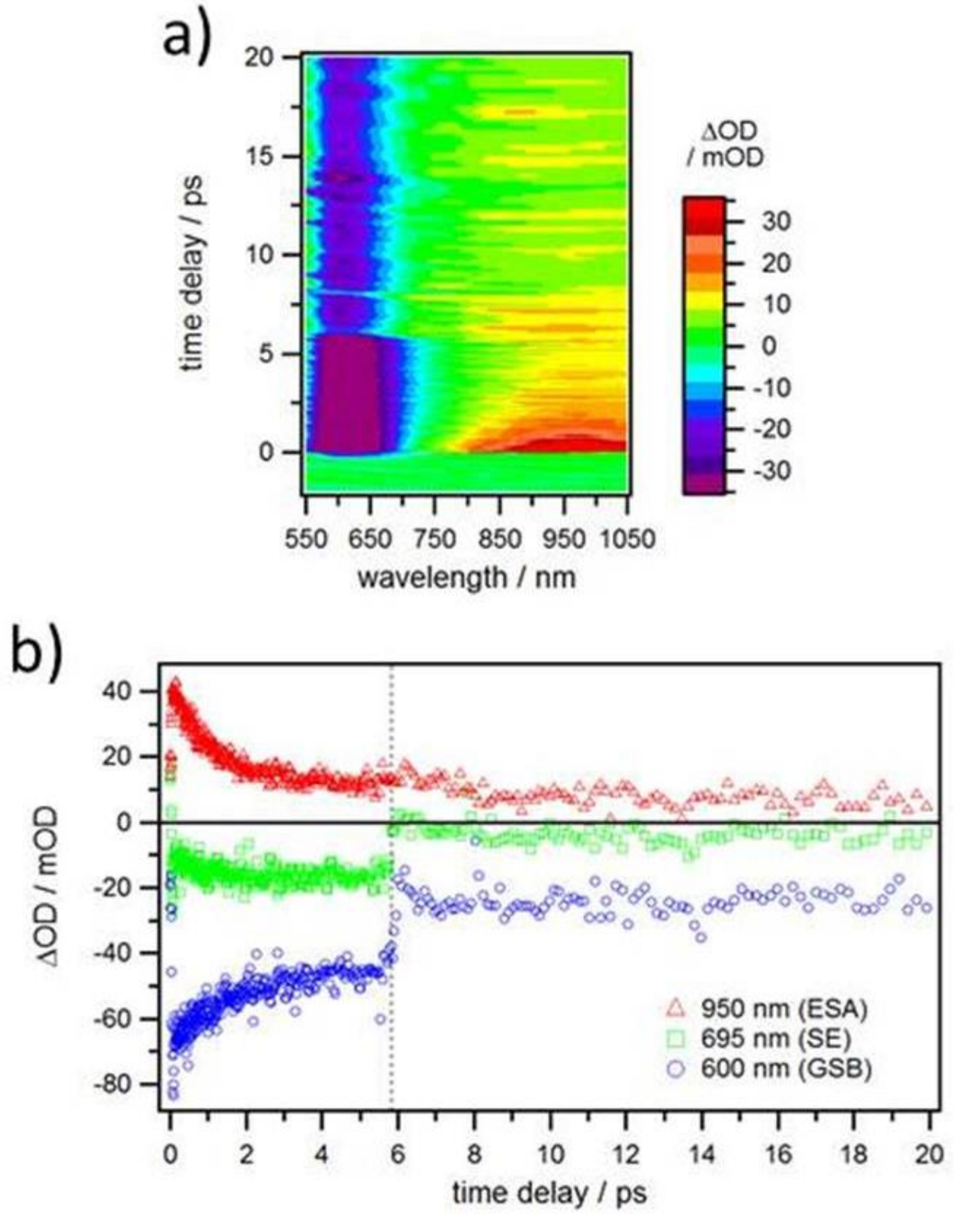

Figure 4.9: a) TA spectrum of CIS/ZnS QDs hole-burned at 6 ps at 772 nm. The kinetics (b) are analysed at the GSB (blue circles), SE (green squares) and ESA (red triangles) spectral positions.

4.4 Discussion

Our results postulate an electron-hole recombination via a trapped electron, which is contradictory to the conclusion drawn in a recent publication by Cadirci *et. al* [153] that also investigated the relaxation dynamics with femtosecond transient absorption spectroscopy. Cadirci *et. al* point out that 'the maximum bleach should be twice the value after electron trapping', which is in good agreement with the data presented here in figure 4.8 c), where the bleach amplitude increases from -70 mOD to a plateau of approximately -32 mOD after 50 ps. Admittedly, a direct comparison between the study by Cadirci *et. al* and the work presented in this paper is difficult as experimental conditions, such as excitation wavelength and pump fluence, are different. Nevertheless, our findings are further supported by a recently published study by Omata *et. al* [155], who carried out a detailed size-dependent photoluminescence study on CIS QDs and attributed the origin of the PL emission to either indium-copper anti-site defects (In_{Cu}) and/or sulphur vacancy (V_S) defect states. Nam *et. al* also summarise the possible donor states as V_S, In_{Cu}, or an interstitial copper (Cu_i) atom [143]. It is argued that the V_S-to-V_{Cu} coupling seems to be the dominant recombination pathway in CIS core-only QDs as the density of V_S and V_{Cu} at the surface is high [55]. This agrees with the interpretation by Klimov *et. al* and also explains the low PLQY measured in Chapter 3 with competitive non-radiative pathways related to surface states [142].

It is thus generally accepted that V_S trap states at the QD surface provide a very efficient de-excitation channel in QDs, and that they can be suppressed by surface treatment [55, 145, 176, 177]. Based also on the enhanced PL observed effect in copper-poor CIS [57, 170, 178], plus the fact that the synthesis technique employed by this study is sulphur-rich, it is clear that V_S states are not involved in the highly radiative recombination route in CIS/ZnS QDs.

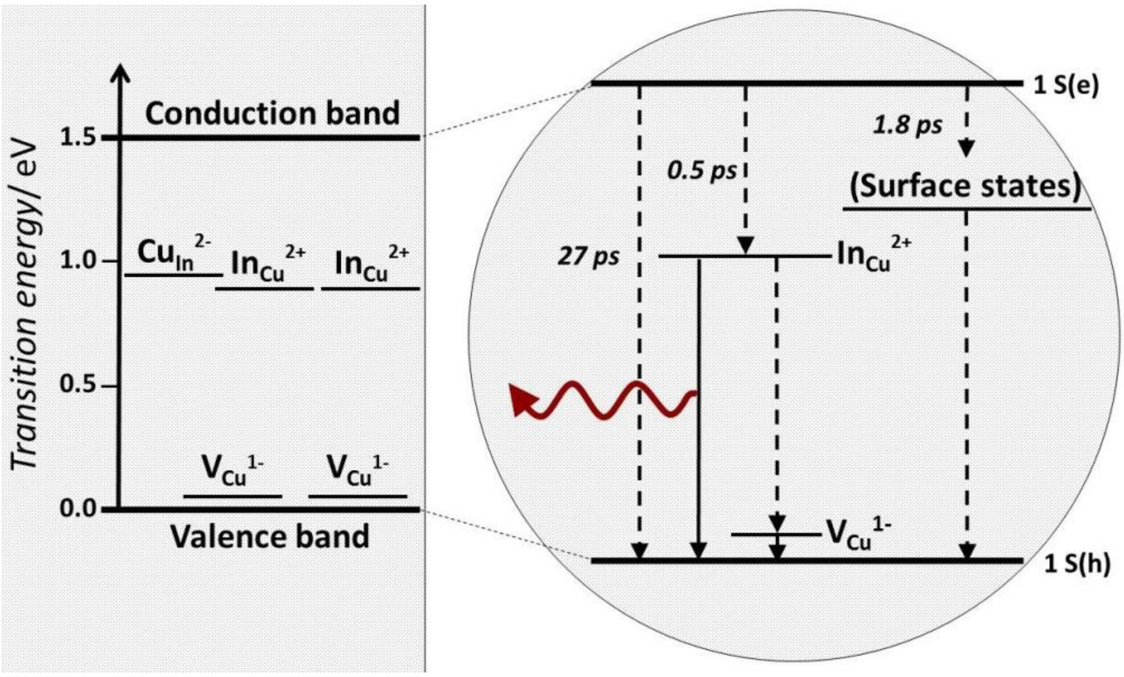

Figure 4.10: Illustration of the reported position within the band gap of the [Cu_{In}^{2-} + In_{Cu}^{2+}] and [In_{Cu}^{2+} + 2V_{Cu}^{+}] defect complexes in bulk CIS (left) and the proposed recombination pathways involving the intra-gap defect states in quantum-confined CIS/ZnS QDs (right). Solid arrows represent proposed radiative transitions and dashed lines represent non-radiative transitions.

Based on studies of the similar semiconductor $CuInSe_2$, in addition to individual defects the neutral defect complexes [In_{Cu} + 2V_{Cu}] and [Cu_{In} + In_{Cu}] can be expected to have relatively low formation energies in CIS, especially in the copper-poor phase [57]. Furthermore, the formation of [Cu_{In} + In_{Cu}] anti-site dimers is promoted in the vicinity of [In_{Cu} + 2V_{Cu}] defects, and large defect ‘clusters’ tend to be formed around sulphur anions, especially in nanocomposite CIS [170]. These defect complexes are illustrated in Figure 4.10. The identification of In_{Cu} or Cu_{In} defects as being involved in the highly radiative recombination process is therefore consistent with observations of the effects of off-stoichiometry on PLQY. From µs-TA studies in bulk it is known that the In_{Cu} state is an effective trap state (~20µs)[150] that can emit to the valence band, as can Cu_{In} states.

Nam et al discount either DAP recombination or a transition directly into the VB on the grounds that the dependency on QD size of the VB and intra-gap states cannot account for the size dependence of the observed PL, concluding that it must be the CB and not the VB that is involved in the radiative transition [142,143,153]. Although the total change in band gap with CIS QD size has been shown to fit reasonably well with such a theoretical treatment, these studies rarely experimentally determine the shift in each individual band edge position separately [149], and the extent to which the intra-gap states depend on QD size is not known. Cyclic voltammetry performed on CIS QDs of various sizes indicates that the CB and VB actually shift much more evenly than predicted from confinement models that are based on the effective-mass approximation [171].

A possible explanation for this apparent deviation from the expected size dependence of the VB position is the complex nature of the valence band in CIS; it is known that the upper-most *p* and *d* orbitals in the valence band of bulk CIS undergo hybridization, shifting the VB edge to higher energy [131, 178]. In CIS QDs, however, the energetic separation between the *p* and *d* orbitals would be expected to increase as a result of quantum confinement, reducing the extent of hybridization and decreasing the energy of the VB edge. Similar effects have been demonstrated in copper-doped CdSe QDs [179] and HgTe nanoparticles[80].

4.5 Concluding Remarks

The excited state dynamics in CIS QDs is accepted to involve intra-gap states associated with point defects in the interior of the QD and surface defects, as discussed in Chapter 3. The formation of a ZnS shell on the CIS QDs saturates ‘dangling bonds’ at the QD surface and eliminates surface defects and the associated non-radiative recombination. The PLQY is dramatically improved as a result, and a slight blue-shift in the PL spectral peak position is observed. Despite this understanding as to why the radiative recombination channel is enhanced in CIS/ZnS QDs relative to CIS QDs, the specific nature of the highly radiative transition remains contested in the literature. A combination of transient absorption spectroscopy and hole-burning has shown that as the state responsible for the photoluminescence is emptied, no change in the excited state absorption (ESA) is detected. Based on the assumption that electrons in the conduction band readily undergo ESA to higher excited states, we conclude that the long-lived PL in CIS and CIS/ZnS QDs must come from the fraction of electrons which undergo an ultra-fast decay into a high-lying donor state.

Chapter 5

Quantifying Absorption: The Size-dependent Molar Extinction Coefficient of CIS Quantum Dots

In this chapter the molar extinction coefficient $\varepsilon(\lambda)$ for CIS QDs is determined in order that the concentration of a given CIS QD sample can be determined by absorption spectroscopy and the Beer-Lambert law. The size dependence of ε is investigated at two wavelengths: the band edge transition, the location of which depends strongly on QD size; and at high energy (3.1 eV), where the absorption of QDs should be relatively size-independent. The size distribution of the QDs and the presence of a ZnS shell are both evaluated and accounted for in the calculations.

In this work, the combined compositional and morphological characterisation of the CIS QDs enables the concentration C of a series of QD suspensions of known sizes to be measured, and therefore for $\varepsilon(\lambda)$ to be determined from UV/visible spectroscopy via the Beer-Lambert law [162].

$$A(\lambda) = \varepsilon(\lambda)Cl\,, \tag{5.1}$$

where $A(\lambda)$ is the absorbance at wavelength λ and l is the path length.

The extinction coefficient is determined at two spectral positions. At high energy, where the density of states is expected to be largely continuous, and the absorption spectrum is expected to be size-independent. Furthermore, the increased absorption towards the UV provides greater sensitivity to low QD concentrations. In addition, the extinction coefficient is determined at the spectral position of the first excitonic transition giving a more accurate indication of the absorbance as a function of QD size.

5.1 Measuring Absorption

The size distributions of CIS QDs in ten suspensions were measured by TEM to be within the size range 2.1 nm to 5.2 nm. These samples are the same as in the PL sizing curve shown in Figure 3.17. The average sizes of ten additional suspensions were estimated based on the sizing formulation derived in equation 3.2 (see section 3.1).

The concentration of copper in the 20 CIS QD suspensions was determined by atomic absorption spectroscopy (AAS). A measured volume of the CIS QD suspensions in hexane was evaporated by drying under nitrogen. The resulting QD powder was digested with acid (Aqua Regia) to enable AAS measurements. The concentration, in parts per million, was then translated into a CIS QD sample concentration in units of mol/L (M), based on the density of bulk CIS and the mean QD volume as determined from the QD size distribution by TEM.

Since the first excitonic feature in the absorption spectrum of CIS QDs is significantly broader than those observed in most other QD materials, the most reliable method of locating the first excitation position E_1 is through the second derivative of the absorption spectrum. This is discussed in more detail in Chapter 3. Gaussian curves were then fitted to the first excitation feature, constrained by the positions of the local minimum in the second order absorption spectrum, and the width of the feature, given by the standard deviation σ_m was be measured. A linear correlation between σ_m and the relative size distribution of the QDs, $\Delta d/d$, as measured by TEM is illustrated in Figure 5.1. A linear fit, extrapolated to the origin, enables an estimate to be made for the expected standard deviation σ_0 of the first excitation feature in a perfectly monodisperse sample, i.e. $\Delta d = 0$.

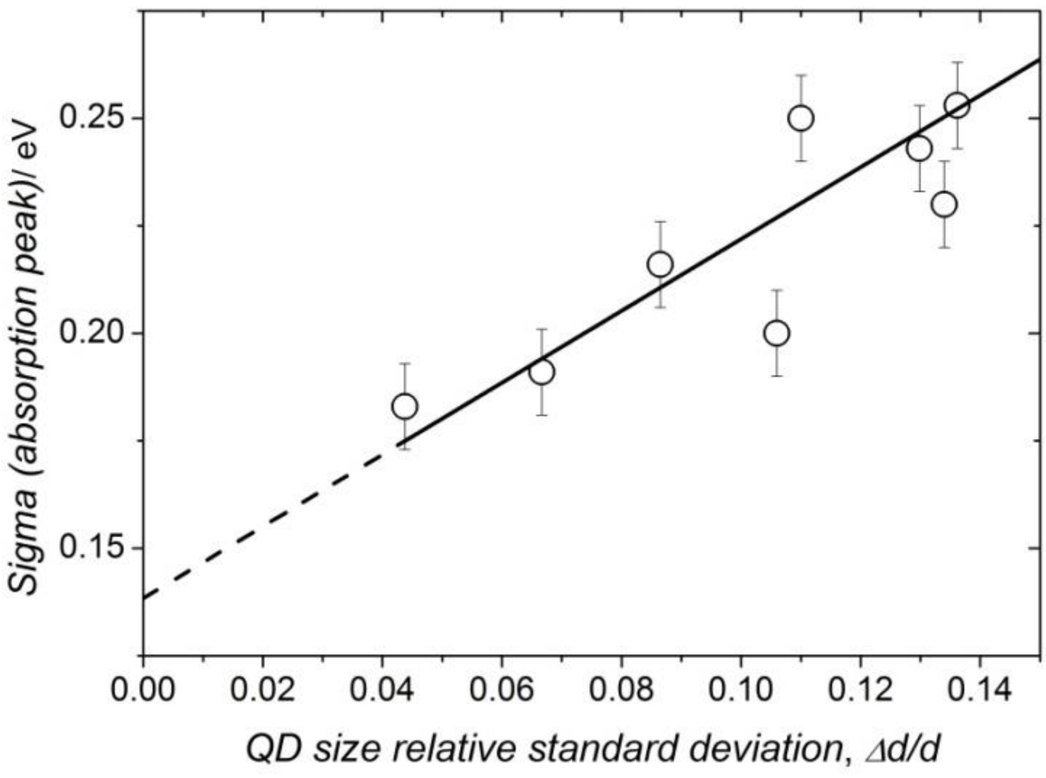

Figure 5.1: The width of the first excitonic feature in the absorption spectrum plotted against the relative size distribution in CIS QDs.

The size distribution of QDs in a suspension was accounted for by multiplying the measured absorption A_m by the ratio of the measured standard deviation σ_m to the 'ideal' deviation σ_0 where A_0 is the calibrated absorption value to be used in the Beer-Lambert law. The value of σ_0 was determined to be 0.146 ± 0.006 for the QD samples in this study.

$$A_0 = A_m \frac{\sigma_m}{\sigma_0} \tag{5.2}$$

5.2 Molar Extinction Coefficient

The molar extinction coefficient (in units of $cm^{-1}M^{-1}$) of the CIS-QDs was empirically related to the mean size d (nm) via a power law in accordance with the power law dependency of $\varepsilon(\lambda)$ on size for other QD materials reported.

$$\varepsilon = xd^y \tag{5.3}$$

The size dependence of the molar extinction coefficient at E_1 was fitted to equation 5.3 with coefficient x equal to 830 $\pm$ 660 and exponent y equal to 3.70 $\pm$ 0.60 (Figure 5.2)

$$\varepsilon(E_1) = 830d^{3.70} \tag{5.4}$$

The exponent y at E_1 is larger than that reported for other QD materials reported (table 5.1) and the coefficient x is an order of magnitude smaller, suggesting a fundamental difference between CIS and other QD materials such as CdTe and CdSe. As the QD size increases the absorbance of CIS-QDs increases at a faster rate than for both CdSe and CdTe QDs, this is consistent with the comparatively large absorption coefficient for bulk CIS ($\sim 5 \times 10^5 \mathrm{cm}^{-1}$ [173]) that is an order of magnitude higher than for bulk CdSe. In addition to an empirical fit, the experimentally observed size dependence of $\varepsilon(E_1)$ a can be modeled using the formulation for the absorption coefficient $\alpha(E)$ of a QD derived in section 1.3

$$\varepsilon(E) = \frac{N_A V_{QD} \alpha(E)}{1000 \ln(10)} = B \sum_{n,l} \frac{(2l+1)}{E\sqrt{2\pi}\Delta E_{n,l}} exp\left[-\frac{\left(E - E_{n,l}\right)^2}{2\Delta E_{n,l}{}^2}\right] \tag{5.5}$$

where

$$B = \frac{N_A}{\ln(10)} \frac{\pi e^2 E_p a_p}{2m_0 c n_r \varepsilon_0 \omega_{exc}} \tag{5.6}$$

In strongly confined QDs the energy spacing to higher excited states is large enough that the absorption at $\lambda(E_1)$ may be assumed to include a negligible contribution from higher transitions. Equation 5.5 is therefore simplified:

$$\varepsilon(E) = \frac{B}{E\sqrt{2\pi}\Delta E_1} exp\left[-\frac{(E - E_1)^2}{2\Delta E_1{}^2}\right]. \tag{5.7}$$

The transition energy of E_1 is bigger than the band gap as shown in equation 1.23 by the kinetic energy of the electron and hole. Since for $n = 1$ the momentum $k = \pi/d$, equation (1.25) is related to equation (1.17):

$$E_1 = E_g + \frac{\pi^2 \hbar^2}{2\mu_{eff} d^2} \tag{5.8}$$

and the second derivative with respect to the QD size d is given by:

$$\Delta E_1 = \frac{\pi^2 \hbar^2}{\mu_{eff} d^3} \Delta d\,. \tag{5.9}$$

Substituting these two expressions into equation 5.7 gives an expression for $\varepsilon(E_1)$ as a function of QD size, d, the bulk band gap $E_{g,bulk}$ and the effective excitonic mass μ_{eff}:

$$\varepsilon(E_1) = \frac{B}{\sqrt{2\pi}\left(E_{g,bulk} + \frac{\pi^2\hbar^2}{2\mu_{eff}d^2}\right)}\frac{\mu_{eff}d^3}{\pi^2\hbar^2\Delta d} \tag{5.10}$$

The material specific constant B/e^2 was empirically determined to be $(1.9 \pm 0.1) \times 10^5 eV^2M^{-1}cm^{-1}$ by fitting equation 5.10 to the molar extinction coefficient data displayed in Figure 5.2. This is the same order of magnitude for CdS [182], CdSe [182-184], CdTe [182] and PbS [185] QDs reported in the literature.

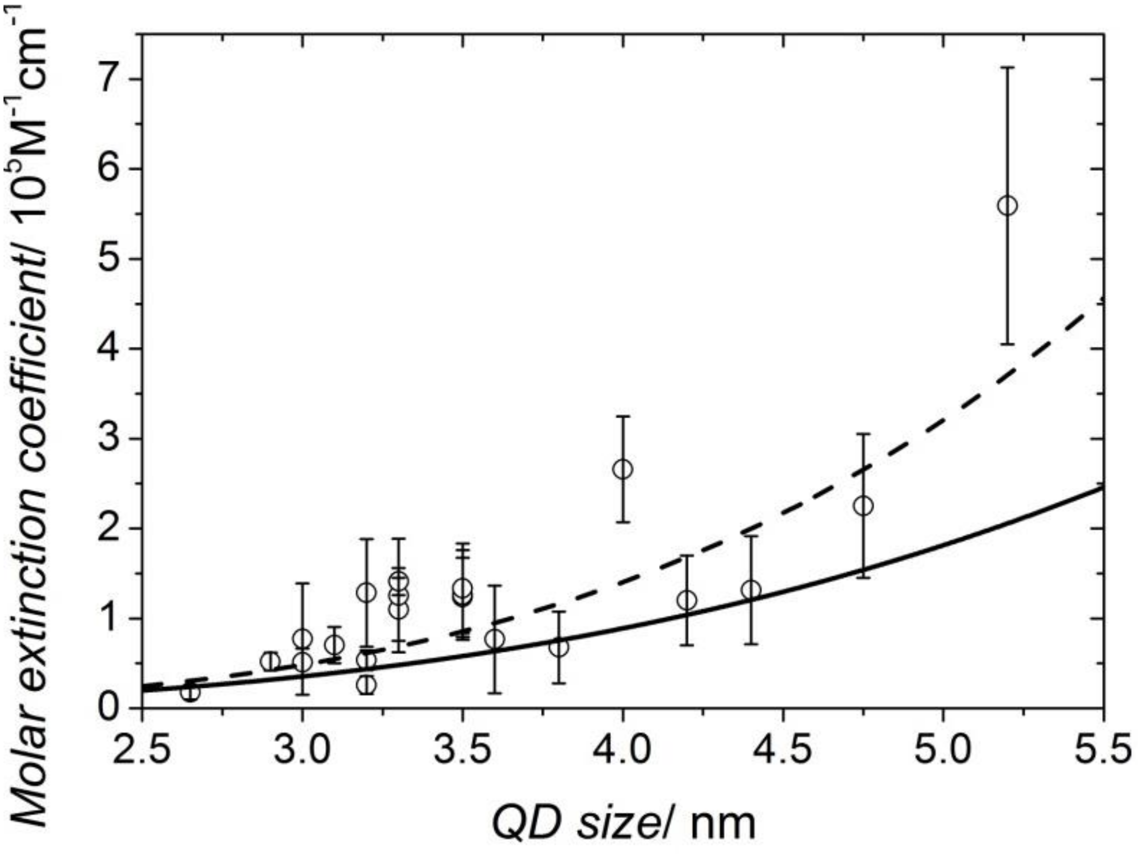

Figure 5.2: The calculated molar extinction coefficient for 20 CIS QD suspensions in the size range of 2.9 nm – 5.2 nm, at the first excitation energy. The solid line represents the theoretical fit described by equation 5.10 and the dashed line is an allometric fit.

This semi-empirical model reproduces the experimental data well; a fit good fit ($R^2 = 0.999$) to the data at E_1 with the exponent determined to be 3.2 ± 0.1, which is lower than that determined by the exponential fit (equation 5.4), i.e. the two fits diverge as the QD size increases. This is most likely due to the fact that the contribution from higher energy transitions is neglected by the model. As the size of the QD increases, the energy levels become less discrete and the energy gap between the first and subsequent transitions decreases, making this approximation less valid and producing the increasing discrepancy between our data (the empirical fit) and the semi-empirical model with increasing QD size.

Table 5.1: List of the reported powers (see equation 5.3) for various QD materials.

Material	Exponent, y
$CuInS_2$	3.70 ± 0.60
CdTe	2.12 [182]
CdS	2.3 [182]
CdSe	2.65 [182]; 3 [183, 184]
PbS	2.32 [185]

The size dependence of the molar extinction coefficient at 3.1 eV can be fitted to equation 5.3 with coefficient x equal to 2123 ± 1090 and exponent y equal to 3.8 ± 0.3 (Figure 5.3).

$$\varepsilon(3.1\ eV) = 2123 d^{3.8} \tag{5.11}$$

As is expected, the value of ε is larger at 3.1 eV than at E_1 for a given QD size. The result of this is that the determination of solution concentration of CIS-QDs using $\varepsilon(3.1\ eV)$ as opposed to $\varepsilon(E_1)$ will provide greater sensitivity and enable lower concentrations to be detected. The data in Figure 5.3 is also fitted with a theoretical expression, given by equation 5.12, which is based on the work by Ricard *et. al* [46] and Klimov *et. al* [186]:

$$\varepsilon(3.1\ eV) = V_{QD}|f_{LF}|^2\alpha_{\mathrm{bulk}}(3.1\ eV). \tag{5.12}$$

It is also important to note that the exponent at 3.1 eV should be closer to 3 than the exponent at E_1, since the absorption at high energies is less size dependent (Figure 5.3, dotted line). The fact that this is not the case is likely to be caused by the contribution at 3.1 eV of the broad first excitation band for large QDs. This is consistent with the hypothesis that large agglomerates are formed during the synthesis stage that was used to explain the static feature at 810 nm that increasingly dominates the PL spectrum of larger QDs (see Figures 3.14 and 3.15).

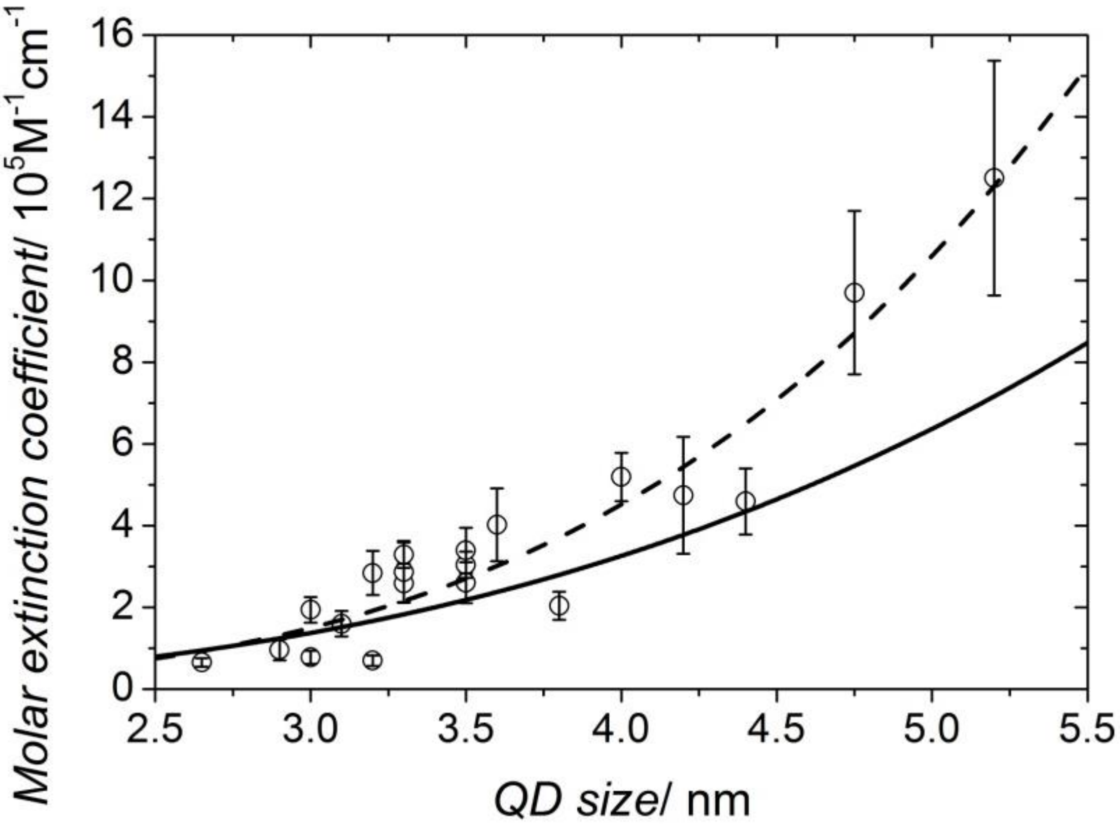

Figure 5.3: The calculated molar extinction coefficient for 20 CIS QD suspensions in the size range of 2.9 nm – 5.2 nm, at 400 nm (3.1 eV). The solid line represents the theoretical fit described by equation 5.12 and the dashed line is an allometric fit (equation 5.11).

Besides the small lattice mismatch (<1%) with CIS [149], a wide band gap (3.1 eV) makes ZnS an ideal shell material for CIS QDs, since, energetically, the position of the conduction band and valence band of the CIS core lie within the band gap of the ZnS shell. This not only further confines excitons within the CIS core, but improves the PLQY significantly by removing surface defects and the non-radiative relaxation pathway associated with them [53-55]. In addition, the band gap-alignment in CIS/ZnS QDs is such that the ZnS will not absorb incident light at wavelengths above 400nm (approximately).

As reported in chapter 4, formation of a ZnS shell both dramatically enhances the PLQY significantly and blue-shifts the PL spectral peak position. The nature of the observed blue-shift is still under contention in the literature and as such presents a problem when considering the effect of surface passivation with ZnS on the magnitude of the extinction coefficient of CIS QDs.

If, as postulated in the literature and supported by the data presented in Chapter 3, the blue-shift reflects a reduced CIS core size originating from cation exchange during shell formation, the assumption that the ZnS shell does not affect the optical density of the CIS core allows equation 5.10 to be used in the case of CIS/ZnS QDs if an ‘effective size’ D of the CIS core component is used in replacement of d. This effective core size is simply the size of CIS QD needed to reproduce the PL spectral peak position of a given sample CIS/ZnS QDs.

This method was validated by preparing two CIS QD suspensions with different mean QD size (CIS_A and CIS_B) and subsequently growing a ZnS shell on each until their PL maxima was observed to occur at the same wavelength (Figure 5.4); the PL spectral peaks of solutions CIS/ZnS_A and CIS/ZnS_B are both centered at 638 ± 1 nm, corresponding to an effective core size D of 2.4 ± 0.2 nm for both solutions based on the PL sizing curve shown in Figure 3.18. The absorption spectra of CIS QD suspensions A and B are shown in Figure 5.4.

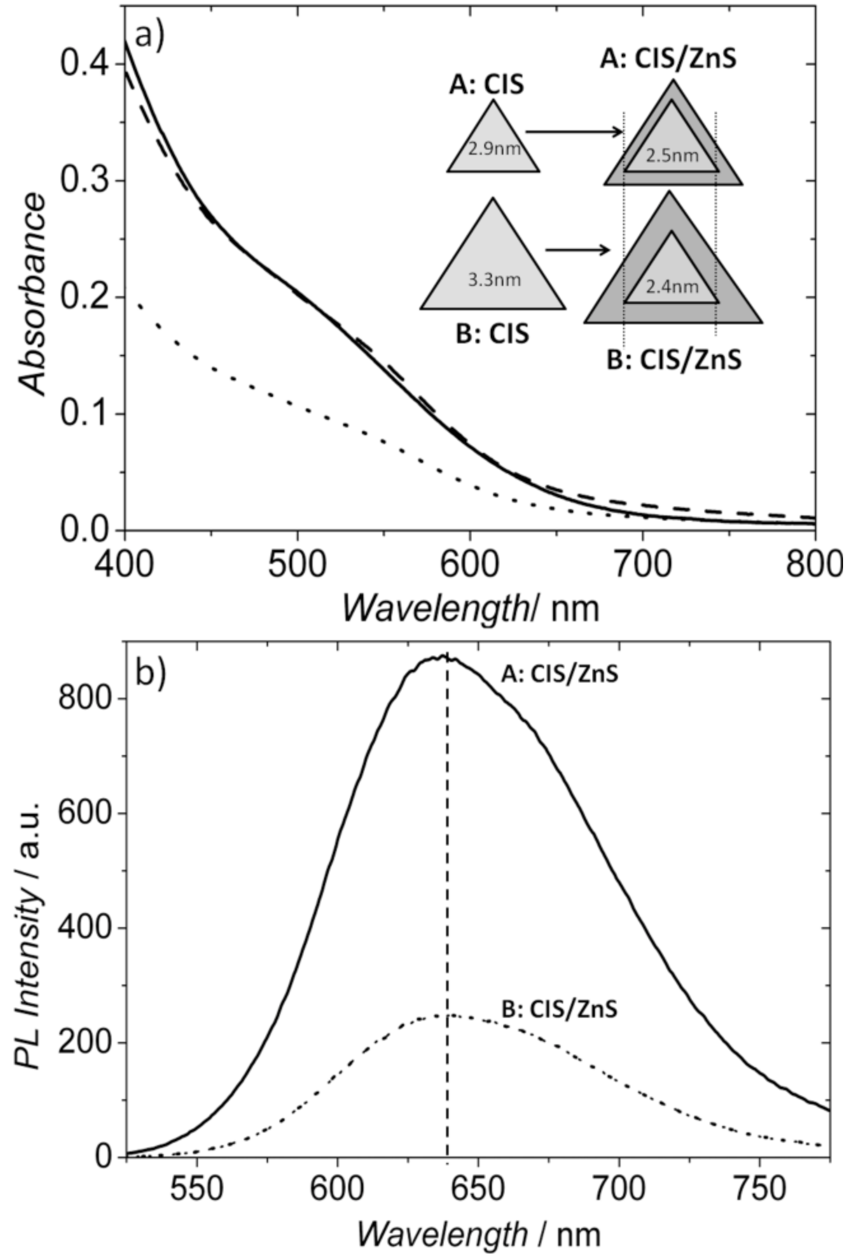

Figure 5.4 a) The absorption spectra of two identically emissive CIS/ZnS QD solutions with different ZnS shell thicknesses (A: solid line and B: dotted line). The absorption spectrum of B:CIS/ZnS is multiplied by a factor of 1.9 (dashed line) to correct for the difference in concentration from A:CIS/ZnS. b) PL emission spectra of solutions A:CIS/ZnS (solid line) and B:CIS/ZnS (dotted line). The dashed vertical line depicts the common PL spectral maxima for both samples.

The overall CIS/ZnS QD size (from TEM) and the volumetric ratio of CIS to ZnS (calculated from AAS data) were combined to estimate the apparent shell thickness and the 'effective' core diameter D. For both solutions, the estimated core sizes were the same as the core sizes predicted from the PL sizing curve for CIS QDs within experimental error. There is little difference between the absorption profiles of solutions A:CIS/ZnS and B:CIS/ZnS when B:CIS/ZnS is normalized to A:CIS/ZnS at 520 nm.

This supports the assumption that the thickness of the ZnS shell has little effect on the absorption properties of the CIS-QDs or, therefore, on the extinction coefficient. The concentration of QDs in solutions A:CIS/ZnS and B:CIS/ZnS were determined using the Beer-Lambert law in an identical manner to the CIS-QDs but using the effective core sizes, D, the molar extinction coefficients of the equivalent effective core size CIS-QDs and the measured absorbance values of the CIS/ZnS solutions (corrected for size distribution). The ratio of concentration between solutions A:CIS/ZnS and B:CIS/ZnS is 1:1.8 (table 5.2), which is close to the factor of 1.9 used to normalize the two absorption profiles (Figure 5.4a).

Table 5.2**.** The concentration of solutions A:CIS/ZnS and B:CIS/ZnS determined from absorption measurements and the effective core diameter obtained from Equation 1.

Solution	Concentration/ µM
A: CIS/ZnS	11.0 ± 0.8
B: CIS/ZnS	6.0 ± 0.4

The main sources of error in the determination of ε at E_1 can be ascribed to the sizing methods used and the uncertainty in the location of the first excitonic absorption peak. The non-unity reaction yield of the synthesis requires compositional analysis to be carried out on digested solutions in order to independently determine the QD concentration in solution. The purification procedure prior to digestion is therefore vital because any un-reacted Cu precursor remaining in solution during AAS measurements will affect the accuracy of the determined concentration.

5.2 Concluding remarks

The size dependent molar extinction coefficient was determined for colloidal CIS QDs suspended in hexane, enabling the concentration of a given CIS QD suspension via applying the Beer-Lambert law to the absorbance as measured by UV/Vis spectroscopy. The data presented in this work allows this method to be applied to CIS QDs in the size range 2.8 to 5.2 nm.

Firstly, the extinction coefficient was determined at the first excitation position for each QD sample suspension. Since the wavelength of this first excitonic transition is strongly dependent on QD size, strong size dependence in the extinction coefficient was expected. The data presented in this chapter was fitted with good accuracy to a power law, with the extinction coefficient increasing as a function of the QD size to the power of 3.7, which is in agreement with the expected strong size dependence. Indeed this exponent is much greater than that reported for other QD materials, as well as for similar studies done on CIS QDs [187]. The slightly larger exponent determined here is most likely a result of either a difference in definition of QD ‘size’. For example, the QDs synthesised from the materials in Table 5.1 are typically spherical and therefore either the radius or diameter are obvious choices to represent QD size. However, for the tetrahedral CIS QDs in this work there is no established way of representing the particle size. The convention used throughout this thesis is discussed in section 2.1.4, however the definition of ‘size’ in references [187] is not clear. The data was also fitted to a semi-empirical model, yielding an excellent fit, despite higher electronic transitions being neglected for simplicity. This further exaggerated the size dependence of the extinction coefficient since absorption by higher transitions was assigned to the first transition.

In addition, the extinction coefficient was determined for each suspension at a set wavelength (400 nm (3.1 eV)). Since the absorption spectrum at high energy is almost identical for each suspension, this data does not reveal any additional information related to size effects. However, since the absorption at low wavelengths is stronger than at the band edge, it does give the method for determining QD concentration greater sensitivity to small concentrations in solution.

Chapter 6

Phase transfer of hydrophobic $CuInS_2$-based QDs into the aqueous phase

Various synthesis techniques have been developed that enable the direct synthesis of QDs in the aqueous phase, resulting in hydrophilic QDs that can be suspended in water over a wide pH range. The synthesis technique outlined for CIS QDs in Chapter 3, however, results in hydrophobic CIS QDs that aggregate when exposed to the aqueous phase, causing the PLQY to be drastically diminished via a self-quenching mechanism. This chapter takes two separate approaches to the fabrication of hydrophilic CIS QDs that form stable colloidal suspensions in the aqueous phase: the development of direct synthesis techniques for hydrophilic CIS QDs with polar surface ligands, eliminating the need for further synthetic steps; and the post-synthesis encapsulation of hydrophobic CIS QDs with amphiphilic polymer to produce hydrophilic QD/polymer hybrid nanoparticles.

6.1 Direct synthesis of hydrophilic $CuInS_2$ QDs

6.1.1 Mercaptoundecanoic acid stabilised $CuInS_2$ QDs

The synthesis of MUA stabilised CIS QDs, described in section 2.1.2, produced highly luminescent QDs, although they displayed extremely poor colloidal stability in water. The rapid degradation in PL intensity of the same sample after 24 hours is illustrated in Figure 6.1. The PL spectrum of the sample immediately after cleaning is comparable in intensity and spectral shape to that of DDT stabilised CIS QDs (see section 3.3). PL spectroscopy was repeated on the same sample 24 hours later, under identical instrument settings. The PL intensity was reduced by an order of magnitude and the spectral profile was significantly distorted.

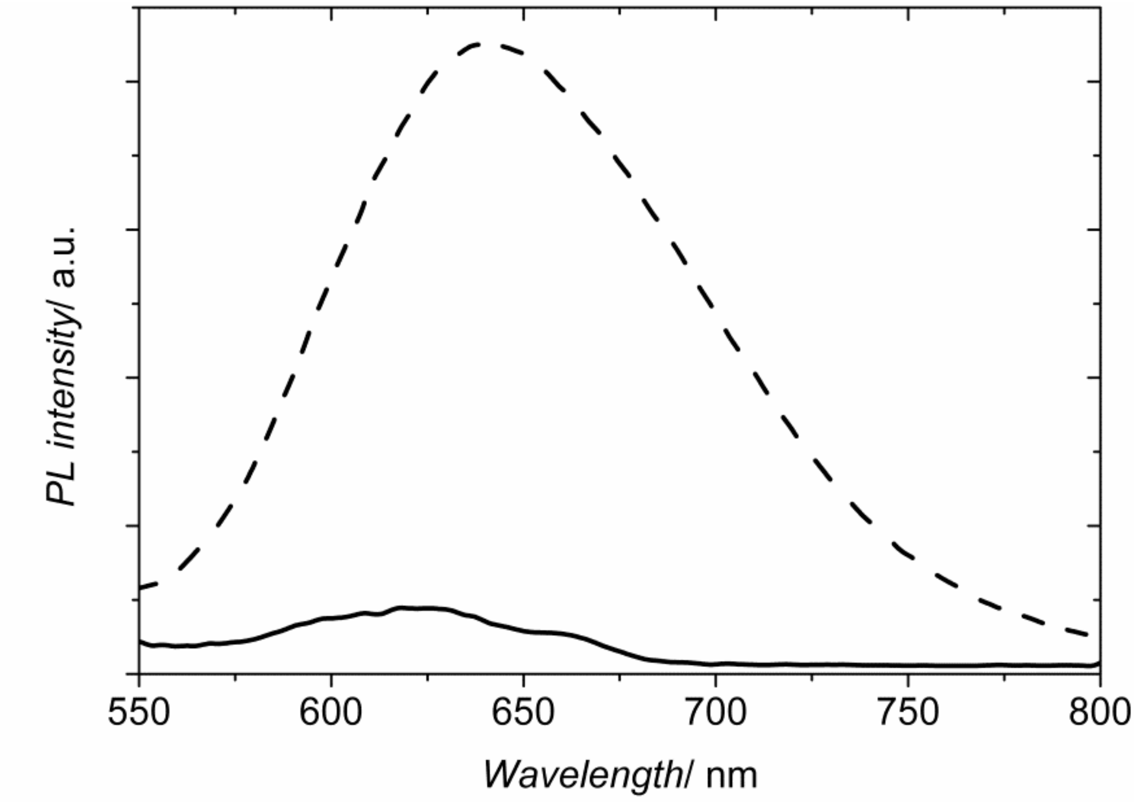

Figure 6.1: PL spectra of MUA stabilised CIS QDs within one hour of synthesis (dashed line) and after 24 hours (solid line).

The structural deterioration of the two samples was illustrated further by XRD. Half of the sample was dried immediately after cleaning and stored in a nitrogen glovebox, and the remainder was dried after 24 hours in ambient conditions. Both XRD patterns are shown in Figure 6.2, showing a dramatic transformation from broad peaks that are in agreement with CIS reference pattern to a multitude of narrow peaks suggesting very small fragments. This suggests that the deterioration in the optical properties is caused by rapid corrosion.

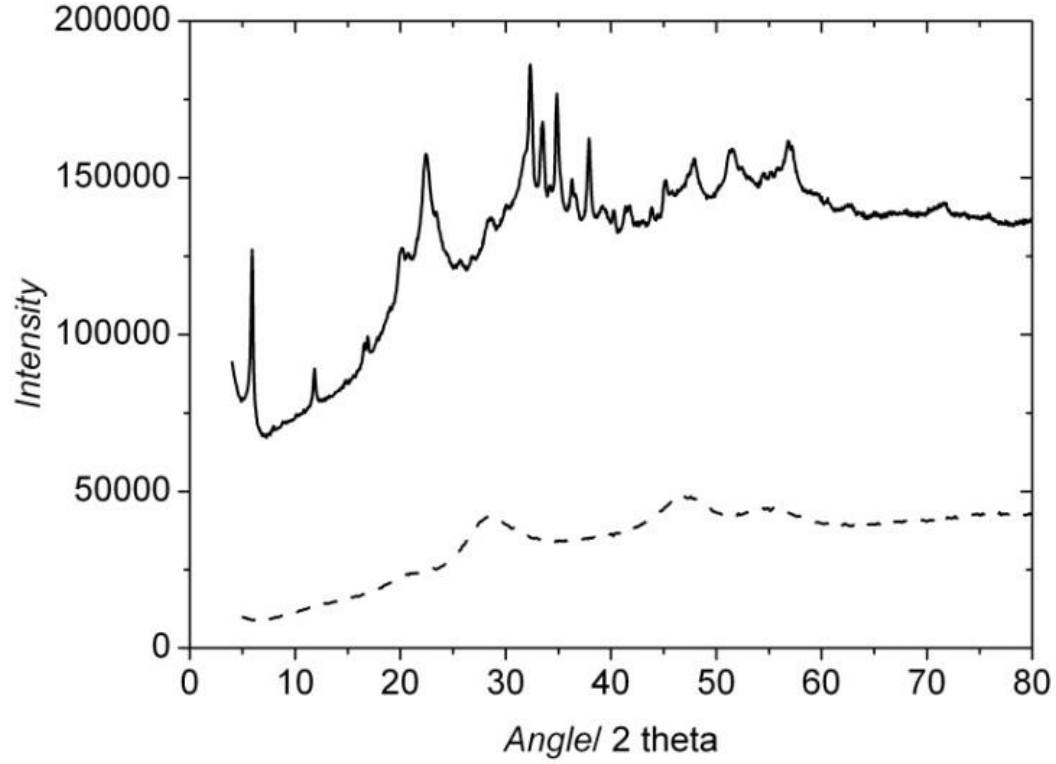

Figure 6.2: XRD patterns of MUA stabilised CIS QDs dried within one hour of synthesis and stored in a nitrogen glove-box (dashed line) and after 24 hours (solid line).

As described in section 2.1.2 the synthesis technique for these QDs used a four-fold molar excess of MUA in relation to the copper and indium sources. Given that the excellent colloidal stability and high crystallinity of the hydrophobic DDT stabilised CIS QDs presented in chapter 3 is attributed to the large molar excess of DDT during QD fabrication, it would be plausible that a four-fold molar quantity of surfactant is not enough to promote full surface coverage, exposing the surface to oxidation and degradation.

6.1.2 Mercaptoundecanol stabilised $CuInS_2$ QDs

The morphology of MUD stabilised CIS QDs, as described in section 2.1.3, was probed by TEM and STEM, as shown in Figure 6.3.

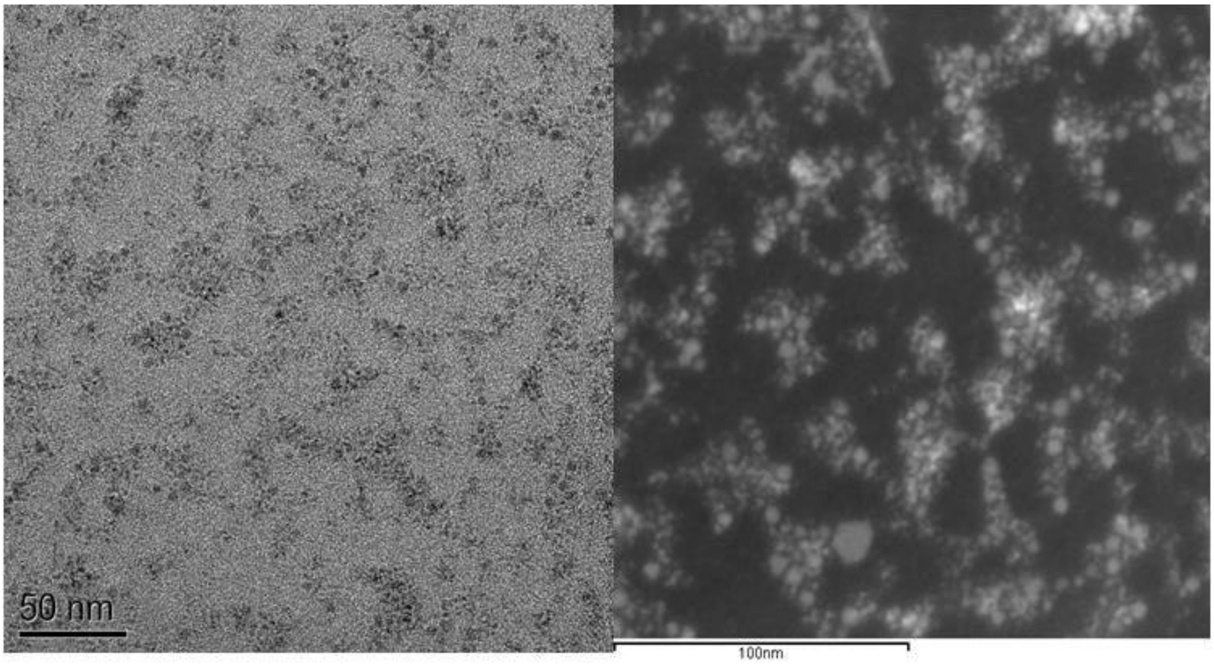

Figure 6.3: TEM (left) and STEM (right) images of CIS/MUD QDs.

The PL and UV/vis spectra of the QDs are shown in Figure 6.4. The PL spectral peak generally resembles that of the DDT stabilised CIS QDs in both spectral position and shape. The absorption spectrum, however, differs in that the first excitonic transition feature is significantly more defined, indicating a narrow size distribution. The Stokes shift in this sample is approximately 170 nm (0.76 eV), significantly larger than DDT stabilised CIS/ZnS QDs.

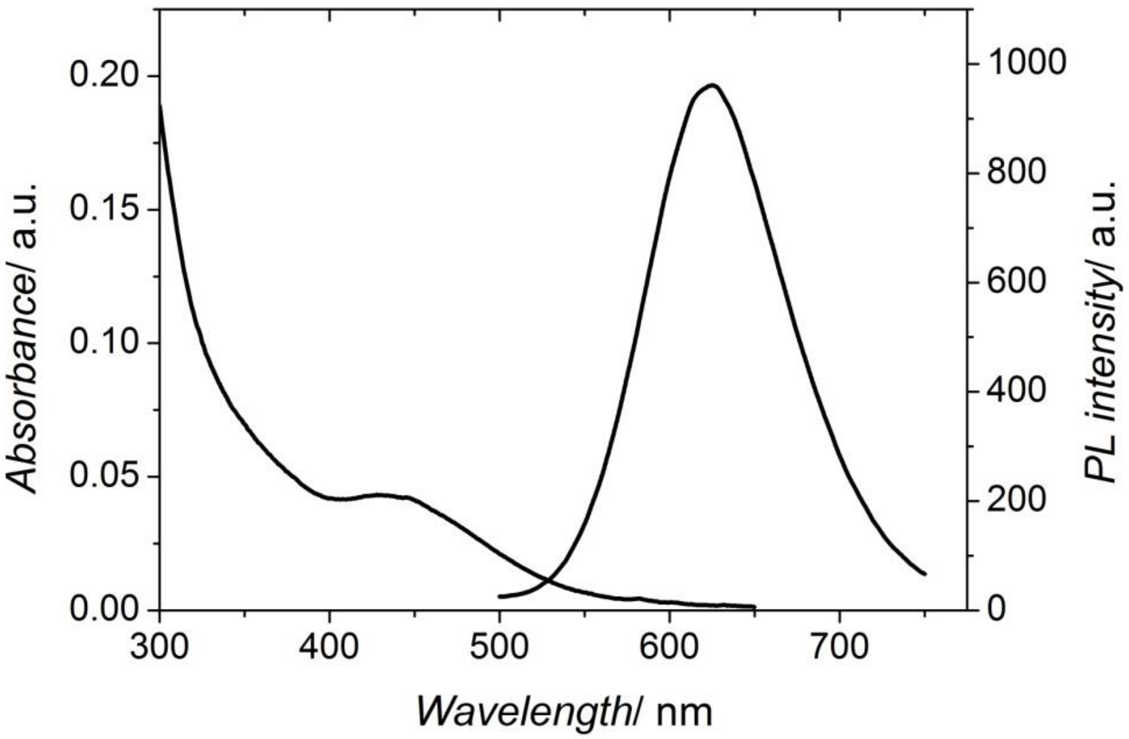

Figure 6.4: PL and absorption spectra of MUD stabilised CIS QDs in methanol.

The MUD stabilised QDs are an ideal system to probe the effect of [Cu]:[MUD] molar ratio during synthesis on the quality of the product CIS QDs. The integrated area of the PL spectral peak, normalised to the absorption at the excitation wavelength, served as a measure of PL efficiency. The molar excess of MUD in relation to Cu was varied between a factor of 4 and 16, whilst all other experimental conditions were kept constant within experimental error. As shown in Figure 6.5, a positive correlation between increasing PL efficiency and an increased molar excess of MUD was observed. The PL enhancement appears to reach a limit before a [Cu]:[MUD] value of 1:10 suggesting that this concentration is the minimum required for complete surface coverage. Assuming a 100% reaction yield and a CIS QD size of 3 nm (based on the PL spectral peak position), the ligand packing density on the QD surface for a tenfold molar excess of MUD over Cu is estimated to be approximately 4 per nm^2. This works out at approximately 60 ligands per QD and seems reasonable for an optimally packed monolayer of MUD on CIS.

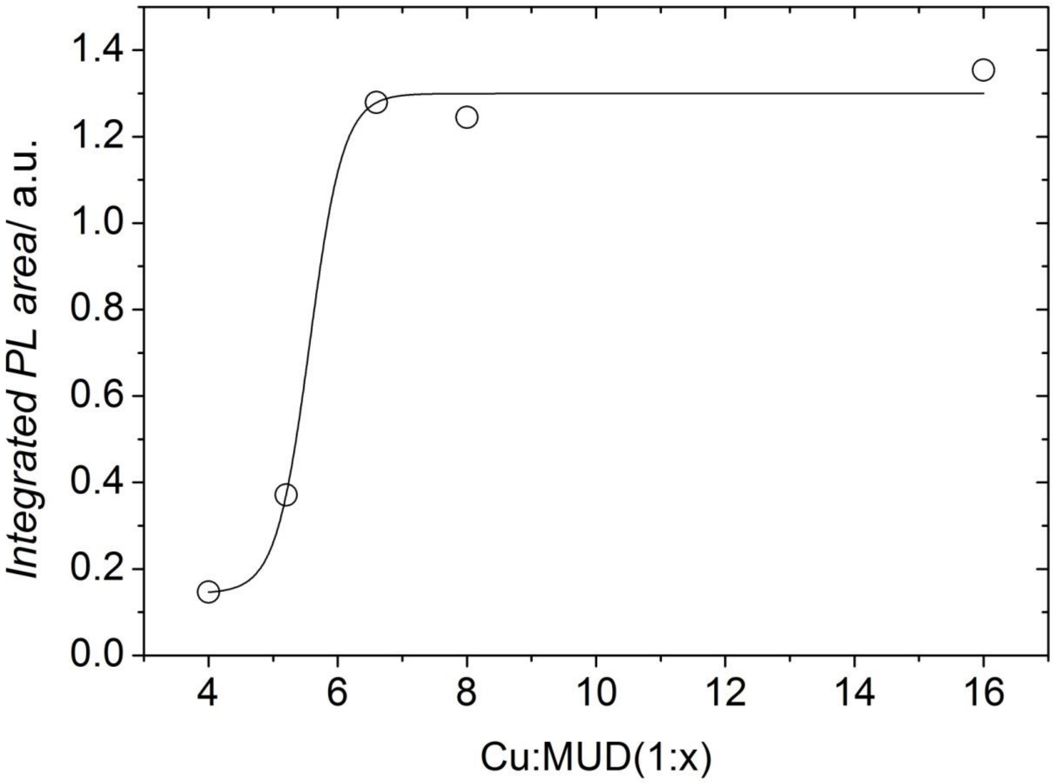

Figure 6.5: Plot of the relative integrated area of the PL spectral peak of MUD stabilised CIS QDs synthesised with varying copper : MUD molar ratios. The black line is a guide to the eye only.

The effect of the Cu to In molar ratio [Cu]/[In] during the synthesis reaction on the PL efficiency of the CIS QDs was examined. The relative quantites of In and MUD were kept constant, with indium:MUD equal to 1:10. The optimal value of [Cu]/[In] at the synthesis stage for PL performance has been reported elsewhere to be approximately 0.7 and it is clear that Cu-poor CIS QDs exhibit enhanced PLQY compared to stoichiometric samples.

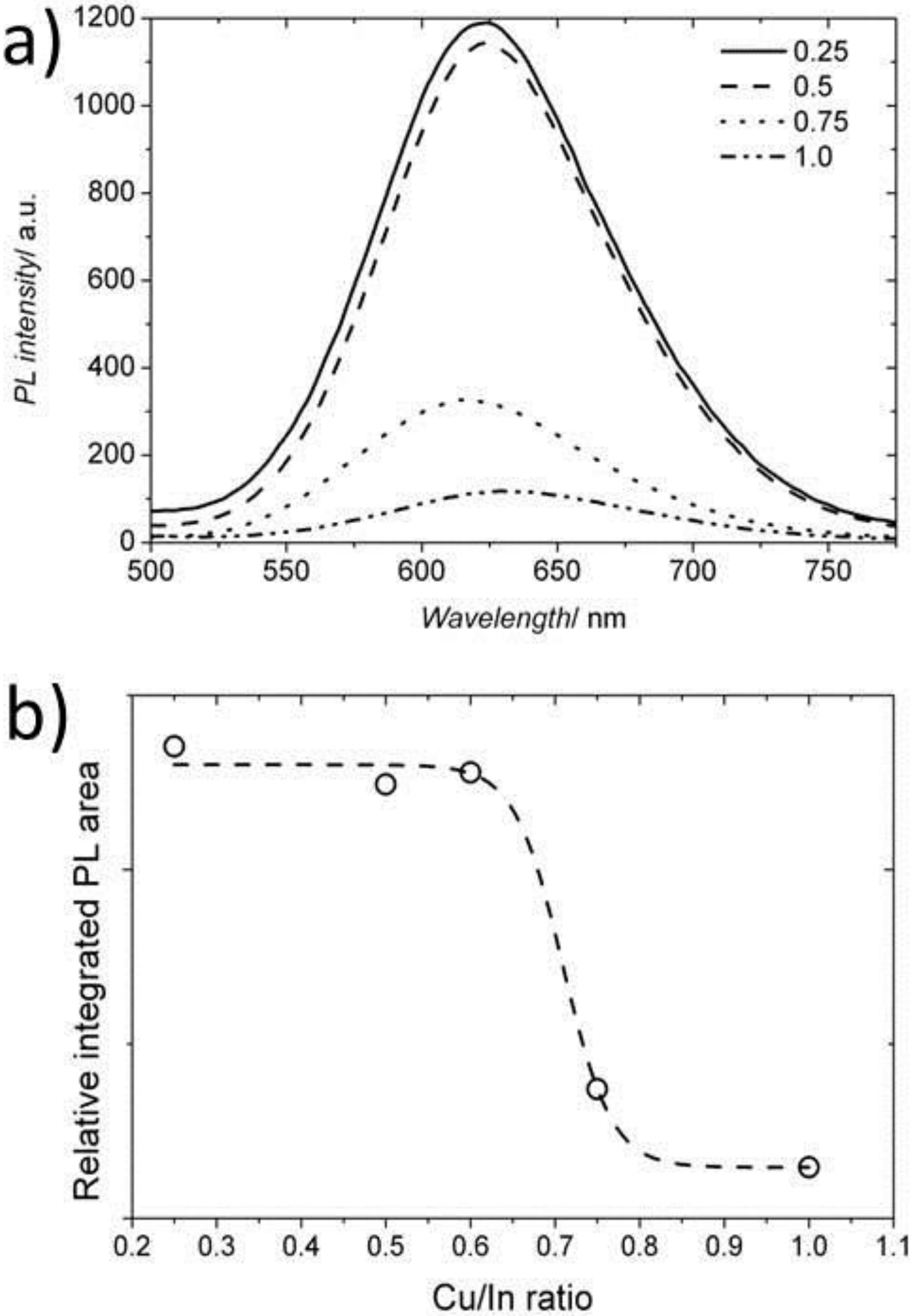

Figure 6.6: a) PL spectra of MUA stabilised CIS QDs synthesised over a range of Cu/In molar ratios; b) Plot of the integrated area of the PL spectral peaks in a) against the concentration of copper relative to indium ([Cu/[In]]. The dashed line is a sigmoidal fit serving as a guide for the eye.

The PL spectra shown in Figure 6.6 illustrate the same trend for the MUD stabilised CIS QDs synthesised here. The PL intensity normalised to the absorption spectrum increases as [Cu]/[In] is reduced. Unlike in the literature, the PLQY does not degrade when [Cu]/[In] is reduced below 0.5 [170]. This is most likely due to variations in synthesis technique. Figure 6.7 shows the absorption at

400 nm of each QD suspension from Figure 6.6. The absorption of the QDs synthesised decreases as the relative concentration of copper is reduced, suggesting lower concentrations and therefore a diminishing reaction yield; rather than forming increasingly Cu-poor CIS QDs, a limit at [Cu]/[In] ~ 0.7 is reached. Reducing the concentration of Cu beyond this point appears to starve the reaction of copper.

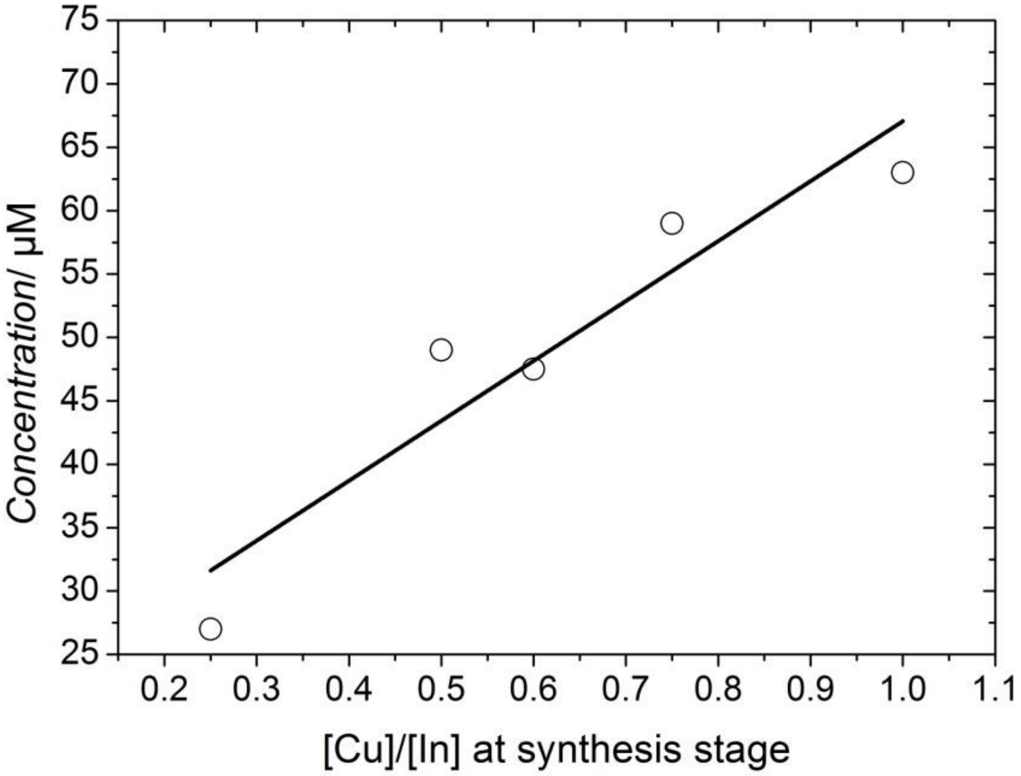

Figure 6.7: The concentration of MUD stabilised CIS/ZnS QDs synthesized with varying [Cu]/[In] values, corresponding to the data shown in Figure 6.6 b).

Only slight spectral shifts were observed (< 10 nm), with no correlation to Cu/In ratio. Therefore this is likely due to sample-to-sample variation in synthesis parameters, rather than an effect of off-stoichiometry, as the band gap of CIS QDs is expected to be stable against off-stoichiometry.

6.2 CuInS$_2$/ZnS/PMAL-d QD/amphipol Hybrid Nanoparticles

6.2.1 Purification

Encapsulation of CIS/ZnS QDs with the zwitterionic, amphiphilic polymer (amphipol) PMAL-d was achieved non-covalently. The solvent evaporation method discussed in section 2.1.4 produced dried nanoparticles (NPs) that were easily re-suspended in deionised water, although the suspension was cloudy, indicating an excess of free unreacted PMAL-d in solution.

Two methods for removal of excess polymer from solution were evaluated. Firstly, the absorption spectrum of the waste solution after each iterative stage of centrifugation in the DCD cleaning method (see section 2.9) was recorded. The absorption at two wavelengths (300 nm and 350 nm) decayed exponentially over subsequent iterations at 3000 rpm, with identical decay constants determined for each wavelength (Figure 6.9):

$$t_{350} = 0.61 \pm 0.04 \tag{6.1a}$$

$$t_{300} = 0.66 \ \pm 0.04 \tag{6.1b}$$

The rate at which the absorption decays over subsequent centrifugations suggests that 3 iterations are required to remove ~ 90% of the unbound PMAL-d in solution.

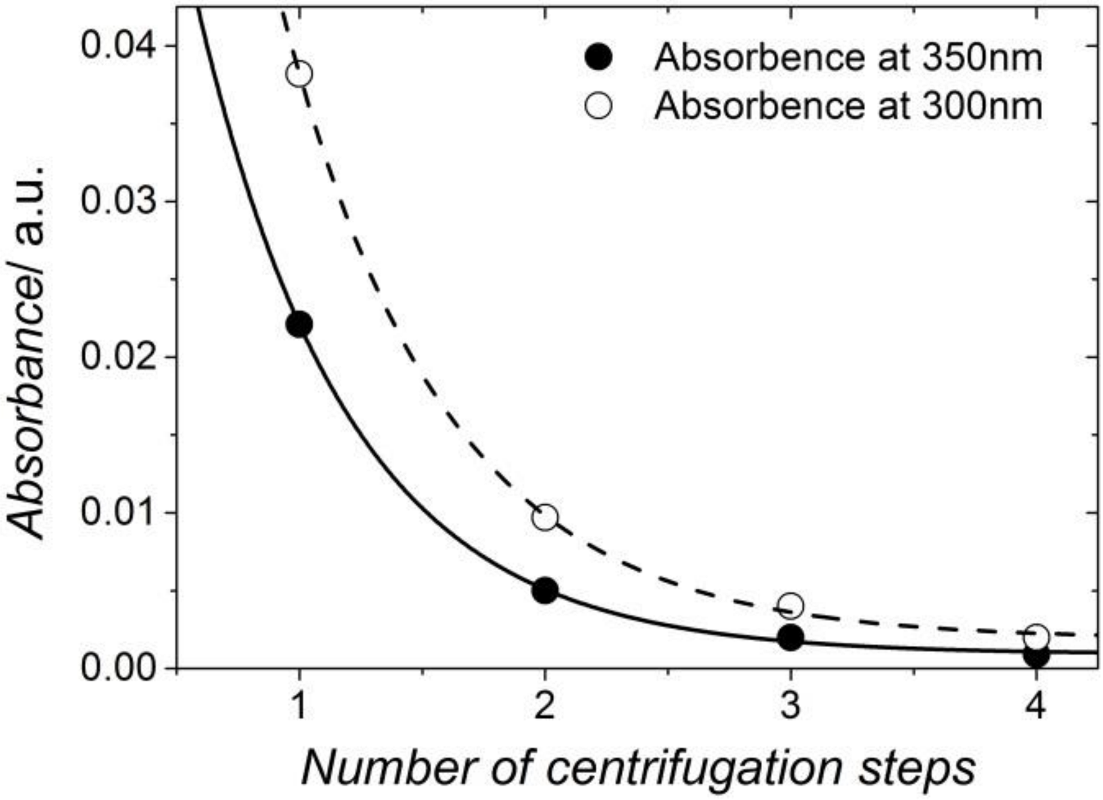

Figure 6.9: The measured absorbance at 350 nm (filled circles) and 300 nm (hollow circles) of the decanted waste solution after each filtration by centrifugation. The data is fit with exponential decay functions.

A second purification method, tangential flow filtration (TFF), was evaluated. The potential superiority of this method is described in section 2.1.4, and was tested against dead-end filtration by comparing the efficiency and absolute cleaning ability of each method.

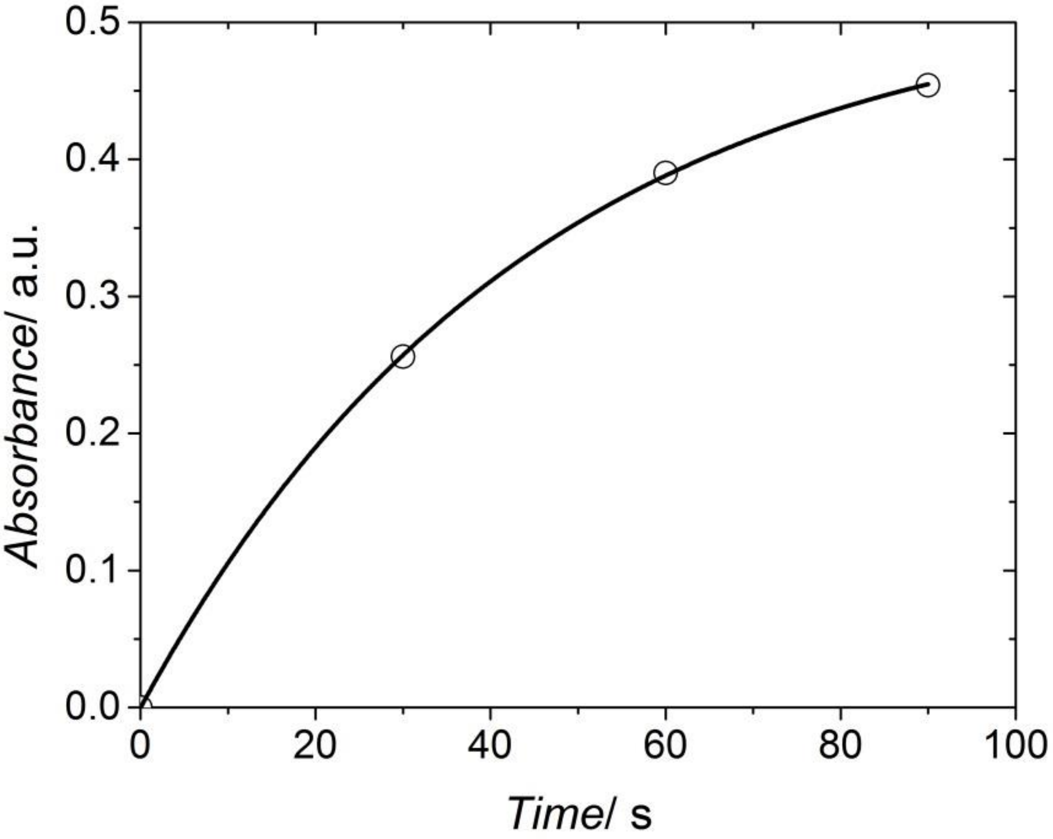

Figure 6.10 The cumulative absorbance of the permeate at 250 nm from TFF method for CIS/ZnS/PMAL-d NPs. The black line represents an exponential fit.

The decay constant determined by the exponential fit to the data was:

$$t_{225} = 44.4 \pm 1.2 \tag{6.2}$$

A comparison between the DCD and TFF filtration methods shows that in terms of efficiency, assuming each centrifugation step in DCD takes 30 minutes to prepare and perform, the two techniques are comparable. The advantage of TFF therefore lies in its economy rather than efficiency.

6.2.2 Characterisation of Colloidal Stability

The CIS/ZnS/PMAL-d QD/Amphipol hybrid NPs, synthesised as reported in section 2.1.4, were visualised with HR-TEM and HAADF. The HR-TEM images in Figure 6.11 show both single QDs and clusters of QDs. This is consistent with drying effects reported for drop-cast colloidal QD suspensions and does not have any implications for the ability of the fabrication method to produce single QDs encapsulated in polymer. The observation of single QDs in the HR-TEM images however suggest that the method is in fact successful. The purification process is thorough enough that it cannot account for the large number of single QDs observed.

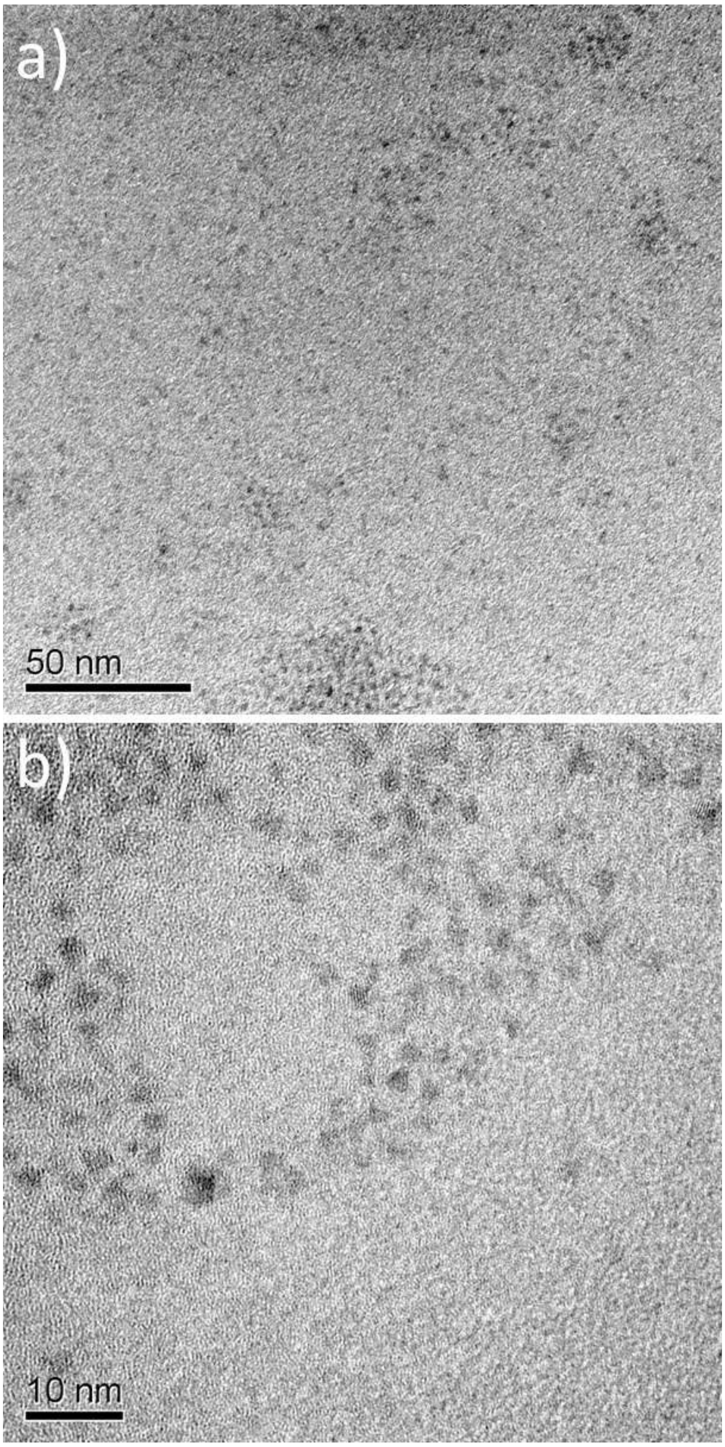

Figure 6.11: HR-TEM images of CIS/ZnS/PMAL-d NPs; a) low magnification image and b) high magnification image.

The size of the NPs in solution was measured by DLS over a wide range of pH (pH 3-11), and as illustrated in Figure 6.12 was found to average 13.0 ± 0.7 nm. This value does not reflect the physical size of the NPs, but their hydrodynamic radius (Stokes radius) and therefore solvent-NP interactions must be considered.

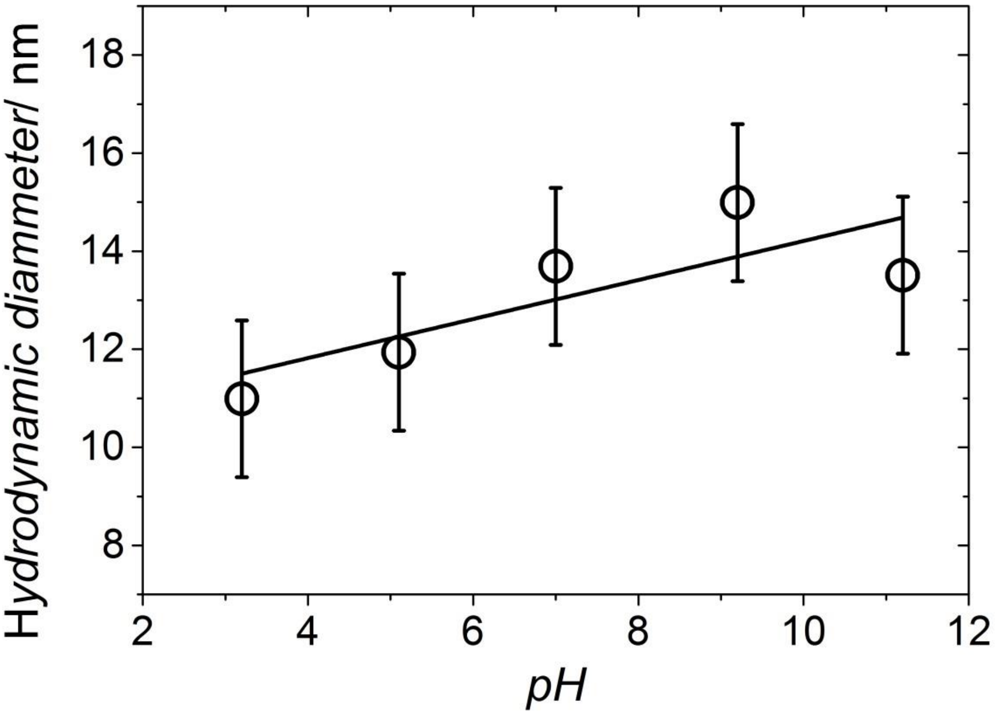

Figure 6.12: The hydrodynamic radius of CIS/ZnS/PMAL-d NPs, as measured by DLS, over a range of solution pH. The black line is a weighted linear fit with no constraints.

The small distribution around the mean hydrodynamic radius demonstrates the ability of the zwitterionic NPs to form a highly stable colloid. The highly charged surface was confirmed by measuring the zeta potential across the same pH range, as shown in Figure 6.13.

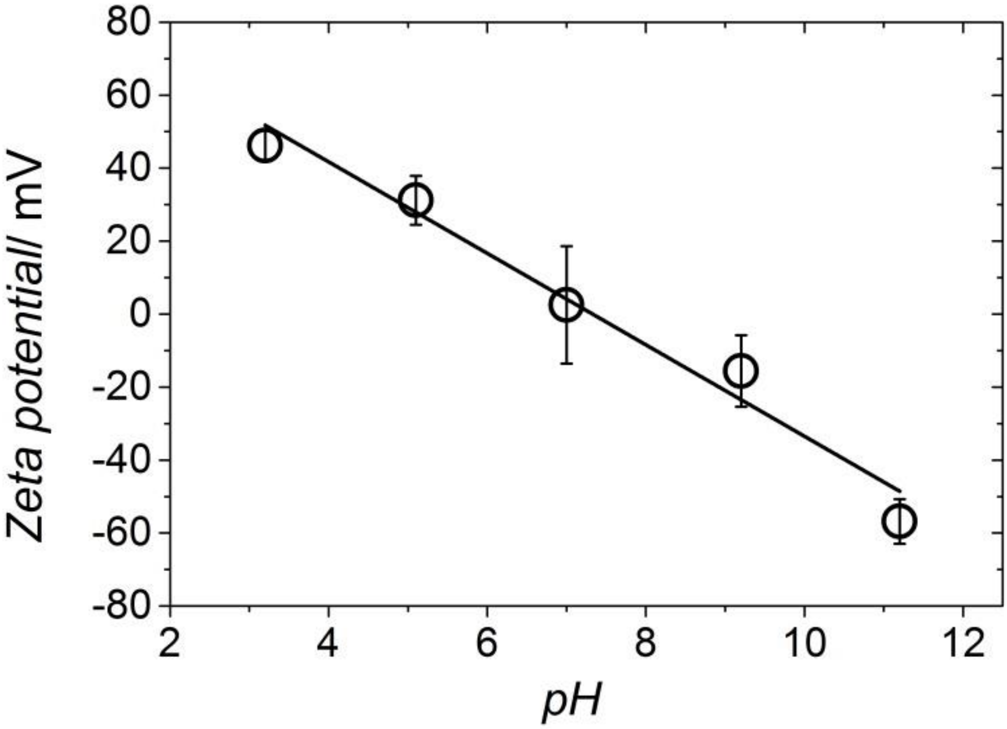

Figure 6.13: The surface zeta potential of CIS/ZnS/PMAL-d NPs over a range of pH. The black line is a weighted linear fit with no constraints.

The zwitterionic nature of PMAL-d provides electrostatic repulsion either side of an isoelectric point at pH 7.1 ± 0.7: at low pH the tertiary amide (see Figure 2.4) is protonated and exhibits a positive charge, providing inter-NP repulsion; and at high pH the carboxylic acid groups become deprotonated and carry a negative charge (Figure 2.4). This is clearly observed in zeta potential measurements of the surface charge across the same pH range and is shown in Figure 6.13.

The absorption and PL spectra of CIS/ZnS/PMAL-d NPs are shown in Figure 6.14 a). Both are consistent with the spectra shown in Chapter 3 for the DDT stabilised CIS/ZnS QDs, demonstrating broad features and a large Stokes shift. Even in the absence of self-quenching between multiple QDs within large NPs, a small decrease in the relative PL intensity is expected in the polymer encapsulated sample purely due to increased absorption by the thicker organic layer. The difference between the refractive indices of water and hexane will also have an effect on the measured PL intensity.

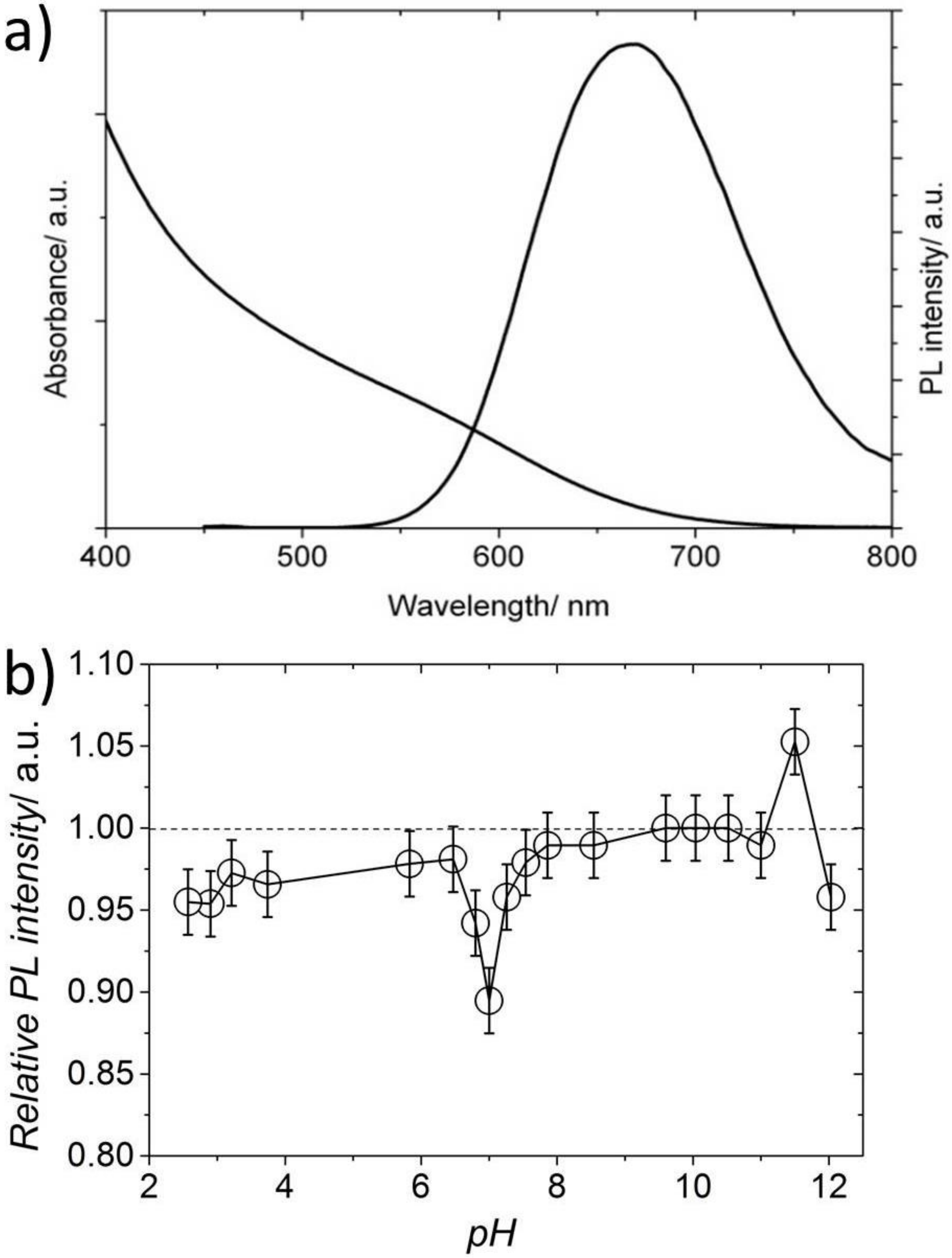

Figure 6.14: a) PL spectrum of typical CIS/ZnS/PMAL-d NPs; and b) integrated area of the PL spectral peak as a function of solution pH, relative to PL intensity at pH 10.5. The black line serves as a guide to the eye and the dashed horizontal line indicates the normalization position.

The PL response of the NPs to the pH of the suspension, expressed as the PL intensity normalised to pH 11.5, is shown in Figure 6.14 b). The PL is sustained between 90-100% of the maximum intensity for the entire pH range, except for between pH 6 to 8, with a minimum at approximately pH

7, in agreement with the measured isoelectric point of the NPs. Since neither of the functional groups is charged in neutral conditions it could therefore be expected that the NPs would aggregate. This does appear to be true to a certain extent, although at neutral pH the PL is still approximately 85% of the maximum at pH 11.5. This apparent lack of aggregation is attributed to stem from steric hindrance between NPs.

To further demonstrate successful polymer encapsulation, the QD:PMAL-d molar ratio was varied during the encapsulation process and the PL intensity of the product NPs was measured, since the PL of the colloidal suspension is generally considered to be a good indicator of stability. A general upwards trend in PL intensity is observed as the relative molar quantity of polymer is increased, which starts to level off at a QD:PMAL-d ratio of 1:20, as can be seen in Figure 6.15. This suggests that the standard ratio used (1:30) is sufficient to produce single QDs encapsulated in PMAL-d.

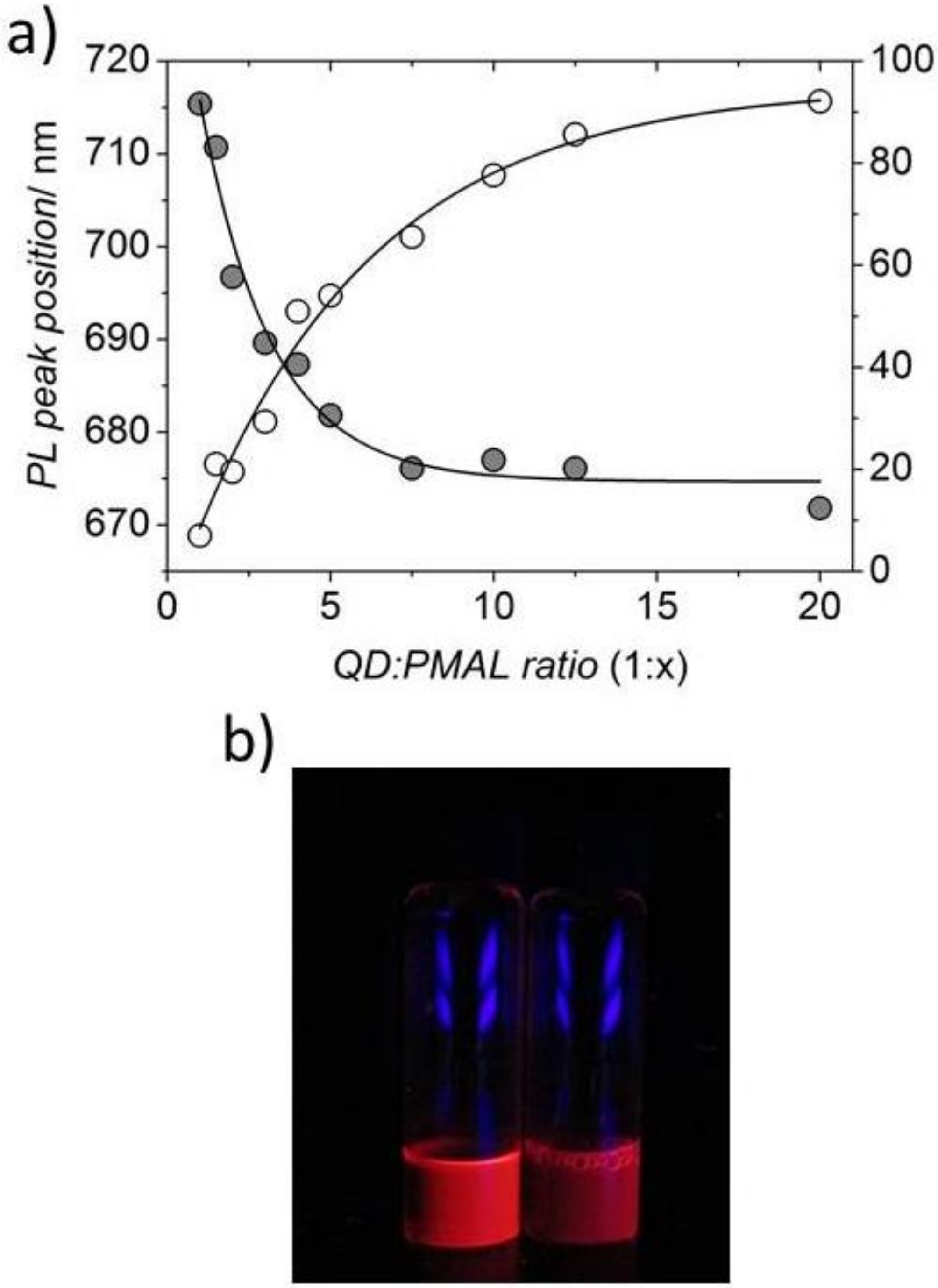

Figure 6.15: a) PL spectral peak position (filled circles) and normalised PL integrated area (hollow circles) of CIS/ZnS/PMAL-d NPs synthesised with varying relative molar quantity of polymer. b) Digital photograph of CIS/ZnS QDs suspended in hexane (left) and CIS/ZnS/PMAL-d NPs suspended in deionised water (right).

A systematic red-shift is obvious as the molar excess of PMAL-d is reduced below tenfold. This observation is consistent with the provided explanation for the concurrent decrease in PL intensity. Self-quenching occurs in colloidal QD suspensions of high concentration by Forster resonant energy transfer. Energy can only be transferred from small to large QDs that are separated by less than 10 nm, thus a global red-shift is observed. The multiple CIS/ZnS QDs within large QD/PMAL-d NPs are likely to be within this range. An example of this phenomenon is illustrated in Figure 6.16. The concentration of CIS/ZnS QDs in hexane was gradually increased as the PL spectrum was repeatedly measured. An initial linear increase with concentration eases as energy transfer processes become dominant; a simultaneous red-shift in peak position and decrease in PL intensity are observed.

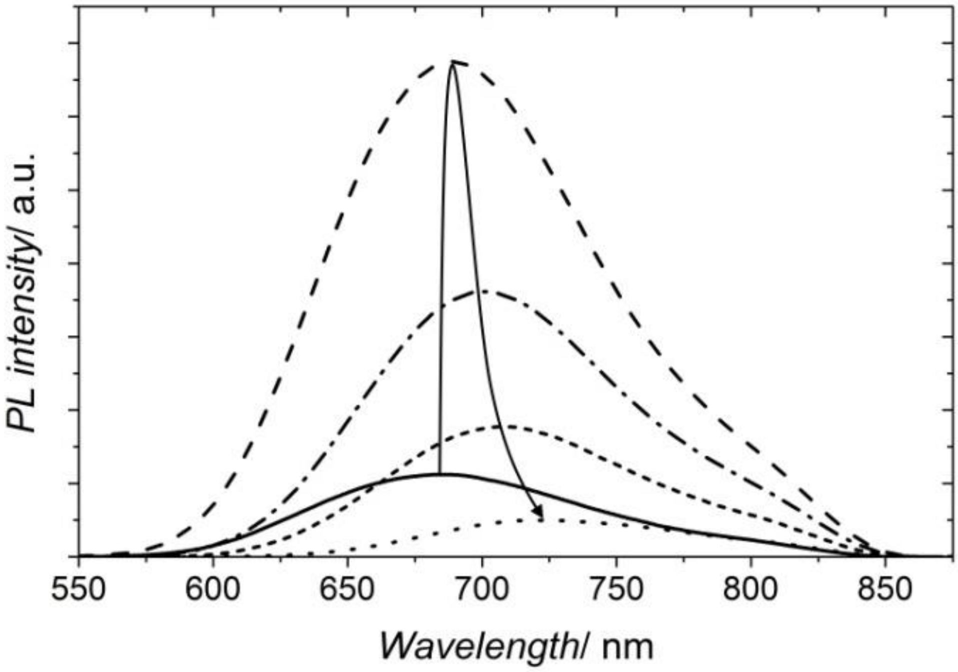

Figure 6.16: Qualitative illustration of the initial increase and subsequent decrease in PLQY of CIS/ZnS QDs suspended in hexane as the solution concentration is increased. The arrow serves as a guide to the eye and highlights the gradual red-shift at high concentrations.

6.2.3 Sensitivity to Metal Ions in Solution

The sensitivity of the CIS/ZnS/PMAL-d NPs against metal ions in solution was tested by performing PL spectroscopy of NP solutions in deionised water in the presence of various biologically relevant metal ions. The relative PL intensity of each solution, relative to a negative control, is shown in Figure 6.17. Copper and iron were the only two metals observed to quench the PL significantly, with copper quenching the PL by nearly 50%.

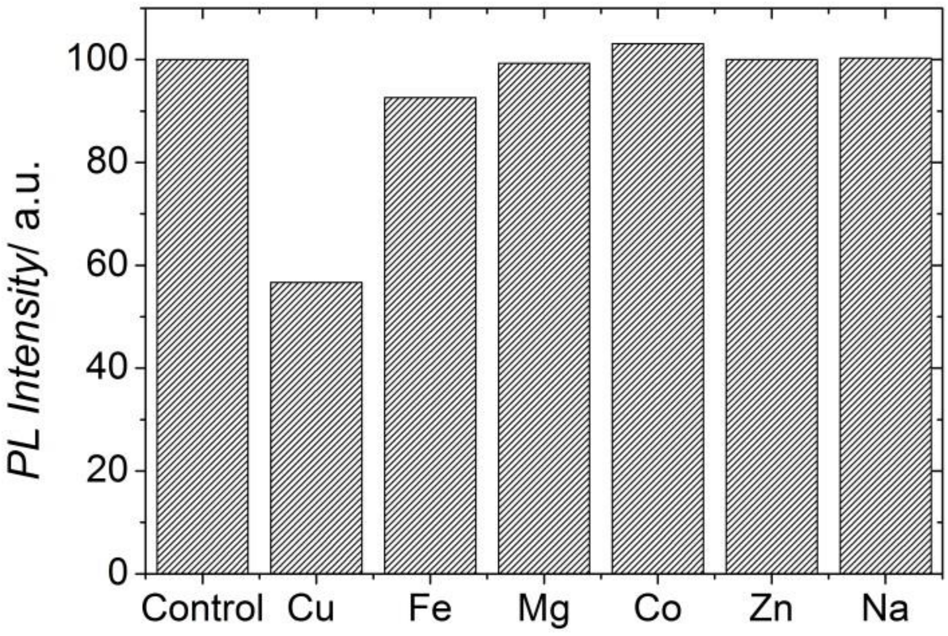

Figure 6.17: The relative PL intensity of CIS/ZnS/PMAL-d NPs suspended in deionised water in the presence of various metal ions.

The possibility that Cu^{2+} ions in solution absorb either the excitation light or the QD photo-emission was determined to be small by taking the absorption spectrum of $CuCl_3$ dissolved in deionised water (Figure 6.18). The overlap between the spectral absorbance of $CuCl_3$ and the emission of CIS/ZnS/PMAL-d NPs is non-zero, and is significant above 700 nm.

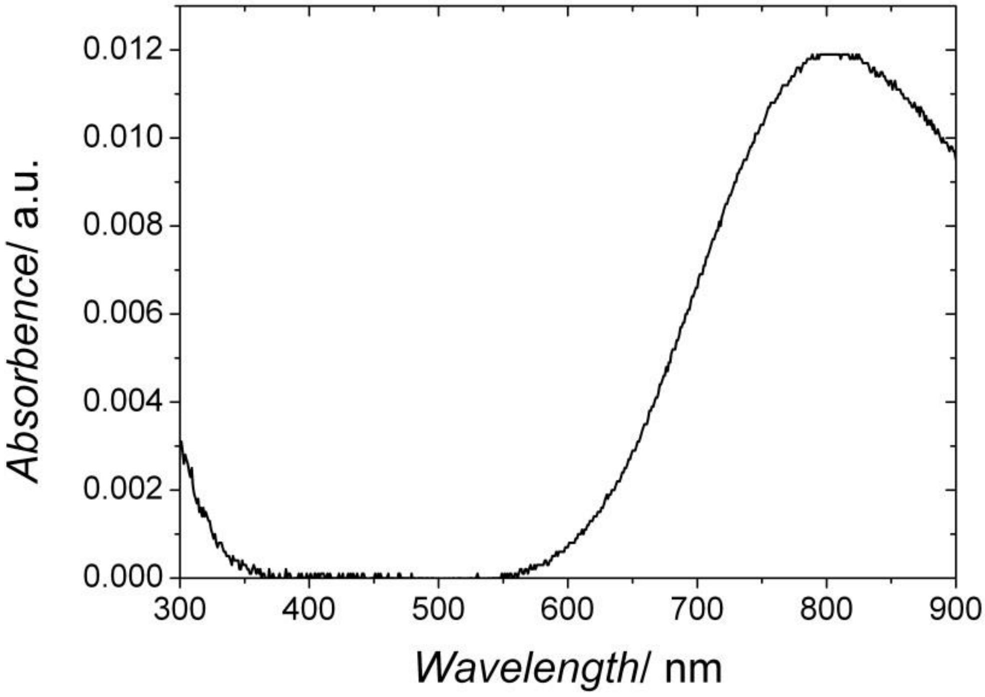

Figure 6.18: Absorption spectrum of $CuCl_3$ in deionised water.

If the absorption of QD PL by $CuCl_3$ was responsible for the dramatic quenching, the PL spectral peak of CIS/ZnS/PMAL-d NPs would be expected to blue-shift significantly as the concentration of Cu in solution is increased, as a result. The static peak position as quenching increases, illustrated by an arrow in the direction of increasing Cu concentration in Figure 6.19 b), shows that this is not the case.

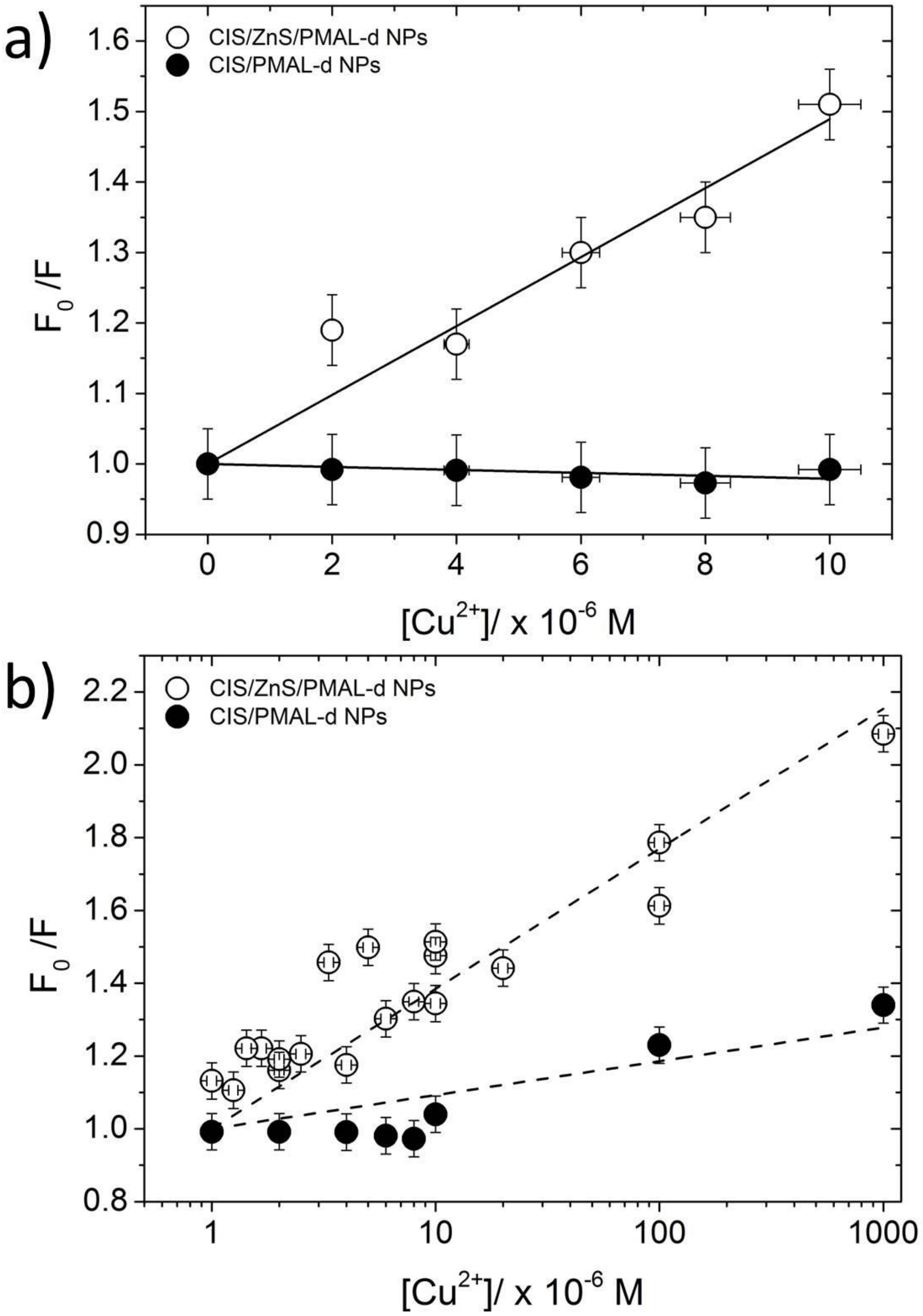

Figure 6.19: a) Relative change in the PL intensity of CIS/ZnS/PMAL-d NPs at 660 nm (hollow circles) and CIS/PMAL-d NPs at 710 nm (filled circles) in the presence of Cu^{2+} ions in solution. a) The low concentration data were fitted (solid lines) to a Stern-Volmer equation (equation 6.2). b) The high concentration data is presented on a logarithmic scale (dashed lines are a guide to the eye).

The concentration-dependent quenching was quantified via the Stern-Volmer relationship [188], which describes a linear relationship between the concentration of the quencher, [Q] and the relative decrease in normalised PL intensity

$$\frac{F_0}{F} = 1 + k_q[Q] \tag{6.2}$$

where F and F_0 are the PL intensity in the presence and absence of the quencher, respectively, and k_q is the Stern-Volmer coefficient of the quencher. This constant describes the quenching rate and depends on the temperature, solvent viscosity and the lifetime of the unquenched PL, and is therefore determined experimentally. The value of k_q for CIS and CIS/ZnS QDs calculated from Figure 6.19 b) were $1.09 \pm 0.02 \times 10^4\ M^{-1}$ and $1.46 \pm 0.02 \times 10^4\ M^{-1}$, respectively.

That the quenching rate for the CIS/ZnS/PMAL NPs is ~ 50% larger than for the CIS/PMAL-d NPs can be understood in the context of physical interactions with the surface. Reports suggest that Cu^{2+} ions can react with the ZnS surface of core-shell QDs creating Cu_xS_y, leading to an increased density of surface trap states. This explanation is consistent with the fact that Cu^{2+} ions have less of a quenching effect on core CIS QDs; CIS QDs already have high densities of surface trap states compared to CIS/ZnS QDs.

The observed quenching effect of $CuCl_3$ is thus more likely to result from physical interactions with the QD surface, despite the thick organic layer. Non-linear quenching is observed in systems where the quencher has limited accessibility to the fluorophore, as is the case for the QDs encapsulated with polymer, and can be modeled by considering a modified Stern-Volmer expression;

$$\frac{F_0}{F_0 - F} = \frac{1}{f_a k_a [Q]} + \frac{1}{f_a} \tag{6.3}$$

where f_a is the fraction of fluorophores which are accessible to the quencher, and k_a is the Stern-Volmer coefficient for the accessible fraction. A plot of $F_0/(F_0 - F)$ against $1/[Cu]$ is shown in Figure 6.20. A linear fit reveals that the y-intercept, which corresponds to $1/f_a$, is 2.7 ± 0.4. This implies that the percentage of the total sample surface area that is accessible to the Cu^{2+} ions was 37 ±

6 %. The combination of the DDT ligands and the thick PMAL-d layer around the CIS/ZnS QDs form an effective barrier to the Cu^{2+} ions in the majority of the sample (~63%); however, ~37% are not fully protected and can allow Cu^{2+} ions to interact with the QDs. The gradient was determined to be $(6.8 \pm 0.9) \times 10^{-6} M$, which corresponds to a Stern-Volmer coefficient for the accessible fraction, k_a, of $(4.0 \pm 0.2) \times 10^{5} M$.

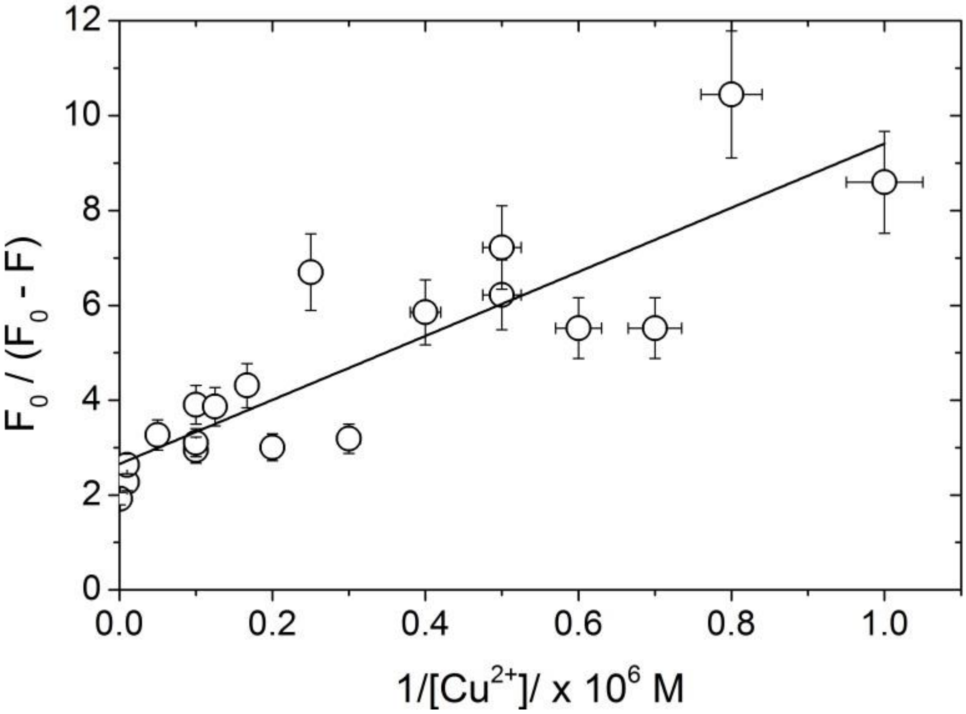

Figure 6.20: Modified Stern-Volmer plot for the data shown in Figure 6.19 a). The black line represents a linear fit, the gradient of which is proportional to the modified Stern-Volmer coefficient and the y-intercept represents the fraction of the total sample surface area accessible to the Cu^{2+} ions.

Quenching of QD fluorescence in the presence of Cu^{2+} ions has been observed for CIS QDs [189] as well as for other QD systems [190, 191] and the quenching mechanism is still under debate. Reports suggest that the Cu^{2+} ions can react with the ZnS surface of core/shell QDs creating Cu_xS_y, which lead to increased density of surface trap states. Another possible explanation is that Cu^{2+} complexes with the QD resulting in a non-radiative recombination pathway. However, for the CIS/ZnS/PMAL-d system, the quenching behavior indicates that only a fraction of the QDs are affected. Quenching caused by complexation of Cu^{2+} at the surface seems less likely given that the organic chemistry of both CIS/ZnS and CIS are identical (and therefore we would expect a similar response to the quencher). It seems more likely that the Cu^{2+} ions react with the ZnS surface and form surface trap states which reduce the PL intensity. This explanation is consistent with the fact that Cu^{2+} ions have less of a quenching effect on core CIS QDs; CIS QDs already have high densities of surface trap states compared to CIS/ZnS QDs.

6.2.4 Assessment of Cytotoxicity by Cell Viability Assays

The *in vitro* effect of CIS/ZnS/PMAL-d NPs on the viability of HaCat cells was assessed by means of an MTT assay and a WST-1 assay. The observed cell viability of the cells was dependent on the chosen assay; the MTT assay seems to artificially exaggerate the reduction in cell viability, probably due to an interaction between the NPs and MTT formazan crystals, similar to that observed with carbon [192-195] and boron nitride [196] nanotubes, in addition to iron oxide [197] and titanium dioxide nanoparticles [198]. Our results reiterate that care has to be taken when interpreting ‘classical’ cell viability assays in the field of nanotoxicology and that multiple cell viability assays must be compared to gain a reliable picture of cytotoxicity.

The results of a MTT assay are shown in Figure 6.21 (white hashed bars). The cells retained a viability greater than 50% up to concentrations of 10 µg/mL and higher. Unbound PMAL-d was also investigated using an identical MTT assay (light grey hashed bars). The viability assay with PMAL-d on its own suggested that the observed CIS/ZnS toxicity at 100 µg/mL can be attributed to PMAL-d, although further studies comparing the cell viability of cells loaded with CIS/ZnS QDs encapsulated in a variety of polymers are needed to confirm this. It is likely, however, that all amphiphilic polymers will have some influence on cell viability.

A further control experiment of thioglycolic acid stabilised CdTe QDs (dark grey bars) showed a loss of viability to levels below 50% at lower concentrations (0.1 µg/mL) than for the CIS/ZnS/PMAL-d NPs, although the cytotoxicity of CIS/ZnS/PMAL-d NPs seems to be comparable to that of TGA stabilised CdTe QDs. However, we note that the health concern with Cd-based QDs is not that they might trigger acute toxic effects, but that accumulation of Cd ions in vital organs, as seen *in-vivo*, may generate severe chronic toxic effects.

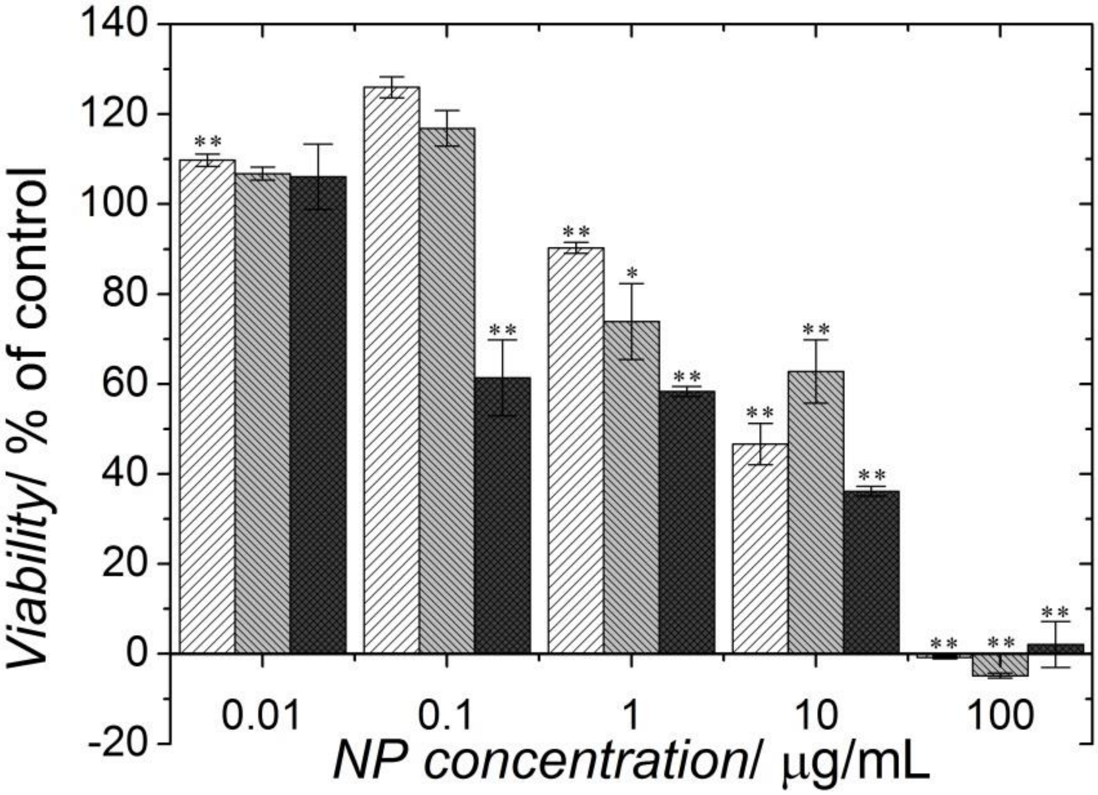

Figure 6.21: MTTcell viability assay results for HaCat cells loaded with CIS/ZnS/PMAL-d NPs (white bars), free PMAL-d (grey bars) and TGA stabilised CdTe/ZnS QDs (black bars). Error bars represent the S.E. (*p < 0.01, **p < 0.001). Incubation conditions for MTT assay are described in section 2.8.

Interestingly, the MTT assay shows a very distinct behavior compared to the WST-1 assay (Figure 6.22). At low concentrations of CIS/ZnS/PMAL-d NPs, viability seems to improve, which is partly caused by the PMAL-d. However, at higher concentrations, viability seems to decrease in a two-step manner. Between 0.1 - 10 µg/mL (20 nM - 200 nM) viability is approximately halved, while at 100 µg/mL (2 µM), a second “step” in viability loss is observed. This is inconsistent with the WST-1 assay which shows full viability up to 10 µg/mL (200 nM). We note that in the MTT assay, either the PMAL-d or QDs remain present in the MTT mixture during the assay. Therefore, we propose that the discrepancy between the two assays is due to artifacts induced by interactions taking place between the NPs and the tetrazolium MTT dye or formazan, a phenomenon which has previously been reported in the literature for various nanostructures [192-198].

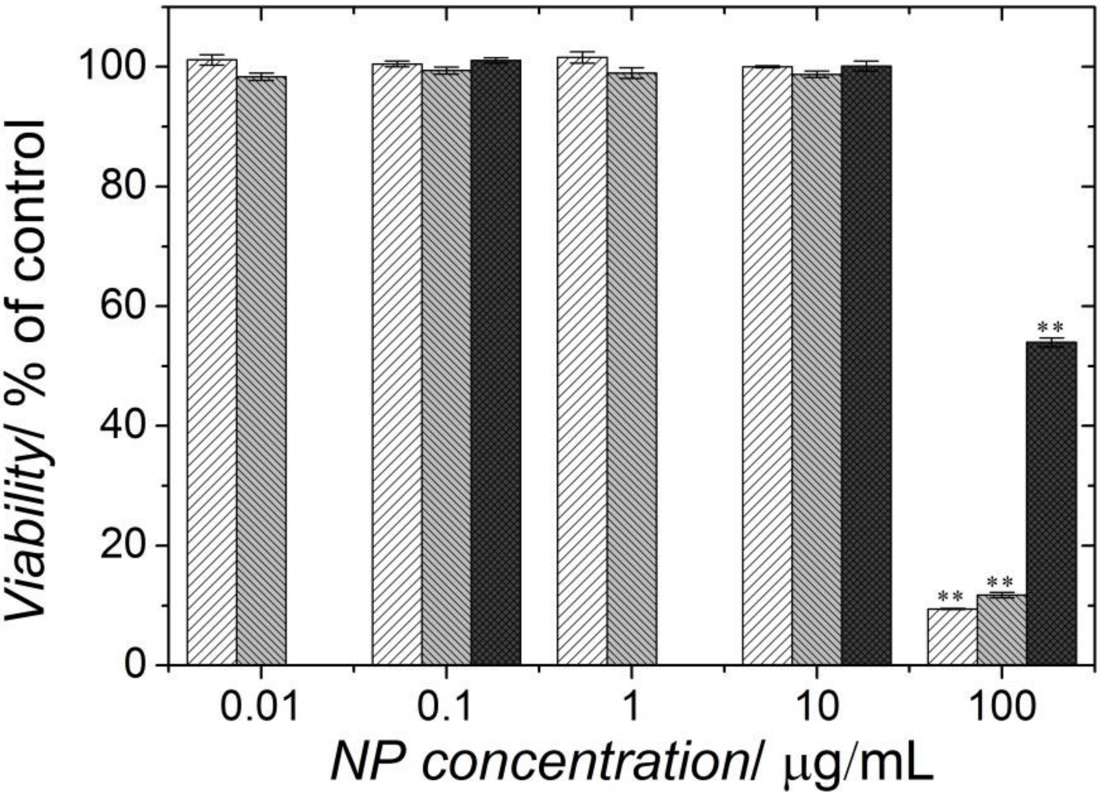

Figure 6.22: Cell viability of HaCat cells loaded with CIS/ZnS/PMAL-d NPs (white dashed bars), free PMAL-d (grey dashed bars) and TGA stabilised CdTe/ZnS QDs (dark grey dashed bars), from a WST-1 cell viability assay. Error bars represent the S.E. (*$p < 0.01$, **$p < 0.001$). Incubation conditions for WST-1 assay are described in section 2.8.

6.3 Concluding remarks

The basic approach to CIS QD synthesis described in chapter 3 produces QDs with a hydrophobic surface that must be transferred to the aqueous phase by post-synthesis surface modification.

Firstly, this work has shown that with different choices of surfactant and solvent alongside slight changes to the reaction conditions, hydrophilic CIS QDs can be synthesised that display comparable optical properties to the state-of-the-art DDT stabilised CIS QDs. Mercaptoundecanoic acid (MUA) and mercaptoundecanol (MUD) were both demonstrated to work in similar synthesis conditions, although MUD appeared to act as a more stable surface coating in aqueous suspensions.

Secondly, a simple polymer encapsulation method for the post-synthesis transfer of hydrophobic CIS/ZnS QDs into the aqueous phase is evaluated in terms of optical performance, colloidal stability and sensitivity to metal ions in solution. The amphiphilic polymer (Amphipol) used is a zwitterionic derivative of poly(maleic anhydride) called PMAL-d. It was shown that if enough polymer is used to encapsulate the CIS/ZnS QDs the PL emission of the QD/polymer hybrid nanoparticles can exceed 90% of the initial PL intensity. Furthermore, the hydrodynamic radius of the NPs was shown to remain small (of the order of 10 nm) and the zwitterionic nature of PMAL-d provides excellent colloidal stability across the entire pH range studied (pH 3-11). In addition the polymer layer was shown to protect the QD surface from quenching by metal ions in solution.

Although the intrinsically low toxicity of CIS QDs in comparison to CdTe QDs is partly counter-acted by the inherent toxicity of PMAL-d, these NPs are suitable for *in-vitro* cell imaging and labeling at concentrations up to 10 µg/mL. In order to further develop this system towards *in-vivo* or clinical applications, more work will be necessary to fine tune the surface chemistry so as to reduce toxicity.

Chapter 7

Conclusions

This thesis is concerned with the synthesis and characterisation of $CuInS_2$ quantum dots (CIS QDs) as a less toxic alternative to the cadmium-based QDs that historically have dominated the literature. CIS is also an extremely interesting material in its own right; complexities which arise from the ternary nature and tetrahedral crystal lattice create an abundance of point defects relative to binary compounds such as CdS and ZnS, which play an integral role in the optical properties. The main applications envisaged for this QD system are as optical probes for the fluorescent imaging of biological systems, as the sensitizing component in the next generation of solar cells and as the emissive components in light-emitting diodes (LEDs). This Chapter concludes the results from the preceding four chapters in the context of these applications.

The principal objectives were to:

1. Fabricate high quality CIS QDs by solvothermal decomposition;
2. Characterise their structural, morphological and compositional properties;
3. Investigate the nature of the highly-radiative long-lived photoluminescence observed in CIS/ZnS (core/shell) QDs;
4. Develop an effective method for measuring the concentration of CIS QDs in suspension;
5. Evaluate alternative synthesis methods and post-synthesis modification steps with the aim of fabricating CIS-based QDs that are stable in the aqueous phase.

In Chapter 3, a well-established general synthesis method from the literature was explored. The technique involves the solvothermal decomposition of equal molar quantities of copper and indium compounds in the presence of a thousand-fold molar excess of dodecanethiol. Compared to many other QD synthesis techniques, such as hydrothermal and microwave-assisted synthesis, this method was evaluated to be quick and straight-forward. Furthermore, the reagents are inexpensive and no harmful bi-products are formed during the reaction.

The product CIS QDs were effectively isolated from the reaction bi-products by an iterative precipitation-centrifugation procedure. The CIS QDs were determined to be approximately stoichiometric by X-ray photoelectron spectroscopy (XPS) and energy-dispersive X-ray spectroscopy. The XPS data however showed an excess of copper and sulfur relative to the EDX data which, considering the inherent surface sensitivity of XPS, suggests a copper and sulfur rich surface. The latter is consistent with the expectation of a self-assembled thiol monolayer on the QD surface.

The crystal structure was analysed by X-ray powder diffraction (XRD) and the zinc-blende tetragonal phase of CIS was identified. The morphology of the CIS QDs as imaged by transmission electron microscopy (TEM) confirmed the presence of tetragonal CIS. The length of the triangular projection in TEM of at least 100 QDs was measured using ‘Image J’ software to determine the ‘size’ of a sample. The range of QD sizes accessible following this method were between 2.5 and 6 nm and the relative standard deviation of the size of the as-synthesised QDs was typically between 0.04 and 0.20, and generally increased with QD size.

The steady-state optical properties of similar CIS QDs (i.e. synthesised by the same method) have been well characterised in the literature and the main observations are replicated here [133-140, 144-148]. The photoluminescence (PL) spectral peak position, as determined by fluorescence spectroscopy, was dependent on QD size, shifting to longer wavelengths with increased synthesis time. The accessible range of emission wavelengths was between approximately 500 nm and 800 nm. Importantly, this enables CIS QDs to be synthesised to emit within the biological window (650 nm – 1200 nm), allowing for deeper penetration of the emitted light through biological tissue.

The CIS QDs demonstrated broadband absorption across the entire visible spectrum with a broad excitonic feature between 500 nm and 600 nm which was also dependent on QD size. The combination of broadband absorption and relatively narrow emission enables the use of these QDs for multiplexed biological imaging; multiple QDs of different sizes (and therefore different PL spectral peak positions) can be excited with the same high energy (UV) source yet emit at different wavelengths, facilitating separate components to be distinctly labelled. The broad absorption of these

QDs matches the visible part of the solar spectrum extremely well; CIS QDs are therefore also excellent candidates for the absorbing component in solar cells.

A large Stoke's shift (up to 135 nm) was consistently measured for the CIS QDs. This is indicative of the involvement of intra-gap states in the radiative recombination and is also a highly desirable property for many optoelectronic applications, for example in QD LEDs, since minimal 'self-absorption' occurs. However, a large Stoke's shift can limit efficiency in photovoltaic applications and can reduce the accessible range of emission wavelengths, compared with band edge emitting QDs.

A systematic comparison with organic dyes of known quantum yield demonstrated that the CIS QDs had a lower quantum yield (< 5 %) compared to those reported for cadmium-based QDs in the literature (up to 90 %) [153, 154]. However, the quantum yield of the CIS QDs is increased by more than a factor of ten upon ZnS 'shell' formation. This observation corroborates similar findings in the literature and is attributed to the suppression of surface trap states, which arise from unsaturated bonds at the QD/solvent interface, and the ultra-fast non-radiative recombination associated with them [133]. Upon ZnS shell formation, a blue-shift of up to 75 nm is observed in the PL spectral peak position. This consistently observed phenomenon is less well understood than the PL enhancement. A leading explanation is that the shell formation mechanism is one of cation exchange, whereby copper and indium atoms at the QD surface are replaced by zinc atoms, effectively reducing the CIS QD 'core' diameter and blue-shifting the PL [135].

Surface treatment with the formation of a ZnS shell is therefore a vital step in order to optimize the optical properties of CIS QDs for both biological imaging and solar harvesting applications: enhancing the PLQY by an order of magnitude enables much 'brighter' emission, meaning that lower doses of QDs are needed to achieve the same signal intensity; and suppression of an ultra-fast decay channel maximises the opportunity to 'capture' excitons before recombination occurs.

In Chapter 4 the excited state dynamics in CIS/ZnS QDs were probed by transient absorption (TA) spectroscopy. A strong negative signal was observed at wavelengths corresponding to the first excitonic transition in the steady-state absorption spectrum indicating a bleaching of the ground state (GSB). The negative band however also stretched out to longer wavelengths and spectral fitting showed that a contribution from stimulated emission (SE) became more significant at higher excitation wavelengths. A broad positive signal either side of the GSB/SE band was attributed to absorption from the conduction band into higher excited states (ESA).

Exponential fits to kinetic cuts at 650 nm and 950 nm, representing the dynamics of the GSB and ESA components, respectively, revealed three decay channels on the ultrafast timescale. The slowest component (27 ps) was assigned to surface trapping and the 1.8 ps component to carrier cooling, in agreement with the literature. The third, fastest component (0.5 ps) was assigned to non-radiative decay from the conduction band into the intra-gap defect state responsible for the observed emission. This result confirmed the involvement of intra-gap states in the excited state dynamics, although provided little information regarding the energetic position of the defect states within the band gap.

In order to investigate further, hole-burning was used to depopulate the emissive state whilst routine TA spectroscopy was used to monitor the response from the GSB, SE and ESA components. Importantly, the SE and GSB signals were reduced significantly (by 45% and 72%, respectively) at the hole-burning position (6 ps) whilst the ESA remained unchanged. Since the ESA signal at 950 nm is associated with absorption from the conduction band, the lack of response to the hole-burning strongly suggests that the conduction band is not the emissive state. In conclusion, therefore, this result not only confirms further the involvement of intra-gap states in the excited state dynamics in CIS QDs but allows us to assign the observed highly radiative PL component to the fraction of electrons that relax from the conduction band into a high-lying, long-lived trap state.

This result is significant for the design of CIS QD-sensitised solar cells (QDSSCs), where the architecture must allow for efficient transfer of electrons from the sensitising material (CIS QDs) into the electrode (typically TiO_2). Typically, the conduction band is assumed to be responsible for the long-lived (>100 ns) PL in CIS QDs [133] yet our results indicate that ultra-fast decay into a high-lying trap states occurs. Therefore, optimally efficient QDSSC architectures must align the band gap of the electrode to these trap states rather than the conduction band.

For biological applications in particular, however, biocompatible surface chemistry can be equally important for successful implementation. The as-synthesised CIS and CIS/ZnS QDs are stabilised with dodecanethiol (DDT) and aggregate in water due to the hydrophobicity of the non-polar surface ligands. This is undesirable since the aggregated QDs self-quench and the PLQY is thus drastically reduced. This thesis attempted to address this concern by modifying the synthesis method outlined in Chapters 2 and 3 to produce hydrophilic CIS QDs by replacing the DDT with polar surfactants such as mercaptoundecanol (MUD) or mercaptoundecanoic acid (MUA). Both alternative synthesis methods produced QDs that were optically comparable to the DDT stabilised CIS QDs. The MUD stabilised CIS QDs showed excellent colloidal stability in methanol however the MUA stabilised CIS QDs were not stable in water, deteriorating significantly over a period of 24 hours.

In Chapter 5 an effective method for measuring the concentration of CIS QDs in suspension was developed in order to enable precise post-synthesis modification steps to be performed. A formula for the molar extinction coefficient as a function of QD size was empirically derived and was shown to provide an accurate means for translating the absorbance, as measured by routine UV/Vis spectroscopy, into QD concentration via the Beer-Lambert law.

In Chapter 6, encapsulation of the CIS/ZnS QDs with a zwitterionic amphiphilic polymer (PMAL-d) was shown to be an effective method for transferring the QDs into the aqueous phase. Self-assembly of the QDs and Amphipol was driven by solvent evaporation, forming hybrid QD/polymer nanoparticles (CIS/ZnS/PMAL-d NPs) that retained up to 95% of the initial PLQY and had a hydrodynamic radius of approximately 13 nm. The NPs were stable against changes in solution pH, due to the zwitterionic nature of PMAL-d, and the thick organic surface coating protected the QDs from quenching by metal ions in solution.

The cytotoxicity of the NPs was evaluated by two cell viability assays (MTT and WST-1). Compared to a control experiment with CdTe QDs, the CIS/ZnS/PMAL-d NPs showed slightly reduced toxicity, which appears to originate from the polymer itself, based on assays performed on cells loaded with free PMAL-d. Importantly, discrepancies between the two separate colorimetric assays indicate that the NPs may react with the MTT formazan crystals producing artificially exaggerated viabilities. This work highlights the importance of conducting multiple assays and of taking care when interpreting their results.

In conclusion, CIS QDs are a widely useful optical material due to their large absorption cross-section and bright emission in the red to NIR region of the spectrum. A well-established synthesis method in the literature was shown to be easily modified to produce CIS QDs with the desired surface chemistry. Furthermore, hydrophobic CIS QDs can be encapsulated with an amphiphilic polymer to provide excellent colloidal stability in the aqueous phase, over a wide pH range and in the presence of Cu^{2+} ions which ordinarily quench the PL.

The defect-tolerant nature of ternary I-III-VI_2 chalcopyrite compounds such as $CuInS_2$ opens up entirely new avenues for control over their optoelectronic properties. For example, the electronic and optical properties of CIS QDs can be controlled by compositional engineering rather than relying solely on quantum size effects. Furthermore, a wide range of off-stoichiometry is accessible, enabling either n-type or p-type CIS to be fabricated, without altering the band gap energy or crystal structure.

This thesis has elucidated the defect-related ultra-fast excited state dynamics in CIS/ZnS QDs by transient absorption spectroscopy and ‘pump-dump-probe’ spectroscopy, demonstrating that the observed PL originates from an electron trapped in a high-lying donor state, most likely In_{Cu} antisites or $[In_{Cu} + Cu_{In}]$ defect complexes, rather than from delocalised electrons in the conduction band. This result has important consequences for all applications of CIS and CIS/ZnS QDs and may provide a basis on which to improve the PLQY of CIS QDs and to enhance the efficiency of solar cell architectures based on CIS QDs.

Chapter 8

Future Work

8.1 Probing the defect population in off-stoichiometric CIS QDs

Given the significant role that defect states play in the optoelectronic properties of CIS QDs, it is desirable to fully understand and characterise the defect population in a given CIS QD suspension in order to optimise the defect-related optical properties. The immediate follow-up work to this thesis would therefore include a systematic investigation into the effects of an off-stoichiometric composition on the excited state dynamics in CIS QDs, as measured by femtosecond transient absorption spectroscopy and the pump-dump-probe scheme discussed in Chapter 4.

In order to evaluate the role which defects have on the optical properties and excited state dynamics, the defect type, location and density must be determined for specific CIS QD suspensions fabricated with varying starting [In]:[Cu] molar ratios. The defect type can be determined by Fourier transform infra-red (FTIR) spectroscopy [199] or electron paramgnetic resonanoce (EPR) spectroscopy [200]. Furthermore, the temperature dependence of IR absorption peaks may be used to determine the activation energy of the defect states and therefore also their intra-gap position.

High magnification abberation corrected scanning transmission electron microscopy (STEM), or ‘superSTEM’, would provide high-resolution and high-magnification TEM images in which defects may be visualised. This would be useful in determining if the defect states are located in the QD interior or at the surface. Electron energy loss spectroscopy (EELS) elemental mapping of Cu and In and may also provide insight into the density and location of defects in CIS QDs [201].

8.2 Synthesis and characterisation of $CuFe_xIn_{1-x}S_2$ QDs for photovoltaic solar cells

A primary conclusion of this thesis was that CIS QDs are excellent candidates for the absorbing component in the next generation of solar cells. However, the band gap of CIS limits their application to the visible and NIR region of the solar spectrum. A similar material with a narrower band gap that could be included in the absorbing layer along with CIS QDs would therefore be required to maximise solar absorption.

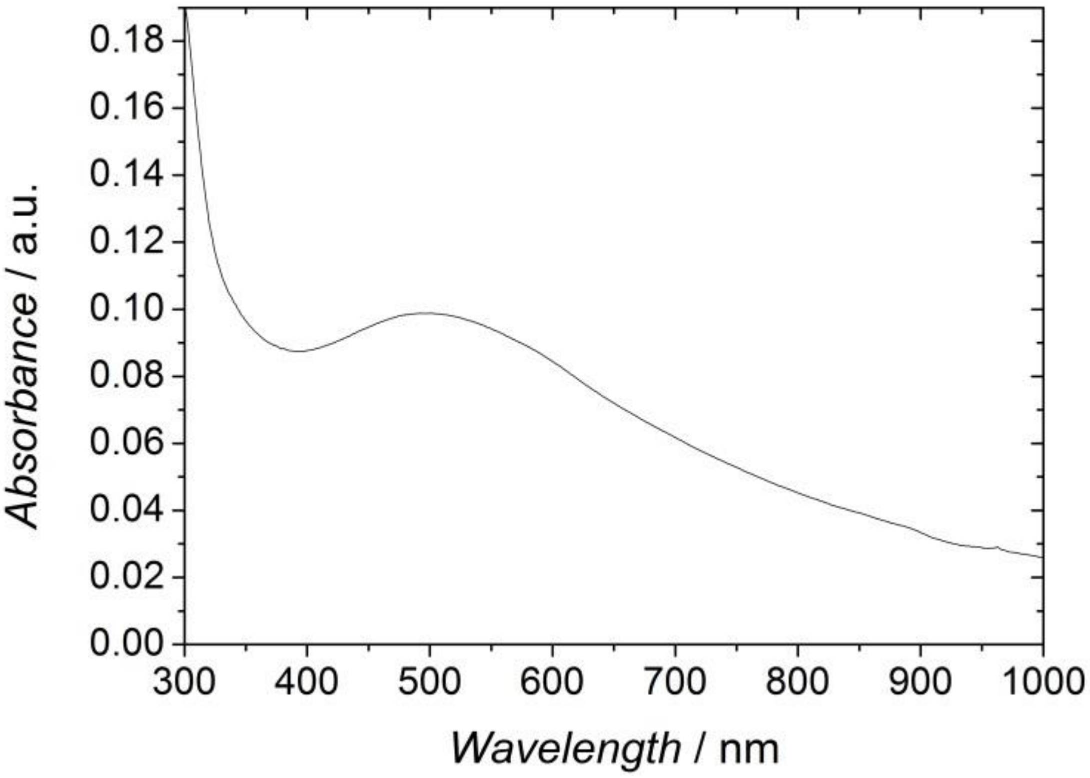

Figure 8.1: Absorption spectrum for CFS NCs in hexane.

$CuFeS_2$ (CFS) has the same crystal structure as CIS and can be synthesised following an almost identical method to that outlined in Chapter 2 for CIS QDs. A typical absorption spectrum for the CFS nanocrystal suspension, as synthesised by this method, is shown in Figure 8.1. A broad absorption band covering the entire visible spectrum is observed. Although the excitonic feature appears to be centred at approximately the same position as the CIS QDs in Chapter 3, the absorption edge stretched much further into the infra-red, showing non-zero absorption at a wavelength of 1000 nm. The photoluminescence (PL) spectrum for the same sample is not shown, since no PL emission was detected in the range accessible to our PL spectrometer. This is consistent with a bulk band gap of approximately 0.6 eV for CFS, corresponding to a band edge PL emission well in the infra-red. In addition, it may be assumed that any PL from the CFS nanocrystals would involve intra-gap states, as demonstrated in this thesis to be the case for CIS QDs, further red-shifting any PL emission.

In addition to the improved optical absorption, in the context of solar harvesting, CFS NCs may prove to be important for alternative applications, once their magnetic properties have been characterised. For example, paramagnetic nanoparticles are used as contrast agents in MRI scans [114] and can also be used for localised hyperthermia treatment of cancers [104].

References

[1] *Handbook on Nanoscience, Engineeering and Technology*, 3rd Ed., Taylor & Francis, 2012

[2] M. R. Bockstaller, *Nanoparticles: From Theory to Application*, John Wiley & Sons, 2005

[3] P. V. Kamat, *J. Phys. Chem. B*, 106, 32, 7729–7744, 2002

[4] R. Rossetti, J. L. Ellison, J. M. Ginson, L. E. brus, *J. Chem. Phys.*, 80, 4464, 1984

[5] T. Trindade, P. O'Brien, N. L. Pickett, *Chem. Mater*., 13, 11, 3843-3858, 2001

(Market estimates from Reuters).

[6] Y. Shirasaki, G. J. Supran, M. G. Bawendi, V. Bulović, *Nature Photonics*, 7, 13-23, 2013

[7] V. I. Klimov, A. A. Mikhailovsky, S. Xu, A. Malko, J. A. Hollingsworth, C. A. Leatherdale, H. J. Eisler, M. G. Bawendi, *Science*, 13, 290, 5490, 314-317, 2000

[8] A. G. Midgett, J. M. Luther, J. T. Stewart, D. K. Smith, L. A. Padilha, V. I. Klimov, A. J. Nozik, M. C. Beard, *Nano Lett*., 13, 7, 3078–3085, 2013

[9] V. Biju, T. Itoha, M. Ishikawaa, *Chem. Soc. Rev*., 39, 3031-3056, 2010

[10] B. R. Masters, *The Development of Fluorescence Microscopy*, John Wiley & Sons, 2010

[11] E. Petryayeva, W. R. Algar, I. L. Medintz, *Applied spectroscopy*, 67, 3, 215-252, 2013

[12] F. Helmchen, W. Denk, *Nature methods*, 2, 12, 932-940, 2005

[13] P. G.Bush, D. L. Wokosin, A. C. Hall, *Frontiers in bioscience*, 12, 2646, 2007

[14] W. Becker, *Journ. microscopy*, 247, 2, 119-136, 2012

[15] S. W. Hell, J. Wichmann, *Opt. lett*., 19, 11, 780-782, 1994

[16] U. Resch-Genger, M.Grabolle, S. Cavaliere-Jaricot, R. Nitschke, T. Nann, *Nature methods*, 5, 9, 763-775, 2008

[17] B. A. Kairdolf, A. M. Smith, T. H. Stokes, M. D. Wang, A. N. Young, S. Nie, *Ann. rev. anal. chem.*, 6, 1, 143, 2013

[18] P. Zrazhevskiy, M. Sena, X. Gao, *Chemical Society Reviews*, 39, 11, 4326-4354, 2010

[19] E. B. Voura, J. K. Jaiswal, H. Mattoussi, S. M. Simon, *Nature medicine*, 10, 9, 993-998, 2004

[20] J. Sun, E. M. Goldys, *The Journal of Phys.Chem. C*, 112, 25, 9261-9266, 2008

[21] M. Booth, A. P. Brown, S. D. Evans, K. Critchley, *Chem. Mat.*, 24, 11, 2064-2070, 2012

[22] D. R. Larson, W. R. Zipfel, R. M. Williams, S. W. Clark, M. P. Bruchez, F. W. Wise, W. W. Webb, *Science*, 300, 5624, 1434-1436, 2003

[23] W. C. Chan, D. J. Maxwell, X. Gao, R. E. Bailey, M. Han, S. Nie, *Curr. opin. biotech.*, 13, 1, 40-46, 2002

[24] X. He, J. Gao, S. S. Gambhir, Z. Cheng, *Trends in molecular medicine*, 16, 12, 574-583, 2010

[25] G. Oberdörster, E. Oberdörster, J. Oberdörster, *Env. health persp.*, 823-839, 2005

[26] S. J. Soenen, P. Rivera-Gil, J. M. Montenegro, W. J. Parak, S. C. De Smedt, K. Braeckmans, *Nano Today*, 6, 5, 446-465, 2011

[27] B. A. Rzigalinski, J. S. Strobl, *Toxicology and applied pharmacology*, 238, 3, 280-288, 2009

[28] V. Brunetti, H. Chibli, R. Fiammengo, A. Galeone, M. A. Malvindi, G. Vecchio, P. P. Pompa, *Nanoscale*, 5, 1, 307-317, 2013

[29] S. Prabakar, A. Shiohara, S. Hanada, K. Fujioka, K. Yamamoto, R. D. Tilley, *Chem. Mat.*, 22, 2, 482-486, 2010

[30] Y. Zhong, F. Peng, F. Bao, S. Wang, X. Ji, L. Yang, Y. He, *J. Am. Chem. Soc*., 135, 22, 8350-8356, 2013

[31] A. Shiohara, S. Prabakar, A. Faramus, C. Y. Hsu, P. S. Lai, , P. T. Northcote, R. D. Tilley, *Nanoscale*, 3, 8, 3364-3370, 2011

[32] H. Wang, S. T. Yang, A.Cao, Y. Liu, *Accounts of chemical research*, *46*, 3, 750-760, 2012

[33] T. Pons, E. Pic, N. Lequeux, E. Cassette, L. Bezdetnaya, F. Guillemin, B. Dubertret, *ACS Nano*, 4, 5, 2531-2538, 2010

[34] K. T. Yong, I. Roy, R. Hu, H. Ding, H. Cai, J. Zhu, P. N. Prasad, *Integrative Biology*, 2, 2-3, 121-129, 2010

[35] J. E. Jaffe, A. Zunger, *Phys. Rev. B*, 28, 10, 5822, 1983

[36] H. Zhong, Z. Bai, B. Zou, J. Phys. Chem. Lett., 3, 21, 3167-3175, 2012

[37] C. Kittel, *An Introduction to Solid State Physics*, John Wiley & Sons, 8th Edition, 2004

[38] H. P. Myers, *Introductory Solid State Physics*, 2nd Ed., Taylor & Francis, 1997

[39] G. Wannier, *Phys. Rev*., 52, 3, 191, 1937

[40] J. Frenkel, *Phys. Rev*. 37, 17, 1931.

[41] L. E. Brus, *J. Chem. Phys.*, 80, 4403, 1984

[42] L. E. Brus, *IEEE J. Quantum Elec*., 22, 9, 1909-1914, 1986

[43] J. Vidal, S. Botti, P. Olsson, J. F. Guillemoles, L. Reining, Phys. rev. lett., 104, 5, 056401, 2010

[44] D. M. Kim, *Introductory Quantum Mechanics for Semiconductor Nanotechnology*, 1st Ed., Wiley VCH, 2010

[45] J. I. Pankove, *Optical Processes in Semiconductors*, Dover, 1971.

[46] D. Ricard, M. Ghanassi, M. C. Schanne-Klein, *Opt. Commun., 108*, 311-318, 1994

[47] D. A. Wheeler, J. Z. Zhang, *Adv. Mat*., 25, 21, 2878-2896, 2013

[48] U. Bockelmann, G. Bastard, *Phys. Rev. B*, 42, 14, 8947, 1990

[49] V. I. Klimov, D. W. McBranch, C. A. Leatherdale, M. G. Bawendi, *Phys. Rev. B*, 60, 19, 13740, 1999

[50] O. Verzelen, R. Ferreira, G. Bastard, *Phys. Rev. lett*., 88, 14, 146803, 2002

[51] M. I. Vasilevsky, E. V. Anda, S. S. Makler. *Phys. Rev. B*, 70, 035318, 2004

[52] V. I. Klimov, A. A. Mikhailovsky, D. W. McBranch, C. A. Leatherdale, M. G. Bawendi, *Science*, 11, 287, 5455, 1011-1013, 2000

[53] M. A. Hines, P. Guyot-Sionnest, *J. Phys. Chem*., 100, 2, 468-471, 1996

[54] M. Kuno, J. K. Lee, B. O. Dabbousi, F. V. Mikulec, M. G. Bawendi, *J. Chem. Phys*., 106, 23, 9869-9882, 1997

[55] M. Jones, S. S. Lo, G. D. Scholes, *Proceedings Nat. Acad. Sciences*, 106, 9, 3011-3016, 2009

[56] B. Mao, C. H. Chuang, J. Wang, C. Burda, *J. Phys. Chem. C*, 115, 18, 8945-8954, 2011

[57] B. Chen, H. Zhong, W. Zhang, Z. A. Tan, Y. Li, C. Yu, B. Zou, *Funct. Mat.*, 22, 10, 2081-2088, 2012

[58] N. Y. Morgan, S. English, W. Chen, V. Chernomordik, A. Russo, P. D. Smith, A. Gandjbakhche, *Academic radiology*, 12, 3, 313-323, 2005

[59] H. Mattoussi, G. Palui, H. B. Na, *Advanced drug delivery reviews*, 64, 2, 138-166, 2012

[60] X. Wu, H. Liu, J. Liu, K. N. Haley, J. A. Treadway, J. P. Larson, M. P. Bruchez, Nature biotechnology, 21(1), 41-46, 2002

[61] Murray *et. al, J. Am. Chem. Soc*., 115, 8706, 1993

[62] M. Gao *et. al*, *Expert Rev. Mol. Diagn*. 6(2), 231-244, 2006

[63] X. Gao, L. Qi, *ACS Nano*, 2008

[64] C. W. Chan, S. Nie, *Science*, 281, 5385, 2016-2018, 1998

[65] M. Bruchez, M. Moronne, P. Gin, S. Weiss, A. P. Alivisatos, Science, 281, 5385, 2013-2016, 1998

[66] A. Albanese, P. S. Tang, W. C. Chan, *Ann. Rev. Biomed. Eng.*, 14, 1-16, 2012

[67] A. Verma, F. Stellacci, *Small*, 6, 1, 12-21, 2010

[68] J. K. Jaiswal, S. M. Simon, *Trends in cell biology*, 14, 9, 497-504, 2004

[69] N. Gomez, J. O. Winter, F. Shieh, A. E. Saunders, B. A. Korgel, C. E. Schmidt, Talanta, 67, 3, 462-471, 2005

[70] T. A. Kelf, V. K. A. Sreenivasan, J. Sun, E. J. Kim, E. M. Goldys, A. V. Zvyagin, *Nanotech*., 21, 28, 285105, 2010

[71] X. Michalet, F. F. Pinaud, L. A. Bentolila, J. M. Tsay, S. Doose, J. J. Li, S. Weiss, S*cience*, *307*, 5709, 538-544.

[72] L. Ju, G. Zhang, C. Zhang, L. Sun, Y. Jiang, C. Yan, J. Yang, *Mutation Research/Genetic Toxicology and Environmental Mutagenesis*, 753, 1, 54-64, 2013

[73] A. J. Keefe, S. Jiang, *Nat. Chem*., 4, 59–63, 2012

[74] X. Liu, H. Zhu, Q. Jin, W. Zhou, V. L. Colvin, J. Ji, J. Adv. Health. mat., 2, 2, 352-360, 2013

[75] E. R. Goldman, E. D. Balighian, H. Mattoussi, M. K. Kuno, J. M. Mauro, P. T. Tran, G. P. Anderson, *J. Am. Chem.Soc*., 124, 22, 6378-6382, 2002

[76] X. Gao, Y. Cui, R. M. Levenson, L. W. Chung, S. Nie, *Nature biotechn*., 22, 8, 969-976, 2004

[77] K. C. Weng, C. O. Noble, B. Papahadjopoulos-Sternberg, F. F. Chen, D. C. Drummond, D. B. Kirpotin, J. W. Park, *Nano lett*., 8, 9, 2851-2857, 2008

[78] D. H. Huang, L. Su, X. H. Peng, H. Zhang, F. R. Khuri, D. M. Shin, *Nanotechnology*, 20, 22, 225102, 2009

[79] B. Dubertret, P. Skourides, D. J. Norris, V. Noireaux, A. H. Brivanlou, A. Libchaber, *Science*, 298, 5599, 1759-1762, 2002

[80] S. Park, Y. S. Kim, W. B. Kim, S. Jon, Nano letters, 9, 4, 1325-1329, 2009

[81] L. W. Zhang, N. A. Monteiro-Riviere, *Toxic. Sciences*, 110, 1, 138-155, 2009

[82] L. Ye, K. T. Yong, L. Liu, I. Roy, R. Hu, J. Zhu, P. N. Prasad, Nature nanotechnology, 7, 7, 453-458, 2012

[83] C. Ladhar, B. Geffroy, S. Cambier, M. Treguer-Delapierre, E. Durand, D. Brèthes, J. P. Bourdineaud, *Nanotox*., 8, 6, 676-685, 2014

[84] A. M. Derfus, W. C. Chan, S. N. Bhatia, *Nano lett.*, 4, 1, 11-18, 2004

[85] A. Hoshino, K. Fujioka, T. Oku, M. Suga, Y. F. Sasaki, T. Ohta, K. Yamamoto, *Nano Lett.*, 4, 11, 2163-2169, 2004

[86] C. Kirchner, T. Liedl, S. Kudera, T. Pellegrino, A. Muñoz Javier, H. E. Gaub, Parak, *Nano lett*., 5, 2, 331-338, 2005

[87] B. I. Ipe, M. Lehnig, C. M. Niemeyer, *Small*, 1, 7, 706-709, 2005

[88] T. S. Hauck, R. E. Anderson, H. C. Fischer, S. Newbigging, W. C. Chan, *Small*, 6, 1, 138-144, 2010

[89] S. Tamang, G. Beaune, I. Texier, P. Reiss, *ACS nano*, 5, 12, 9392-9402, 2011

[90] F. Dubois, B. Mahler, B. Dubertret, E. Doris, C. Mioskowski, *J. Am. Chem. Soc*., 129, 3, 482-483, 2007

[91] H. Yang, Y. Liu, Q. Shen, L. Chen, W. You, X. Wang, J. Sheng, *J. Am. Chem. Soc*., 22, 45, 24132-24138, 2012

[92] C. W. Lai, Y. H. Wang, Y. C. Chen, C. C. Hsieh, B. P. Uttam, J. K. Hsiao, P. T. Chou, *J. Mater. Chem.*, 19, 44, 8314-8319, 2009

[93] L. Jing, Y. Li, K. Ding, R. Qiao, A. L. Rogach, M. Gao, *Nanotechnology*, 22, 505104, 2011

[94] J. Nam, N. Won, J. Bang, H. Jin, J. Park, S. Jung, S. Kim, *Adv. drug deliv. rev.*, 65, 5, 622-648, 2013

[95] I. Potapova, R. Mruk, S. Prehl, R. Zentel, T. Basché, A. Mews, *J. Am. Chem. Soc*., 125, 2, 320-321, 2003

[96] T. Pellegrino, L. Manna, S. Kudera, T. Liedl, D. Koktysh, A. L. Rogach, W. J. Parak, *Nano Lett*, 4(4), 703-707, 2004

[97] R. E. Anderson, W. C. Chan, *ACS Nano*, 2, 7, 1341-1352, 2008

[98] D. Nida, N. Nitin, W. W. Yu, V. L. Colvin, R. Richards-Kortum, *Nanotechnology*, 19, 035701, 2008

[99] S. A. Diaz, G. O. Menendez, M. H. Etchehon, L. Giordano,T. M. Jovin, E. A. Jares-Erijman, *ACS Nano*, 5, 4, 2795–2805, 2011

[100] H. Duan, M. Kuang, Y. A. Wangi, *Chem. Mater*., 22, 4372–4378, 2010

[101] R. Koole, W. J. Mulder, M. M. Van Schooneveld, G. J. Strijkers, A. Meijerink, K. Nicolay, *Nanomed. Nanobiotech.*, 1, 5, 475-491, 2009

[102] L. Cheng, K. Yang, Y. Li, J. Chen, C. Wang, M. Shao, Z. Liu, *Angewandte Chemie*, 123, 32, 7523-7528, 2011

[103] S. Mornet, S. Vasseur, F. Grasset, E. Duguet, *J. Mater. Chem.*, 14, 14, 2161-2175, 2004

[104] C. S. Kumar, F. Mohammad, *Advanced drug delivery reviews*, 63, 9, 789-808, 2011

[105] D. A. Schwartz, N. S. Norberg, Q. P. Nguyen, J. M. Parker, D. R. Gamelin, *J. Am. Chem. Soc.*, 125, 43, 13205-13218, 2003

[106] D. J. Norris, N. Yao, F. T. Charnock, T. A. Kennedy, *Nano Lett.*, 1, 1, 3-7, 2001

[107] S. Wang, B. R. Jarrett, S. M. Kauzlarich, A. Y. Louie, *J. Am. Chem. Soc*., 13, 3848-3856, 2007

[108] J. E. Lee, N. Lee, T. Kim, J. Kim, T. Hyeon, *Acc. Chem. Research*, 44, 10, 893-902, 2011

[109] J. Kim, J. E. Lee, J. Lee, J. H. Yu, B. C. Kim, K. An, T. Hyeon, *J. Am. Chem. Soc*., 128, 3, 688-689, 2006

[110] T. R. Sathe, A. Agrawal, S. Nie, *Anal. chem*., 78, 16, 5627-5632, 2006

[111] W. J. Mulder, R. Koole, R. J. Brandwijk, G. Storm, P. T. Chin, G. J. Strijkers, A. W. Griffioen, *Nano lett*., 6, 1, 1-6, 2006

[112] F. Erogbogbo, C. W. Chang, J. L. May, L. Liu, R. Kumar, W. C. Law, P. N. Prasad, *Nanoscale*, 4, 17, 5483-5489, 2012

[113] J. Gao, B. Zhang, Y. Gao, Y. Pan, X. Zhang, B. Xu, *J. Am. Chem. Soc*., 129, 39, 11928-11935,

2007

[114] G. J. Strijkers, M. Mulder, J. Willem, F. van Tilborg, A. Geralda, K. Nicolay, Anti-Cancer Agents Med. Chem., 7, 3, 291-305, 2007

[115] J. Dobson, *Gene therapy*, 13, 4, 283-287, 2006

[116] W. K. Leutwyler, S. L. Bürgi, H. Burgl, Science, 271, 5251, 933-937, 1996

[117] C. Murray, D. J. Norris, M. G. Bawendi, *J. Am. Chem. Soc*., 115, 19, 8706-8715, 1993

[118] J. E. B. Katari, V. L. Colvin, A. P. Alivisatos, *J. Phys. Chem. 98*, 4109-4117, 1994

[119] J. Chang, E. R. Waclawik, *Cryst. Eng. Comm.*, 15, 28, 5612-5619, 2013

[120] A. Kharkwal, S. N. Sharma, K. Jain, A. K. Singh, *Mat. Chem. Phys*., 144, 3, 252-262, 2014

[121] X. Peng, J. Wickham, A. P. Alivisatos, *J. Am. Chem. Soc.*, 120, 21, 5343-5344, 1998

[122] V. Lesnyak, N. Gaponik, A. Eychmüller, *Chem. Soc. Rev*., 42, 7, 2905-2929, 2013

[123] J. W. Haus, H. S. Zhou, I. Honma, H. Komiyama, *Phys.Rev. B*, 47, 3, 1359, 1993

[124] A. R. Kortan, R. Hull, R. L. Opila, M. G. Bawendi, M. L. Steigerwald, P. J. Carroll, L. E. Brus, *J. Am. Chem. Soc.*, 112, 4, 1327-1332, 1990

[125] S. S. Lo, T. Mirkovic, C. H. Chuang, C. Burda, G. D. Scholes, *Adv. Mat*., 23, 2, 180-197, 2011

[126] Y. Desmet, L. Deriemaeker, e. Parloo, r. Finsy**.** *Langmuir*, **15,** 2327-2332, 1999

[127] J. B. Rivest, P. K. Jain, *Chem. Soc. Rev*., 42, 1, 89-96, 2013

[128] B. Tell, J. L. Shay, H. M. Kasper, *Phys. Rev. B*, 4, 8, 2463, 1971

[129] H. Y. Ueng, H. L. Hwang, *J. Phys. Chem. Sol.*, 50, 12, 1297-1305, 1989

[130] J. L. Shay, B. Tell, H. M. Kasper, L. M. Schiavone, *Phys. Rev. B*, 5, 12, 5003, 1972

[131] K. Yoodee, J. C. Woolley, V. Sa-Yakanit, *Phys. Rev. B*, 30, 10, 5904, 1984

[132] F. Abou-Elfotouh, D. J. Dunlavy, D. Cahen, R. Noufi, L. L. Kazmerski, K. J. Bachmann, *Prog. Crys. Growth Char*., 10, 365-370, 1984

[133] C. Czekelius, M. Hilgendorff, L. Spanhel, I. Bedja, M. Lerch, G. Müller, U. Bloeck, D. S. Su, M. Giersig, *Adv. Mater.*, 11, 643-646, 1999

[134] P. Reiss, M. Protiere, L. Li, *Small*, 5, 154−168, 2009

[135] M. Yakushev, R. W. Martin, A. V. Mudryi, A. V. Ivaniukovich, *Appl. Phys. Lett.*, 92, 11, 2008

[136] T. Rajh, O. I. Micic, A. J. Nozik, *J. Phys. Chem*., 97, 11999−12003, 1993

[137] J. Z. Zhang, *J. Phys. Chem. B*, 104, 7239−7253, 2000

[138] M. Chamarro, C. Gourdon, P. Lavallard, O. Lublinskaya, A. I. Ekimov, *Il Nuovo Cimento D*, 17, 1407−1412, 1995

[139] M. Yakushev, A. V. Mudryi, I. V. Victorov, J. Krustok, E. Mellikov, *Appl. Phys. Lett*., 88, 11922, 2006

[140] L. Rosenblum, N. Kosaka, M. Mitsunaga, P. Choyke, H. Kobayashi, *Mol. Membr. Biol*., 7, 274−285, 2010

[141] B. Zhang, *Nanotechnology*, 14, 443, 2003

[142] L. Li, A. Pandey, D. J. Werder, B. P. Khanal, J. M. Pietryga, V. I. Klimov, *J. Am. Chem. Soc.*, 133, 1176-1179, 2011

[143] D. E. Nam, W. S. Song, H. Yang, *J. Colloid Interface Sci.*, 361, 491-496, 2011

[144] J. Park, S.W. Kim, *J. Mater. Chem.*, 21, 3745-3750, 2011

[145] H. Z. Zhong, Y. Zhou, M. F. Ye, Y. J. He, J. P. Ye, C. He, C. H. Yang, Y. F. Li, *Chem. Mater.*, 20, 6434-6443, 2008

[146] L. Li, T. J.Daou, I. Texier, T. K. C. Tran, Q. L. Nguyen, P. Reiss, *Chem. Mater.*, 21, 2422-2429,